



Kent Academic Repository

Assimakopoulos, Philippos (2012) *Nonlinear effects in OFDM signal transmission over radio over fibre links*. Doctor of Philosophy (PhD) thesis, University of Kent.

Downloaded from

<https://kar.kent.ac.uk/94180/> The University of Kent's Academic Repository KAR

The version of record is available from

<https://doi.org/10.22024/UniKent/01.02.94180>

This document version

UNSPECIFIED

DOI for this version

Licence for this version

CC BY-NC-ND (Attribution-NonCommercial-NoDerivatives)

Additional information

This thesis has been digitised by EThOS, the British Library digitisation service, for purposes of preservation and dissemination. It was uploaded to KAR on 25 April 2022 in order to hold its content and record within University of Kent systems. It is available Open Access using a Creative Commons Attribution, Non-commercial, No Derivatives (<https://creativecommons.org/licenses/by-nc-nd/4.0/>) licence so that the thesis and its author, can benefit from opportunities for increased readership and citation. This was done in line with University of Kent policies (<https://www.kent.ac.uk/is/strategy/docs/Kent%20Open%20Access%20policy.pdf>). If you ...

Versions of research works

Versions of Record

If this version is the version of record, it is the same as the published version available on the publisher's web site. Cite as the published version.

Author Accepted Manuscripts

If this document is identified as the Author Accepted Manuscript it is the version after peer review but before type setting, copy editing or publisher branding. Cite as Surname, Initial. (Year) 'Title of article'. To be published in *Title of Journal*, Volume and issue numbers [peer-reviewed accepted version]. Available at: DOI or URL (Accessed: date).

Enquiries

If you have questions about this document contact ResearchSupport@kent.ac.uk. Please include the URL of the record in KAR. If you believe that your, or a third party's rights have been compromised through this document please see our [Take Down policy](https://www.kent.ac.uk/guides/kar-the-kent-academic-repository#policies) (available from <https://www.kent.ac.uk/guides/kar-the-kent-academic-repository#policies>).

Nonlinear effects in OFDM signal transmission over radio over fibre links

A Thesis Submitted to The University of Kent

For the Degree of Doctor Of Philosophy In Electronic Engineering

By

Philippos Assimakopoulos

June, 2012

Abstract

The dynamic range limitations that arise from nonlinearity in low-cost and low complexity directly modulated radio over fibre (RoF) links are examined. Statistical nonlinear models are presented and applied to the case of a RoF link with a low biased laser diode. The effects of distortion on the Error Vector Magnitude (EVM) performance of Orthogonal Frequency-Division Multiplexing (OFDM) signals with different numbers of subcarriers and the connection to the Peak-to-Average Power Ratio (PAPR) of the signals are investigated. Statistical distributions of the EVM over a large number of transmitted OFDM frames are gained from experimental measurements and analyses of idealized processes. The measurement results show that as the number of subcarriers is reduced the distribution means are not dependent in the expected way on the statistical PAPR of the transmitted OFDM signals. Instead, it is shown that in regions of moderate distortion the median of the EVM is more closely related to the statistical PAPR and to the required back-off for signals with different numbers of subcarriers. Through the employed statistical analysis, the asymptotic convergence of the EVM result to that expected in the idealized case is observed. The results of this analysis also show, how, including the EVM variance in estimations for back-off might be useful, how, in a measurement, the number of transmitted OFDM frames affects the estimated mean EVM. Differing EVM results for subcarriers at the edge and middle of the signal band show that distortion affects the subcarriers at the middle of the band to a stronger degree and that their behaviour is correlated to the statistical PAPR of the individual signals. Then, a laser model validated against measured performance is designed and used for simulating the performance of a subcarrier multiplexed 4th generation mobile/wireless RoF transmission system. Predictions indicate that the architecture provides adequate performance in terms of EVM, for different IFFT sizes and modulation levels of up to 256 QAM (at least), and a combined raw data rate of up to 3.2 Gbps. Based on a 1.5% EVM transmitter requirement with 256 QAM, a system dynamic range of approximately 5.1 dB is predicted. Finally, the use of companding in a directly modulated RoF link, with the aim of reducing the amplification (and isolation) requirements in the remote antenna unit, is demonstrated, quantified through EVM measurements. The resulting improvements in output power are approximately 4.7 dB at an EVM transmitter requirement of 5.6 %, while in terms of the point of onset of distortion-induced EVM increase, the improvement is approximately 7.6 dB.

Acknowledgements

I would foremost like to thank my supervisor Dr Nathan Gomes, for giving me the opportunity to work in this field and for his valuable guidance and support that were necessary for the completion of this work.

I thank Anthony Nkansah, for his help and for being a good collaborator and a friend.

I am grateful to Dr David Wake, for his feedback in some aspects of this work.

I acknowledge the financial support from the EU project "FUTON" (FP7), for some of the main parts in this thesis.

Finally, I thank my friends and family for their support throughout these years.

List of Publications

Publications that have directly contributed into the Thesis:

[P1] P. Assimakopoulos, L. Vieira, A. Nkansah, D. Wake, N. J. Gomes, and F. van Dijk, "Modelling of a DFB laser at low bias directly modulated with an OFDM signal for RoF applications," in *Proc. IEEE Int. Topical Meeting on Microwave Photonics*, Valencia, Spain, 2009, pp. 1-4.

[P2] D. Wake, A. Nkansah, P. Assimakopoulos, N. Gomes, M. Violas, L. Zhansheng, S. Pato, F. Ferreira, G. De Valicourt, R. Brenot, and F. Van Dijk, "Design and performance of radio over fibre links for next generation wireless systems using distributed antennas," in *Proc. Future Network and Mobile Summit*, Florence, Italy, 2010, pp. 1-9.

[P3] P. Assimakopoulos, A. Nkansah, N. J. Gomes, and D. Wake, "Multi-channel signal transmission through radio over fiber architecture," in *Proc. IEEE Globecom Workshops*, Houston, TX, 2011, pp. 152-156.

[P4] P. Assimakopoulos, A. Nkansah and N. J. Gomes, "Use of Companding to Reduce Isolation Requirements in the Remote Antenna Unit of an OFDM Radio over Fiber Link," in *Proc. IEEE Int. Conf. of Communications (ICC)*, Budapest, Hungary, 2013.

[P5] P. Assimakopoulos, A. Nkansah, N. J. Gomes and D. Wake, "Statistical distribution of EVM measurements for direct-modulation radio over fiber links transporting OFDM signals," *IEEE Trans. Microw. Theory Tech.*, vol. 61, no. 4, pp. 1709-1717, Apr. 2013.

[D1] FUTON deliverable D5.3, "Modelling and interim predicted performance of radio overfibre distribution network". Available: <http://www.ict-futon.eu/deliverables.aspx>.

[D2] FUTON deliverable D5.7, "Performance of radio over fibre distribution network". Available: <http://www.ict-futon.eu/deliverables.aspx>.

Additional publications:

[P6] P. Assimakopoulos, A. Nkansah, and N. J. Gomes, "Use of commercial Access Point employing spatial diversity in a Distributed Antenna Network with different fiber lengths," in *Proc. IEEE Int. Topical Meeting on Microwave Photonics*, Gold Coast, Australia, 2008, pp. 189-192.

[P7] P. Assimakopoulos, V. Sittakul, A. Nkansah, N. Gomes, M. Cryan, and D. Wake, "Comparison between remote Antenna Units with Detachable antennas and Photonic Active Integrated Antennas for indoor applications," in *Proc. General Assembly and Scientific Symp. (URSI)*, Istanbul, Turkey, 2011, pp. 1-4.

[P8] P. Assimakopoulos, A. Nkansah and N.J. Gomes, "Use of Commercial Access Point Employing Spatial Diversity with Switched Combining in a Distributed Antenna Network", *6th IIS Workshop of FTTH, Wireless Communications and their Interaction*, Stockholm, Sweden, 2008.

[P9] L.C. Vieira, A. Nkansah, P. Assimakopoulos and N.J. Gomes, "Performance of 802.11g Signals over a Multimode Fibre-fed Distributed Antenna System incorporating Optical Splitting", *European Workshop on Photonic Solutions for Wireless, Access and In-house Networks*, Duisburg, Germany, 2009.

Table of Contents

1	INTRODUCTION	9
1.1	Analogue radio-over-fibre links	9
1.2	Motivation for the Thesis	11
1.3	Research Aims.....	13
1.4	Structure of the Thesis.....	15
2	BACKGROUND THEORY.....	16
2.1	Orthogonal Frequency Division Multiplexing	16
2.1.1	Cyclic prefix	19
2.1.2	Synchronization issues in OFDM	21
2.1.3	IQ modulator and IQ imbalance	24
2.2	Error Vector Magnitude and other measures of link performance.....	24
2.3	Direct IM-DD radio-over-fibre links	28
2.3.1	Gain of direct IM-DD links	28
2.3.2	Noise performance.....	29
2.3.3	Nonlinear performance	33
2.3.4	Dynamic range definitions for analogue optical links	37
2.3.5	OFDM transmission through direct IM-DD radio-over-fibre links.....	40
3	PAPR ANALYSIS AND TRANSMISSION OF OFDM THROUGH NONLINEARITIES 43	
3.1	Introduction.....	43
3.2	Peak-to-Average Power Ratio.....	43
3.2.1	PAPR general case	43
3.2.2	PAPR of OFDM.....	47
3.3	Transmission of OFDM through nonlinearities.....	52
3.3.1	Direct method	52
3.3.2	Output autocorrelation function.....	58
3.4	Modelling of low bias laser using the direct method	62
3.4.1	Polynomial modelling.....	63
3.4.2	Simulation results.....	65
3.5	Modelling of low biased laser using the output autocorrelation function.....	67
3.6	Extension to arbitrary AM/AM characteristic with phase distortion	73

3.7	Conclusions	73
4	STATISTICAL DISTRIBUTION OF EVM MEASUREMENTS FOR DIRECT-MODULATION RADIO OVER FIBRE LINKS TRANSPORTING OFDM SIGNALS	75
4.1	Introduction	75
4.1.1	Some initial remarks	76
4.2	Statistical Methodology	79
4.3	Measurement procedure	83
4.4	Initial results	85
4.5	EVM per frame distributions	89
4.5.1	Additional measures of normality	96
4.6	Raw EVM distributions	98
4.7	Conclusions	106
5	BACK-OFF ESTIMATIONS AND EVM AT DIFFERENT LOCATIONS IN THE SIGNAL BAND	107
5.1	Introduction	107
5.2	Back-off estimation from the mean EVM per frame	107
5.3	Effect of the number of transmitted frames in the back-off estimation from the EVM measured result	113
5.4	EVM of subcarriers at different locations in the signal band	116
5.5	Conclusions	124
6	USE OF COMPANDING FOR RADIO OVER FIBRE LINKS	125
6.1	Introduction	125
6.2	Amplifier stability and crosstalk issues	127
6.3	Companding procedure	130
6.4	Measurement procedure	135
6.5	Measurement Results	136
6.6	Conclusions	139
7	RATE EQUATION MODELLING	140

7.1	Introduction.....	140
7.2	Rate Equations.....	141
7.2.1	Steady state conditions	144
7.2.2	Dynamic effects.....	146
7.3	Laser modelling.....	146
7.3.1	Model results.....	149
7.3.2	Model validation with EVM 802.11g measured results	156
7.3.3	Model validation with EVM 802.11n measured results	160
7.4	Multi-channel performance predictions.....	162
7.5	Conclusions	167
8	CONCLUSIONS AND FUTURE WORK	169
8.1	Conclusions	169
8.2	Main Contributions of the Thesis	172
8.3	Future work	173

List of abbreviations

ADC	Analogue-to-Digital Converter
AM/AM	Amplitude Modulation-to-Amplitude Modulation
AM/PM	Amplitude Modulation-to-Phase Modulation
AP	Access Point
AWGN	Additive White Gaussian Noise
BS	Base Station
CCDF	Complementary Cumulative Distribution Function
CDF	Cumulative Distribution Function
CLT	Central Limit Theorem
CU	Central Unit
CP	Cyclic Prefix
DAS	Distributed Antenna System
DAC	Digital-to-Analogue Converter
DBWS	Distributed Broadband Wireless System
DFB	Distributed Feedback
DFT	Discrete Fourier Transform
DL	Downlink
DSB-SC	Double-Sideband Suppressed Carrier
E/O	Electrical-to-Optical
EVM	Error Vector Magnitude
FDD	Frequency Division Duplex
FFT	Fast Fourier Transform
FT	Fourier Transform
FUTON	Fibre Optic Networks for Distributed and Extendible Heterogeneous Radio Architectures and Service Provisioning
Gbps	Gigabits-per-second
ICI	Inter-Carrier Interference
IF	Intermediate Frequency
IFFT	Inverse Fast Fourier Transform
i.i.d	Independent and Identically Distributed
IM/DD	Intensity Modulation and Direct Detection
IP ₂	2 nd order Interception Point
IP ₃	3 rd order Interception Point
ISI	Inter-Symbol Interference
JPU	Joint Processing Unit

LO	Local Oscillator
LTE	Long-Term Evolution
MIMO	Multiple-Input Multiple-Output
MMF	Multimode Fibre
NF	Noise Figure
O/E	Optical-to-Electrical
OFDM	Orthogonal Frequency Division Multiplexing
OFDMA	Orthogonal Frequency Division Multiple Access
P1dB	1-dB Compression Point
P/S	Parallel-to-Serial
PAPR	Peak-to-Average Power Ratio
PDF	Probability Distribution Function
PIN-PD	PIN Photodiode
PoF	Power-over-Fibre
PSD	Power Spectral Density
QAM	Quadrature Amplitude Modulation
QPSK	Quadrature Phase Shift Keying
RAU	Remote Access Unit
RF	Radio Frequency
RIN	Relative Intensity Noise
RMS	Root-Mean-Square
RoF	Radio-over-Fibre
S/P	Serial-to-Parallel
SCM	Sub-Carrier Multiplexing
SFDR	Spurious Free Dynamic Range
SMF	Single-Mode Fibre
SNR	Signal-to-Noise Ratio
TDD	Time Division Duplex
VCSEL	Vertical Cavity Surface Emitting Laser
VSA	Vector Signal Analyzer
VSG	Vector Signal Generator

List of Figures

Fig. 1.1: Example of a DAS with two RAUs serving mobile users in different locations.	9
Fig. 1.2: A typical direct modulation and direct detection RoF link. E/O: Electro-optical conversion, O/E: Optical-electrical conversion, Amp: Amplifier.....	10
Fig. 1.3: Typical direct IM-DD RoF link with electrical amplification showing main performance issues and impairments.....	12
Fig. 1.4: The FUTON architecture [15].....	13
Fig. 2.1: OFDM transmitter and receiver architectures.	16
Fig. 2.2: Frequency domain representation of the OFDM signal.	18
Fig. 2.3: PSD of OFDM signal with 512 subcarriers	18
Fig. 2.4: Example of CP insertion with time duration t_{CP}	20
Fig. 2.5: Time misalignment between received symbol and FFT time window.	21
Fig. 2.6: Wrong sampling times due to LO offsets	22
Fig. 2.7: Diagram of IQ modulator showing the various parts that can cause imbalance.	24
Fig. 2.8: The magnitude and phase errors as defined on the IQ constellation plane.	25
Fig. 2.9: Normalization to an average power of 1 of a received constellation that has experienced some arbitrary gain and phase rotation from a link.	27
Fig. 2.10: Example of an EVM plot versus input power.	28
Fig. 2.11: Noise figure versus average photocurrent and noise figure dependencies on the individual noise sources for $RIN=150 \text{ dBHz}^{-1}$, $G=-10 \text{ dB}$	31
Fig. 2.12: Set-up for noise measurements using a spectrum analyzer.	32
Fig. 2.13: Harmonic distortion components and amplitudes for a polynomial model.	34
Fig. 2.14: Example of 1 dB compression measurement result. Two different methods are shown, one using the output power versus input power result and the other using the gain versus input power result.	35
Fig. 2.15: Representation of Intermodulation products in the frequency domain.....	36
Fig. 2.16: Measurement set-up for 2-tone test using a spectrum analyzer.....	37
Fig. 2.17: Example of 2-tone measurement result, showing IP_2 and IP_3 points with the fundamental frequency at 2.4 GHz.....	37
Fig. 2.18: Dynamic range definition based on the P1dB.	38
Fig. 2.19: SFDR definition based on the 3rd order intercepts point.	39
Fig. 2.20: Dynamic range definition based on the EVM.....	40
Fig. 2.21: Comparison of throughput results for different fibre lengths when fed by both AP ports (diversity) and when fed by a single AP port (no diversity). The lines between symbols are only an aid for viewing the results and do not represent predicted trends. Distance measured is between the two RAUs [47].....	41
Fig. 2.22: Throughput results for 802.11g experiment a) downlink and b) uplink. The red lines indicate the maximum theoretical throughput of 802.11g [49].....	42
Fig. 3.1: Information signal (envelope)	44
Fig. 3.2: Modulated carrier.....	44
Fig. 3.3: Plot of the amplitude of the modulated signal squared.	45

Fig. 3.4: CCDF of PAR for different number of carriers (N= 64, 512, 1024, 2048), including the case when the symbols are bandlimited (oversampling) for N=64 and N=2048.....	50
Fig. 3.5: CCDF plots of the PAPR of the up-converted OFDM signal.....	51
Fig. 3.6: PDF of PAPR of 128, 512, 2048 and 4096 subcarriers.	52
Fig. 3.7: Rapp model [62] approximating the soft limiter. This is done by using a high value for the parameter controlling the sharpness of the region between the linear and saturation parts.	55
Fig. 3.8: EVM versus clipping ratio for simulation and analytical. Modulation is QPSK and No. of subcarriers = 2048.....	56
Fig. 3.9: Variation between simulated and analytical EVM for different number of subcarriers. Clipping ratio = 1.75 (4.9 dB), modulation is QPSK.	57
Fig. 3.10: Plot of variation between simulated and analytical EVM for different QAM level. Clipping ratio = 1.75 (4.9 dB), No. of subcarriers = 1024.	57
Fig. 3.11: PSD of input signal.....	58
Fig. 3.12: (a) 3-fold convolution, (b) 5-fold convolution of input PSD (Fig. 3.11).	60
Fig. 3.13: Simulation and analytic results for different CR values.	61
Fig. 3.14: Optical link equivalent circuit.	62
Fig. 3.15 : Input Rayleigh PDF (dotted black line) and output PDF (red line) of clipping nonlinearity.....	63
Fig. 3.16: Experimental set-up for AM/AM measurements.....	64
Fig. 3.17: AM/AM characteristic of the DFB laser using (a) a 7 th -order polynomial model and (b) the modified Rapp model.	65
Fig. 3.18: Simulation results for biases of 35 mA and 37 mA.....	66
Fig. 3.19: Comparison between modified Rapp and polynomial models at 35 mA with respect to the analytical result.	66
Fig. 3.20: Static response of laser diode and normalised to zero mean input.....	67
Fig. 3.21: Input (right) and output (left) PDFs of the nonlinearity.....	68
Fig. 4.1: Ensemble of the EVM measurements.	77
Fig. 4.2: Simulated EVM results for 128 and 512 subcarriers using a clipping (soft-limiter) nonlinearity.	78
Fig. 4.3: The RoF link. DFB: Distributed Feedback laser; PD: Photodiode; Att optical attenuator.	79
Fig. 4.4: Diagram showing how the EVM measurement results are interpreted for the employed statistical methodology.....	81
Fig. 4.5: Detailed Flow-chart of the measurement procedure.	84
Fig. 4.6: P1dB measurement result.....	84
Fig. 4.7: Un-equalized average EVM versus input power for different number of subcarriers with QPSK modulation over 450 OFDM frames.....	85
Fig. 4.8: Average EVM versus input power for different number of subcarriers with QPSK modulation over 450 OFDM frames with a) Equalizer 1 and b) Equalizer 2.....	87
Fig. 4.9: Average EVM variance for different number of subcarriers for a) Equalizer 1 and b) Equalizer 2.	88
Fig. 4.10: EVM per frame CCDFs for 128 and 512 subcarriers at two input powers at the noise limited end of the EVM. The distributions have equal means but the SD of 128 subcarriers is approximately double that of 512 subcarriers.	89

Fig. 4.11: Histogram plot of the average EVM per frame over 450 frames for 128, 512 and 4096 subcarriers at input powers of (a) 9.45 dBm, (b) 11.8 dbm and c) 13.6 dBm with fitted log-normal distributions using Equalizer1.....	91
Fig. 4.12: Histogram plot of the average EVM per frame over 450 frames for 128, 512 and 4096 subcarriers at input powers of (a) 9.45 dBm, (b) 11.8 dbm and (c) 13.6 dBm with fitted log-normal distributions using Equalizer 2.....	92
Fig. 4.13: Variance of measured EVM per frame for different numbers of subcarriers normalized by the variance of the 128 subcarrier signal result.....	94
Fig. 4.14: Skew of the distributions at different input powers for (a) Equalizer 1 and (b) Equalizer 2.....	95
Fig. 4.15: Effect of randomizing the location (or order in time) of the raw EVM values prior to averaging across frames.....	96
Fig. 4.16: Comparison of measured CCDFs with normal CCDFs.....	97
Fig. 4.17: Kurtosis of the distributions at different input powers.....	97
Fig. 4.18: Distributions of the raw EVM for 128 and 512 subcarriers at input powers of (a) 9.45 dBm and (b) 13.2 dbm for Equalizer 1. The dashed traces are Rayleigh fits.....	99
Fig. 4.19: Distributions of the raw EVM for 128 and 512 subcarriers at input powers of (a) 9.45 dBm and (b) 13.6 dbm for Equalizer 2. The dashed traces are Rayleigh fits.....	100
Fig. 4.20: Skew and kurtosis of the raw EVM distributions for 128, 512 and 4096 subcarriers. The dotted lines are the Rayleigh distribution skew and kurtosis.....	101
Fig. 4.21: Absolute difference between mean and median for 128 and 512 subcarriers.....	103
Fig. 4.22: Mean and median results of the raw EVM distributions versus input power for Equalizer 1.....	104
Fig. 4.23: Mean and median results of the raw EVM distributions versus input power for Equalizer 2.....	104
Fig. 4.24: Normalized median result for 128, 512 and 4096 subcarriers.....	105
Fig. 5.1: Theoretical variation of the log-normal sigma parameter with variance for a log-normal distribution at different mean values.....	108
Fig. 5.2: Theoretical variation of skew with variance for a log-normal distribution at different mean values.....	109
Fig. 5.3: CCDF at an input power of 10.9 dBm with log-normal and Gaussian fits for (a) 1024 subcarriers and (b) 2048 subcarriers.....	111
Fig. 5.4: Gaussian fitted PDFs for 1024 and 2048 subcarriers at an input power of 10.9 dBm with annotated confidence intervals at one and two standard deviations from the mean.....	111
Fig. 5.5: CCDF plots for 128 and 512 subcarriers at an input power of 10.9 dBm with log-normal fits.....	112
Fig. 5.6: Original PDF for 512 subcarriers at an input power of 10.9 dBm and the log transformed PDF showing confidence intervals at one and two standard deviations from the mean. The corresponding EVM values at those confidence intervals for the original distribution are obtained by taking anti-logs of the values of the log-transformed distribution.....	112
Fig. 5.7: Average EVM versus input power result for 512 sub-carriers and 4QAM modulation for different numbers of OFDM frames showing the differences in the average result between different selections of frames.....	114

Fig. 5.8: Average EVM versus input power result for 4096 sub-carriers and 4QAM modulation for different numbers of OFDM frames showing the differences in the average result between different selections of frames.	115
Fig. 5.9: 95 % confidence interval size versus number of OFDM frames for different IFFT sizes.	115
Fig. 5.10: Evm versus subcarrier number across 10 symbols with 512 (420 data) subcarriers at an input power of 8.5 dBm.	117
Fig. 5.11: EVM versus subcarrier number for (a) 512 subcarriers and (b) 4096 subcarriers at an input power of 8.5 dBm.	118
Fig. 5.12: Evm versus subcarrier number over 10 symbols with 512 (420 data) subcarriers at an input power of 13.2 dBm.	118
Fig. 5.13: Mean EVM results for subcarriers at the edge and middle of the band and average EVM across all transmitted subcarriers in all the frames for a signal with 4096 subcarriers...	120
Fig. 5.14: Mean EVM results for subcarriers at the edge and middle of the band and average EVM across all transmitted subcarriers in all the frames for a signal with 512 subcarriers.....	120
Fig. 5.15: Mean EVM results for subcarriers at the edge and middle of the band and average EVM across all transmitted subcarriers in all the frames for a signal with 128 subcarriers.....	121
Fig. 5.16: Variation of four statistical measures (mean, median, variance and skew) with input power for a subcarrier located at the edge of the band for a signal with 512 subcarriers.	122
Fig. 5.17: Variation of four statistical measures (mean, median, variance and skew) with input power for a subcarrier located at the middle of the band for a signal with 512 subcarriers...	122
Fig. 5.18: Variation of four statistical measures (mean, median, variance and skew) with input power for a subcarrier located at the edge of the band for a signal with 4096 subcarriers.	123
Fig. 5.19: Variation of four statistical measures (mean, median, variance and skew) with input power for a subcarrier located at the middle of the band for a sign al with 4096 subcarriers.	123
Fig. 6.1: Diagram of directly modulated IM-DD RoF architecture. Att: Attenuator, Amp: Amplifier, PIN-PD: PIN photodiode.	126
Fig. 6.2: Simplified diagram of SCM architecture.....	126
Fig. 6.3: RAU diagram showing the two issues discussed here.....	127
Fig. 6.4: Diagram of the downlink section of a RAU, showing how the crosstalk signal interferes with the signal exiting the PD.	128
Fig. 6.5: Effect on downlink signal power in the presence of in phase and out of phase feedback crosstalk interference.	129
Fig. 6.6: Downlink amplifier gain and antenna/photodiode isolation requirements for different levels of RF power at the photodiode output for targeted RAU transmit powers of 20dBm and 30dBm. Antenna-PD isolation also incorporates a targeted wanted and feedback signal ratio (R) of 10dB. PPD = RF power exiting photodiode.....	130
Fig. 6.7: Diagram of the RoF link showing the envelope companding process.....	131
Fig. 6.8: Compression functions for different μ values.	132
Fig. 6.9: Different companding regimes based on the choice of the V_{max} parameter for a given μ value. $x_{max}(t)$ is the maximum amplitude of the input signal and PAPR is the peak-to-average power ratio of the signal.	133
Fig. 6.10: Input and output PDFs for μ values of 1, 2 and 10 with $V_{max}=1$ and $\sigma=0.1$	134
Fig. 6.11: Flow-chart of the measurement procedure. LD: Laser Diode, PD: Photodiode, VSG: Vector Signal Generator , VSA: Vector Signal Analyser.....	135

Fig. 6.12: EVM versus input power for $V_{max}= 1/4$ and μ of 10, 2 and 1. Optical link b2b is the case without companding	137
Fig. 6.13: EVM versus output power for $V_{max}= 1/4$ and μ of 10, 2 and 1. Optical link b2b is the case without companding	138
Fig. 7.1: Dependence of material gain to carrier density. Above transparency, the dependence is approximately linear.....	143
Fig. 7.2: Example of laser diode static response showing the two parameters that are fit: threshold current and slope efficiency.	148
Fig. 7.3: Example of laser diode dynamic response showing how the intrinsic response is “masked” by parasitic packaging filtering.....	149
Fig. 7.4: Modelled and measured P-I characteristics (output light power versus input bias current).	151
Fig. 7.5: Measured and modelled frequency responses at a bias of 40 mA.	152
Fig. 7.6 : Subtracted frequency responses obtained by subtracting the response at 10 mA bias current from the responses at 15 mA, 25 mA and 40 mA bias currents.	152
Fig. 7.7: Measured and modelled P1dB results at 1.2 GHz.	153
Fig. 7.8: Measured and modelled P1dB results at 1.8 GHz.	154
Fig. 7.9: Modelled and measured 2-tone test results with overlaid linear trend lines (dark traces) for intercept point estimation. The main tone frequency is at 1.8 GHz. Note that for these results no optical attenuation was used as it was found that in this way the measurement results were more stable. The effect of a 10 dB optical attenuator would be to reduce the OIP ₃ by 20 dB while the IIP ₃ would remain the same.....	155
Fig. 7.10: Set up for single channel 802.11g simulations in VPI™ (note that some blocks that were used during simulation have been omitted to simplify the diagram).	157
Fig. 7.11: Set up for single channel 802.11g simulations in VPI™.	157
Fig. 7.12: Measured and modelled EVM results at carrier frequencies of (a) 1.2GHz, (b) 1.4 GHz, (c) 1.6 GHz and (d) 1.8 GHz.	160
Fig. 7.13: Measured and modelled EVM 802.11n results at carrier frequencies of (a) 1.2GHz and (b) 1.8 GHz.....	161
Fig. 7.14: Simplified diagram of SCM RoF system. IF is Intermediate Frequency, λ is wavelength.	162
Fig. 7.15: Actual SCM RoF system simulation set-up in VPI™	162
Fig. 7.16: Prediction of EVM performance for simultaneous 4-channel and single 1.2 GHz channel transmissions for 512 OFDM subcarriers and 256 QAM.....	165
Fig. 7.17: Prediction of EVM performance for simultaneous 4-channel transmission for 128 OFDM subcarriers and 64 QAM.	165
Fig. 7.18: Prediction of EVM performance for simultaneous 4-channel transmission for 512 OFDM subcarriers and 64 QAM.	166
Fig. 7.19: Prediction of EVM performance for simultaneous 4-channel transmission for 1024 OFDM subcarriers and 64 QAM.	166
Fig. 7.20: Comparison between 512 and 2048 IFFT sizes with 256 QAM modulation at a frequency of 1.2 GHz.....	167

List of Tables

Table 2.1: Typical NF values for commercially available optical transceiver modules.	32
Table 2.2: Typical IIP ₃ and SFDR values for commercially available optical transceiver modules.	39
Table 2.3 [35, 44]: Transmitter EVM specification requirements for different modulation formats. Note that these values depend on the coding rate used.	40
Table 3.1 [55, p. 162]: PAPR of different QAM levels	47
Table 4.1: Summary of fitted normal distribution parameters (mean and standard deviation) for the noise limited end performance (Fig. 4.10).	90
Table 4.2: Summary of fitted log-normal distribution parameters for Equalizer 1: σ^2 is the variance, μ is the median and m is the mean.	93
Table 4.3: Summary of fitted log-normal distribution parameters for Equalizer 2: σ^2 is the variance, μ is the median and m is the mean.	93
Table 4.4: Coefficient of variation (CV) results at different input powers.	98
Table 4.5: Goodness of fit measures for the fitting between the raw EVM distributions and the Rayleigh distributions. SSE: Standard Squared Error; RMSE: Root Mean Square Error.	101
Table 6.1: PAPR values for different μ parameters when $V_{max}=1/4$	137
Table 7.1: Parameters used for the modelling of the DFB laser diode.	150
Table 7.2: Summarized results for measured and modelled P1dB results at 1.2 GHz, 1.4 GHz, 1.6 GHz and 1.8 GHz.	154
Table 7.3: Summarized results for 2-tone test at 1.8 GHz. (M) stands for Model and (E) stands for experiment, IIP stands for Input Intercept Point and OIP stands for Output Intercept Point.	156

1 Introduction

1.1 Analogue radio-over-fibre links

The use of Radio-over-Fibre (RoF) techniques for the distribution of analogue signals has attracted much attention in the last few years [1-5]. The use of fibre instead of co-axial cables in the distribution of Radio Frequency (RF) has certain advantages, namely low attenuation at RF frequencies, low cost and ease of installation. Therefore, fibre links can, in principle, span much longer distances. Applications for such systems include antenna remoting, Distributed Antenna Systems (DAS) and more recently base station hotels, that are of interest to mobile phone signal providers [1]. An example of a typical DAS is shown in Fig. 1.1.

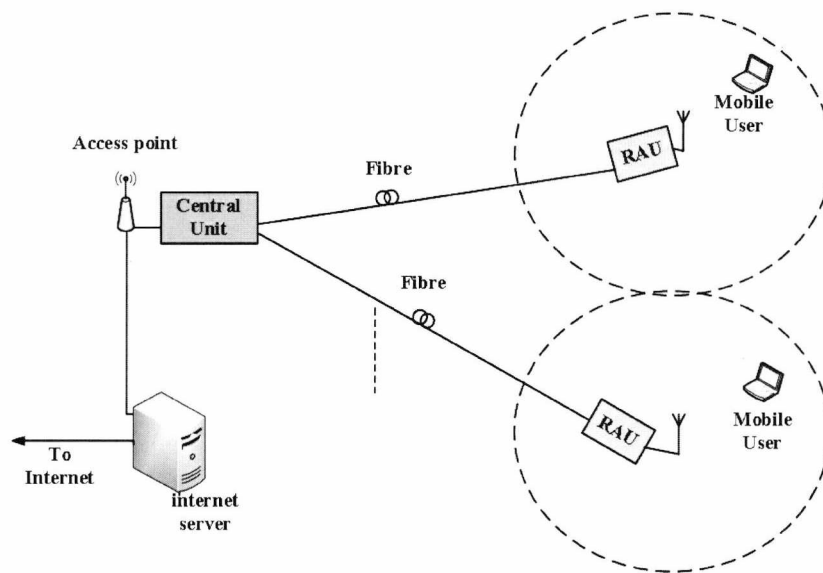


Fig. 1.1: Example of a DAS with two RAUs serving mobile users in different locations.

Here, signals from an access point located in a central location are distributed through a fibre architecture to Remote Antenna Units (RAU). The RAUs transmit and receive signals from mobile users located at different geographical areas. The most cost-effective option for these links is the use of direct Intensity Modulation and Direct Detection (IM-DD) where the RF signals directly intensity modulate the laser diode and are directly detected by a photodiode

[6]. While analogue signals can be transmitted at intermediate frequencies (IF over Fibre) or at baseband (baseband over fibre) the most typical case is the transmission of the signals at RF frequencies. This is due to practical reasons as base stations usually produce up-converted (at some RF frequency) outputs. But most importantly, RF transmission means that in principle, the RAUs do not contain other forms of processing hardware (e.g. QAM modulators and mixers) in the electrical domain, other than RF amplification. As a result they have low cost and low complexity. A diagram of a typical RoF link is shown in Fig. 1.2. The E/O conversion function is typically carried out by a semiconductor laser diode. The O/E conversion function is carried out by a photodiode, with PIN photodiodes being the typical option due to their superior linearity compared to other structures (e.g. avalanche photodiodes). The advantage of such an architecture is that all the complexity is concentrated in the Central Unit (CU). As such, improvements in the coverage and capacity that these systems provide would require only the placement of additional low cost and low complexity RAUs.

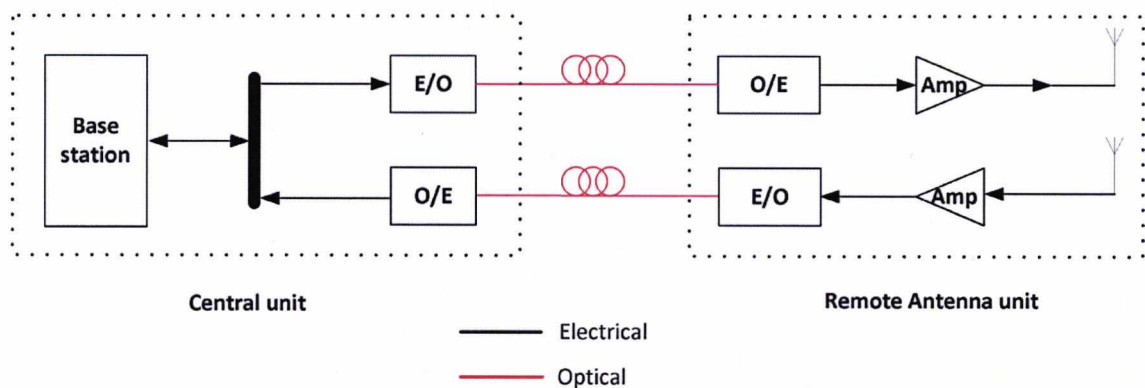


Fig. 1.2: A typical direct modulation and direct detection RoF link. E/O: Electro-optical conversion, O/E: Optical-electrical conversion, Amp: Amplifier.

Transmission of Orthogonal Frequency Division Multiplexing (OFDM) signals through RoF is of particular importance due to the adoption of OFDM in current systems such as 802.11 WiFi [7], 802.16 WiMAX [8] and DVB-T [9] as well as future 4th generation systems (e.g. LTE-Advanced). This is due to the robustness of OFDM against wireless channel impairments (linear distortion and multipath fading) and its advantages with equalization over single carrier systems [10]. Furthermore, it has the ability to be employed in multiple access schemes (OFDMA).

1.2 Motivation for the Thesis

The downlink direction of a typical direct IM-DD RoF link is shown in Fig. 1.3. The input signal coming from some base station is first power limited to a level appropriate for the specific laser diode power handling capability. The signal then directly intensity-modulates the laser diode and the resulting optical signal is transmitted through a length of optical fibre before being directly detected by a PIN photodiode (PIN-PD). The resulting electrical signal is then amplified (typically) for transmission through a wireless channel. In Fig. 1.3 some of the most important impairments and performance issues are noted. Also shown are two interface points. The actual RoF link is between the two interface points. Interface I1 will be the one to some sort of Base station (BS), Access Point (AP) or Joint Processing Unit (JPU). Note also that the interface to only one RoF link is shown here although it is assumed that there may be multiple connections to multiple RoF links, each transmitting to and receiving from geographically separate RAUs. Optical links of the form shown here are inherently lossy (in the electrical or RF domain). Therefore it is advantageous to have electro-optical components that incur the minimum losses (E/O and O/E conversion losses). Having smaller conversion losses is advantageous as the Signal-to-Noise ratio (SNR) of the system can be maintained and also the requirements for amplification after the optical link can be relaxed. Note that the SNR degradation due the optical link is due to the RF loss incurred but also due to the addition of noise [11]. The noise performance of these links is important for two reasons. The first has to do with spectral mask requirements. If the noise level reaching the antenna is too high then the transmission can violate spectral mask requirements. The second has to do with maintaining an SNR that meets the standard requirements for a specific modulation format. While one end of the dynamic range is limited by noise the other end is fundamentally (at least for the link types under consideration here) limited by the laser diode nonlinearity [12]. Due to limitations in the power handling capabilities of the laser diode, the power of the RF signals modulating the laser diode needs to be backed-off (this is evident by the need for attenuation at the input of the link) so that the effects of distortion are minimised, resulting again in reduced SNRs and higher amplification requirements in the remote antenna unit. In the case where the laser diode is overdriven either due to insufficient back-off (defined as the amount of input power reduction from to the 1 dB compression point of the laser diode) or due to high peaks in the signal (higher than the signals average level) being transmitted, distortion will occur, both in-band, which will reduce the effective SNR, and out-of-band, which may fall in adjacent channels and/or violate the spectral mask requirements of the transmitted signal.

The amount of back-off that can be applied, as well as the amount of amplification required, depend on the sensitivity requirements of the mobile unit. In general, higher level modulation formats will have more stringent requirements. The performance of the link components is a strong function of their cost with low cost lasers for example offering limited dynamic range while more expensive ones offering higher dynamic ranges and wider electrical modulation bandwidths.

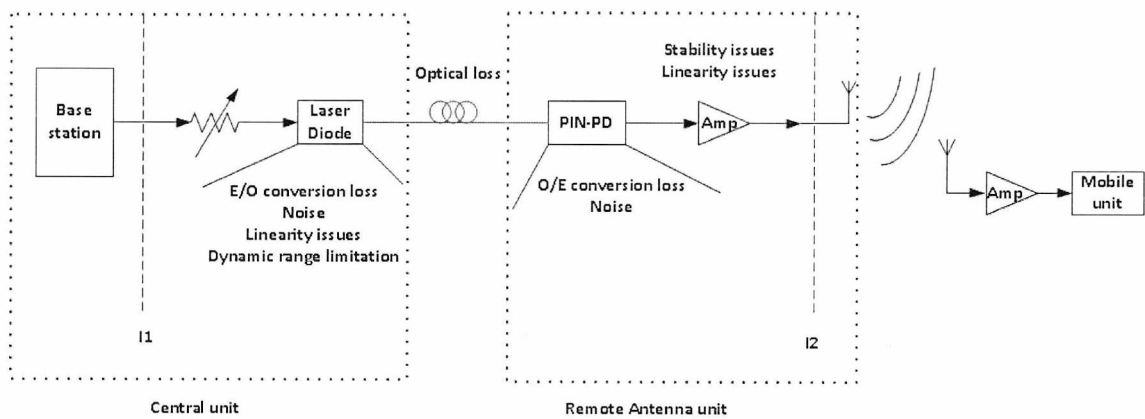


Fig. 1.3: Typical direct IM-DD RoF link with electrical amplification showing main performance issues and impairments.

In the envisaged 4th generation systems, the demand for high capacity, means that virtual MIMO techniques will be required to enable the proper reception of very high level modulation formats. The use of RoF can enable the distribution of signals that are received from multiple RAUs and are then transmitted to a CU where joint processing can be carried out. An example of such a system is the one proposed in the FUTON project [13, 14]. The FUTON architecture is shown in Fig. 1.4. Here, signals from users are received by RAUs placed in separate geographical locations, and are then transmitted through a transparent architecture employing direct IM-DD links and subcarrier multiplexing. They are then received in a CU (termed a joint processing unit) for joint processing. The FUTON architecture can transport any of the existing signal standards but also defines a 4th generation signal termed DBWS with very high QAM levels (>256 QAM) and modulation bandwidths on the order of 100 MHz.

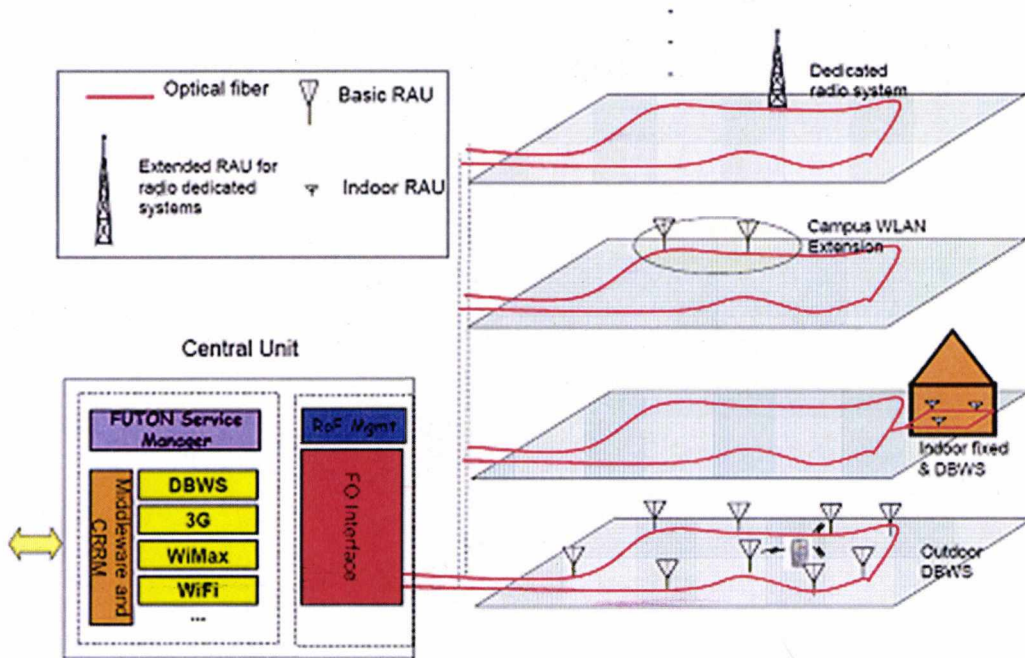


Fig. 1.4: The FUTON architecture [15].

1.3 Research Aims

Modelling the nonlinear behaviour of RoF links can be a rather mathematically involved process. One option for modelling systems that are transporting OFDM signals, are nonlinear statistical models [16-18]. Testing the effectiveness of such models on predicting the EVM performance of nonlinear links can be useful. An interesting regime of operation for an IM-DD link for Power over Fibre (PoF) applications [19], is one where the laser diode is operated at a low bias. This regime represents a limiting case that makes these models more tractable (mathematically). Thus, statistical nonlinear models can be formulated and used to predict the behaviour of an IM-DD RoF link with a low biased laser diode.

The main drawback of OFDM is that it possesses a high peak-to-average power ratio (PAPR) [20]. As a result it is sensitive to non-linear distortion. The PAPR of the OFDM signal is a function of the number of subcarriers (or the IFFT size). One method for quantifying the performance of RoF links, is through error vector magnitude (EVM) measurements [2, 21]. In the literature, the result that is usually produced from such a measurement is, through an

averaging process, the mean of the EVM. It is therefore interesting to examine the connection of PAPR with the EVM performance. More precisely whether signals with different numbers of OFDM subcarriers require different amounts of input power back-off. This information is important as the different signals need to adhere to EVM standard specifications. Additionally, the statistical behaviour of the EVM results can be analysed, so that further knowledge concerning the performance of signals with different numbers of subcarriers can be gained.

For subcarrier modulated systems transporting OFDM signals, such as the one proposed in the FUTON project, nonlinear performance is also important and may require more stringent input power back-off requirements due to the transportation of more channels. One method of modelling the behaviour of such systems is through the use of models based on the laser rate-equations (coupled differential equations that describe the dynamics of photons and carriers within the active region of a laser diode). Such models are typically complicated due to the number of intrinsic parameters that control the laser dynamics. Therefore, it is interesting to attempt to fit a model that is based on a simple form of the rate equations, to measured performance results across the different frequencies of operation of such a system. Once this is done, simulation based predictions can be carried out, that can be used to define acceptable dynamic ranges (ranges of input powers that can be applied at the input of the laser diode).

Another issue with RoF links is that the amount of amplification that can be implemented in the RAU is limited by stability issues. These in turn, depend on the isolation between different parts of the architecture [22]. It is therefore advantageous to be able to reduce the amplification requirements through a reduction in the PAPR of the signals, while still being able to meet the sensitivity requirements of mobile users. That is, a reduction in PAPR can allow for the laser diode to be driven at higher input powers. Thus, potentially, higher RF signal powers can be achieved at the output of the optical link while the EVM performance of the signals can still adhere to standard specifications.

1.4 Structure of the Thesis

The Thesis is divided into 8 chapters. More specifically:

Chapter 2 presents the background theory for the thesis, including among others, the theory of OFDM, directly modulated IM-DD RoF links and error vector magnitude.

Chapter 3 deals with the theory of PAPR and the statistics that describe it. It then moves on to the transmission of OFDM through nonlinearities and describes analytical models from the RF domain that can also be applied to laser diode nonlinearities.

Chapter 4 deals with the statistical distributions of EVM measured results following the transmission through a direct intensity modulation and direct detection RoF link of a large number of OFDM frames with different numbers of subcarriers. It then examines how these statistical distributions depend on the number of subcarriers and input power and whether the statistical PAPR can be related to the required back-off levels for the different signals.

Chapter 5 continuous based on the conclusions from the previous chapter and uses some basic statistical concepts to show how back-off points can be defined based on the statistics of the EVM results. These concepts are also used to show how the required number of OFDM frames for a reliable estimate of the mean EVM, can be determined. Finally, the performance of different subcarriers within the signal band is investigated.

Chapter 6 deals with companding and how it can be employed in a RoF link with the aim of reducing the PAPR of the OFDM signals so that isolation and amplification requirements in the RAUs are reduced.

Chapter 7 shows how a simple rate equation model can be designed and used to predict, through simulations, the performance of a 4-channel subcarrier multiplexed system transporting 4th generation signals.

Chapter 8 presents the conclusions and future work.

2 Background Theory

2.1 Orthogonal Frequency Division Multiplexing

A simplified block diagram for the transmitter and receiver sections of an Orthogonal Frequency Division Multiplexing (OFDM) system is shown in Fig. 2.1. Upper case characters are used for frequency domain samples, while lower case are used for time domain samples. The input data bits arrive at a certain rate ($f_m=1/T_s$, where T_s is the input symbol rate), go through Serial-to-Parallel (S/P) conversion and are mapped to Quadrature Amplitude Modulation (QAM) constellation points. The resulting QAM symbols form the vector of frequency domain samples $[X_0 X_1 \dots X_{N-1}]^T$. At this point, the rate of the samples is reduced by the IFFT size. The frequency domain samples then go through the IFFT block which produces the vector of time domain samples $[x_0 x_1 \dots x_{N-1}]^T$. After Parallel-to-Serial conversion (P/S) a Cyclic Prefix (CP) is appended at the beginning of each OFDM symbol. The resulting frames (note that the term “frame” is used here to denote an OFDM symbol that has a CP appended to it) then go through a Digital-to-Analog Converter (DAC) before being up-converted to pass-band (modulating the RF carrier) for transmission through a physical channel. At the receiver, the opposite processes are carried out to retrieve the original QAM symbols.

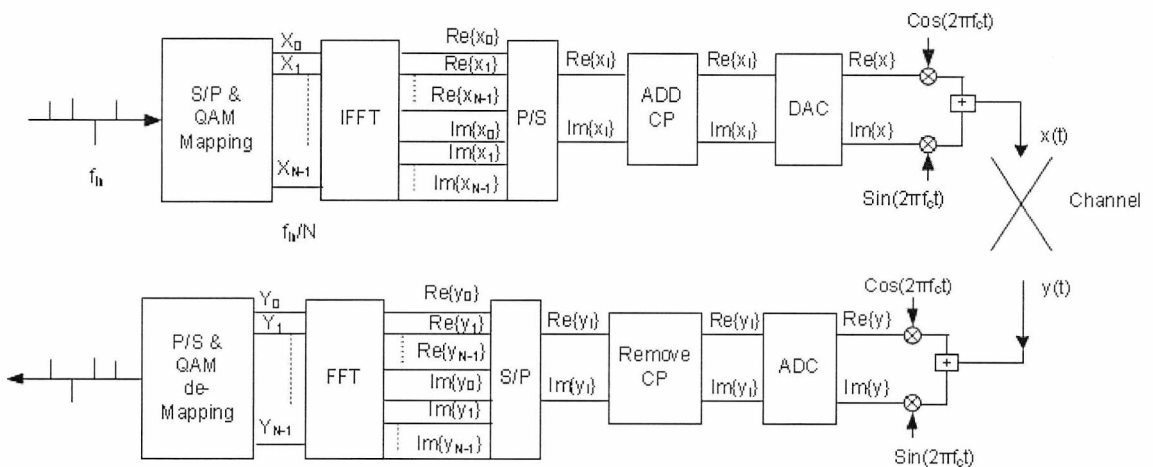


Fig. 2.1: OFDM transmitter and receiver architectures.

The output of the IFFT modulator for a single symbol is given by [23]:

$$x[n] = \frac{1}{\sqrt{N}} \sum_{k=0}^{N-1} X[k] e^{j2\pi kn/N} \quad (2.1)$$

where the $x[n]$ are the time domain samples and the $X[k]$ are the frequency domain samples at the output and input of the IFFT block respectively.

The signal at the output of the DAC is given by:

$$x(t) = \sum_{s=0}^{\infty} x[n] g(t - sNT_s) \quad (2.2)$$

where $g(t)$ is a filter or window function used to band-limit the signal (may include the contribution of any other filter or windowing function in the signal chain) and s is the symbol index. If no band-limiting is applied to the signal, then, the filter $g(t)$, is by default a rectangular filter that in the frequency domain results in a *sinc* response for each subcarrier with nulls at intervals of $1/NT_s$. An example of the resulting frequency domain representation of the OFDM signal for a few subcarriers is shown in Fig. 2.2. The orthogonality of the subcarriers is evident in this figure by the fact that at the sampling instances, the contribution of all other subcarriers except that which is being sampled is at a zero crossing.

Fig. 2.3 shows the power spectral density (PSD) of an OFDM signal with 512 subcarriers obtained in a simulation in Matlab, showing the characteristic box-shaped behaviour.

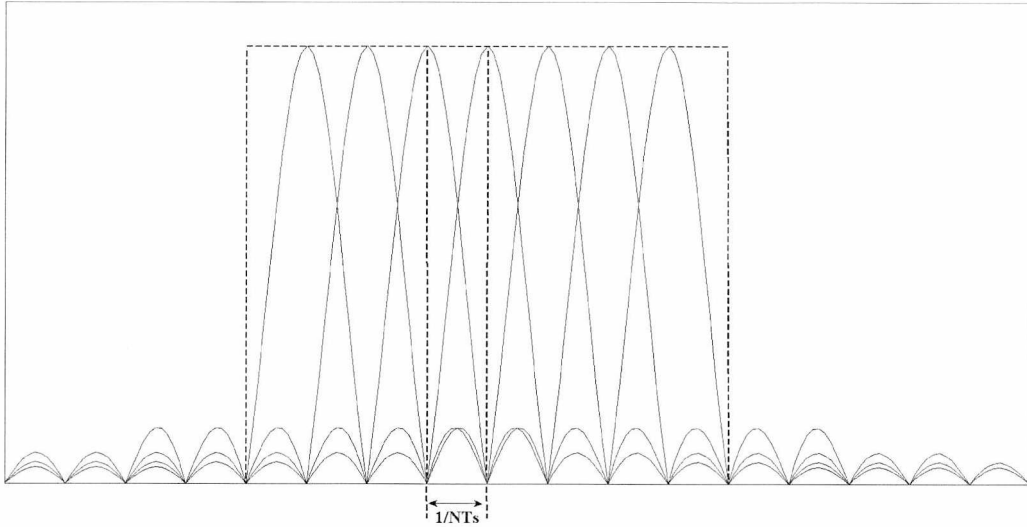


Fig. 2.2: Frequency domain representation of the OFDM signal.

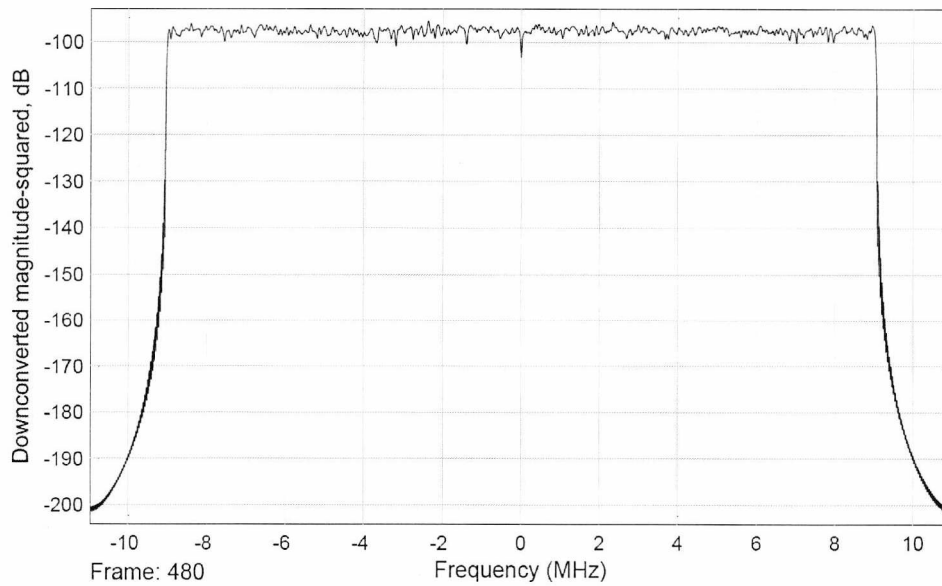


Fig. 2.3: PSD of OFDM signal with 512 subcarriers obtained in Matlab.

In order to reduce the filtering requirements at the output of the IFFT, oversampling is typically applied. This is given by [20, p.18]:

$$x \left[\frac{n}{Z} \right] = IFFT \sqrt{Z} \left(\left[X_0 \dots X_{\frac{N}{2}-1} \underbrace{0 \dots 0}_{N(Z-1)} X_{\frac{N}{2}} \dots X_{N-1} \right]^T \right) \quad (2.3)$$

where Z is the oversampling factor.

After RF up-conversion and some manipulation of (2.1), the RF output will be given by:

$$x_{RF}(t) = \sum_{k=0}^{N-1} |X[k]| \cos \left[2\pi \left(f_c + \frac{n}{NT_s} \right) t + \Phi[k] \right] \quad (2.4)$$

where $|X[k]|$ and $\Phi[k]$ are the magnitude and phase respectively of the complex symbols as defined by the constellation of the chosen modulation scheme (e.g. QAM, QPSK) and NT_s is the time duration of the symbols at the input of the IFFT. Eq. (2.1) and (2.4) clearly show the creation of the different sub-carriers which have a frequency separation of $1/NT_s$ and are therefore orthogonal.

The OFDM transmitter succeeds in taking a high symbol rate input and dividing it into many (N) low symbol rate signals with each signal modulating a different orthogonal sub-carrier. Each sub-carrier can therefore have a bandwidth smaller than the coherence bandwidth of the channel and as such the system is clearly advantageous under multipath and linear distortion conditions compared to single carrier systems. In single carrier systems, the Inter-Symbol Interference (ISI) may span over many symbols. In OFDM, the ISI is expected to affect just the next symbol but with the use of a guard band (Cyclic Prefix) the effects of ISI can be eliminated.

2.1.1 Cyclic prefix

Taking the original OFDM symbol consisting of N samples in the discrete time domain, the addition of a CP means that the OFDM symbol obeys the following rule:

$$x_{-c} = x_{N-c} \quad (2.5)$$

where c is the number of samples used to describe the CP. Therefore, the new sequence of samples will have a length of $N + c$. The length of the CP is chosen to be at-least equal to the discrete impulse response of the channel. The insertion of the CP is shown in Fig. 2.4.

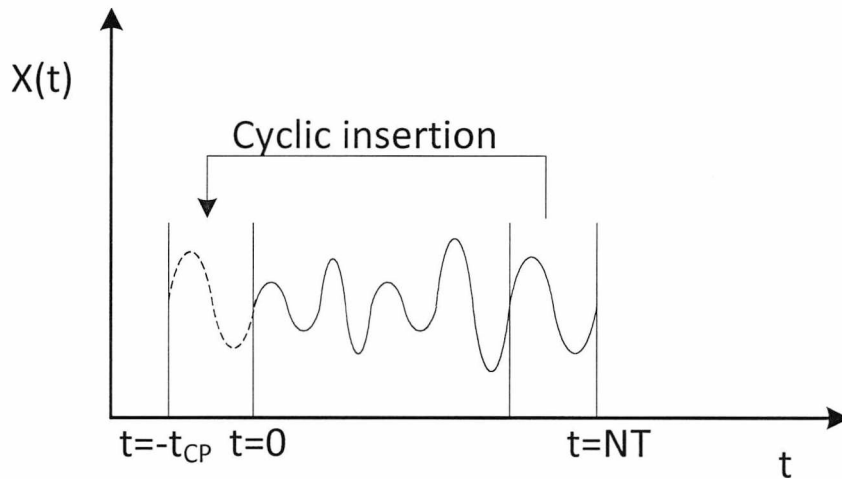


Fig. 2.4: Example of CP insertion with time duration t_{CP} .

The advantage of adding a CP is that the convolution of the input OFDM signal with the channel impulse response becomes circular [24, p. 119]. Circular convolution of discrete time finite length sequences is equivalent to multiplication in the frequency domain (multiplication of the DFTs). This is a consequence of the periodic extension of the original signal performed by the DFT: As a result of this periodicity, linear convolution with a channel (for example) will cause energy from the previous and subsequent periodic extensions to leak into the current signal (edge effects). The number of samples affected at the beginning and end of the signal will be equal to $c-1$ where c is the number of samples of the discrete channel impulse response. This is equivalent to cyclic convolution since the energy leaking into the beginning of the current signal, is due to the convolution of the discrete channel impulse response with the last samples of the previous periodic extension, equivalent to convolution with the last samples of the current signal. As the insertion of a CP (size of $c-1$) together with linear convolution with the channel results mathematically in circular convolution, the transmitted signal can be recovered from the received signal by multiplication with $1/H(i)$ where $H(i)$ is the DFT of the channel response. In effect, the CP being a guard interval avoids ISI and in addition simplifies the equalisation procedure when equalising for the inter-carrier interference (ICI) in

order to maintain the orthogonality between the subcarriers. Since the CP is a copy of the original signal it will not have an effect on the Peak-to-Average Power Ratio (PAPR). The CP results in bandwidth and power penalties by a factor of $(N+c)/N$.

2.1.2 Synchronization issues in OFDM

Time variations between the start of the received OFDM symbol and the FFT time window at the receiver (Fig. 2.5) can result in severe distortion, with the worst case being when the window is applied to more than one OFDM symbol at the same time leading to ISI. In practice though, some misalignment (Δt) can be tolerated providing that it is within the CP duration. The shift in time results in a phase shift, $\Delta\theta(\Delta t, f)$, in the frequency domain:

$$\hat{X}(f) = X(f)e^{j\Delta\theta(\Delta t, f)} = X(f)e^{j2\pi\Delta t f} \quad (2.6)$$

where $\hat{}$ denotes estimate.

For a given time shift, the phase error varies linearly with frequency, meaning that outermost subcarriers experience a higher phase error in their constellation.

Synchronization can be achieved through some form of correlation of the received signal with some known characteristic.

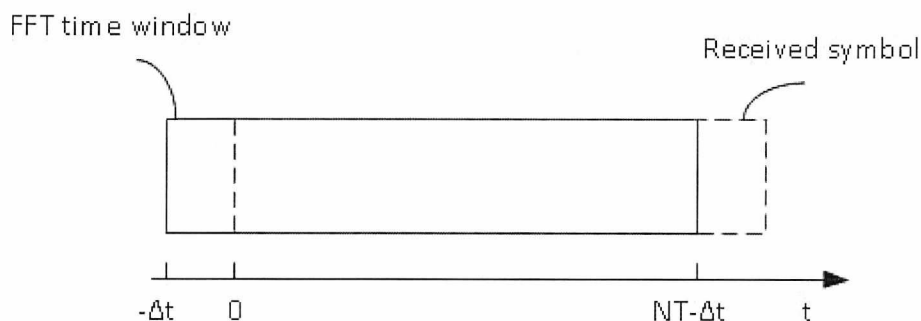


Fig. 2.5: Time misalignment between received symbol and FFT time window.

Frequency synchronization is a more critical issue in OFDM. Errors in frequency synchronization occur due to local oscillator frequency mismatches (LO offsets) between transmitter and receiver as well as due to sampling frequency mismatches. LO offset is shown conceptually in Fig. 2.6. The frequency error results in loss of orthogonality between the subcarriers through a leakage process in the receiver FFT.

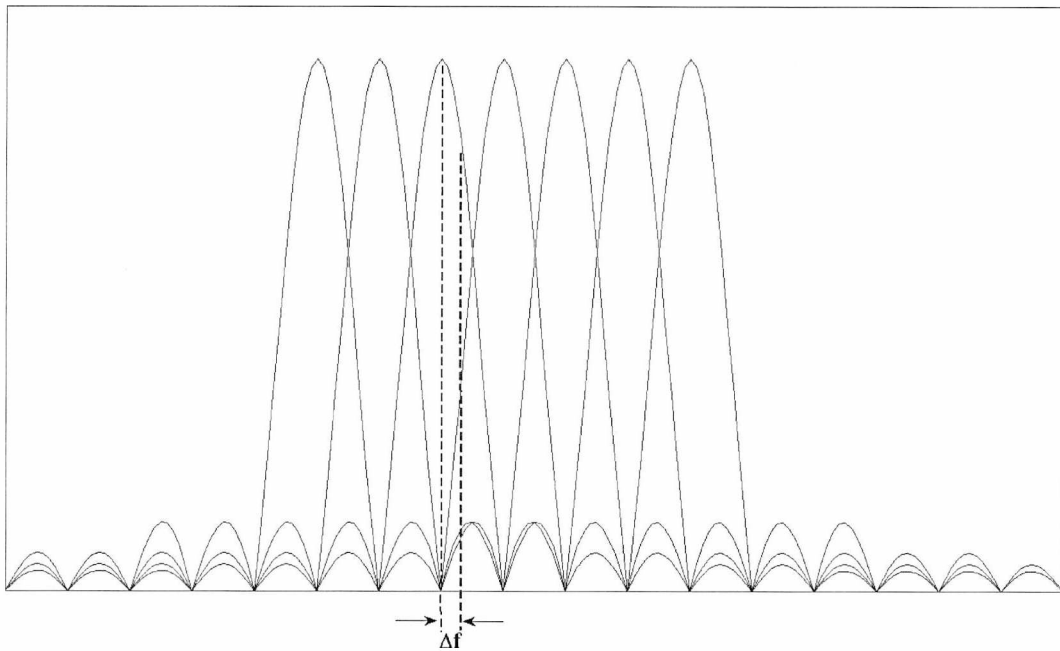


Fig. 2.6: Wrong sampling times due to LO offsets

The result is a form of frequency modulation imposed on the time domain signal. In the frequency domain the effect is expressed by:

$$\hat{X}(f) = X(f - \Delta f). \quad (2.7)$$

The result of LO offset is a continuously rotating constellation.

The effects of non-ideal synchronization and the resulting bit-error rate increase have been investigated analytically in [25]; for a brief overview of these impairments *see* [23].

Various estimation methods exist - either blind or non-blind (where redundant information is sent from transmitter to receiver) - that can provide information at the receiver so that some form of compensation can be applied.

For simulation purposes, time synchronization can be obtained by cross-correlating the received signal, $x_r(t)$, with the input signal, $x_t(t)$, by:

$$R_{x_t x_r}(\tau) = \int_0^{NT} x_t^*(t) x_r(t + \tau) dt \quad (2.8)$$

where * denotes complex conjugate, and the output signal is given by:

$$x_r(t) = x_t(t - t_d) + n(t) + d(t) \quad (2.9)$$

where t_d is the delay experienced by the signal through the link, $n(t)$ is Gaussian noise and $d(t)$ is distortion.

The peak of the integral in (2.8) occurs at $t=t_d$ and thus the delay can be extracted and then applied to the FFT window at the receiver.

In practical systems, a similar procedure can be applied with the use of a known sequence or preamble that will allow the receiver to synchronise the FFT window. The known sequence and the received one can then be applied to the integral in (2.8) in order to obtain the delay experienced by the signal due to the channel. Alternatively, a frequency domain technique can be employed by which pilot symbols are inserted in the frequency domain [26]. This is termed Pilot Symbol Assisted Modulation (PSAM) and is implemented so that the receiver can extract information of the relative phase shifts of the subcarriers. For correct estimation, the distance between adjacent pilot tones must be less than or equal to half the period of the channel transfer function [26]. Additional synchronization methods exist that can be used for both frequency and time offset correction. These include methods employing pilot tones or training sequences [27-29], while an alternative technique makes use of the inherent redundancy in the CP [30, 31].

2.1.3 IQ modulator and IQ imbalance

IQ imbalance is a result of phase and gain variations that take place in the IQ modulators and demodulators [32, 33]. Therefore, they can occur either in the transmitter, in the receiver, or in both. Fig. 2.7 shows the simplified layout of an IQ modulator. Imbalance occurs when $g_1 \neq g_2$, $g_3 \neq g_4$ and $\Delta\theta \neq 0$. The result of IQ imbalance is mutual inter-carrier interference between a subcarrier and its image subcarrier [34]. Additional impairments from the modulation process include noise, inter-modulation distortion from the mixing process and LO to RF leakage. In the demodulator, LO to RF leakage can lead to DC offsets in the received constellation.

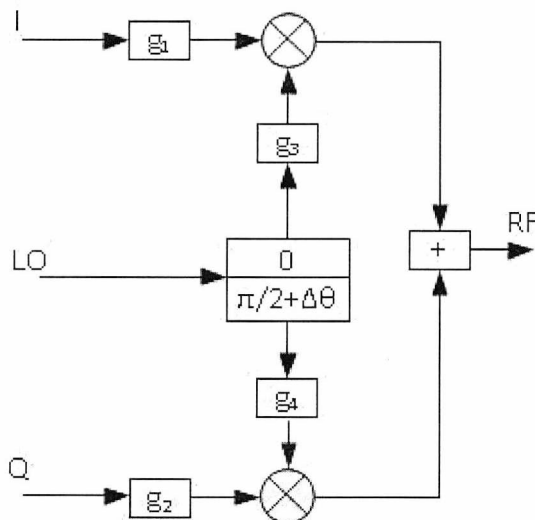


Fig. 2.7: Diagram of IQ modulator showing the various parts that can cause imbalance.

2.2 Error Vector Magnitude and other measures of link performance.

The Error Vector Magnitude (EVM) is a direct indication of modulation quality. It describes the error (in terms of the Euclidean distance) between a received and an ideal point in a given QAM constellation. This is shown conceptually in Fig. 2.8.

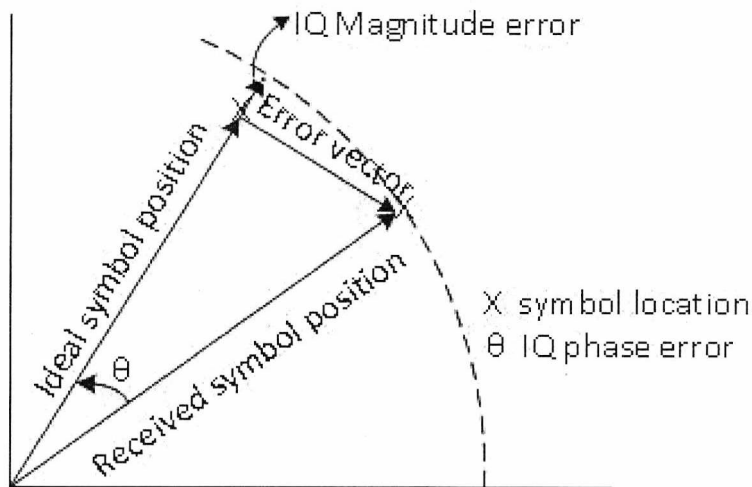


Fig. 2.8: The magnitude and phase errors as defined on the IQ constellation plane.

EVM is defined in various ways in the literature depending on the standards of the system. Some definitions are the following [24 p. 138, 35, 36]:

$$EVM (\% rms) = 100 \sqrt{\frac{\frac{1}{N} \sum_{n=1}^N ([I\{X_r - X_i\}]^2 + [Q\{X_r - X_i\}]^2)}{\frac{1}{N} \sum_{n=1}^N ([I\{X_i\}]^2 + [Q\{X_i\}]^2)}} \quad (2.10)$$

$$EVM(\% peak) = 100 \sqrt{\frac{\frac{1}{N} \sum_{n=1}^N ([I\{X_r - X_i\}]^2 + [Q\{X_r - X_i\}]^2)}{\max_i \{ [I\{X_i\}]^2 + [Q\{X_i\}]^2 \}}} \quad (2.11)$$

$$EVM (\%rms) = 100 \frac{1}{S} \sum_{s=1}^S \sqrt{\frac{\frac{1}{N} \sum_{n=1}^N ([I\{X_r - X_i\}]^2 + [Q\{X_r - X_i\}]^2)}{\frac{1}{N} \sum_{n=1}^N ([I\{X_i\}]^2 + [Q\{X_i\}]^2)}} \quad (2.12)$$

where X_r is the received symbol, X_i is the ideal symbol from a given QAM constellation point and S is the number of OFDM symbols. The EVM is usually given as a percentage of the RMS value of the constellation and this is evident in (2.10). In some cases however, it is defined in terms of the peak constellation power, as shown in (2.11). The averaging method will depend on the system under consideration. For simple QAM based systems (non OFDM) the averaging will be carried out over a certain number of QAM symbols. For OFDM based systems it will generally be carried out over all the data subcarriers within an OFDM symbol and depending on the standard, across a number of OFDM symbols as shown in (2.12). EVM is related to the *Modulation Error Rate* (MER) which is given by:

$$MER (dB) = 10 \log \frac{\frac{1}{N} \sum_{n=1}^N ([I\{X_i\}]^2 + [Q\{X_i\}]^2)}{\frac{1}{N} \sum_{n=1}^N ([I\{X_r - X_i\}]^2 + [Q\{X_r - X_i\}]^2)}. \quad (2.13)$$

From (2.10) and (2.13), the EVM and MER are related by:

$$MER (dB) = -20 \log EVM. \quad (2.14)$$

From (2.10) the EVM can be given in terms of the SNR by the following:

$$EVM = \sqrt{\frac{1}{SNR}} \quad (2.15)$$

Both EVM and MER can provide a measure of the end-to-end quality of the link, which means that for links that suffer from multiple impairments, the causes of EVM (or MER) degradation can become significantly "blurred".

In order to obtain the EVM after a signal has been transmitted through a link, the constellation has to be normalised so that a comparison can be made with the ideal reference constellation. A constellation will in general experience some phase rotation and gain from the link. In addition, the frequency response of the link has to be equalized. Exactly how these processes are rectified will depend on the particular design of the system. Fig. 2.9 shows a generalization of how this process is carried out. The received constellation is de-rotated and equalized, while the amounts of rotation and gain required to normalize it are determined by the reference constellation. The received constellation is normalised to some average power (in this example to an average power of 1) so that a comparison with the reference constellation can be carried out. The normalization process will increase both the signal and noise amplitude by the same amount and thus will leave the SNR unchanged.

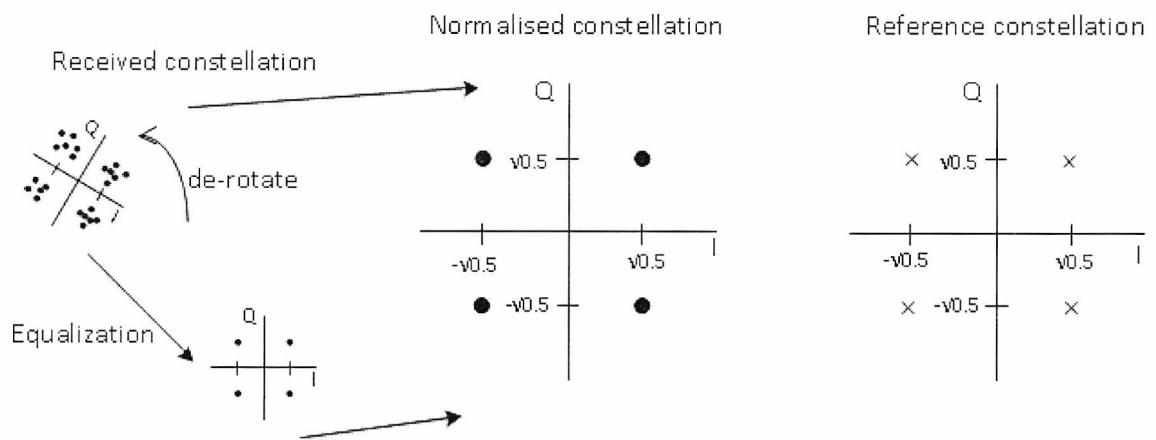


Fig. 2.9: Normalization to an average power of 1 of a received constellation that has experienced some arbitrary gain and phase rotation from a link.

Fig. 2.10 is an example of a typical EVM versus input power plot for a nonlinear link, showing three distinct regions of operation, with the lowest input power in Region 1 and the highest in Region 3. Assuming that the modulation and demodulation processes in the communication link and the timing and frequency corrections are ideal, the performance in the first region is determined predominantly by the receiver and link noise. In the second region it is limited by the transmitter noise and the frequency response of the link (assuming it is not perfectly equalized). In the third region, performance depends mainly on the distortion.

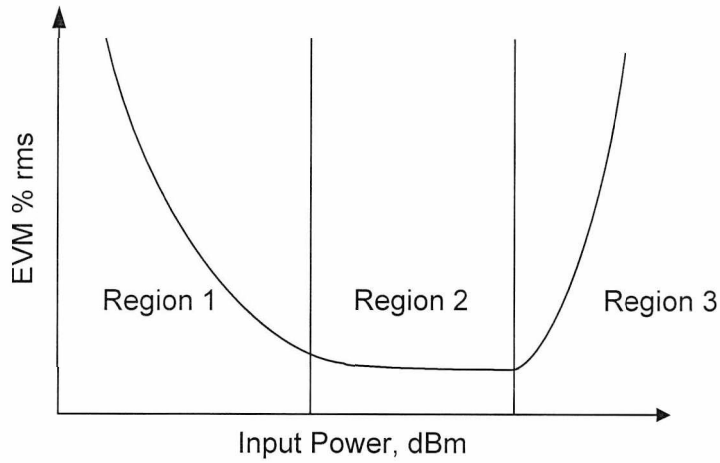


Fig. 2.10: Example of an EVM versus input power plot.

2.3 Direct IM-DD radio-over-fibre links

2.3.1 Gain of direct IM-DD links

The optical link small signal gain is a function of laser efficiency, photodiode responsivity and fibre attenuation. For resistively matched links, it is given by [11]:

$$G = \left(\frac{\eta R}{L}\right)^2 \frac{Z_{out}}{Z_{in}} \quad (2.16)$$

where η is the laser slope efficiency (W/A), R is the photodiode responsivity (A/W), Z_{out} and Z_{in} are the input and output impedances respectively of the optical link, and L is the insertion loss of the fibre, given by:

$$L = \frac{P_{out}}{P_{in}} \quad (2.17)$$

where P_{out} is the output power from the fibre and P_{in} is the power input to the fibre.

The insertion loss includes the optical attenuation experienced by the signal travelling through the optical fibre and might also include the optical coupling loss between the laser diode and fibre connection. The average photocurrent, $\overline{I_d}$, at the PD for a given laser bias current, $\overline{I_b}$, will be given by:

$$\overline{I_d} = R\eta L(\overline{I_b} - \overline{I_{Th}}) \quad (2.18)$$

where $\overline{I_{Th}}$ is the threshold current.

The squared term in (2.16) means that in dB, a loss in the optical domain will be doubled in the electrical domain. In other words, for every 3 dB of loss in the optical domain there will be a loss of 6 dB in the electrical domain. Also, for typical RoF links, $G \ll 1$. In order to improve the gain of the link, non-resistive matching can be used both in the laser diode and photodiode ends [37, 38]. While resistive matching is a broadband approach, non-resistive matching techniques can increase the gain at the expense of reduced modulation bandwidths [12]. Other techniques involve the use of matching elements between PD and antenna connections [37, 39]. Additionally, instead of matching, impedance bridging could be used, for example in the laser diode, with the aim of maximizing the current transfer instead of the power transfer. However, such an implementation would suffer from reflections.

2.3.2 Noise performance

The degradation of the signal-to-noise ratio as a result of the noise added by the system is given by the noise figure (NF):

$$NF(dB) = N_{out} - 10 \log_{10}(KT) - G \quad (2.19)$$

where, N_{out} is the noise power density ($dBmHz^{-1}$) at the output of the optical link and G is the gain of the optical link, given by (2.16). The quantity KT is the thermal noise density at the input of the link ($= -174 dBmHz^{-1}$) at room temperature (290 K), where K is Boltzman's constant and T (K) is the temperature.

The NF in linear terms is termed the Noise Factor, F , and for a cascade of components it is given by the *Friis formula* [40]:

$$F = F_1 + \frac{F_2 - 1}{G_1} + \frac{F_3 - 1}{G_1 G_2} + \dots \quad (2.20)$$

From (2.20) the importance of high dynamic range in the optical link becomes obvious. If the G_1 term represents the gain of the amplifier before the laser diode, then maximizing this gain can make F approach its lower bound which is F_1 . Therefore, having laser diodes which can handle high input powers is clearly advantageous. The noise at the output of the optical link, N_{out} , is given by

$$N_{out} = KTG + N_{OL} \quad (2.21)$$

where N_{OL} is the noise added by the optical link.

For typical links $G \ll 1$, therefore, the contribution of the term KTG to N_{out} is very small and thus, $N_{out} \approx N_{OL}$. The major sources of noise that are added by the optical link are Relative Intensity Noise (RIN) from the laser diode, shot and thermal noises from the photodiode [12]. The noise added by the optical link is given by:

$$N_{OL} = N_{Sh} + N_{RIN} + N_{Th} \quad (2.22)$$

where N_{Sh} is shot noise, N_{RIN} is RIN noise and N_{Th} is thermal noise.

The noise power densities of these contributions are given by [11]:

$$N_{Sh} = 2q\bar{I}_d Z_{out} \quad (2.23)$$

$$N_{RIN} = RIN\bar{I}_d^{-2} Z_{out} \quad (2.24)$$

$$N_{Th} \approx KT \quad (2.25)$$

where q is the electron charge and RIN is the Relative Intensity Noise.

From (2.23) to (2.25) it is evident, by the average photocurrent dependencies, that RIN dominates at high light powers at the receiver, shot noise at intermediate light powers and thermal noise at low light powers. Of course, whether a specific noise source dominates will depend on link design and component specification. Fig. 2.11 shows a plot of NF versus the average photocurrent and of the dependencies of NF on each individual noise source. Note that the NF is lower bounded by the thermal noise dependence trace. This is because if the only noise source in the optical link is thermal noise from the photodiode, then, $N_{out} \approx N_{OL} = KT$, and from (2.19):

$$NF_{LB}(dB) = -G. \quad (2.26)$$

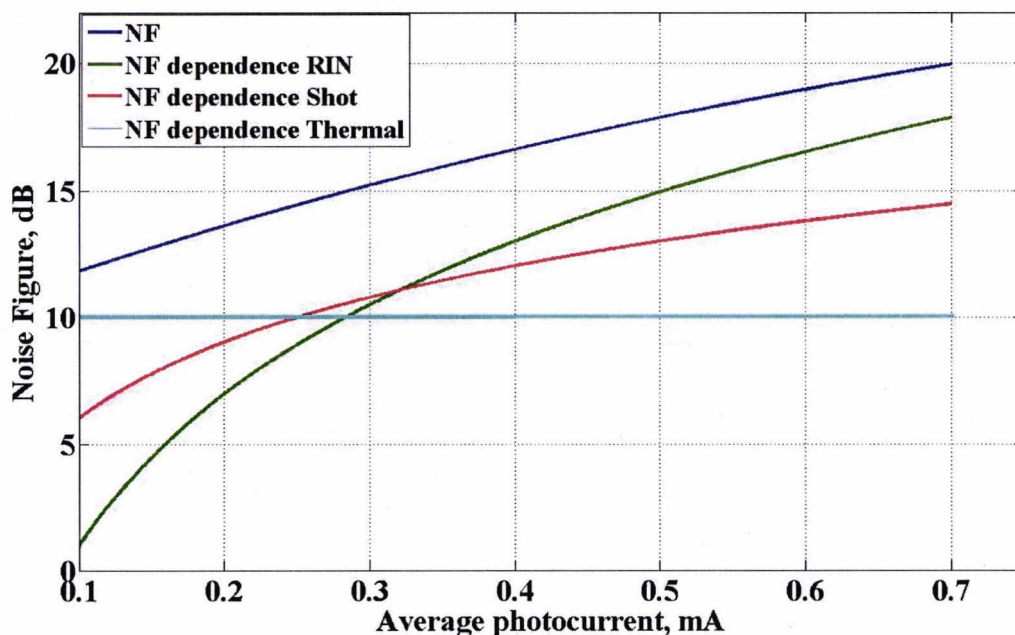


Fig. 2.11: Noise figure versus average photocurrent and noise figure dependencies on the individual noise sources for $RIN=150 \text{ dBHz}^{-1}$, $G=-10 \text{ dB}$.

Some typical NF values for commercial optical transceiver units are shown in Table 2.1. The noise density at the output of the optical link can be measured with a spectrum analyser using a matched load (typical 50 Ω) at the input of the link, as shown in Fig. 2.12, with the resolution bandwidth of the spectrum analyzer set to 1 Hz. Optionally a pre-amplifier can be used if needed, to raise the noise level above the spectrum analyser noise floor. The noise density at the optical link output will be given by:

$$N_{OL} = N_{out} - N_s + KTG \quad (2.27)$$

where N_s is the spectrum analyzer noise floor and N_{out} is the total noise power measured by the set-up of Fig. 2.12.

Table 2.1: Typical NF values for commercially available optical transceiver modules.

Type	λ (nm)	NF (dB)
Emcore WiBa cooled DFB	1310	50
	1550	(@ 2GHz)
MP-5000 TX cooled DFB	1550	30 (max)
	1310	(@ 3 GHz)
MP-2320TX cooled DFB	1550	35 (max)
	1310	

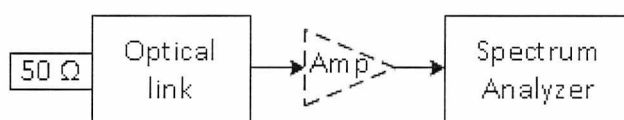


Fig. 2.12: Set-up for noise measurements using a spectrum analyzer.

2.3.3 Nonlinear performance

The nonlinear performance of direct IM-DD links for short to medium reach (<20Km) applications depends mainly on the laser diode [12]. The nonlinear characteristic of the laser diode leads to the creation of harmonics and inter-modulation products that result in in-band distortion and out-of-band radiation.

The nonlinear characteristic of any device can be described by a polynomial model of the form:

$$y(t) = c_1x(t) + c_2x(t)^2 + c_3x(t)^3 + c_4x(t)^4 + c_5x(t)^5 + \dots \quad (2.28)$$

where $x(t)$ is the input signal, $y(t)$ is the output and c_1 to c_5 are the model coefficients.

Assuming that the input is a single tone given by:

$$x(t) = A \cos(\omega t + \varphi) \quad (2.29)$$

where A is the amplitude and φ is the phase, inserting (2.29) into (2.28) and collecting the various terms, the harmonics and their relative amplitudes in terms of the polynomial coefficients can be obtained. The result up to the 5th harmonic is shown in Fig. 2.13. The polynomial coefficients depend on the nonlinear function. For example, for a small-signal laser diode model, the coefficients will be given by [11]:

$$c_n = \frac{1}{n!} \frac{\partial^n y}{\partial x^n} \Big|_{\bar{x} = x_b} \quad \text{for } n = 1, 2, \dots \quad (2.30)$$

where $y(t)$ is the optical power, $x(t)$ is the current into the laser and x_b is the bias current.

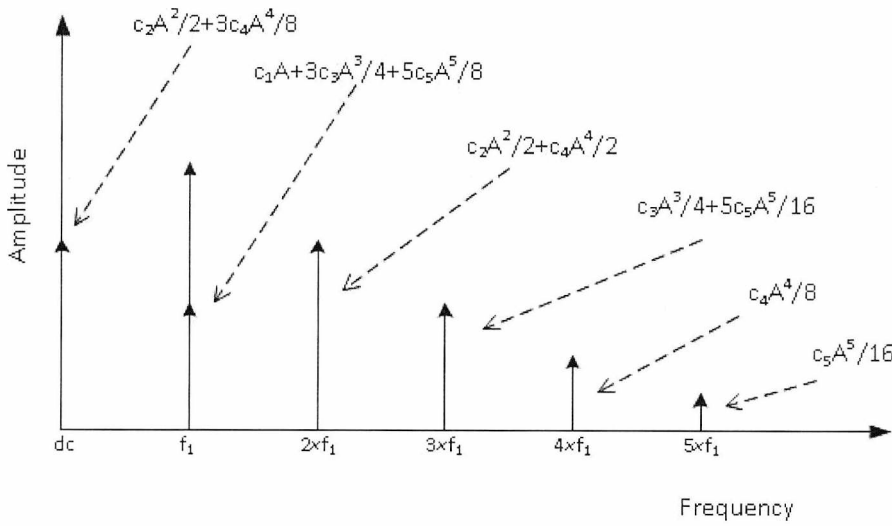


Fig. 2.13: Harmonic distortion components and their amplitudes for a polynomial model.

Gain compression of laser diodes can be measured through a single tone measurement as shown in Fig. 2.14 [41]. In this case, the linear part of the fundamental response is extrapolated to the point where the actual response deviates from the ideal (linear) response by 1 dB. The input power where this happens is termed the input 1 dB compression point ($P_{1dB,in}$) while when referred to the output, it is termed the output 1 dB compression point ($P_{1dB,out}$).

The two are related by the small signal gain (G) of the link by:

$$P_{1dB,out}(dB) = P_{1dB,in} + G - 1. \quad (2.31)$$

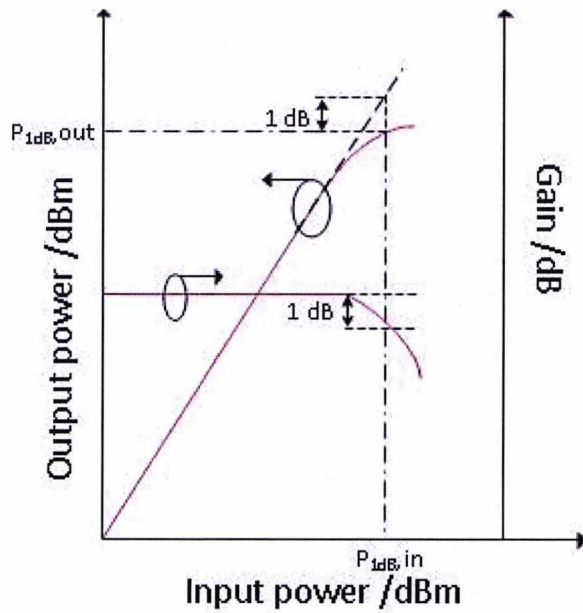


Fig. 2.14: Example of 1 dB compression point measurement result. Two different methods are shown, one using the output versus input power result and the other using the gain versus input power result.

Inter-modulation distortion is a result of mixing between frequency components within the signal band, when a signal is transmitted through a nonlinear component. Again, the output of a nonlinearity can be investigated using the model in (2.28), when the input signal is the sum of two sinusoids with a frequency difference between them smaller than the IF bandwidth of the system under consideration. The result of inter-modulation distortion for two fundamental tones, f_1 and f_2 , is shown in Fig. 2.15. The different mixing components are given by:

$$af_1 \mp bf_2 \quad \text{for } a, b = 1, 2, \dots$$

while the order of the mixing products is given by $|a| + |b|$.

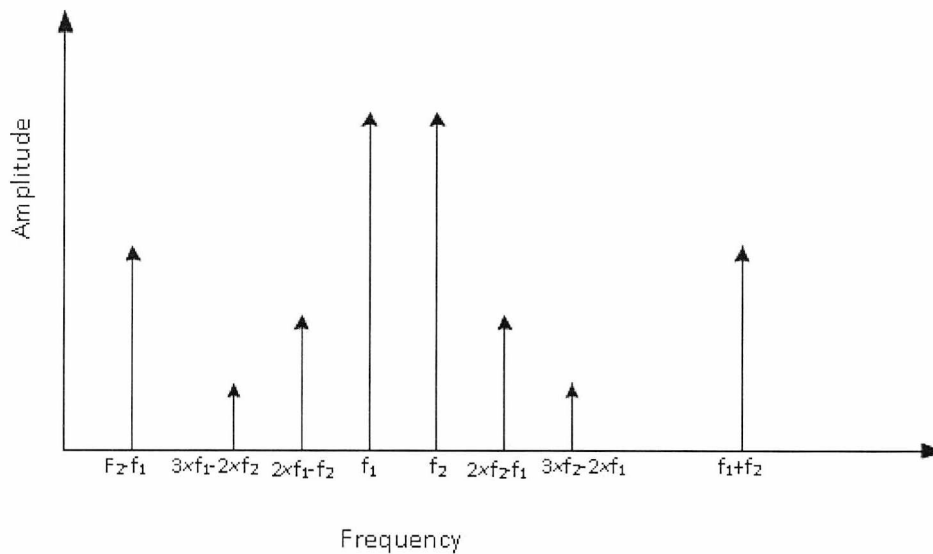


Fig. 2.15: Representation of Intermodulation products in the frequency domain

The power-law dependence of the mixing products in (2.28) means that the 2nd order products increase two times faster than the fundamental, the 3rd order products three times faster and so forth. For sub-octave (narrowband) systems, odd order products (3rd, 5th etc) are the most troublesome as they fall in-band while even order terms are far removed from the pass-band and can be filtered out. For multi-octave (wideband) systems even order terms are also of interest. In general, higher order terms (say above 5th order) have reduced amplitudes and in most cases can be ignored. The set-up for an inter-modulation distortion measurement (2-tone test) is shown in Fig. 2.16. The two fundamental tones are generated using two signal generators; they are combined through an RF combiner and transmitted through the optical link before being received by a spectrum analyzer that is used to measure the power of each individual inter-modulation product. The isolators are used so that the signal generators do not inter-modulate each other. An example of a result from a 2-tone measurement is shown in Fig. 2.17. The points where the extrapolated response of the system to the fundamental tone intercepts the 2nd or 3rd order extrapolated responses, are termed the 2nd and 3rd order intercept points respectively (IP_2 and IP_3). These intercept points are found by extrapolation as they cannot be measured in practice due to the onset of saturation at much lower input powers. The intercepts can be referred to the input (IIP) or to the output (OIP). A rule of thumb approximation is that the IIP_3 occurs at an input power that is 10 dB higher than the 1-dB compression point (P1dB) [42].

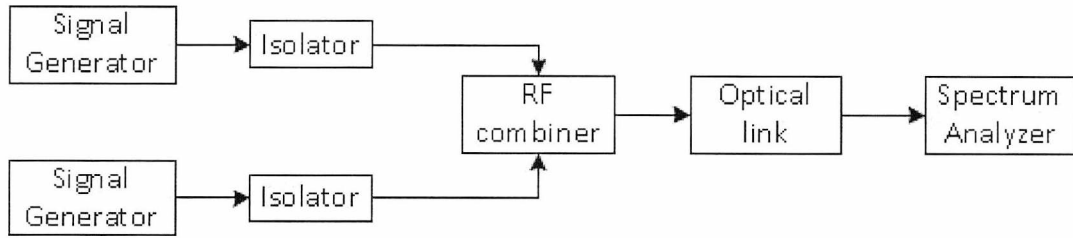


Fig. 2.16: Measurement set-up for a 2-tone test using a spectrum analyzer.

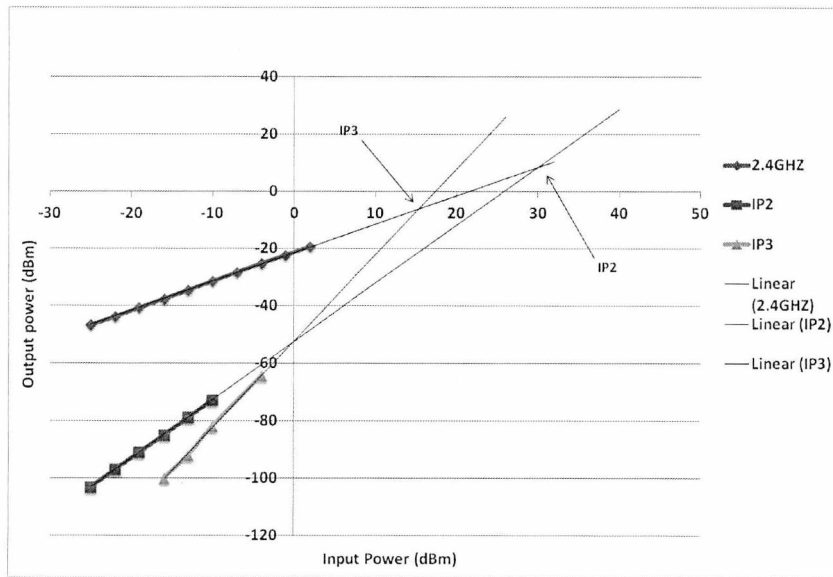


Fig. 2.17: Example of a 2-tone measurement result, showing IP_2 and IP_3 points with the fundamental frequency at 2.4 GHz.

2.3.4 Dynamic range definitions for analogue optical links

There are different methods that can be used to define the dynamic range of an optical link (note that these methods apply in general to nonlinear links and are not specific to optical links). One method uses the definition of the P1dB as shown in Fig. 2.18. In this case the minimum signal level is either at the noise floor of the link or at a level 3 dB above the noise floor [43].

For the case where the minimum signal is defined as being at the noise floor level, the dynamic range, D_R , is given by:

$$D_R(dB) = P_{1dB,out} - 10 \log_{10}(KT) - G - NF. \quad (2.32)$$

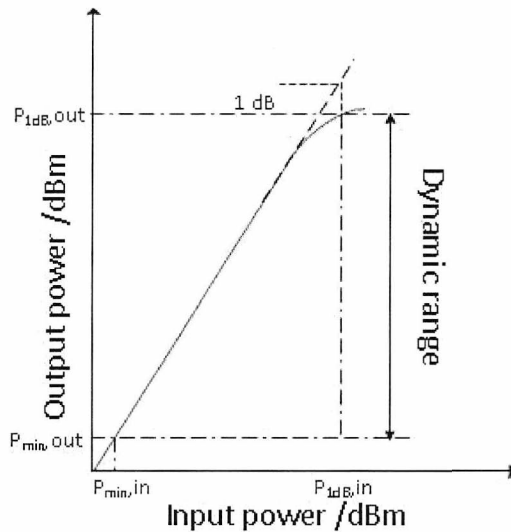


Fig. 2.18: Dynamic range definition based on the P1dB.

Another method uses the definition of the intercept point as shown in Fig. 2.19. The dynamic range in this case is termed the Spurious Free Dynamic Range (SFDR) and it is the difference between the power of the fundamental tone and the noise floor, when the distortion power crosses the noise floor. In other words, it is the range of input powers that can be applied to the system before the power in the distortion term crosses the noise floor level and starts to reduce the effective signal-to-noise ratio and limit the performance. The SFDR for 3rd order distortion is given by [41]:

$$SFDR(dBmHz^{-\frac{2}{3}}) = \frac{2}{3} [IIP_3 - 10 \log_{10}(KT) - NF]. \quad (2.33)$$

The $\frac{2}{3}$ term in (2.33) is due to the fact that the power in the 3rd order product at any given time prior to saturation, is below the fundamental response by twice the amount (in dB) the fundamental is below the intercept point, as indicated in Fig. 2.19. Table 2.2 shows some typical SFDR and IIP_3 values for commercially available optical transceivers. Up to this point, all the definitions presented are based on noise densities. This is done so that these definitions are independent of modulation bandwidth. For a specific system of interest that has some

finite modulation bandwidth, the preceding definitions have to be altered by including the appropriate bandwidth factor. For example it is straight forward to show that for a bandwidth, B , the SFDR in (2.33) will reduce by $(2/3) 10\log B$.

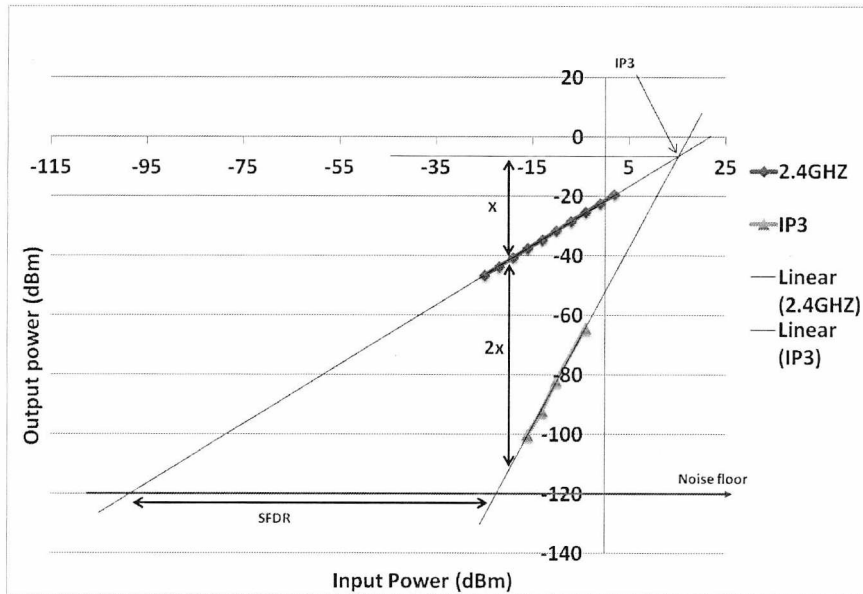


Fig. 2.19: SFDR definition based on the 3rd order intercepts point.

Table 2.2: Typical IIP_3 and SFDR values for commercially available optical transceiver modules.

Type	λ (nm)	SFDR (dB.Hz ^{2/3})	IIP_3 (dBm)
Zonu OZ404 cooled FP laser	1310	107	28
Zonu OZ510 cooled DFB laser	1550 1310	109	30
Fiber-span AC 231-2.5 cooled DFB	1550 1310	98 (min)	26 (min)
Emcore 1933 (un-cooled)	1310	-	30 (min)

A third method makes use of the EVM to define a dynamic range based on some standard specifications. Note that this definition is for modulated signals only. The definition is shown in Fig. 2.20. The EVM_{max} is the maximum permissible EVM (as defined in the standards) for a given system and signal specification. Some of the transmitter EVM requirements from commercial standards for different modulation formats are shown in Table 2.3.

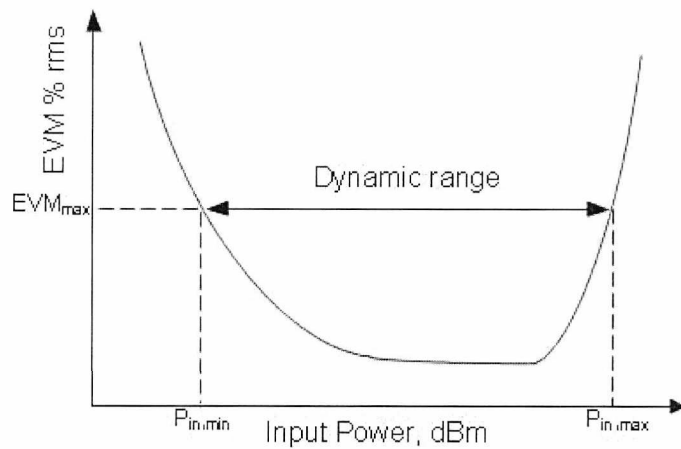


Fig. 2.20: Dynamic range definition based on the EVM.

Table 2.3 [35, 44]: Transmitter EVM specification requirements for different modulation formats. Note that these values depend on the coding rate used.

Modulation	EVM %	
	802.11n	WiMAX
QPSK	22.4	11.9
16 QAM	11.2	5.6
64 QAM	4	2.8

2.3.5 OFDM transmission through direct IM-DD radio-over-fibre links

A lot of work has concentrated on the distribution of OFDM signals (although not limited to those) over low cost direct IM-DD links employing Multi-Mode Fibre (MMF) and Vertical Cavity

Surface Emitting Laser diodes (VCSEL) for short-range indoor applications [2, 3, 5, 22, 45-49], including dual band transmission with other non-OFDM signal standards [3, 5]. The interest in these implementations arises from the ability to transmit at subcarrier frequencies beyond the fibre's 3 dB bandwidth where the fibre exhibits a relatively flat response [50] and the dominance of MMF in short distances (<300 m) over single mode fibre (SMF) in current installations [51]. The aforementioned works have shown good performance when transmitting OFDM signals mainly of the 802.11g standard with null-to-null bandwidths of approximately 20 MHz.

An issue when distributing OFDM signals to multiple RAUs is the use of different fibre lengths. This problem arises from the limited ability of the CP in OFDM systems to prevent ISI as a result of signals being received from multiple RAUs and experiencing different delays [47, 52]. For example, in 802.11g the CP interval is sufficient for delay spreads of up to $0.25 \mu\text{s}$ (approximately) which correspond to a difference in silica fibre lengths of approximately 50 m. One method to overcome this effect is by the use of simple switched diversity receivers [47]. Fig. 2.21 shows throughput results using a commercial AP feeding two RAUs with and without diversity. With diversity, the throughput is maintained at a high level even at the midpoint between the RAUs where the ISI is normally at maximum effect.

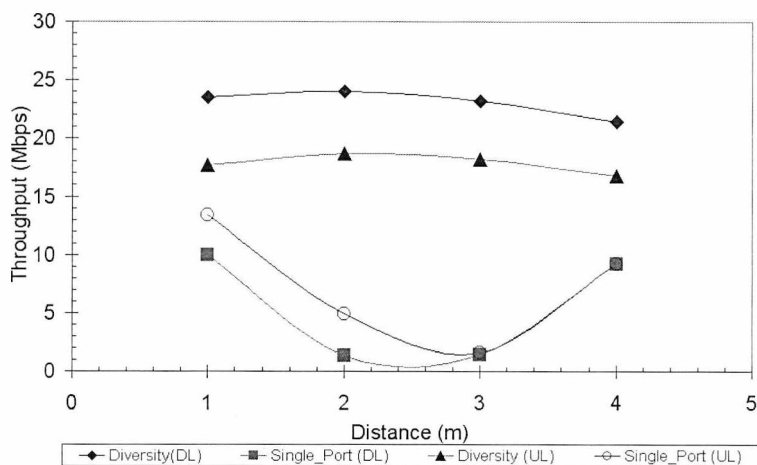


Fig. 2.21: Comparison of throughput results for different fibre lengths when fed by both AP ports (diversity) and when fed by a single AP port (no diversity). The lines between symbols are only an aid for viewing the results and do not represent predicted trends. Distance measured is between the two RAUs [47].

Another problem with OFDM transmission (although not limited to OFDM) is amplifier stability and cross-talk in the RAU (more information on this issue in Chapter 6). This effect is stronger in integrated RAUs where isolation between uplink and downlink paths is harder to maintain. Fig. 2.22 shows throughput results for two different architectures [49]. One is based on integrated components (RAU1) while the other is based on discrete components (RAU2). The integrated approach shows throughput limitations when transmitting 802.11g signals due to increased cross-talk between the uplink and downlink paths in the RAU.

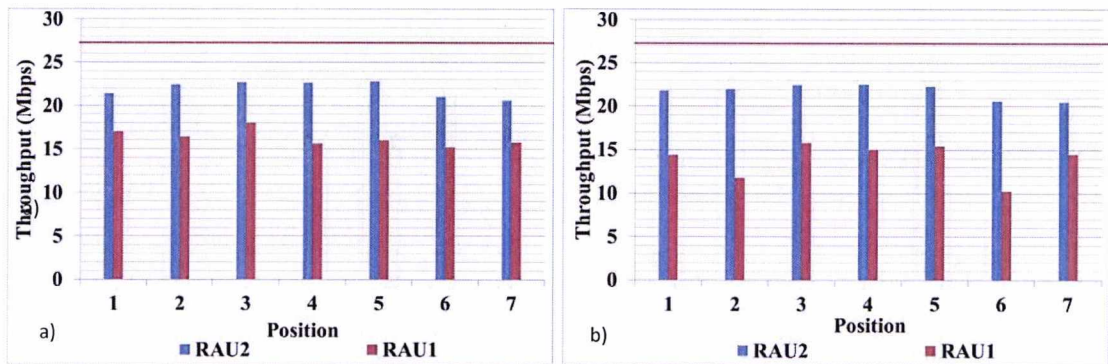


Fig. 2.22: Throughput results for 802.11g experiment a) downlink and b) uplink. The red lines indicate the maximum theoretical throughput of 802.11g [49].

The transmission of new 4th generation broadband standards creates additional challenges. The envisaged standards aim to replace existing 3G standards that are predominately outdoor, requiring higher wireless ranges compared to indoor systems. The increased capacity demand, compared to current systems, will also require higher level modulation formats (as these systems are fundamentally bandwidth limited), necessitating links with higher gains and dynamic ranges. One approach is based on the FUTON project [13, 14], for the transmission and distribution of subcarrier multiplexed signals, each with a 3-dB channel bandwidth of 100 MHz and high level modulation formats (~ 256 QAM) leading to data rates on the order of 1 Gbps per channel. Predictions for the system performance have been presented in [53, 54]. It is also shown that the noise performance of direct IM-DD links based on commercially available DFB laser diodes, does not limit the achievable wireless range provided that there is adequate power control in the uplink [54].

3 PAPR analysis and Transmission of OFDM through Nonlinearities

3.1 Introduction

The first part of this chapter presents the PAPR of amplitude and phase modulated (digital and analogue) signals and then extends to the case of OFDM. The different expressions for the baseband PAPR are presented as well as an empirical expression for the pass-band PAPR with very good agreement with simulation results. The second part of the chapter deals with models from the available literature for OFDM transmission through nonlinear elements. These models are statistical ones, based on instantaneous functions, i.e. memoryless nonlinearities. Two methods from the relevant literature are presented. These are then applied to the case of an optical link where the distortion arises purely from clipping below the threshold current which is assumed to be close to the case of a low biased laser diode.

3.2 Peak-to-Average Power Ratio

3.2.1 PAPR general case

Fig. 3.1 shows a low frequency harmonic signal that represents an information signal (envelope) before modulating a carrier. The RMS value is 0.354 V, while the peak amplitude is 0.5 V. The PAPR will be given by:

$$PAPR (dB) = 10 \log_{10}(CF^2) = 20 \log_{10}\left(\frac{V_{peak}}{V_{rms}}\right) = 3 \text{ dB} \quad (3.1)$$

where CF stands for Crest Factor (the square root of the PAPR).

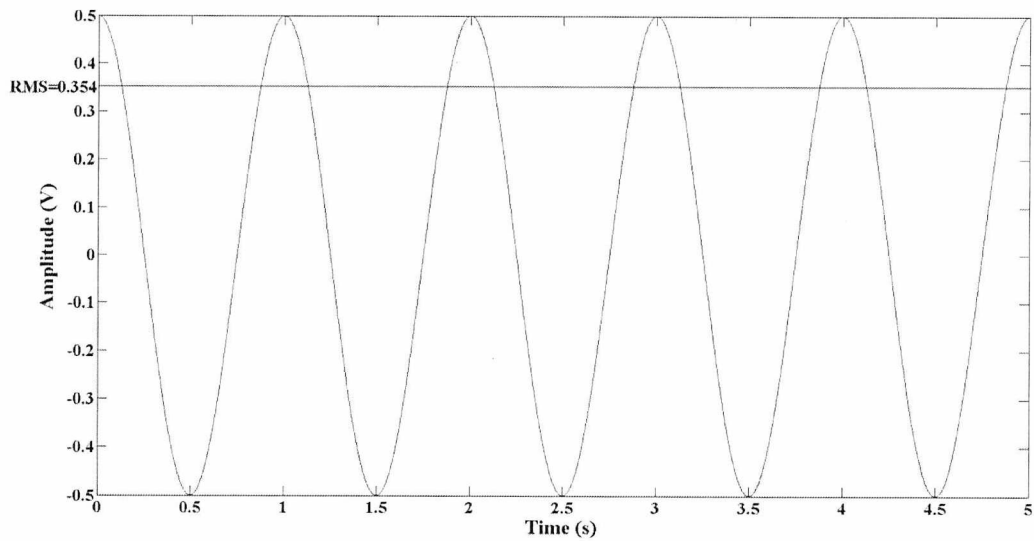


Fig. 3.1: Information signal (envelope).

Fig. 3.2 shows a carrier modulated by the information signal of Fig. 3.1, representing double sideband modulation (DSB-M) with a modulation index (m) of 0.5. The RMS value of the composite signal is 0.75 V while the peak is at 1.5 V.

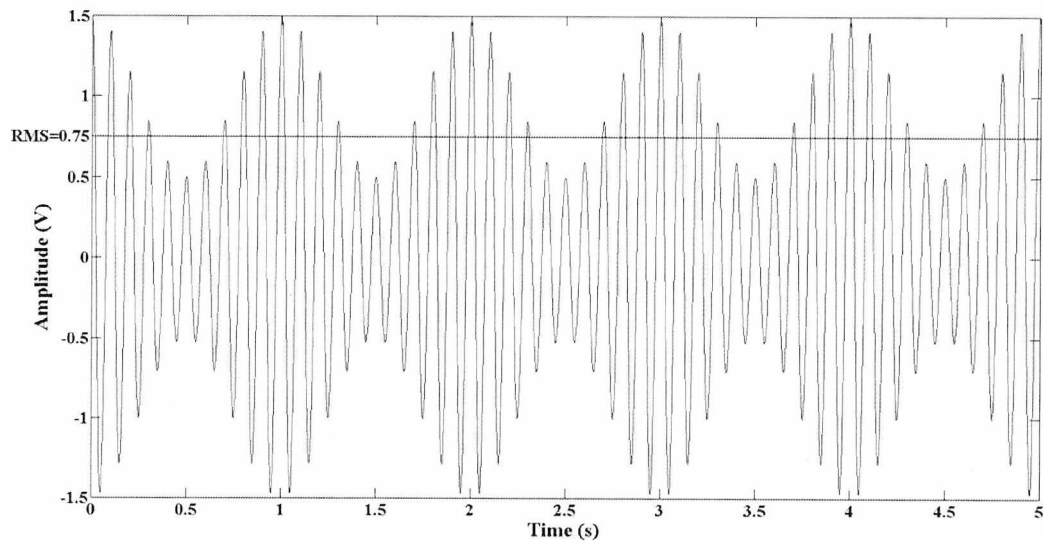


Fig. 3.2: Modulated carrier signal.

The PAPR will be given by:

$$PAPR (dB) = 10 \log_{10}(CF^2) = 20 \log_{10}\left(\frac{V_{peak}}{V_{rms}}\right) = 6 \text{ dB}. \quad (3.2)$$

The increase in PAPR by 3 dB for the modulated signal is due to the presence of the carrier. A similar conclusion can be made in the case of constant envelope signals (or nearly constant) such as QPSK, where the information signal itself has a PAPR of 0 dB but the RF signal will have a PAPR of 3 dB due to the presence of the carrier. The reason for the increase in the PAPR is due to the modulation process itself. The envelope controls the output in the sense that the presence of not of the signal will depend on the envelope. In other words, the information signal turns the carrier on or off. This is true even in the case of suppressed carrier modulation (DSB-SC). This can be shown in Fig. 3.3 which is a plot of the squared amplitude of a DSB-SC signal with the information signal (envelope) superimposed. In the half-cycles of the envelope the carrier amplitude decreases until the carrier is off and then starts to progressively increase again. The result of this is an average value of 0.0625 W instead of 0.125 W which is the average value of the envelope. This effect is always true since the carrier frequency is much higher compared to the frequency of the information signal (i.e. $f_c \gg f_m$). It will not hold in the case where $f_c \approx f_m$.

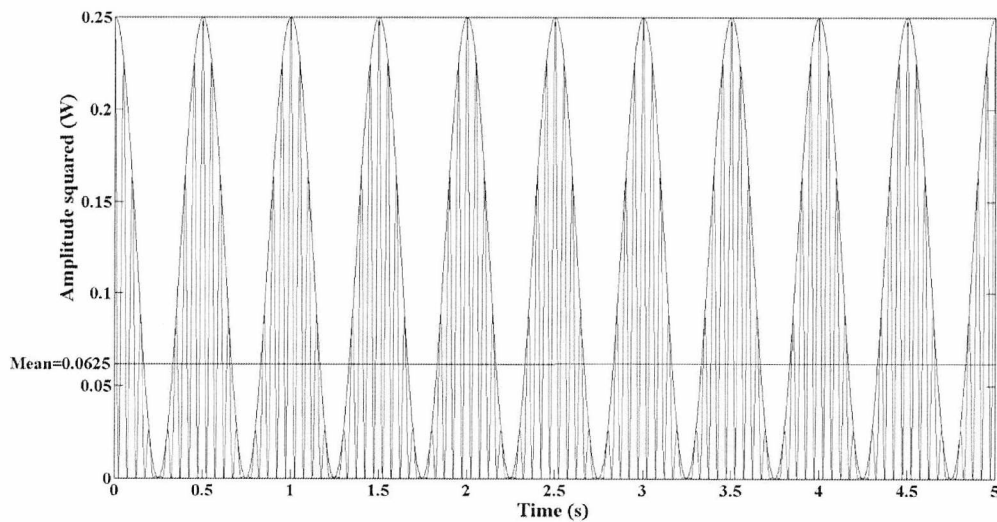


Fig. 3.3: Plot of the squared amplitude of the modulated signal.

For QAM modulation, the effect of the carrier can be shown analytically using:

$$x(t) = m(t) \cos(\omega t + \vartheta) = m(t) \frac{1}{2} e^{j\varphi} + m(t) \frac{1}{2} e^{-j\varphi} \quad (3.3)$$

where $\phi = \omega t + \theta$ and $m(t)$ is the modulation signal.

From (3.3) it is easy to show that:

$$\overline{x(t)^2} = \frac{1}{2} \overline{m(t)^2}. \quad (3.4)$$

That is, the mean power of the modulating carrier is half that of the information (envelope) signal. This reduction by half corresponds to the increase in PAPR by 3 dB.

The PAPR of a given digital modulation scheme is given by the ratio of the peak constellation power to the mean constellation power:

$$PAPR = \frac{\max_i \{I\{i\}^2 + Q\{i\}^2\}}{\frac{1}{M} \sum_{i=1}^M ([I\{i\}]^2 + [Q\{i\}]^2)} \quad (3.5)$$

where M is the constellation size. For large constellation sizes the calculation from (3.5) can become cumbersome. However, for rectangular constellations, (3.5) can be simplified due to the symmetry they possess. By taking into account only one quadrant of the constellation the PAPR will be given by:

$$PAPR = \frac{\max_i \{I\{i\}^2 + Q\{i\}^2\}}{\frac{1}{\sqrt{M}} 4 \sum_{i=1}^{\sqrt{M}/2} ([I\{i\}]^2)} \quad (3.6)$$

Table 3.1 shows the PAPR of various QAM levels. Note that the PAPR does not increase steadily with QAM level and instead reduces for the non-rectangular constellations. This result shows how dependent PAPR is on the type of symmetry of a given constellation.

Table 3.1 [55, p. 162]: PAPR for different QAM levels .

QAM level	PAPR (dB)
4	0
16	2.55
64	3.7
128	3.16
256	4.23
512	4
1024	4.5

3.2.2 PAPR of OFDM

The main problem with OFDM (and multi-carrier systems in general) is its sensitivity to non-linear distortion. This is a result of high PAPR. Peak power values occur when the individual carriers peak in phase. This means that the ADCs and DACs used in the system must have a high dynamic range and enough quantisation levels for adequate performance while any Power Amplifiers used must either be linear over a high dynamic range and therefore expensive or power inefficient.

Expanding (2.1), the output of the IFFT modulator in Fig. 2.1 is given by:

$$x[n] = \frac{1}{\sqrt{N}} \left[\sum_{k=0}^{N-1} \left[|X[k]| \cos\left(\frac{2\pi kn}{N}\right) + \arg(X[k]) \right] + j \sum_{k=0}^{N-1} \left[|X[k]| \sin\left(\frac{2\pi kn}{N}\right) + \arg(X[k]) \right] \right] \quad (3.7)$$

where the $x[n]$ are the time domain samples and the $X[k]$ are the frequency domain samples at the output and input of the IFFT block respectively.

The absolute PAPR over one OFDM frame before the DAC is given by [20, p. 24]:

$$PAPR(x[n])_{0-N-1} = \frac{\max|x[n]|^2}{E\{|x[n]|^2\}} \leq N \frac{\max|X[k]|^2}{E\{|X[k]|^2\}} \quad (3.8)$$

where $E\{\cdot\}$ is the expectation operator and N is the sample size of the OFDM symbol. Equality is achieved when $X[0] = X[k]$ for all k and the symbol with maximum amplitude is chosen, while for the case of Quadrature Phase-Shift Keying (QPSK) modulation, the equality in (3.8) is obtained when the $X[k]$ have the same phase. The term absolute is used here to differentiate this quantity from the statistical PAPR that will be presented shortly. From (3.8), the absolute PAPR with QPSK modulation can have a value of N . For example, for a 256 subcarrier system, the absolute PAPR will be equal to 24.1 dB. However all the carriers being in phase is a highly improbable condition and therefore it is usually neglected. Instead, effective PAPR values can be obtained which are more practical and stem from a statistical analysis of the signal waveform. Assuming the underlying processes acting on the In-phase and Quadrature components of (3.7) are independent and identically distributed (i.i.d), the $X[k]$ will also be i.i.d. The independence assumption is met by randomizing the input symbols. Specifically, the input symbols can be assumed to follow a uniform distribution. The assumption for identical distribution is met by deriving all symbols from the same constellation. As the number of subcarriers increases, the Central Limit theorem (CLT) can be invoked [56, p. 214]: In-phase and Quadrature components tend to zero mean Gaussian variables with variance σ^2 . The envelope $|x[n]| = r$, corresponding to the magnitude of the uncorrelated In-phase and Quadrature components, becomes Rayleigh distributed with parameter σ . The probability that the PAPR over n samples at the output of the IFFT will be smaller than some value, z , will be given by:

$$P(PAPR < z) = (1 - e^{-z})(1 - e^{-z}) \dots (1 - e^{-z}) = (1 - e^{-z})^n \quad (3.9)$$

where $z=r^2/2\sigma^2$.

Therefore, the Complementary Cumulative Distribution Function (CCDF) of the PAPR over n samples at the output of the IFFT modulator will be given by:

$$P(\text{PAPR} > z) = 1 - (1 - e^{-z})^n. \quad (3.10)$$

For $n=N$, (3.10) gives the statistical PAPR per OFDM frame. When the OFDM signal goes through the DAC (assuming it has sufficient dynamic range and does not itself limit the peaks), some extra peak growth may occur due to interpolation [20]. Therefore:

$$\text{PAPR}_{\text{discrete}} \leq \text{PAPR}_{\text{continuous}}. \quad (3.11)$$

This can be avoided with the use of oversampling. In that case, (3.10) will underestimate the PAPR. This is understandable, as oversampling in effect increases the value of n in (3.10) by the oversampling factor, resulting in a higher statistical PAPR. But this increase cannot go on forever as at some point adjacent samples become more and more correlated. In light of this effect, in [57], a factor determined by simulations, is used to increase n in (3.10), while in [58] a level crossing rate analysis is used to provide analytical predictions for the oversampled PAPR. A comparison of the result from (3.10) and the result from [58] is shown in Fig. 3.4. A reasonable clipping probability is 10^{-4} [59] as indicated by the line in Fig. 3.4. Therefore, the PAPR is about 11.2 dB, 11.9 dB, 12 dB and 12.3 dB for ascending order of N . The PAPR for the bandlimited case is about 11.7 dB and 12.6 dB for $N=64$ and $N=2048$ respectively. However, some parameter adjustment in the final expressions provided for the statistical PAPR in both [57] and [58] is required as the number of subcarriers is reduced, as the agreement with simulation results becomes worse for smaller N .

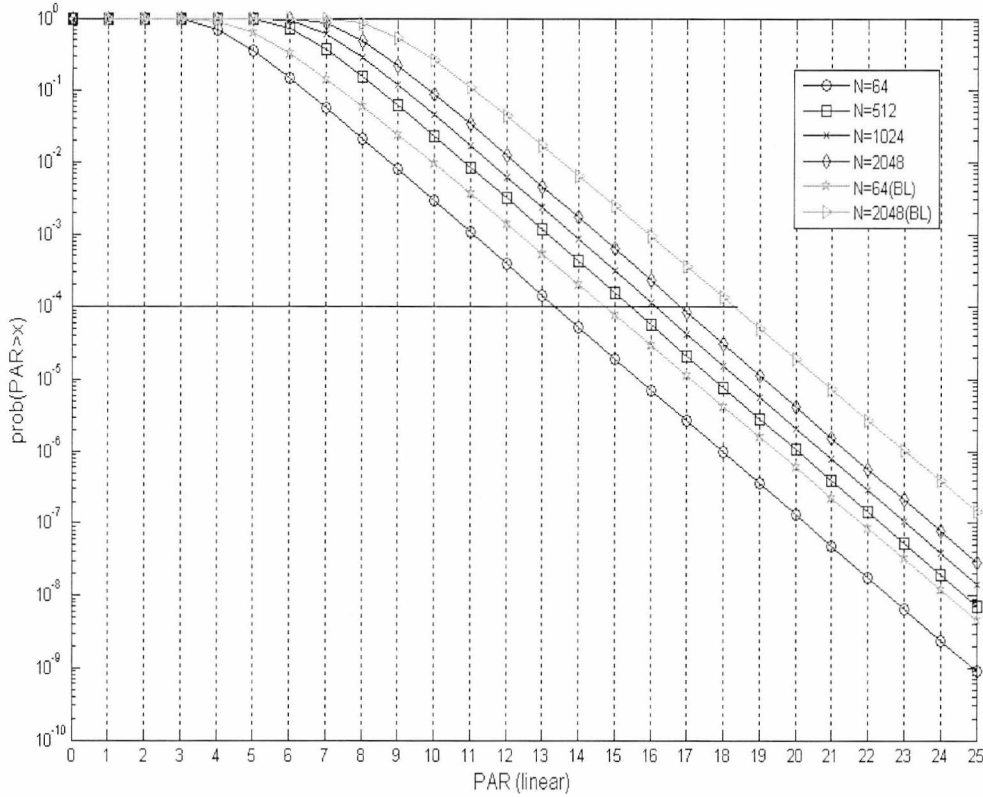


Fig. 3.4: CCDF of PAPR for different number of carriers ($N= 64, 512, 1024, 2048$), including the case when the symbols are bandlimited (oversampling) for $N=64$ and $N=2048$.

Equation (3.10) describes the statistics of the PAPR of the baseband OFDM signal. But in RoF systems it is the up-converted signal (modulating an RF carrier) that modulates the laser diode. The up-converted signal can be described as a narrowband random process of the form [16]:

$$x(t) = r(t) \cos[2\pi f_c t + \Phi(t)] \quad (3.12)$$

where $\Phi(t)$ is the phase with a uniform distribution $\sim [0 - 2\pi]$ and f_c is the RF carrier frequency. As (3.12) comprises the multiplication of two Random Variables, the envelope, $r(t)$, with a Rayleigh distribution, and the cosine distribution of the random phase, $\Phi(t)$, the resulting distribution is Gaussian. Thus, the CCDF of the PAPR per OFDM frame can be given directly in terms of the Gaussian distribution of the up-converted signal:

$$P(\text{PAPR} > g) = 1 - \left\{ \frac{1}{2} \left[1 + \text{erf} \left(\sqrt{\frac{g}{2}} \right) \right] \right\}^{lN} \quad (3.13)$$

where erf is the error function, $g=x^2(t)/\sigma^2$ and l is a factor empirically estimated (through simulations). Fig. 3.5 shows the statistical PAPR given by (3.13) for 128 subcarriers ($l=23$), 512

subcarriers ($l=27$), 2048 subcarriers ($l=29$) and 4096 subcarriers ($l=31$). Also shown for comparison is the PAPR obtained from a simulation in Matlab. The simulation is carried out by generating, oversampling by a factor of 4 and up-converting 4000 frames for each IFFT size and by calculating the PAPR for each frame.

The Probability Distribution Function (PDF) of the PAPR is given by:

$$p_{PAPR}(g) = \frac{d}{dg} \left\{ \left[\frac{1}{2} \left[1 + \operatorname{erf} \left(\sqrt{\frac{g}{2}} \right) \right] \right]^{LN} \right\}. \quad (3.14)$$

The result of (3.14) is shown in Fig. 3.6. Also shown are the median points of the distributions. For IFFT sizes up to 2048, the median increases by approximately 0.4 dB for each doubling of the number of subcarriers. Above 2048 subcarriers, this value of increase reduces to approximately 0.3 dB.

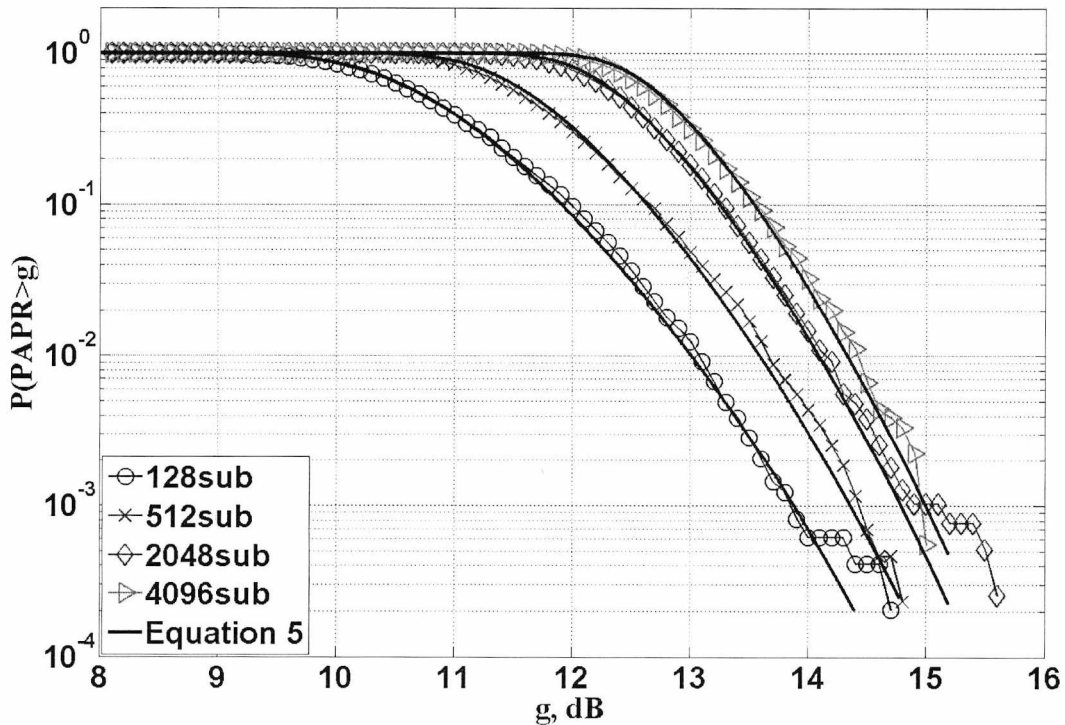


Fig. 3.5: CCDF plots of the PAPR of the up-converted OFDM signal.

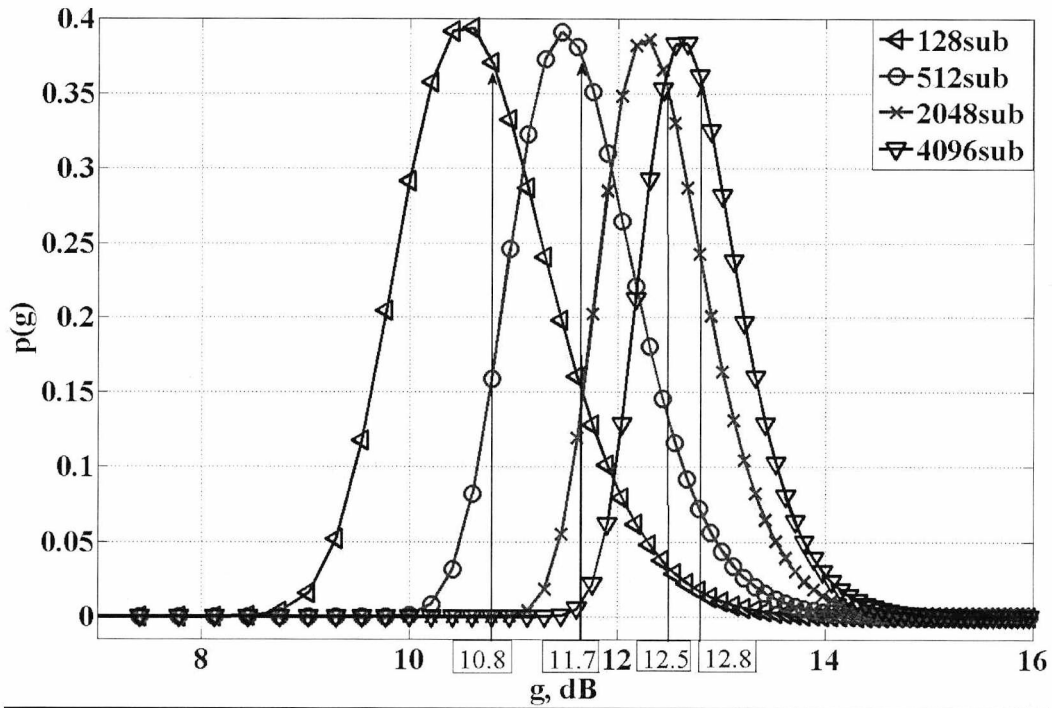


Fig. 3.6: PDF of PAPR of 128, 512, 2048 and 4096 subcarriers.

Note that the expressions for the baseband and pass-band PAPR that have been presented here do not contain any information about the modulation level. Although, as was discussed in Section 3.2.1, different modulation levels do have different PAPRs and the absolute PAPR in (3.8) does depend on the constellation PAPR, the statistical PAPR does not. This was also verified through measurements with different modulation levels in [53].

3.3 Transmission of OFDM through nonlinearities

3.3.1 Direct method

For an input signal, $x(t)$, with a Gaussian distribution (justification for this assumption was discussed in Section 3.2.2), the output, $y(t)$, of a nonlinearity will be given by the sum of a useful attenuated version of the input signal and an uncorrelated distortion term, $d(t)$ [60]:

$$y(t) = \alpha x(t) + d(t) \quad (3.15)$$

where α is a function of the nonlinearity that describes the gain compression and is proportional to the cross-correlation of the input signal with the output signal. It is given by:

$$\alpha = \frac{R_{xy}(\tau)}{R_{xx}(0)} = \frac{1}{R_{xx}(0)} \int_{-\infty}^{\infty} f(x) x p_X(x) dx \quad (3.16)$$

where $\alpha \in [0,1]$

where $f(x)$ is the nonlinear function, $p_X(x)$ is the input signal PDF and R_{xx} is the input autocorrelation function. The distortion term is treated as a form of additive noise termed *distortion noise* owing to the assumption that it is uncorrelated with the output signal. Here, the real version of the theorem has been used where α will be a real quantity, assuming a pure amplitude-to-amplitude nonlinearity (i.e. no phase distortion).

After the ADC and CP removal in the OFDM receiver (see Fig. 2.1), the received signal at subcarrier k and symbol s will be given by:

$$\begin{aligned} X^s[k] &= \sum_0^{N-1} \{(\alpha x[n]) \otimes h[n] + d[n] \otimes h[n] + n[n]\} e^{-\frac{j2\pi kn}{N}} \\ &= \alpha X^s[k] H^s[k] + D^s[k] H^s[k] + N^s[k] \end{aligned} \quad (3.17)$$

where $h[n]$ is the channel impulse response contribution, $n[n]$ is the Gaussian additive noise contribution (AWGN) and \otimes denotes circular convolution.

Assuming a zero forcing equalization scheme, the estimate for the transmitted symbol at subcarrier k and OFDM symbol s will be given by:

$$\begin{aligned} \hat{X}^s[k] &= \alpha X^s[k] + \{D^s[k] + \hat{N}^s[k]\} \\ \text{where } \hat{N}^s[k] &= \frac{N^s[k]}{H^s[k]} \end{aligned} \quad (3.18)$$

The first part on the right hand side of (3.18) represents the useful signal while the terms in brackets represent the samples of the distortion and other noise contributions at the location of subcarrier k .

The soft limiter nonlinear model (Fig. 3.7) is a good choice for testing the model as it leads to closed form expressions for the distortion noise, $d(t)$, and the attenuation factor, α . Also, the soft limiter model is interesting as it can lead to performance estimations for a laser biased at a low bias where most of the nonlinearity will come from the response below threshold. Additionally, it is a good model of an ideal pre-distorter [18]. The nonlinearity is implemented in the simulation as an envelope limiter, in other words, it only operates on the envelope, $r(t)$, of the input signal and not the phase. The nonlinearity is described by:

$$f(r) = \begin{cases} r, & r \leq A \\ A, & r > A \end{cases} \quad (3.19)$$

Therefore, (3.16) is modified to:

$$\alpha = \frac{R_{ry}(\tau)}{R_{rr}(0)} = \frac{1}{2\sigma^2} \int_{-\infty}^{\infty} f(r) r p_R(r) dr \quad (3.20)$$

where $p_R(r)$ is the envelope PDF which follows a Rayleigh distribution, and $2\sigma^2$ is the input power.

In order to normalise the input power to the saturation level of the nonlinear function, the clipping ratio γ is defined as:

$$\gamma = \frac{A}{\sqrt{2}\sigma} \quad (3.21)$$

The expressions for the soft limiter are given by [24 p.138, 61]:

$$\alpha = 1 - e^{-\gamma^2} + \frac{\sqrt{\pi}\gamma}{2} \text{erfc}(\gamma) \quad (3.22)$$

$$\sigma_d^2 = 2\sigma^2 + (1 - e^{-\gamma^2} - \alpha^2). \quad (3.23)$$

The effective SNR is then calculated using:

$$SNR_{RX} = \frac{2\alpha\sigma^2}{\sigma_d^2 + \sigma_n^2} \quad (3.24)$$

where σ_d^2 is the distortion noise variance and σ_n^2 is the AWGN noise variance.

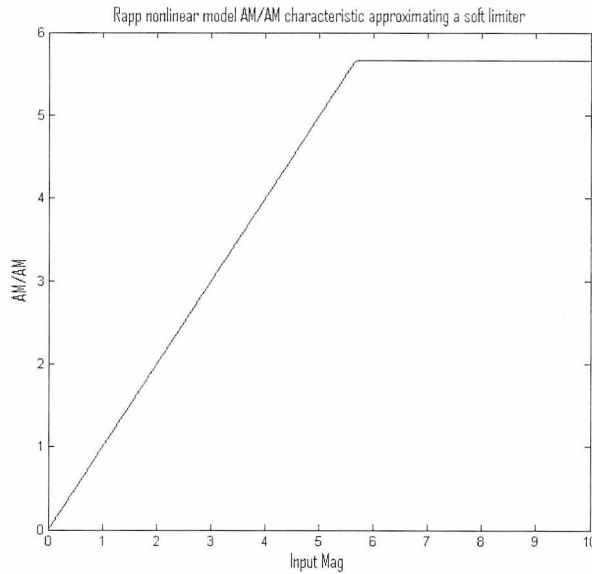


Fig. 3.7: Rapp model [62] approximating the soft limiter. This is done by using a high value for the parameter controlling the sharpness of the region between the linear and saturation parts.

The EVM is then given by (2.15). The variance in (3.24) represents the variance of the total noise after the nonlinearity. For Nyquist rate sampling, the noise will fall in-band and this expression is correct. However, in the case where oversampling is applied in the OFDM system, the result provided by (3.24) will underestimate the SNR as some of the distortion noise will fall out-of-band.

Fig. 3.8 is a plot of EVM (%) and EVM variation versus clipping ratio. The blue trace represents the analytically obtained EVM while the green and red traces are the simulated without zeros (null subcarriers) and with zeros respectively. The traces on the secondary axis represent the ratio of the analytically obtained EVM to the EVM obtained by the simulation ($EVM_{ana.}/EVM_{sim.}$). The difference or variation between the two is highest at high clipping levels and this represents one of the limits of this model.

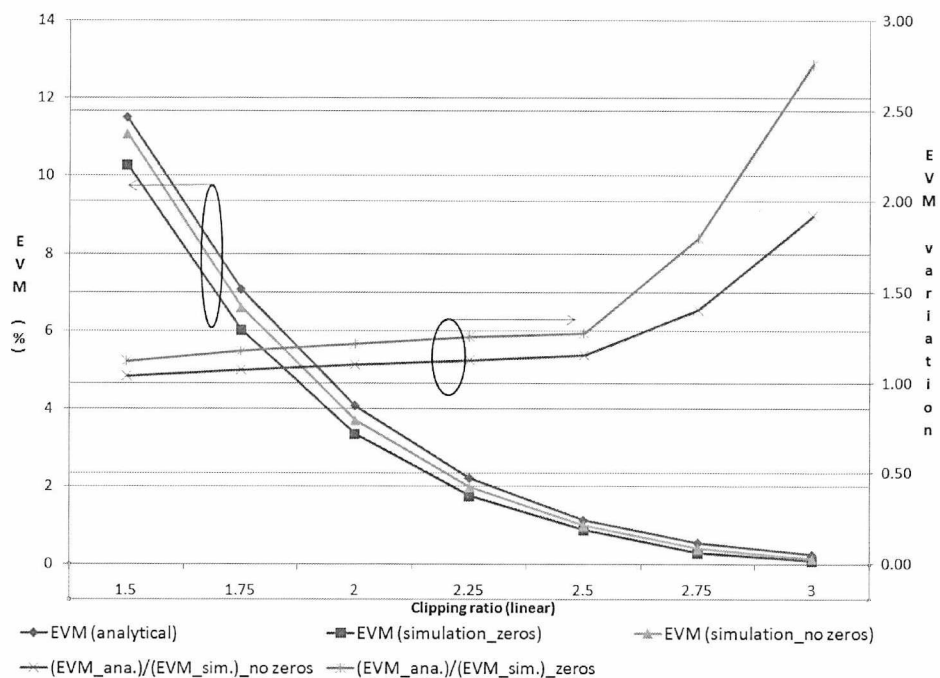


Fig. 3.8: EVM versus clipping ratio for simulation and analytical results. Modulation is QPSK and No. of subcarriers = 2048.

Fig. 3.9 is a plot of the variation between the analytical and simulated EVM values for different number of subcarriers. The modulation (QPSK) and clipping ratio (=1.75) are kept constant. The variation is higher for low number of subcarriers. Fig. 3.10 is a plot of the EVM variation as the QAM level changes while the number of subcarriers and clipping ratio are kept constant. The variation increases for high QAM levels.

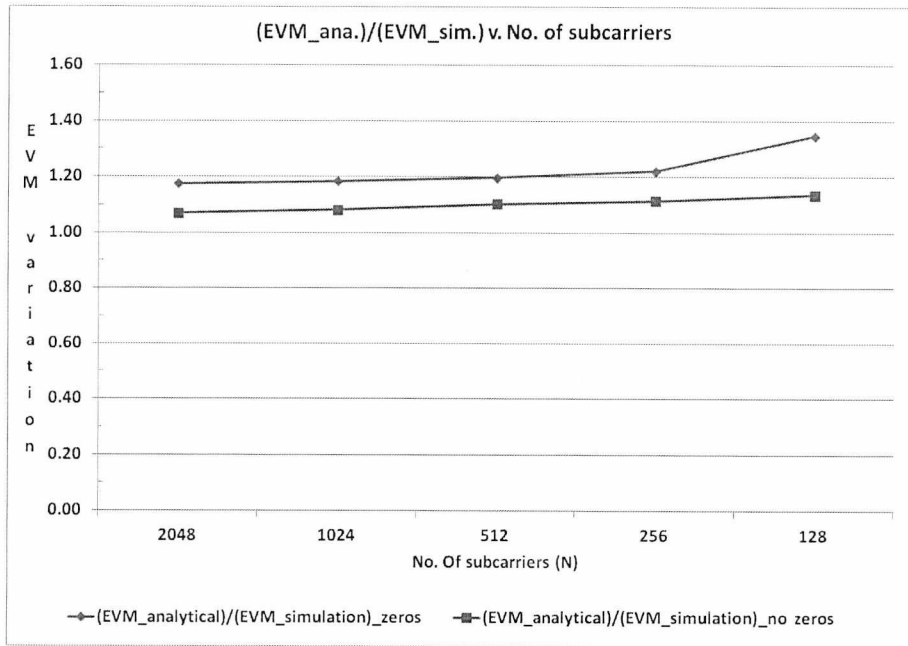


Fig. 3.9: Variation between simulated and analytical EVM for different number of subcarriers. Clipping ratio = 1.75 (4.9 dB), modulation is QPSK.

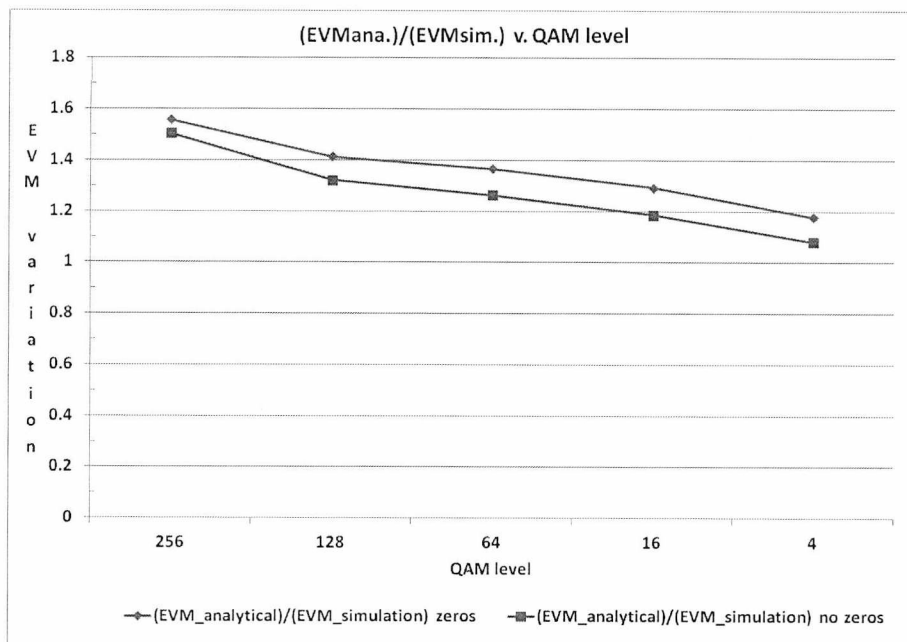


Fig. 3.10: Plot of variation between simulated and analytical EVM for different QAM level. Clipping ratio = 1.75 (4.9 dB), No. of subcarriers = 1024.

3.3.2 Output autocorrelation function

The direct method described in the previous Section has a main disadvantage: It does not separate in-band and out-of-band distortion. An alternative method, which does not suffer from this problem, makes use of the fact that the autocorrelation function and the PSD are a Fourier transform (FT) pair. The output autocorrelation function, $R_{yy}(\tau)$, can be expressed in terms of the input autocorrelation function and the nonlinear function. In other words, it requires knowledge of the input autocorrelation function or the input PSD. Expressing the distortion in terms of the output auto-correlation function is advantageous as it allows for the direct calculation of the PSD through an FT of $R_{yy}(\tau)$. For a thorough description of this method for real signals see [16, p. 251]

In the case of passband clipping, it is the real up-converted signal that will get clipped. The input OFDM signal can be represented as a narrowband Gaussian process, according to (3.12). The PSD of the input signal can be assumed flat over the considered bandwidth and is shown in Fig. 3.11.

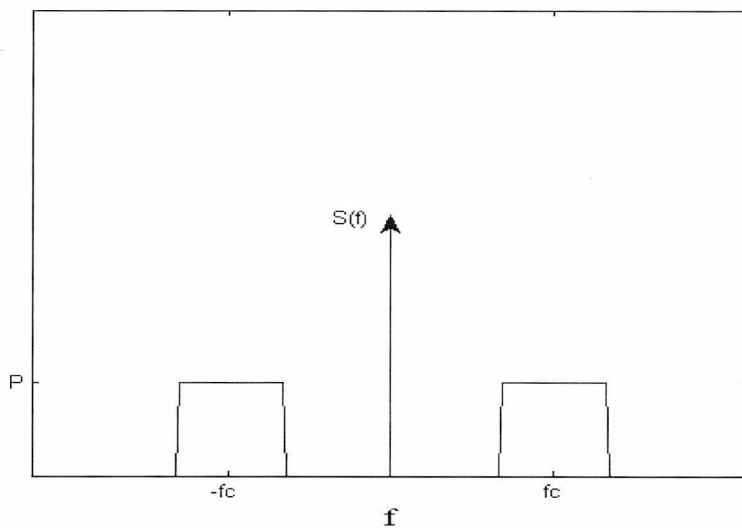


Fig. 3.11: PSD of input signal.

The in-band power is given by $2P\Delta f$, where Δf is the bandwidth of the signal.

The aim now, is to find an expression for the output autocorrelation function:

$$E\{y(t_1)y(t_2)\} \stackrel{\text{def}}{=} R_{yy}(\tau) = \iint_{-\infty}^{\infty} g[x(t)]g[x(t+\tau)]p_X(x_1,x_2)dx_1dx_2 \quad (3.25)$$

where $\tau=t_2-t_1$ (stationary process assumption), and $p_X(x_1,x_2)$ is the bi-variate Gaussian distribution.

To solve this function it is required to separate the double integral in (3.25). This can be done by first simplifying the integral using *Price's theorem* [63] and then separating it using *Hermite polynomials* [17, 64] or by using *Laguerre polynomials* [18]. The general form of the result for a soft limiter nonlinearity is given by:

$$R_{yy}(\tau) = R_{xx}(\tau)\text{erf}^2\left(\frac{A}{\sqrt{2}\sigma_x}\right) + \sigma_x^2 \sum_{2i}^{\infty} d_{2i} \left[\frac{R_{xx}(\tau)}{\sigma_x^2}\right]^{2i+1}. \quad (3.26)$$

From (3.15) and (3.26), we can observe that:

$$\alpha = \text{erf}\left(\frac{A}{\sqrt{2}\sigma_x}\right) \quad (3.27)$$

$$d(t) = \sigma_x \sqrt{\sum_{2i}^{\infty} d_{2i} \left[\frac{R_{xx}(\tau)}{\sigma_x^2}\right]^{2i+1}}. \quad (3.28)$$

The first term in (3.26) is the desired signal term (attenuated version of the original signal in the original bandwidth) while the summation represents the distortion terms. The $2i + 1$ exponent in the second term, represents a multiplication of the input autocorrelation function with itself. In the frequency domain this multiplication corresponds to a $(2i+1)$ fold convolution of the input spectral density with itself. This convolution creates the spectra of the distortion terms (see Fig. 3.12) while the d_n 's are just the weights for the amount of distortion in the different frequency bins. For example, if the nonlinear function was a pure second order

nonlinearity of the form $y=x^2$, then the signal term would be equal to zero and the distortion term would be a 1-fold convolution of the input spectral density with its self, resulting in spectral components at dc and $2f_c$. Also, note that only odd order distortion terms are produced from (3.26) as the soft limiter nonlinearity for real signals is an odd function.

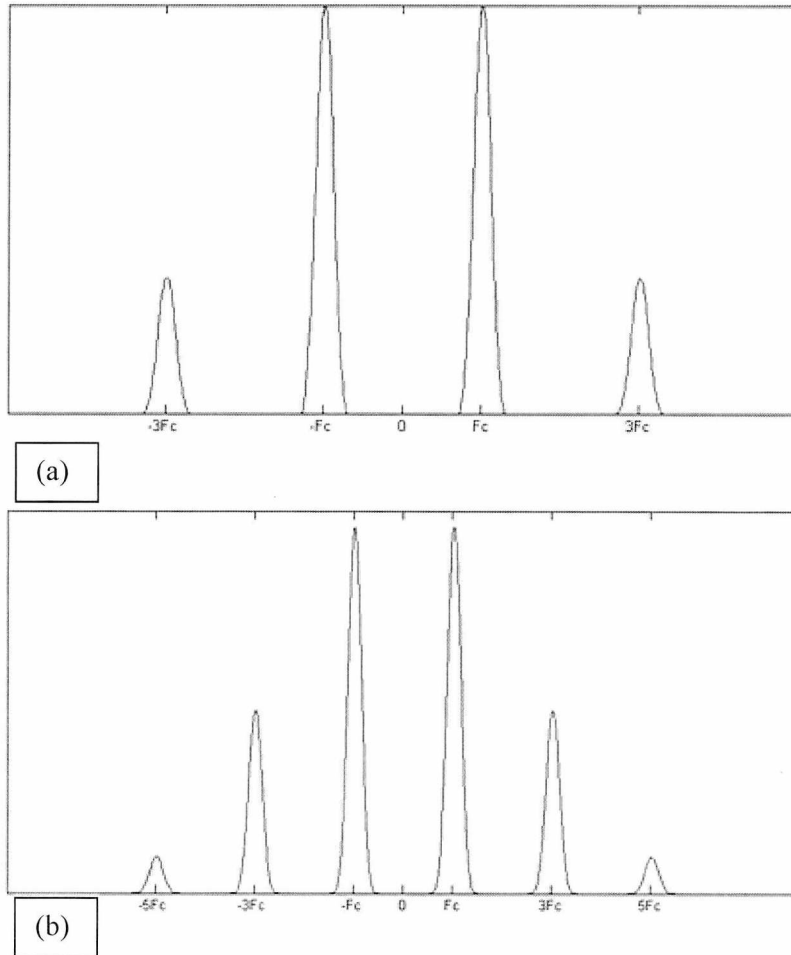


Fig. 3.12: (a) 3-fold convolution, (b) 5-fold convolution of input PSD (Fig. 3.11).

The variance of the output will be given by:

$$\sigma_y^2 = E\{y^2(t)\} = R_{yy}(0) = \sigma_x^2 \operatorname{erf}^2\left(\frac{A}{\sqrt{2}\sigma_x}\right) + \sigma_x^2 \sum_{2i}^{\infty} d_{2i}. \quad (3.29)$$

The first part of the right hand side of (3.29) is the signal power while the second part is the distortion power. In the case of Nyquist rate sampling, the ratio of these two will give the Signal-to-Distortion Ratio (SDR) as all the distortion noise will lay in-band.

In the case of oversampling, some of the distortion noise will fall out-of-band. To obtain the distortion noise contributions at different frequency ranges analytically, requires solving the n -fold convolutions resulting from the FT of the distortion noise part in (3.26). In a simulation environment, if filtering is applied to remove the out-of-band components, a weighting function will need to be included to scale the output PSD, $S_y(f)$:

$$G(f) = S_y(f)|H(f)|^2 \quad (3.30)$$

where, $H(f)$ is the frequency response of the filter.

A simulation was carried out for an OFDM signal with a bandwidth of 10 MHz, 1024 subcarriers and no zeros (Nyquist rate sampling). The simulated and analytic results at different clipping ratios are shown in Fig. 3.13. The SDR was obtained through the variances from (3.29).

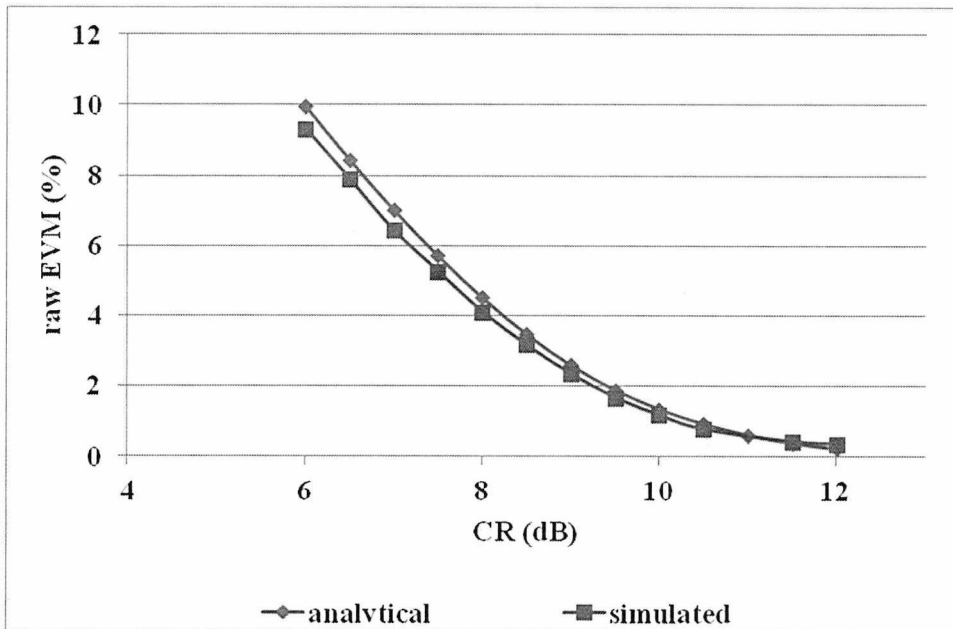


Fig. 3.13: Simulation and analytic results for different clipping ratios (CR).

3.4 Modelling of low bias laser using the direct method

A laser biased at a low bias point offers certain advantages, namely low power consumption and longer life time. Low power consumption may be particularly important for Power over Fibre (PoF) applications [19], where the RAU is remotely powered through a separate optical fibre feed, by employing a high power laser diode at the CU and a PD in photovoltaic mode at the RAU to generate the required power for biasing the RAU components.

The RF response at low bias approximates a soft limiter nonlinearity and thus the direct method can be applied without requiring the use of numerical solutions since closed form expressions can be readily obtained. In a RoF link, the nonlinearity is mainly due to the laser. The distortion from the nonlinear power transfer function of the laser will result in distortion noise that will degrade the SNR of the system. Based on (3.15) a model can be used that is shown in Fig. 3.14. For Nyquist rate sampling, the distortion noise will fall in-band and the effective signal to noise ratio, assuming that the impulse response of the link, $h(t)$, is properly equalized at the receiver, will be given by (3.24). In this case, σ_n^2 will be the variance of the other noise contributions, given by:

$$\sigma_n^2 = \sigma_{RIN}^2 + \sigma_{shot}^2 + \sigma_T^2 \quad (3.31)$$

where σ_{RIN}^2 is the laser RIN noise variance, σ_{shot}^2 is the PD shot noise variance and σ_T^2 is the thermal noise variance.

The distortion noise variance and the attenuation coefficient are given by (3.22) and (3.23).

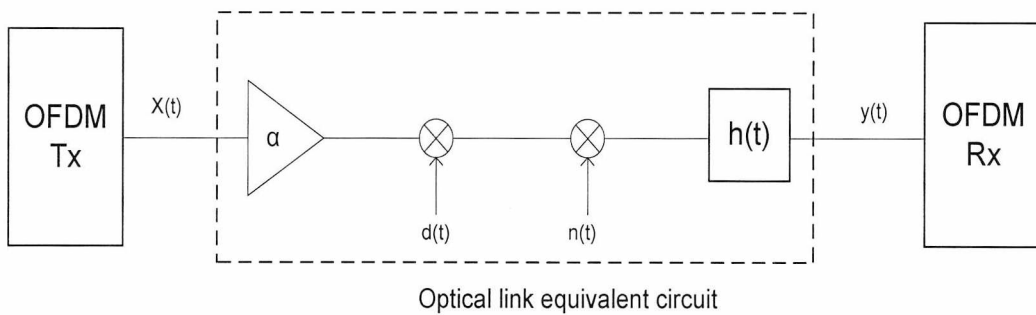


Fig. 3.14: Optical link equivalent circuit.

The EVM will be given by:

$$EVM = \sqrt{\frac{1}{SNR_{RX}}} \quad (3.32)$$

For baseband clipping, the nonlinear function is assumed to be the one shown in Fig. 3.7.

For an input signal that is Rayleigh distributed with PDF $p_x(x)$, the PDF at the output of the clipping function, $p_y(y)$, will be given by:

$$p_Y(y) = \frac{y}{\sigma_x^2} e^{-\frac{y^2}{2\sigma_x^2}} [u(0) - u(A)] + P(X > A)\delta(A) \quad (3.33)$$

where $P(X>A)$ is the probability that the input signal amplitude will exceed the saturation point, A , and is given by $\exp(-A^2/2\sigma^2)$. The result of (3.33) is plotted in Fig. 3.15 for $\sigma_x=1$ and $A=2$.

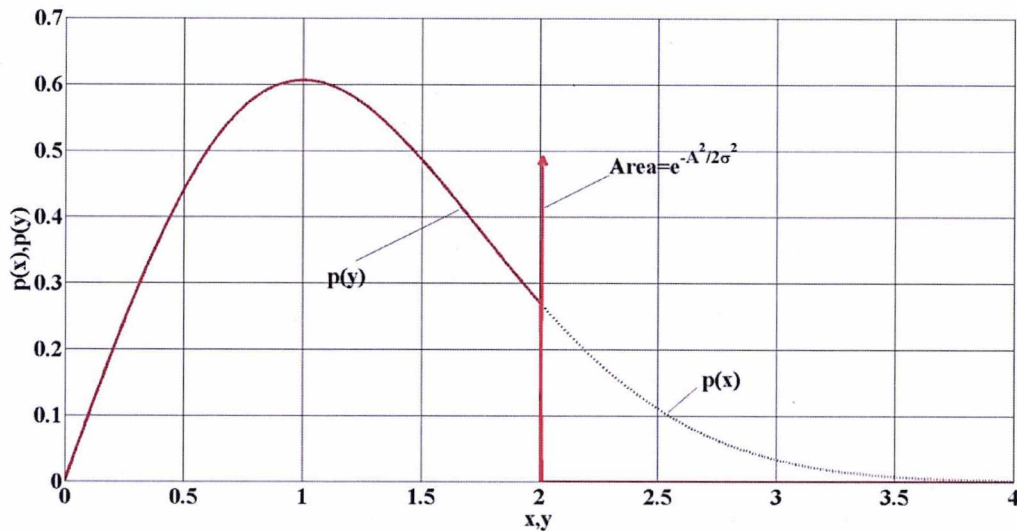


Fig. 3.15 : Input Rayleigh PDF (dotted black line) and output PDF (red line) of clipping nonlinearity.

3.4.1 Polynomial modelling

Previous work has shown that the nonlinearity in a RoF link is mainly due to AM/AM effects [65]. Based on this result, and the fact that most of the nonlinearity is due to the laser, here it is assumed that for simulation purposes an AM/AM model for the laser can adequately model the

real device. AM/AM models were extracted for a low biased DFB laser diode with a threshold current of 29 mA at two different bias levels of 35 mA and 37 mA [66].

A sinusoidal signal at 2.4 GHz was applied by an Agilent E4438C Vector Signal Generator (VSG), and the output power was measured after the PIN-PD by an Agilent E4440A Vector Signal Analyser (VSA) connected to a laptop with Agilent VSA software. The input power at the laser was varied from -41 dBm to +9 dBm, in order to find a hard clipping laser operation. The experimental set-up is shown in Fig. 3.16. Fig. 3.17 (a) shows the AM/AM characteristics fitted with a 7th order polynomial.

Due to the fact that the measurement data comes from a strong nonlinear behavior, a second model was also extracted based on the Rapp model, termed *modified Rapp model*, given by [66]:

$$g_{Rapp} = \frac{kA}{\left[1 + \left(\frac{A}{SAT}\right)^{As}\right]^{\frac{1.6}{2s}}} \quad (3.34)$$

where A is the input amplitude, SAT the saturation level and s the smoothness coefficient.

The AM/AM characteristics are shown in Fig. 3.17 (b).

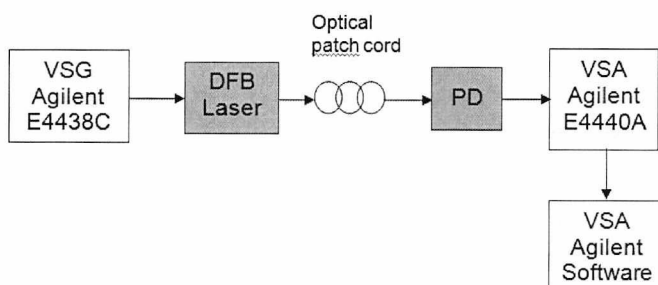


Fig. 3.16: Experimental set-up for AM/AM measurements.

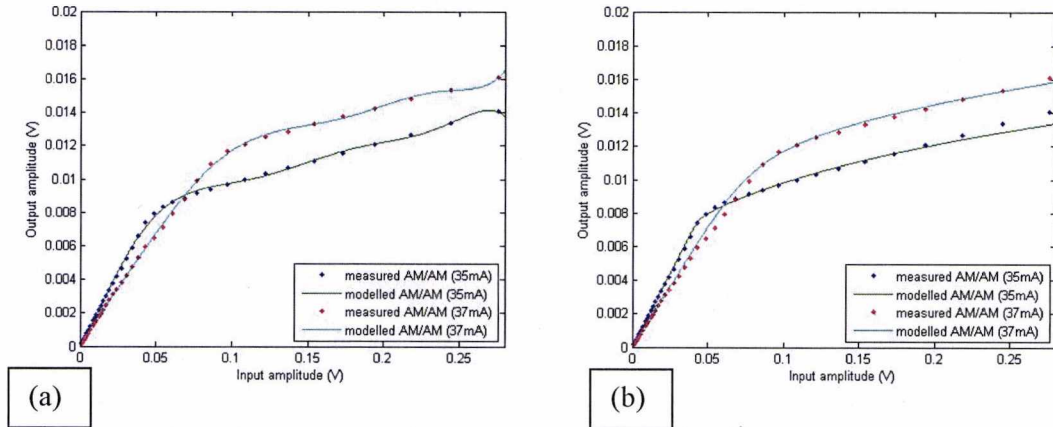


Fig. 3.17: AM/AM characteristic of the DFB laser using (a) a 7th-order polynomial model and (b) the modified Rapp model.

3.4.2 Simulation results

The simulation was carried out in Matlab-Simulink, for an OFDM signal with 2048 subcarriers and QPSK modulation. The analytical EVM obtained from the expressions outlined in Section 3.4 was compared to the EVM obtained by simulating an OFDM link with a nonlinearity given by the modified Rapp and polynomial functions of Section 3.4.1. The sampling was done at the *Nyquist rate* i.e. no oversampling was performed. The other optical noise contributions were not taken into account. Fig. 3.18 shows the EVM result plotted against the clipping ratio, γ , in a linear scale (corresponding to 3.5 dB to 9.5 dB). The simulation result shows that there is some agreement between the analytical and simulated results but the correlation between the two depends, as expected, on the bias point. The result for 37 mA deviates more from the analytical curve. This is a result of the change in the laser response as the bias is increased: more distortion is coming from points in the laser response away from the threshold point and as a result the response is less similar to a soft limiter. However, the deviation between the analytical and simulated curves depends on the AM/AM modelling and how well this fits the measurements. This is shown in Fig. 3.19 as a comparison between the modified Rapp and the polynomial models. The deviation from the analytical curve at low clipping ratios is higher for the polynomial model which has a smoother turning point into the saturation or clipping region compared to the modified Rapp model. The deviation at higher clipping ratios which appears like an overshoot from the analytical curve is due in-part to the smoother transition into the clipping region which affects a higher range of amplitudes of the signal and due to the deviation

between the modelled and measured data in the linear region of the DFB laser response. Furthermore, the DFB laser response below threshold, although close, is not a soft limiter response.

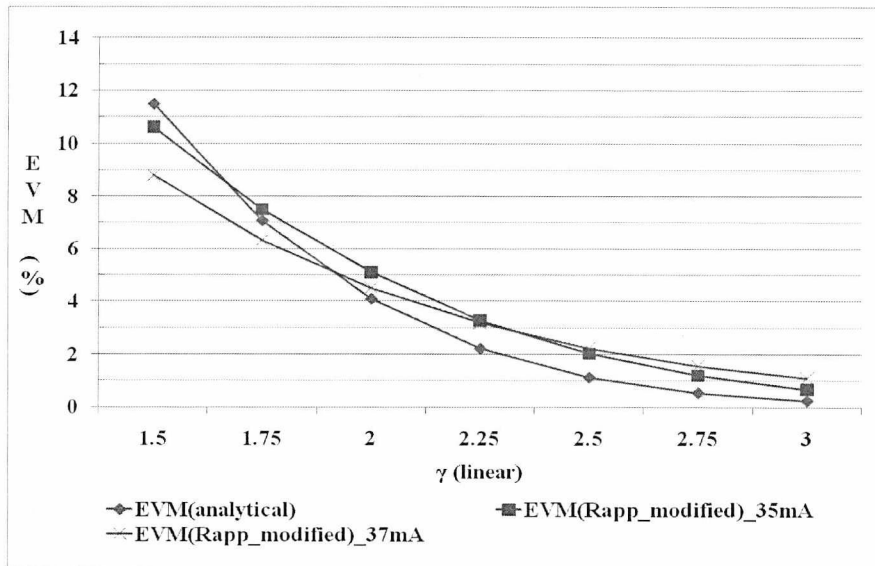


Fig. 3.18: Simulation results for biases of 35 mA and 37 mA.

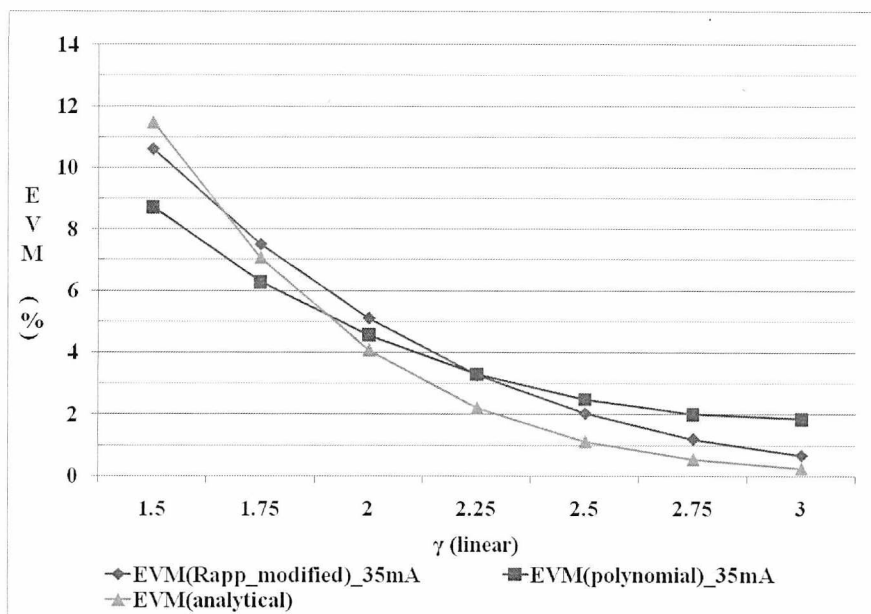


Fig. 3.19: Comparison between modified Rapp and polynomial models at 35 mA with respect to the analytical result.

3.5 Modelling of low biased laser using the output autocorrelation function

The static response of a RoF link is shown in the left part of Fig. 3.20. The response below threshold is assumed to be negligible. The input signal is shown as a Gaussian process centred about a bias point I_B . The output photocurrent is given by:

$$I_p = g(I_x - I_{TH}) \quad \text{where } I_p \in [0, \infty) \quad (3.35)$$

where I_{TH} is the threshold current and g is the current gain of the optical link.

In order to simplify the solution, the response is normalised so that the input signal can be treated as a zero mean Gaussian process. This is shown in the right part of Fig. 3.20. The output current is now given by:

$$I_p = g(I_x - I_{TH} + I_B) = gI_x + g(I_B - I_{TH}) = gI_x + K. \quad (3.36)$$

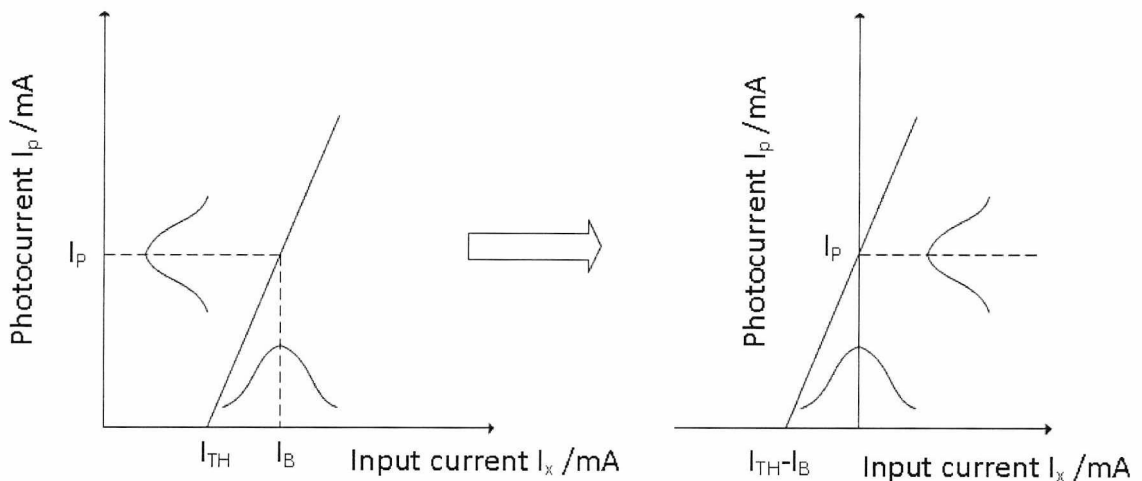


Fig. 3.20: Static response of laser diode and normalised to zero mean input.

For simplicity we set: $I_p = y$ and $I_x = x$.

The PDF of the output signal will be given by:

$$p_Y(y) = \frac{1}{\sqrt{2\pi}g\sigma_x} e^{-\frac{(y-K)^2}{2g^2\sigma_x^2}} u(0) + P\left(X < -\frac{K}{g}\right) \delta(0) \quad (3.37)$$

where $P(X < -K/g)$ is the probability that the input signal will be lower than $-K/g (=I_{TH}-I_B)$ and is given by $0.5+0.5\text{erf}[-K/(g\sigma_x)]$.

The result of (3.37) is plotted in Fig. 3.21 for $I_B = 15$ mA, $I_{TH}=10$ mA, $g= 0.09$ and $\sigma_x^2=0.1$ (=20 dBm).

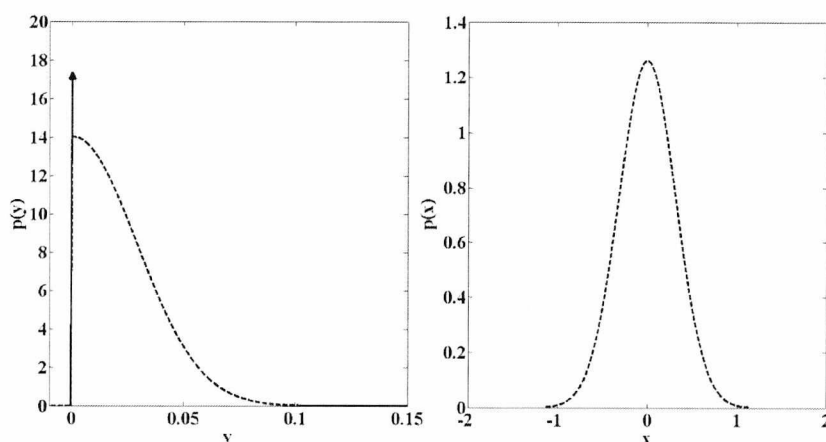


Fig. 3.21: Input (right) and output (left) PDFs of the nonlinearity. The area under the Delta function in the right part of the figure is given by $0.5+0.5\text{erf}[-K/(g\sigma_x)]$.

The mean of the output signal will be given by:

$$E[y] = 2 \int_0^{\infty} (gx + K) p_X(x) dx \quad (3.38)$$

where $p_X(x)$ is the PDF of the input signal. From (3.38):

$$E[y] = \frac{2g\sigma_x}{\sqrt{2\pi}} + K \quad (3.39)$$

To get the output autocorrelation function, Price's theorem [63] can be used:

$$\frac{\partial R_{yy}(\tau)}{\partial R_{xx}(\tau)} = E \left[\frac{\partial y}{\partial x_1} \frac{\partial y}{\partial x_2} \right] = g^2 \iint_{-(I_B - I_{TH})}^{\infty} p_X(x_1, x_2, r) dx_1 dx_2 \quad (3.40)$$

where $b = I_B - I_{TH}$ and $p_X(x_1, x_2, r)$ is the bi-variate Gaussian distribution or joint PDF of the input signal, given by [56, p.138]:

$$p_X(x_1, x_2, r) = \frac{1}{2\pi\sigma_x^2\sqrt{1-r^2}} e^{-\frac{x_1^2 + x_2^2 + 2rx_1x_2}{2\sigma_x^2(1-r^2)}} \quad (3.41)$$

where $\sigma_x = \sigma_{x_1} = \sigma_{x_2}$ is the standard deviation of the input and $r(\tau) \stackrel{\text{def}}{=} r$, where $r \in [-1, 1]$, is the correlation coefficient or normalized co-variance given by:

$$r(\tau) = \frac{E[x_1x_2]}{\sigma_x^2} = \frac{R_{xx}(\tau)}{\sigma_x^2} \quad (3.42)$$

In order to solve the double integral in (3.40) the result from [67, p. 75] can be used:

$$\int_{-(I_B - I_{TH})}^{\infty} dx \int_{-(I_B - I_{TH})}^{\infty} dx e^{-x_1^2 - x_2^2 - 2\cos\theta x_1x_2} = \frac{1}{2} \theta \csc\theta + b \quad (3.43)$$

where $b = 1.92(I_B - I_{TH})$ is an empirical correction factor, that is required so that the result of (3.43) takes into account values smaller than zero.

By setting $-r = \cos\theta$ (see for example [16, p. 270]) in (3.40) and Substituting the result of (3.43) into (3.40):

$$\begin{aligned} \frac{\partial R_{yy}(\tau)}{\partial R_{xx}(\tau)} &= \frac{g^2}{4\pi\sigma_x^2\sqrt{1-r^2}} \theta \csc\theta + d = \\ &= \frac{g^2}{4\pi\sigma_x^2(1-r^2)} \cos^{-1}(-r) + d \end{aligned} \quad (3.44)$$

where \cos^{-1} is the inverse cosine function and $d = bg^2/[2\pi\sigma_x^2(1-r^2)^{1/2}]$.

Now, $\cos^{-1}(-r)$, $(1-r^2)^{-1}$ and $(1-r^2)^{-1/2}$ can be expanded using *Taylor series*:

$$\cos^{-1}(-r) = \frac{\pi}{2} + r + \frac{r^3}{6} + \frac{3r^5}{40} + \frac{15r^7}{336} + \dots \quad (3.45)$$

$$(1-r^2)^{-1} = 1 + r^2 + r^4 + r^6 + r^8 + \dots \quad (3.46)$$

$$(1-r^2)^{-1/2} = 1 + \frac{r^2}{2} + \frac{3r^4}{8} + \dots \quad (3.47)$$

By inserting (3.45), (3.46) and (3.47) into (3.44), multiplying out and collecting the terms up to the fourth power:

$$\begin{aligned} \frac{\partial R_{yy}(\tau)}{\partial R_{xx}(\tau)} &\approx \frac{g^2}{\sigma_x^2} \left(\frac{b}{2\pi} + \frac{1}{8} \right) + \frac{g^2 r}{4\pi\sigma_x^2} + \frac{g^2 r^2}{\sigma_x^2} \left(\frac{b}{4\pi} + \frac{1}{8} \right) + \frac{7g^2 r^3}{24\pi\sigma_x^2} + \dots \\ &\dots + \frac{g^2 r^4}{\sigma_x^2} \left(\frac{3b}{16\pi} + \frac{1}{8} \right) \end{aligned} \quad (3.48)$$

Now, substituting (3.42) into (3.48):

$$\begin{aligned} \frac{\partial R_{yy}(\tau)}{\partial R_{xx}(\tau)} &\approx \frac{g^2}{\sigma_x^2} \left(\frac{b}{2\pi} + \frac{1}{8} \right) + \frac{g^2 R_{xx}(\tau)}{4\pi\sigma_x^4} + \frac{g^2 R_{xx}(\tau)^2}{\sigma_x^6} \left(\frac{b}{4\pi} + \frac{1}{8} \right) + \dots \\ &\dots + \frac{7g^2 R_{xx}(\tau)^3}{24\pi\sigma_x^8} + \frac{g^2 R_{xx}(\tau)^4}{\sigma_x^{10}} \left(\frac{3b}{16\pi} + \frac{1}{8} \right) \end{aligned} \quad (3.49)$$

Proceeding to solve for $R_{yy}(\tau)$:

$$\begin{aligned} R_{yy}(\tau) &\approx \int \left[\frac{g^2}{\sigma_x^2} \left(\frac{b}{2\pi} + \frac{1}{8} \right) + \frac{g^2 R_{xx}(\tau)}{4\pi\sigma_x^4} + \frac{g^2 R_{xx}(\tau)^2}{\sigma_x^6} \left(\frac{b}{4\pi} + \frac{1}{8} \right) + \frac{7g^2 R_{xx}(\tau)^3}{24\pi\sigma_x^8} \right. \\ &\quad \left. + \frac{g^2 R_{xx}(\tau)^4}{\sigma_x^{10}} \left(\frac{3b}{16\pi} + \frac{1}{8} \right) \right] dR_{xx} \end{aligned} \quad (3.50)$$

$$\begin{aligned} R_{yy}(\tau) &= \frac{g^2}{\sigma_x^2} \left(\frac{b}{2\pi} + \frac{1}{8} \right) R_{xx}(\tau) + \frac{g^2}{8\pi\sigma_x^4} R_{xx}(\tau)^2 + \frac{g^2}{3\sigma_x^6} \left(\frac{b}{4\pi} + \frac{1}{8} \right) R_{xx}(\tau)^3 + \dots \\ &\dots + \frac{7g^2}{96\pi\sigma_x^8} R_{xx}(\tau)^4 + \frac{g^2}{5\sigma_x^{10}} \left(\frac{3b}{16\pi} + \frac{1}{8} \right) R_{xx}(\tau)^5 + C \end{aligned} \quad (3.51)$$

What remains now is to determine the integration constant, C . This is carried out by solving the boundary conditions for $R_{xx}(\tau)=0$. Using (3.36), the output autocorrelation function is given by:

$$R_{yy}(\tau) = \iint_{-\infty}^{\infty} (gx_1 + K)(gx_2 + K)p_X(x_1, x_2, r)dx_1dx_2 \quad (3.52)$$

Now, setting $R_{xx}(\tau)=0$ which implies that $r=0$ and re-arranging:

$$R_{yy}(\tau)|_{R_{xx}(\tau)=0} = \frac{2}{\pi\sigma_x^2} \left(\int_0^{\infty} gx_1 e^{-\frac{x_1^2}{2\sigma_x^2}} dx_1 + \int_0^{\infty} Ke^{-\frac{x_1^2}{2\sigma_x^2}} dx_2 \right)^2 \quad (3.53)$$

$$R_{yy}(\tau)|_{R_{xx}(\tau)=0} = \frac{4g\sigma_x}{\sqrt{2\pi}} \left(\frac{g\sigma_x}{\sqrt{2\pi}} + K \right) + K^2 \quad (3.54)$$

By substituting (3.54) for C in (3.51), the final result is obtained:

$$\begin{aligned} R_{yy}(\tau) &= \left[\frac{4g\sigma_x}{\sqrt{2\pi}} \left(\frac{g\sigma_x}{\sqrt{2\pi}} + K \right) + K^2 \right] + \frac{g^2}{\sigma_x^2} \left(\frac{b}{2\pi} + \frac{1}{8} \right) R_{xx}(\tau) + .. \\ &.. + \frac{g^2}{8\pi\sigma_x^4} R_{xx}(\tau)^2 + \frac{g^2}{3\sigma_x^6} \left(\frac{b}{4\pi} + \frac{1}{8} \right) R_{xx}(\tau)^3 + \frac{7g^2}{96\pi\sigma_x^8} R_{xx}(\tau)^4 + .. \\ &.. + \frac{g^2}{5\sigma_x^{10}} \left(\frac{3b}{16\pi} + \frac{1}{8} \right) R_{xx}(\tau)^5 \end{aligned} \quad (3.55)$$

By taking the FT of (3.55) the frequency domain representation is obtained:

$$\begin{aligned} S_y(f) &= \left[\frac{4g\sigma_x}{\sqrt{2\pi}} \left(\frac{g\sigma_x}{\sqrt{2\pi}} + K \right) + K^2 \right] \delta(f) + \frac{g^2}{\sigma_x^2} \left(\frac{b}{2\pi} + \frac{1}{8} \right) S_x(f) + .. \\ &.. + \frac{g^2}{8\pi\sigma_x^4} S_x(f)^2 + \frac{g^2}{3\sigma_x^6} \left(\frac{b}{4\pi} + \frac{1}{8} \right) S_x(f)^3 + \frac{7g^2}{96\pi\sigma_x^8} S_x(f)^4 + .. \\ &.. + \frac{g^2}{5\sigma_x^{10}} \left(\frac{3b}{16\pi} + \frac{1}{8} \right) S_x(f)^5 \end{aligned} \quad (3.56)$$

The first term in (3.56) is the dc term, the second term is the signal term while the next terms are the second, third, fourth and fifth order distortions. Note also that the dc term is equal to the square of the mean value result from (3.39).

3.6 Extension to arbitrary AM/AM characteristic with phase distortion

Phase distortion can be taken into account by including in the model the amplitude-modulation-to-phase-modulation (AM/PM) response [68]. A model that includes phase is useful in cases where the laser diode is modulated at frequencies close to its resonance frequency or in general when the frequency response of the laser diode within the bandwidth of the input signal is not smooth and imposes filtering effects on the signal. A model that includes phase distortion is generally termed a quasi-memory model [69]. While spectrum analysers can be used to obtain the AM/AM response, they cannot provide any information regarding phase. Therefore, the AM/PM measurement can be carried out using a vector network analyzer. Once the AM/AM and AM/PM responses of the link have been obtained following a measurement, they can be fitted to a Bessel series expansion [70]. Then the output autocorrelation integral in (3.25) can be solved analytically using the method described in [18].

3.7 Conclusions

The PAPR analysis using the statistical description of the amplitude of the OFDM signal shows a close match with simulation results. The empirical result presented includes the effects of oversampling and thus takes into account any band-limiting effects that may result from filtering processes in the transmitter such as DAC interpolation and windowing.

For the analysis of the nonlinear transmission through the optical link, the results indicate that the analytical approach following from the direct method for the case of a soft limiter

nonlinearity can offer a crude estimate of certain metrics such as SNR and EVM. In that sense, it represents a simple method for predicting the performance of a RoF link with a light source biased at low bias and represents the “worst case” scenario. Furthermore, a modified Rapp model can better model the AM/AM characteristic of a laser at low bias compared to a polynomial model. However, the AM/AM approach is a complex envelope method and does not relate directly to the parameters of the laser transfer function such as the bias point and threshold current. Additionally, the AM/AM response of the link is not really a soft limiter response.

The output auto-correlation method on the other hand is based directly on the link static response and allows for the nonlinearity to be modelled in a straightforward manner which includes the aforementioned link parameters.

For PoF applications, where power consumption is of prime importance, depending on the system requirements, a certain amount of distortion may be tolerated. The simple analytical approaches shown here can be used to define the operational parameters for which the system requirements are fulfilled. That is, a balance point can be defined between low power consumption and tolerable distortion.

4 Statistical Distribution of EVM

Measurements for Direct-Modulation Radio over Fibre Links Transporting OFDM Signals

4.1 Introduction

Previous work has shown that IM-DD RoF links with external or direct modulation can offer good performance when transmitting wireless standards employing OFDM modulation in the microwave frequency range. Examples of this approach include the transmission of pre-existing standards including, amongst others, the WiMAX and WiFi standards [21], [71], as well as future, 4th generation standards [6]. One of the limitations in the dynamic range of IM-DD architectures comes from distortion arising from nonlinear components in the transport architecture. In the case of direct IM-DD links, the major source of nonlinearity is the laser diode [12].

The transmission of OFDM signals through nonlinearities has been investigated extensively in the literature [17, 64, 72-75] by using clipping and other simple nonlinear models. Specifically for RoF implementations, [76], [77] investigated the effects of the nonlinearity of a Mach-Zehnder external modulator, [78] investigated the nonlinearity of a directly modulated laser diode using a simple polynomial model and making use of the output autocorrelation function, while in [66] a comparison between a clipping function and a direct IM-DD link with a laser diode at low bias was carried out.

However, only very little work, [74], [53], has been carried out to explore the effects of different numbers of subcarriers, and whether this results in variation of required input power back-off due to changes in the PAPR. In [53] a difference in back-off from the P1dB of 0.5 dB at 4% EVM between 64 and 2048 OFDM subcarriers was reported for a direct IM-DD link. However this comparison was not optimized for exploring the effects of different numbers of subcarriers. The two signals were generated and measured using two different methods that included different equalization techniques and the comparison was carried out over a relatively small number of transmitted OFDM frames.

In this chapter, OFDM signals with different numbers of subcarriers are transmitted through a directly modulated IM-DD RoF link. Then, a statistical analysis of the measured EVM results is carried out from two perspectives: the first examines the distribution of the mean EVM in each transmitted OFDM frame (note that the term "frame" is used to denote a single OFDM symbol with a CP appended to it); the second examines the distributions of the EVM of every subcarrier in all the transmitted frames. The results of this statistical analysis are compared to what would be expected in the case where the EVM results were obtained from an i.i.d white noise process. The difference between the measured result and the prediction for an i.i.d white noise process is used to better understand the effects of distortion.

4.1.1 Some initial remarks

The EVM measurement can be seen as an ensemble of the different realizations of a random process as shown in Fig. 4.1. Each time series $EVM_1(t), EVM_2(t), \dots, EVM_n(t)$ from the ensemble represents a single EVM measurement sample record. The ensemble average is given by the mean (m_n) of all the realizations at a point in time t_n . Assuming that temperature differences and other external factors are not in effect, we can expect that the ensemble average will not vary with time. That is, we can assume the process is stationary. Another assumption is that ensemble and sample averages can be equated (i.e. $m(EVM_n) = m_n$).

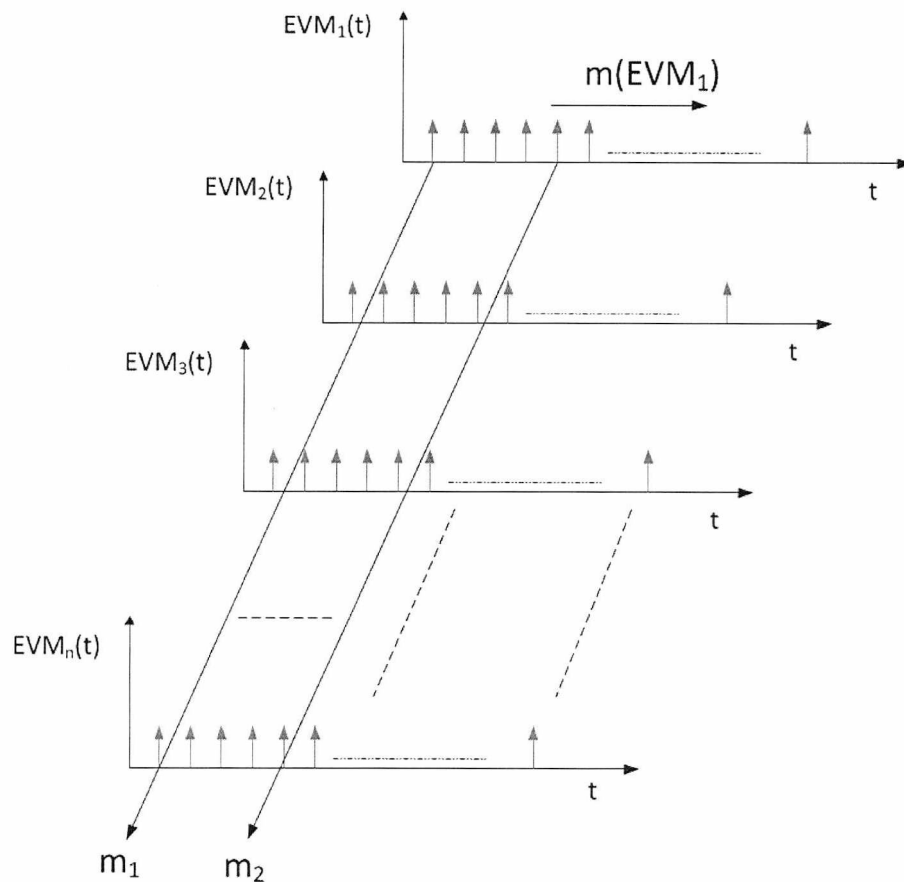


Fig. 4.1: Ensemble of the EVM measurements.

Fig. 4.2 shows the EVM results at varying input powers from simulations with 128 and 512 OFDM subcarriers when a clipping function (soft-limiter) nonlinearity similar to the one discussed in Section 3.3 is used. As no channel effects are simulated in this case, no equalization was used for these results. The results demonstrate the differences in the EVM between signals with different numbers of subcarriers when the median of the EVM is used instead of the mean. While the mean traces almost overlap, the median traces do not. There is a clear difference in the rate of increase of the EVM with the 512 subcarrier result increasing at a faster rate. Also shown is the absolute difference between mean and median for the two signals. At lower input powers this difference is the same for both signals. At the point where the EVM starts to rise, as distortion begins to dominate over the noise in the link, the difference between mean and median becomes greater for 128 subcarriers. As the input power is further increased the difference starts to reduce again and the median traces meet and begin to overlap once again.

In the following sections, similar results will be obtained based on an experimental measurement of an optical link. The aim is to see whether a similar trend can be observed and to establish the possible causes behind the observed behaviour. Furthermore, the central limit theorem assumptions will be used wherever applicable, for summands of at least 112 terms, without any further justification. Additionally, two sets of results will be shown obtained by using two different equalization methods (Equalizer 1 and Equalizer 2). This is done in order to establish whether any observed trends in the results will be the same for the two different equalization methods. It can be said that any observed behaviour should, in theory, be independent of the equalization process as ideally an equalizer will equalize the linear distortion of the channel and will not have an effect on the nonlinear response. It has to be noted that in the results that will follow, whenever the equalization method is not specified, it can be assumed that Equalizer 1 has been used. Equalizer 1 is based on a recursive least square filter algorithm [79, p. 916] that is available in Matlab-Simulink, that attempts to minimize the mean square error between the received and ideal constellation points. Equalizer 2 uses a minimization algorithm that was developed in-house.

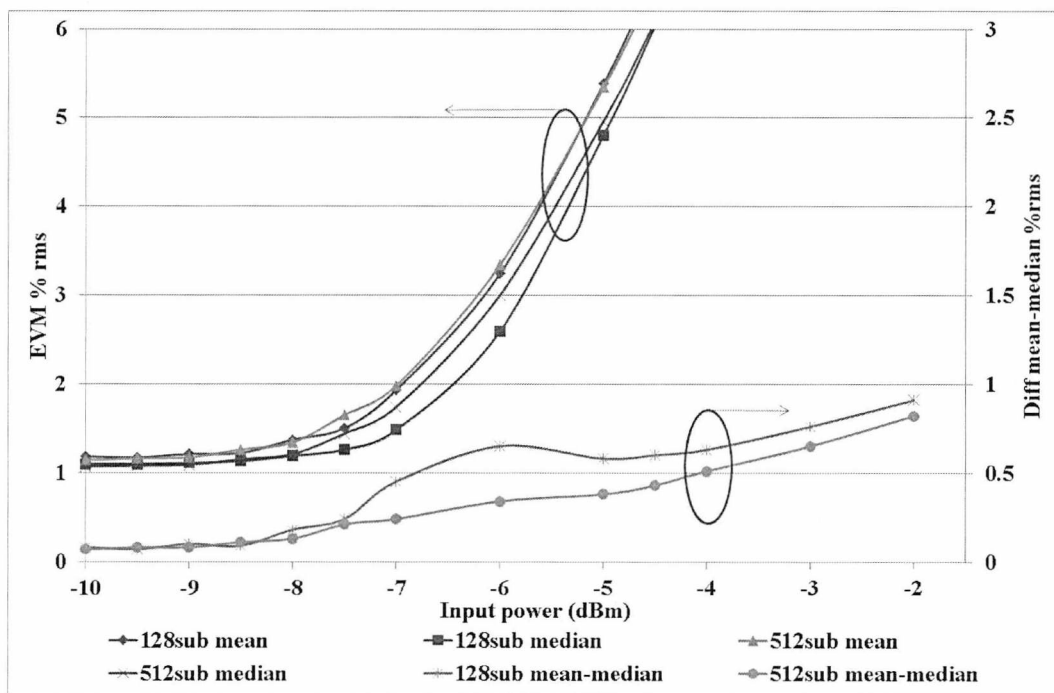


Fig. 4.2: Simulated EVM results for 128 and 512 subcarriers using a clipping (soft-limiter) nonlinearity.

4.2 Statistical Methodology

An IM-DD RoF link is shown in Fig. 4.3. The link corresponds to the physical channel between the OFDM transmitter and receiver sections shown in Fig. 2.1. The up-converted signal directly modulates the laser diode and the resulting modulated light is transmitted through a 10 dB optical attenuator and short length of fibre patch-cord before being directly received by a PIN PD. The optical attenuator is used in order to reduce the optical power reaching the PD. Two gain controlling components are shown. One at the input of the link is used to control the input RF power into the laser diode, while an RF amplifier following the optical link is used to counteract the RF loss the signal has experienced due to the optical link. The link will add a noise contribution $n'(t)$ which includes laser diode RIN and PD shot and thermal noises. As this is an analogue link it will also introduce a distortion component, $d(t)$.

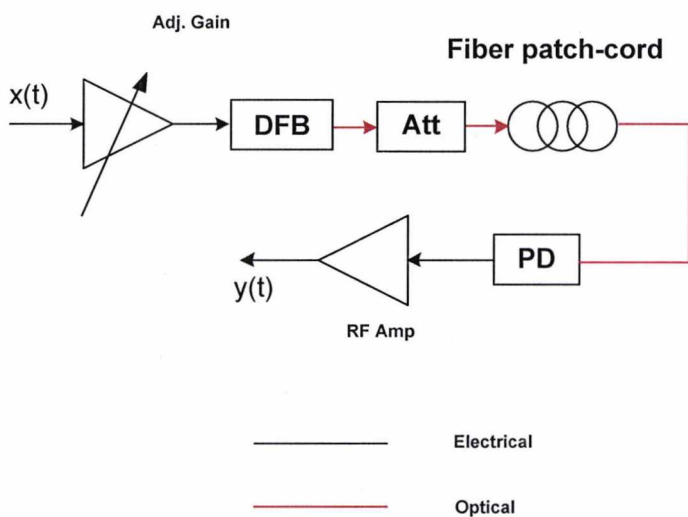


Fig. 4.3: The RoF link. DFB: Distributed Feedback laser; PD: Photodiode; Att optical attenuator.

Now, it is assumed that the processes acting on the OFDM signals are i.i.d white noise processes. This is the case for RIN, shot and thermal noise introduced by the RoF link (note that although, RIN and shot noise do vary with frequency, in most cases, for the electrical bandwidths considered these can be assumed as white noise processes). However, it is also assumed that the distortion introduced by the link is an i.i.d white noise process. This assumption simplifies the analysis and can provide a “base-line” prediction for comparisons with the measured results in the Sections that will follow.

After an appropriate equalization technique has been used to equalize the link frequency response, the signal at the output of the receiver FFT will be given by (see Section 3.3.1):

$$Y[k] = S[k] + (D[k] + N'[k]) = S[k] + N[k] \quad (4.1)$$

where

$$S[k] = \frac{1}{\sqrt{N}} \sum_{n=0}^{N-1} s[n] e^{-\frac{j2\pi kn}{N}} \quad (4.2)$$

$$N[k] = \frac{1}{\sqrt{N}} \sum_{n=0}^{N-1} n[n] e^{-\frac{j2\pi kn}{N}} \quad (4.3)$$

The first part on the right hand side of (4.1) represents the useful signal sample $S[k]$, while the terms in brackets represent the samples of the distortion, $D[k]$, and noise contributions, $N'[k]$, at the location of subcarrier k .

There are two statistical distributions of interest: one is the distribution of the mean EVM (each mean EVM value is obtained by averaging across the EVM values of all the subcarriers within the frame) of every transmitted OFDM frame. This distribution is termed the *EVM per frame* distribution. The second is the distribution of all of the EVM values, that is, of every OFDM subcarrier in all the transmitted OFDM frames. This is termed the *raw EVM* distribution. Fig. 4.4 shows how the results from an EVM measurement are interpreted for the analysis that will follow. A long time series of m EVM measurements is obtained. Each of these measurements is a raw EVM value (EVM_1 - EVM_m). As the OFDM signal demodulation is inherently done per frame, there are sets of N contiguous values from this time series which are from the same frame, where N is the number of data subcarriers in the measured OFDM frame. In this way, the measurements are partitioned into sample sizes equal to the number of data subcarriers in the received OFDM frame. Therefore, in addition to the raw EVM values, a set of m/N values are obtained which represent the mean EVMs for each OFDM frame (these

are the EVM per frame values). The raw EVM values within each frame correspond to different frequencies within the signal band and are “received” simultaneously (as they belong to the same frame). But, due to the P/S conversion in the receiver section of Fig. 2.1, these measurements are separated in time.

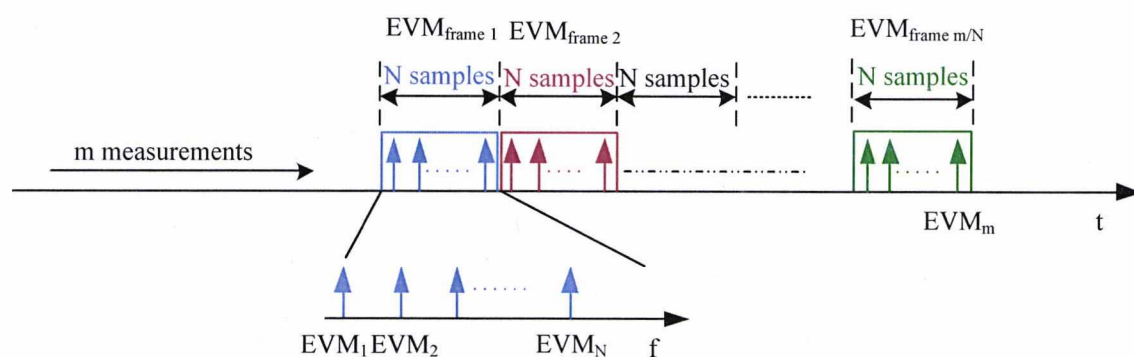


Fig. 4.4: Diagram showing how the EVM measurement results are interpreted for the employed statistical methodology.

The EVM for subcarrier r is given by:

$$EVM_r = \sqrt{\frac{P_{N[r]}}{\bar{P}}} = \frac{\sqrt{[\text{Re}\{N[r]\}]^2 + [\text{Im}\{N[r]\}]^2}}{v_{rms}} \xrightarrow{\text{tends}} \text{Rayleigh}(\sigma') \quad (4.4)$$

for $r = 1, 2, \dots, m$

where $P_{N[r]}$ is the power of the total noise sample (i.e. including distortion and other noise contributions) in subcarrier r , \bar{P} is the mean power of the constellation and σ' is the standard deviation of the In-phase and Quadrature components of the total noise contribution. Note that now, the frequency index k , is replaced with the index r , to reflect the change to a time domain representation for the measurement results in accordance with the statistical methodology of Fig. 4.4. The Real and Imaginary components in the numerator of (4.4) will tend to Gaussian distributions due to the averaging in the receiver FFT and the CLT, as N is large. Therefore, the numerator being the magnitude of the two components will tend

to a Rayleigh distribution. Since this is at the output of the FFT, the v_{rms} term is simply the RMS magnitude of the QAM constellation.

The measured EVM per frame is the arithmetic mean over a whole frame:

$$EVM_f = \frac{1}{N} \sum_{r=(f-1)N+1}^{fN} \left(\sqrt{\frac{P_{N[r]}}{\bar{P}}} \right) \xrightarrow{\text{tends}} \mathcal{N}(\mu_f, \sigma_f) \quad (4.5)$$

$$\text{for } f = 1, 2, \dots, \frac{m}{N}$$

where N is the number of data subcarriers in the frame.

Note that the averaging performed in (4.5) is slightly different from the one discussed in Section 2.2 and shown in (2.10). In this case the averaging is carried out outside the fraction. So, instead of averaging the noise power across all subcarriers in the frame, the EVM itself is averaged across all the subcarriers in the frame. This is done so that (4.5) is directly related to (4.4) as it will be demonstrated shortly. It is worth noting that the resulting EVM from both calculations is very close in value and both methods lead to identical distributions. Assuming that the raw EVM is an i.i.d process, with mean μ_r and variance σ_r^2 , the EVM per frame will have a mean μ_f and variance σ_f^2 given by:

$$\mu_f = \mu_r \quad (4.6)$$

$$\sigma_f^2 = \frac{\sigma_r^2}{N} \quad (4.7)$$

Equations (4.6) and (4.7) are a direct result of the Weak Law of Large Numbers [56]. They show that the EVM per frame will have a variance inversely dependent on the number of subcarriers, and a mean equal to the mean of the raw EVM distribution. In terms of estimation theory, it can be said that μ_f is an un-biased estimator of the mean of the raw EVM, while σ_f^2 is a biased estimator of the variance of the raw EVM. Additionally, as N is large, due to the CLT, the distribution of the EVM per frame will converge to a Gaussian distribution.

In the literature, it is often assumed that the effects of distortion (above some input power level) are equivalent to those of an i.i.d white noise process [18, 80] . But, when distortion takes effect, this assumption may not hold. Specifically, within a frame the distortion may not affect each subcarrier equally or even if it does, from one frame to another the PAPR will be different.

The aim of the following Sections is to see whether (and under which conditions) the raw EVM distribution will converge to a Rayleigh distribution in accordance with (4.4) and whether the EVM per frame will conform to (4.6) and (4.7), and also converge to a Gaussian distribution.

4.3 Measurement procedure

The measurement setup and procedure are illustrated in Fig. 4.5. The directly modulated RoF link comprises a Teradian DFB laser diode, a 10 dB optical attenuator and an Appointech PIN-PD. The baseband OFDM signal is generated in Matlab-Simulink and is then downloaded to an Agilent VSG which performs RF up-conversion. The signal is then transmitted over the RoF link and is received by an Agilent VSA which down-converts the signal. The down converted signal is saved as a Matlab data file for offline signal processing. The offline processing includes timing synchronization, blind equalization and blind frequency offset correction. The generated OFDM signals have a bandwidth of 20 MHz and the RF frequency is 1.4 GHz. The ratio of data carriers to zeros (null subcarriers) is based on the WiMAX specifications [24], except for the case of 128 subcarriers, where 16 zeros are used. A short CP is used at a ratio of 1/8 of the symbol duration. Any distortion observed will be mainly due to the laser diode, as both the VSG and RF amplifier were operated far below their individual compression points. The input P1dB of the unamplified optical link was measured as 19 dBm (Fig. 4.6).

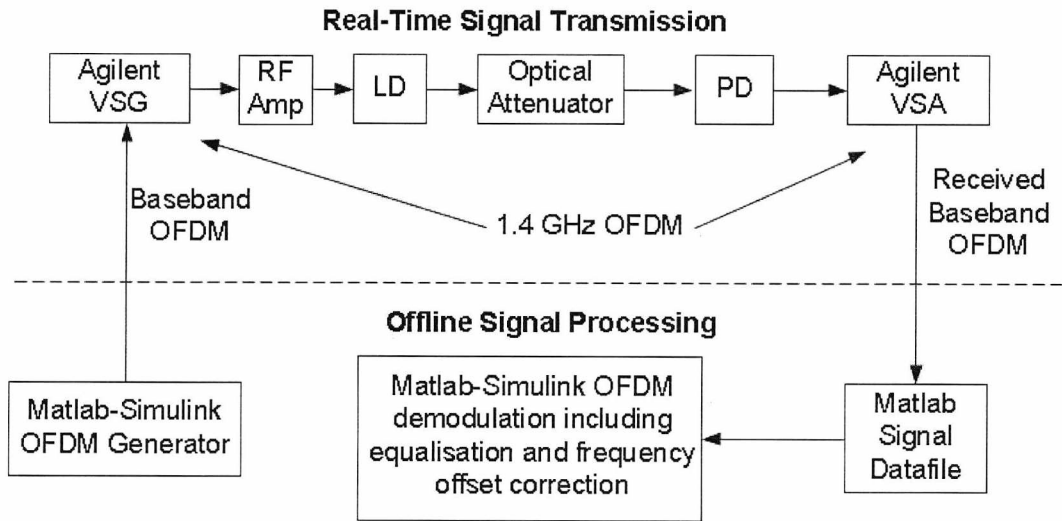


Fig. 4.5: Detailed Flow-chart of the measurement procedure.

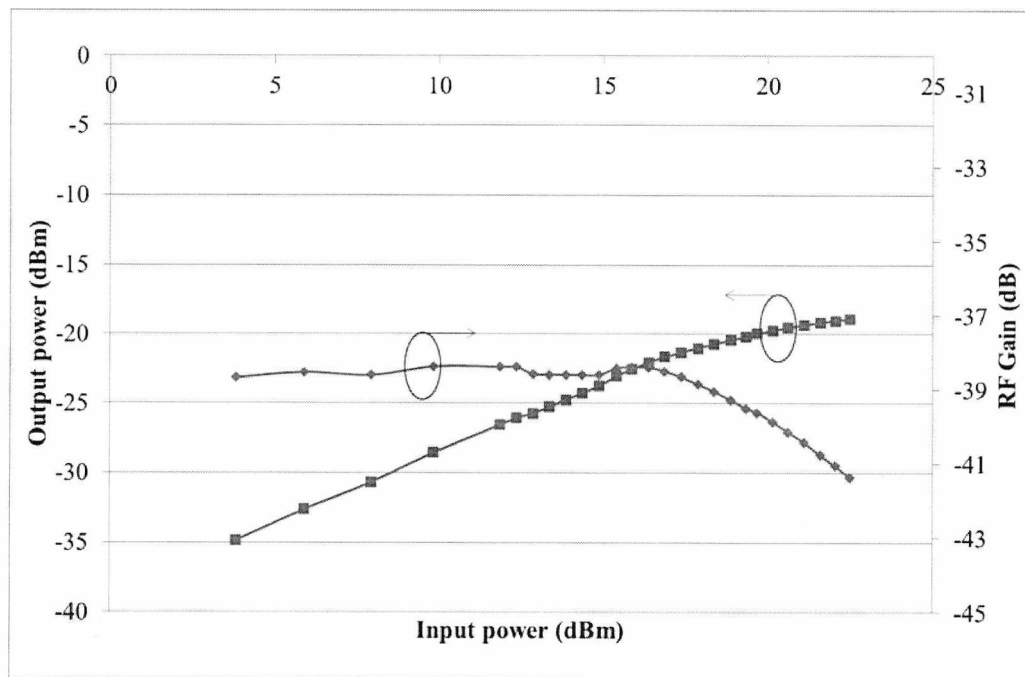


Fig. 4.6: P1dB measurement result for the optical link.

4.4 Initial results

The measured results in this Section are obtained as follows: at every RF input power, 450 OFDM frames are transmitted, and for each frame the mean EVM is calculated by averaging across the EVM values of all the subcarriers within the frame. The average EVM result for each RF input power is the average of all the mean EVMs transmitted at that particular RF input power. Therefore, the average EVM at each input power is given by:

$$EVM(\% rms) = 100 \frac{1}{F} \sum_{f=1}^F EVM_f \quad (4.8)$$

where $f=1,2,\dots,F$ is the number of frames. For these results, $F=450$.

Fig. 4.7 shows the un-equalized average EVM versus input power result for different numbers of subcarriers (128, 512 and 4096 subcarriers) with QPSK modulation over 450 OFDM frames.

Fig. 4.8 shows the equalized result for the two different equalization methods.

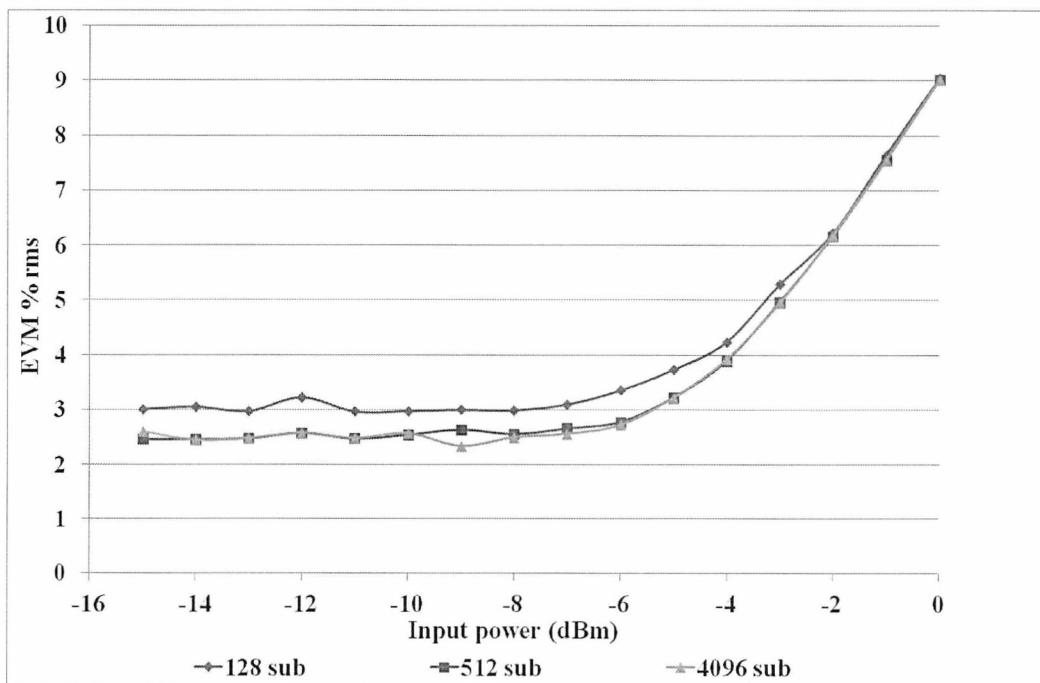
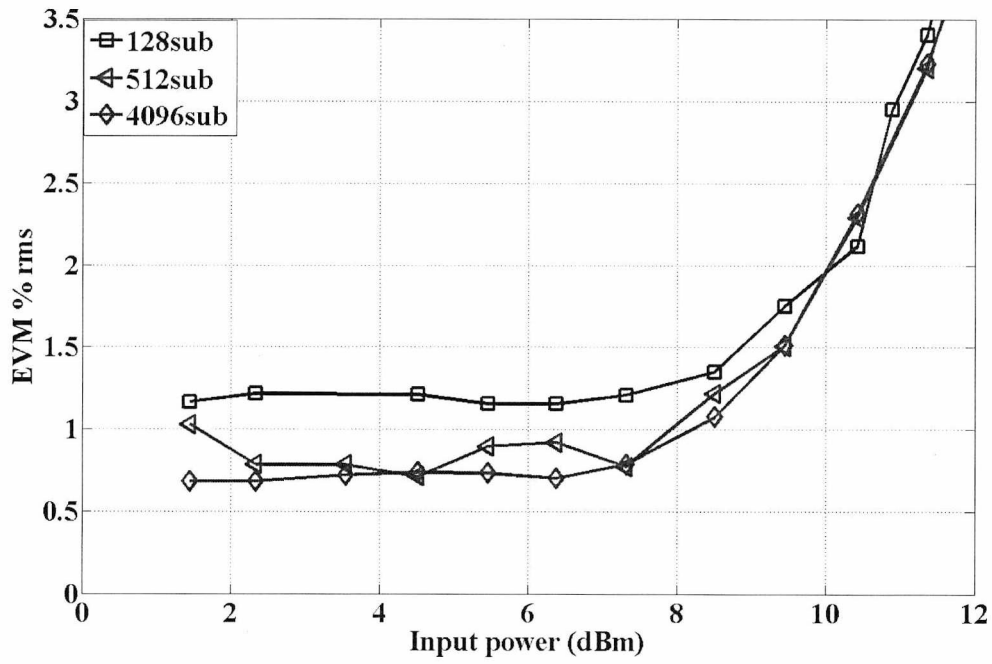


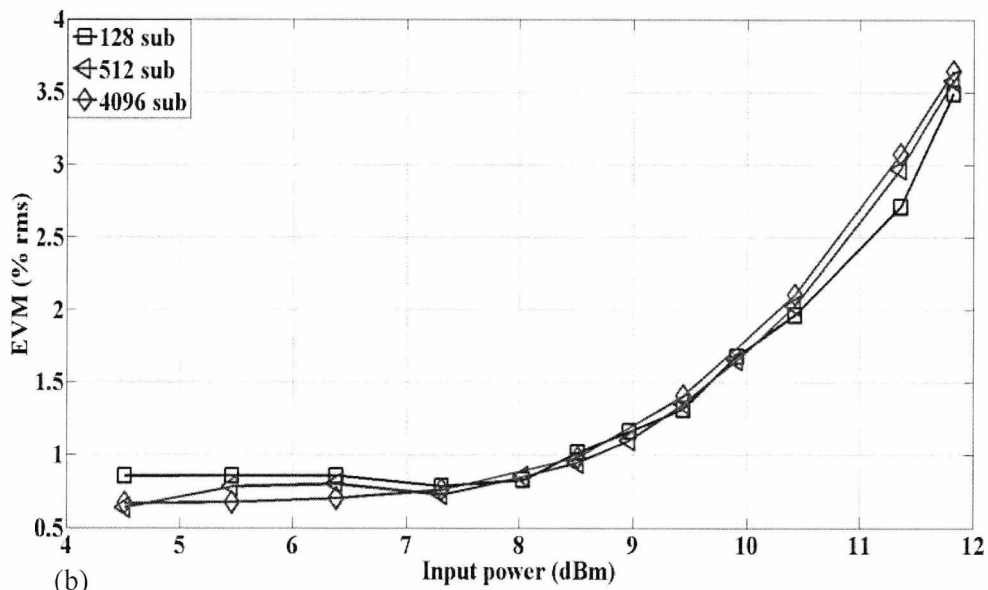
Fig. 4.7: Un-equalized average EVM versus input power for different number of subcarriers with QPSK modulation over 450 OFDM frames.

Wireless standards usually define EVM transmitter requirements. An appropriate input power can be chosen so that the EVM will meet a specified requirement. Generally, then, the input power can be reduced in order to maintain an EVM below the specified limit, and the input power can therefore be expressed in terms of a power back-off from the P1dB of the optical link. It is seen in Fig. 4.8 that the back-off requirements are almost the same for the different numbers of subcarriers. In terms of the EVM turning point (the point where the EVM starts to rise quickly due to distortion), a back-off of 12 dB from the P1dB is a good choice and is close to the expected value of the median of the statistical PAPR result (Fig. 3.6). However, the expected difference in the required back-off for the cases of the signals with different numbers of subcarriers due to the statistical PAPR (Fig. 3.6) is not observed in this result. In general, following the transmission through the optical link, signals will be transmitted through a wireless channel. Therefore, the optical link should have a minimum effect (in terms of performance degradation) on the quality of the transmitted signals. Thus, here, we are mostly interested in the relatively low EVM distortion limited range. Higher input powers will be investigated in terms of the statistics of the EVM results in the following sections.

Fig. 4.9 is a plot of the EVM variance with input power. Although the average EVM is almost the same for different numbers of subcarriers, as seen in Fig. 4.8, the variance is not. As expressed in (4.7), the EVM variance is higher for lower numbers of subcarriers.

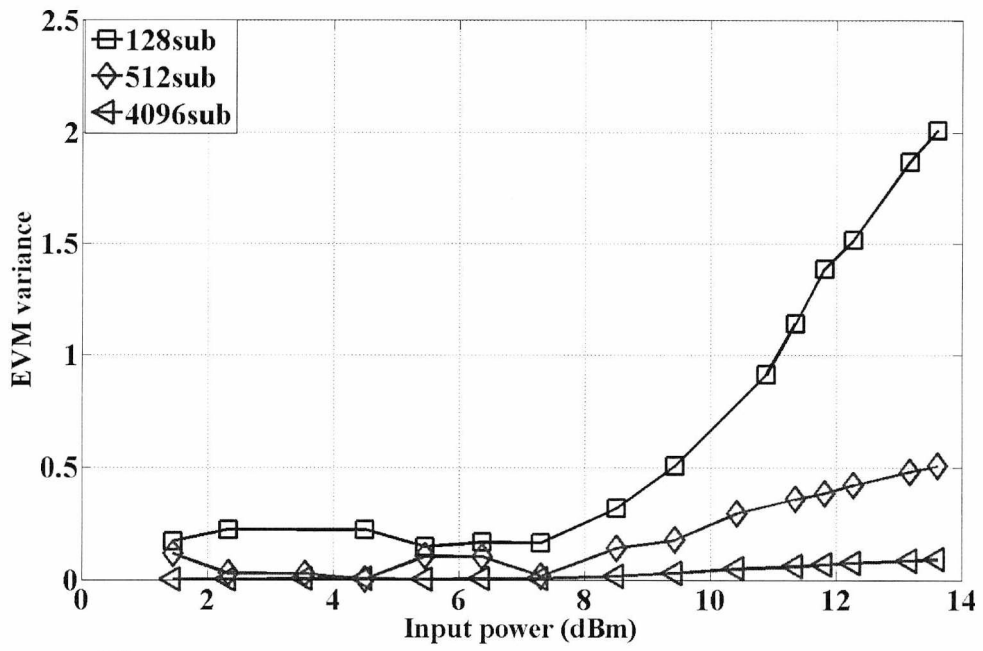


(a)

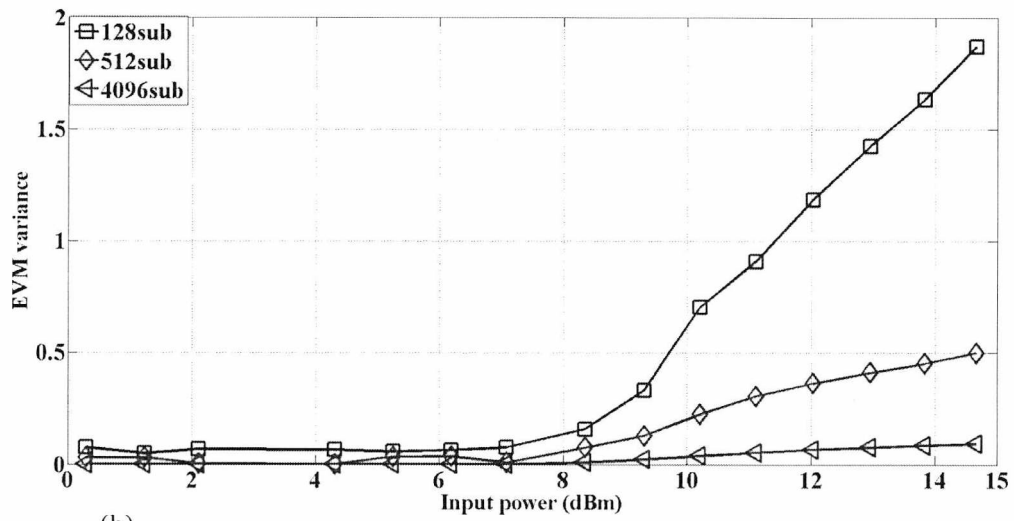


(b)

Fig. 4.8: Average EVM versus input power for different number of subcarriers with QPSK modulation over 450 OFDM frames with a) Equalizer 1 and b) Equalizer 2.



(a)



(b)

Fig. 4.9: Average EVM variance for different number of subcarriers for a) Equalizer 1 and b) Equalizer 2.

4.5 EVM per frame distributions

In Fig. 4.10, plots of the CCDFs of the EVM per frame for 128 and 512 subcarriers, with Gaussian fits, for operating points in the noise limited region of the EVM measurements (first region in Fig. 2.10) are presented. It can be seen that the distributions are approximately Gaussian. At each input power, the means are approximately equal while, in agreement with (4.7), the standard deviations for the 128 subcarriers results are approximately double that of the 512 subcarriers results, for both input powers (see the fitting parameters presented in Table 4.1). Note that due to the even nature of the Gaussian distribution, the means of the distributions can be equal while the standard deviations are not.

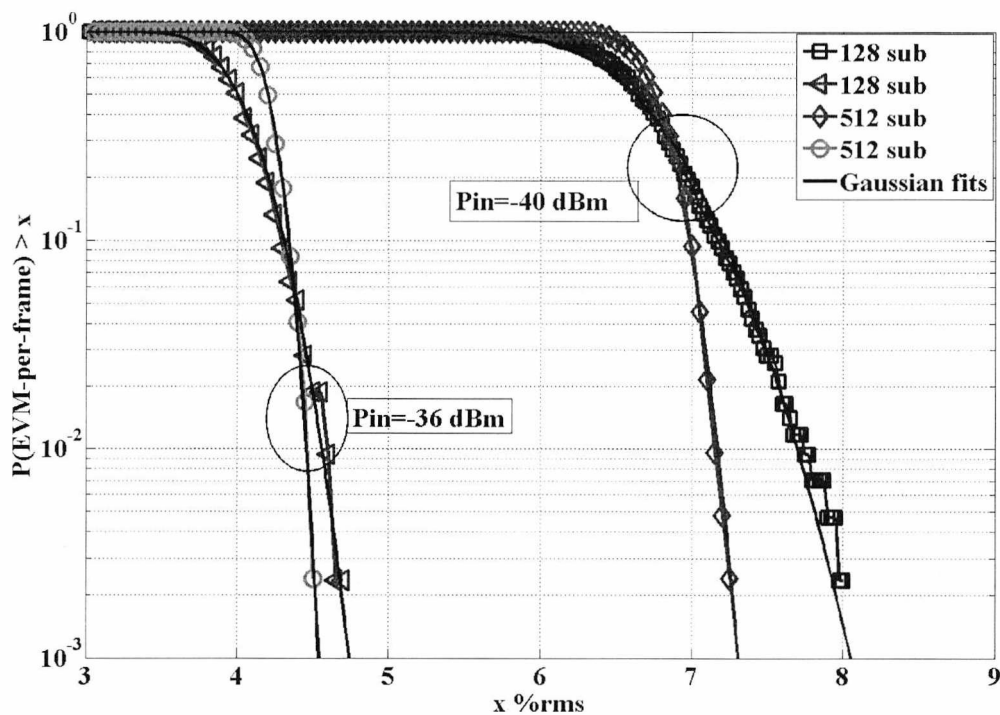


Fig. 4.10: EVM per frame CCDFs for 128 and 512 subcarriers at two input powers at the noise limited end of the EVM (i.e. negligible distortion). The distributions have equal means but the standard deviation of 128 subcarriers is approximately double that of 512 subcarriers.

Table 4.1: Summary of fitted normal distribution parameters (mean and standard deviation) for the noise limited end performance (Fig. 4.10).

Subcarrier number	-40 dBm		-36 dBm	
	σ	m	σ	m
128	0.4	6.65	0.2	4.2
512	0.19	6.72	0.11	4.1

Fig. 4.11 shows histogram plots of the EVM per frame for 128, 512 and 4096 subcarriers over 450 frames at input powers of 9.45 dBm, 11.8 dBm and 13.6 dBm respectively while Fig. 4.12 shows the same plots with Equalizer 2. These input powers are within 10 dB from the P1dB of the link and thus all correspond to operation where distortion from the link dominates the performance. In general, it can be seen that lower powers and lower numbers of subcarriers lead to more positively skewed distributions. Statistical skewness is a measure of the asymmetry in the shape of a distribution. The skewness (or skew), γ , is defined in terms of the 3rd central moment and for a random variable X , is given by [81, p. 47]:

$$\gamma = \frac{E[(x - m)^3]}{\sigma_x^3} \quad (4.9)$$

Positively skewed distributions have longer right tails and in such cases the mean of the distribution will be higher than the median. That is, the positive skew results in a “push” or right-wise move of the mean value of the distribution. In this case the measured distribution can be better approximated by a log-normal distribution [82], with parameters M and s , which matches the positive skew quite adequately. The fitted distributions (dashed traces) are shown superimposed on the histograms. Note that the fitting becomes worse as the input power is reduced (this is a result of non-ideal equalization). The fitting with the log-normal distributions is carried out using the CDFs of the measured distributions. From Fig. 4.11 it is seen that the left tail of the distribution is bounded, that is, the EVM cannot be lower than some value while the right tail is unbounded. This shows that the effect of distortion results in a change in the even nature of the distributions. The distortion will tend to increase the EVM while at the

same time the minimum EVM is determined by other sources of impairment (including noise, non-ideal equalization etc.).

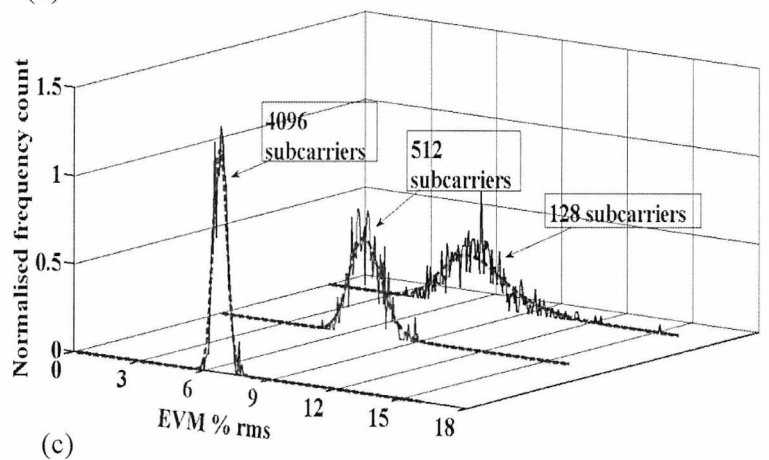
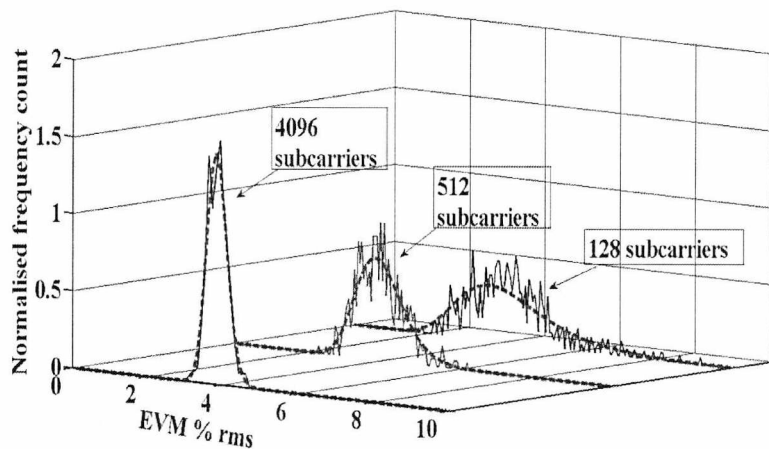
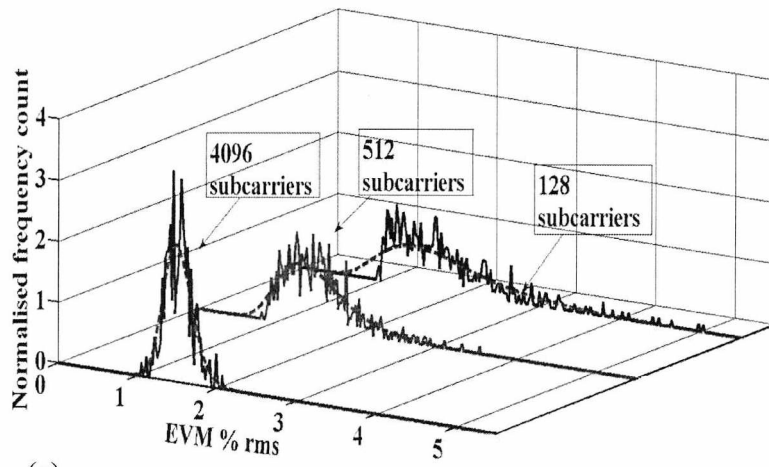


Fig. 4.11: Histogram plot of the average EVM per frame over 450 frames for 128, 512 and 4096 subcarriers at input powers of (a) 9.45 dBm, (b) 11.8 dbm and c) 13.6 dBm with fitted log-normal distributions using Equalizer1.

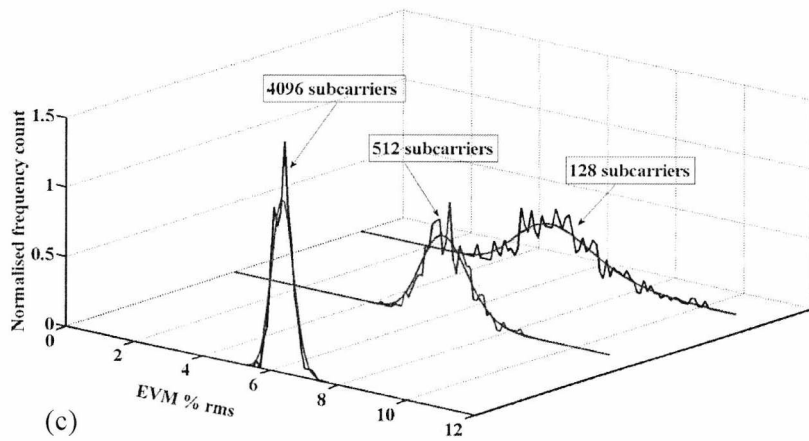
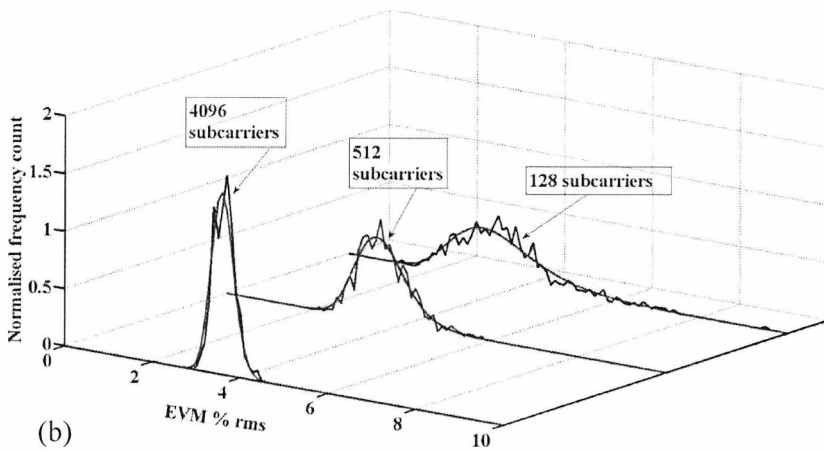
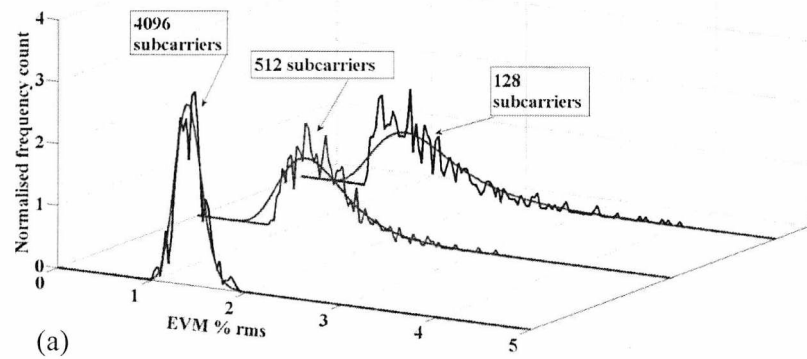


Fig. 4.12: Histogram plot of the average EVM per frame over 450 frames for 128, 512 and 4096 subcarriers at input powers of (a) 9.45 dBm, (b) 11.8 dbm and (c) 13.6 dBm with fitted log-normal distributions using Equalizer 2.

Tables 4.2 and 4.3, summarize the fitted parameters (mean, median and variance) for the log-normal distributions at the three input powers for the two equalizers.

Table 4.2: Summary of fitted log-normal distribution parameters for Equalizer 1: σ^2 is the variance, μ is the median and m is the mean.

	9.45 dBm			11.8 dBm			13.6 dBm		
Sub no.	σ^2	m	μ	σ^2	m	μ	σ^2	m	μ
128	0.34	1.33	1.22	1.05	3.46	3.32	1.43	5.9	5.8
512	0.15	1.3	1.25	0.32	3.54	3.49	0.47	6.21	6.17
4096	0.019	1.38	1.38	0.064	3.6	3.6	0.1	6.36	6.35

Table 4.3: Summary of fitted log-normal distribution parameters for Equalizer 2: σ^2 is the variance, μ is the median and m is the mean.

	9.45 dBm			11.8 dBm			13.6 dBm		
Sub no.	σ^2	m	μ	σ^2	m	μ	σ^2	m	μ
128	0.57	1.7	1.57	1.6	4.12	3.94	2.33	6.85	6.69
512	0.2	1.5	1.45	0.4	3.91	3.86	0.55	6.73	6.69
4096	0.03	1.5	1.49	0.07	3.83	3.82	0.1	6.7	6.69

With distortion, the differences in variance between the different signals do not agree with (4.7). While they do tend to agree with (4.7) as the input power is increased, this tendency is faster for the signals with lower numbers of subcarriers. This is shown in Fig. 4.13 that plots the variances of signals with different numbers of subcarriers normalized by the variance of the 128 subcarrier signal.

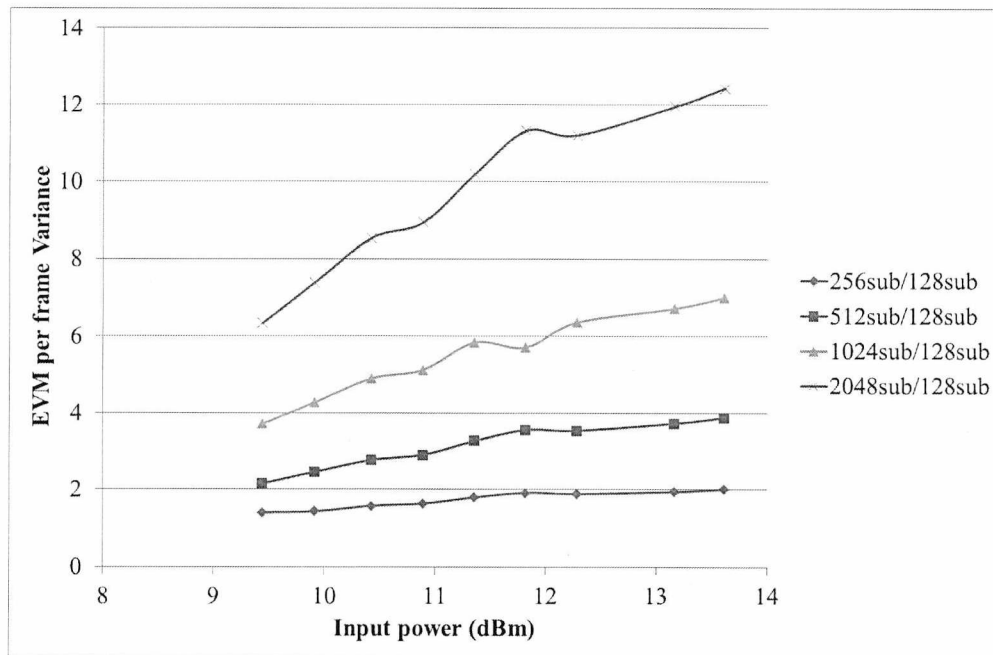
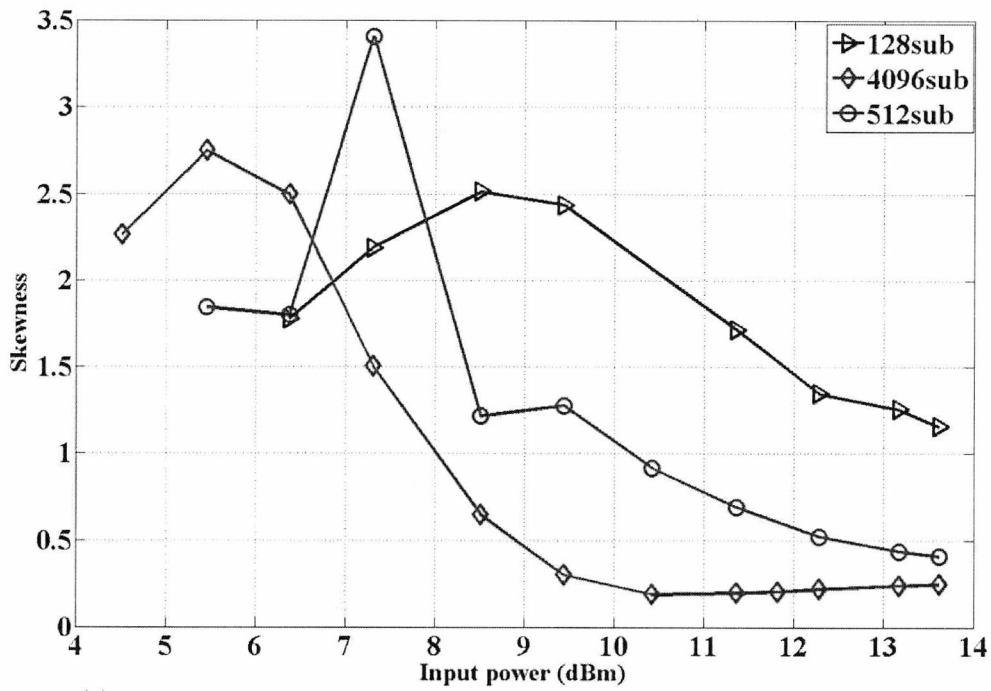


Fig. 4.13: Variance of measured EVM per frame for different numbers of subcarriers normalized by the variance of the 128 subcarrier signal.

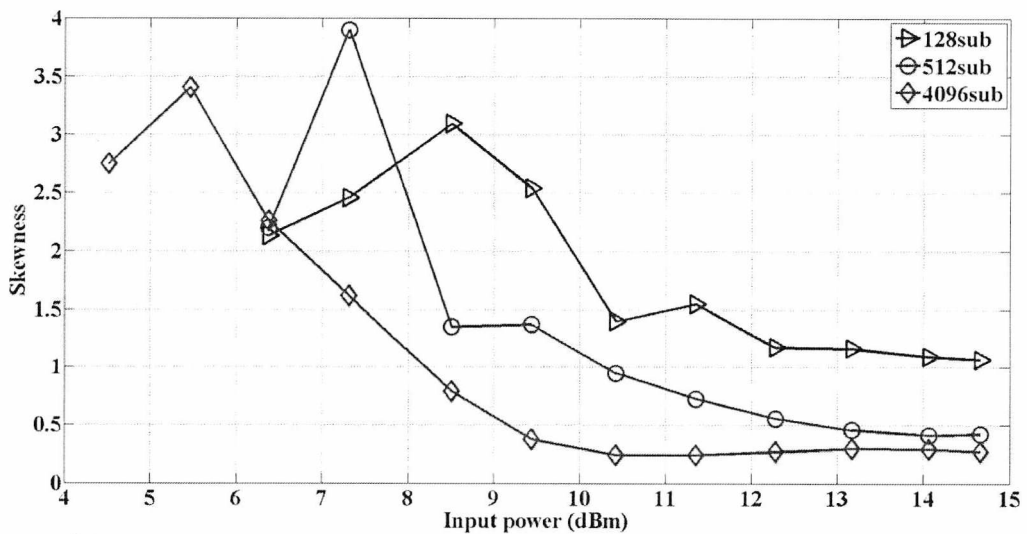
For higher input powers and/or higher number of subcarriers, the skew of the distributions reduces (Fig. 4.14). Therefore, it can be said that in the limit of these progressions (to a higher input power and/or higher number of subcarriers), the distribution will agree with (4.5). It is also noted that the peak in the skew occurs at lower input powers as the IFFT size is increased. This behaviour indicates some correlation with the statistical PAPR result of Fig. 3.6 as the higher IFFT sizes possess a larger median PAPR. Generally, it is these regions of large skew which are of most interest when analysing the limitations to EVM performance due to distortion.

The fact that the distributions are skewed and not Gaussian (the skew of a Gaussian distribution is zero) is due to the grouping of subcarriers into frames (which is simply how OFDM modulation and demodulation operate). An OFDM frame with high PAPR will lead to a higher mean EVM for that specific frame as a compression (or clipping) event will generally affect the whole frame. This will lead to some frames with a high mean EVM resulting in the extreme values observed in the distributions. This can be verified by randomizing the location (or order in time) of the raw EVM values prior to grouping them into sample sizes equal to the OFDM frame size and averaging. This randomization is done by changing the location of each raw EVM value at random. As a result every N contiguous EVM values are not from the same

frame any longer since the raw EVM values have been randomly mixed. Fig. 4.15 shows the result of randomizing the location of the raw EVM data in the case of 128 subcarriers at an input power of 9.45 dBm. The distribution now becomes Gaussian but has the same mean value as before.



(a)



(b)

Fig. 4.14: Skew of the distributions at different input powers for (a) Equalizer 1 and (b) Equalizer 2.

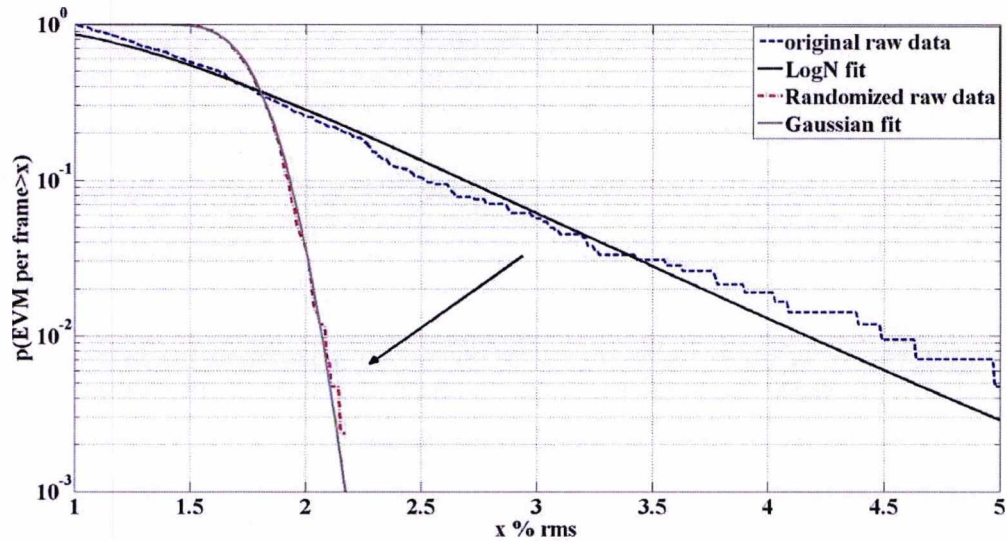


Fig. 4.15: Effect of randomizing the location (or order in time) of the raw EVM values prior to averaging across frames.

4.5.1 Additional measures of normality

Although the reduction in skew observed in Fig. 4.14 is a strong indication that the distributions tend to normality, additional tests of normality can improve this estimation. Fig. 4.16 shows the differences in the tails of the distributions with those of normal distributions (for the same parameters). As the input power is increased, the heaviness of the tail reduces and tends to that of a Gaussian.

Fig. 4.17 shows the results of the kurtosis [81, p. 50] of the distributions at varying input powers. Note that the normal distribution has zero kurtosis. The results follow a similar trend with the skew results of Fig. 4.14. As the input power is increased, the Kurtosis peaks due to the onset of distortion and then reduces for higher powers.

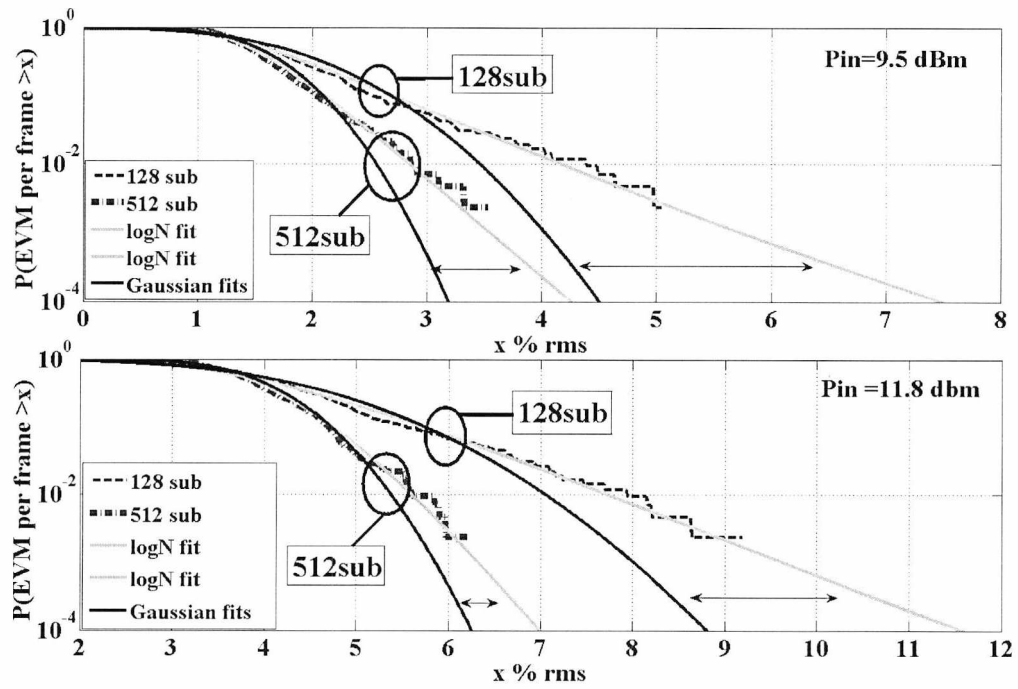


Fig. 4.16: Comparison of measured CCDFs with normal CCDFs.

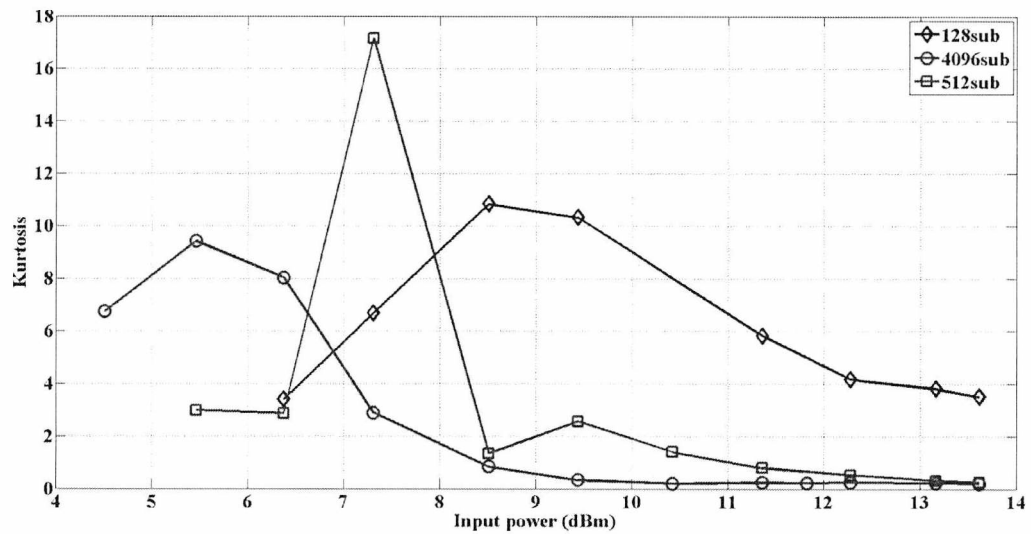


Fig. 4.17: Kurtosis of the distributions at different input powers.

Another measure of normality is the Coefficient of Variation (CV). The CV is given by [82]:

$$CV = \frac{\text{variance}}{\text{mean}} = \sqrt{e^{s^2} - 1}. \quad (4.9)$$

The CV is an interesting measure because a reduction in the CV value means that a log-normal distribution tends to a normal distribution. Table 4.4 shows the CV results at three different input powers. It can be seen that the CV reduces for higher numbers of subcarriers as well as higher input powers.

Table 4.4: Coefficient of variation (CV) results at different input powers.

	9.45 dBm	11.8 dBm	13.6 dBm
Sub. no.	CV	CV	CV
128	0.44	0.31	0.22
512	0.3	0.16	0.11
4096	0.12	0.07	0.047

4.6 Raw EVM distributions

Fig. 4.18 shows plots of the raw EVM distributions for 128 and 512 subcarriers with fitted Rayleigh distributions in accordance with (4.4), at input powers of 9.45 and 13.2 dBm. Fig. 4.19 shows the same plots for Equalizer 2. It can be seen that the fitting with the Rayleigh distributions becomes less accurate as the input power and/or number of subcarriers are reduced. This can be seen in Table 4.5 that summarizes goodness of fit parameters for the distributions. Both error parameters in Table 4.5 reduce with input power and number of subcarriers. The skew in the distributions is an indication that the Real and Imaginary components in the numerator of (4.4) are not normally distributed as in the i.i.d case, but with distortion are skewed, resulting in skewed Rayleigh distributions. Note that the mechanism that causes the skew in these distributions is different from the one in the EVM per frame distributions of Section 4.5.

Fig. 4.20 shows the skew and kurtosis of the raw EVM distributions. The dashed trace represents the Rayleigh distribution limit for these statistical measures. Higher skew results in an increase in the distance between the mean and the median.

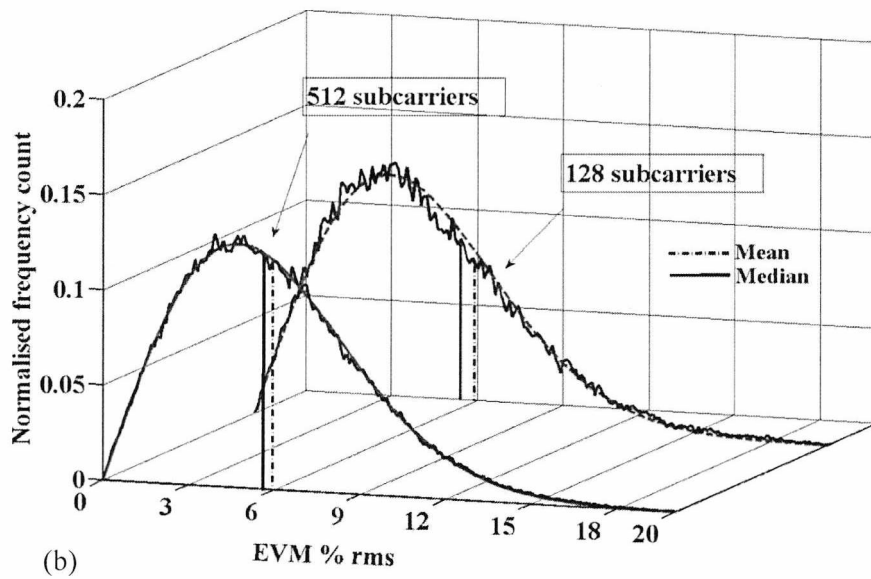
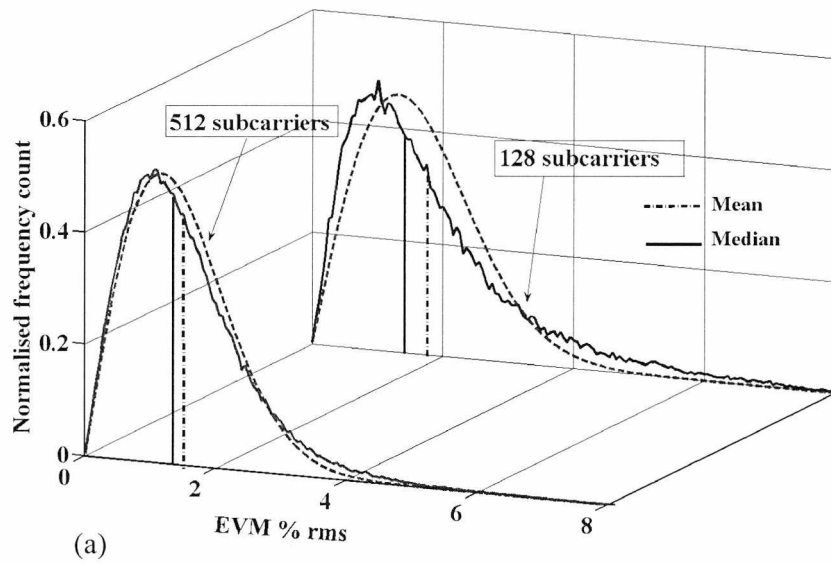


Fig. 4.18: Distributions of the raw EVM for 128 and 512 subcarriers at input powers of (a) 9.45 dBm and (b) 13.2 dbm for Equalizer 1. The dashed traces are Rayleigh fits.

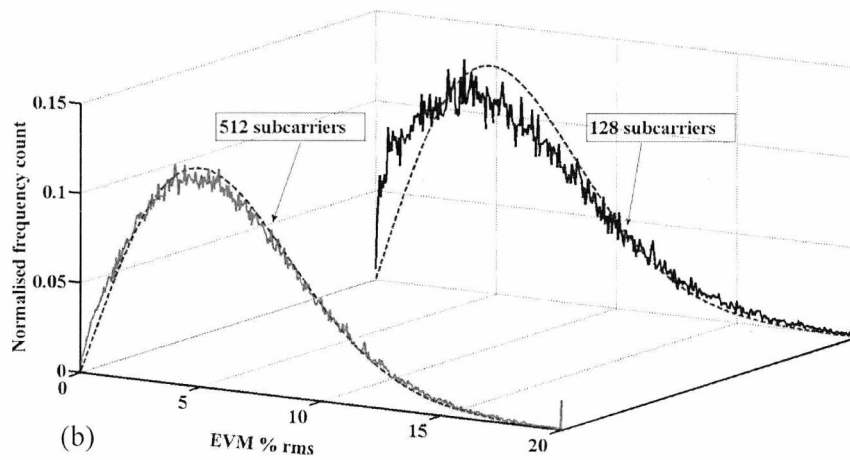
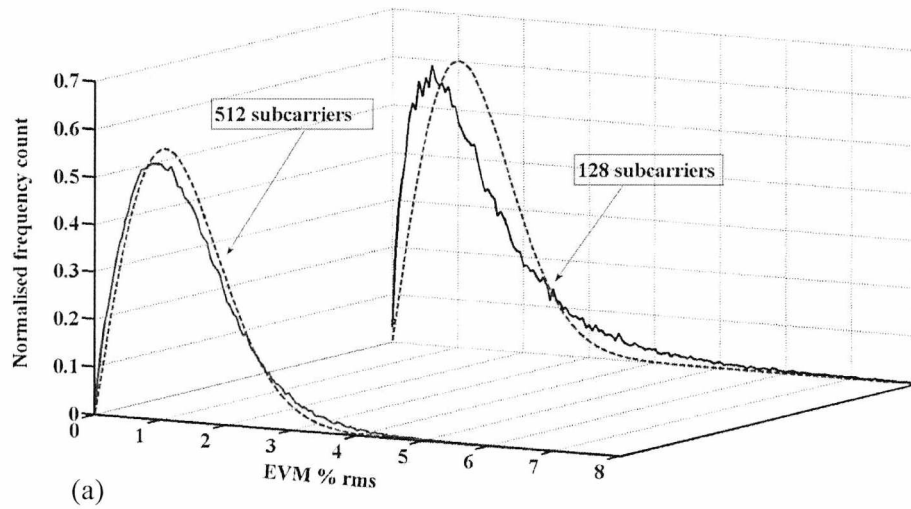


Fig. 4.19: Distributions of the raw EVM for 128 and 512 subcarriers at input powers of (a) 9.45 dBm and (b) 13.6 dBm for Equalizer 2. The dashed traces are Rayleigh fits.

Table 4.5: Goodness of fit measures for the fitting between the raw EVM distributions and the Rayleigh distributions. SSE: Standard Squared Error; RMSE: Root Mean Square Error.

	9.45 dBm		11.35 dBm		13.2 dBm	
Sub no.	128	512	128	512	128	512
SSE	1.26	0.15	0.4	3.7e-2	9.9e-2	8.4e-3
RMSE	3.7e-2	1.5e-2	1.7e-2	6e-3	7e-3	2.2e-3

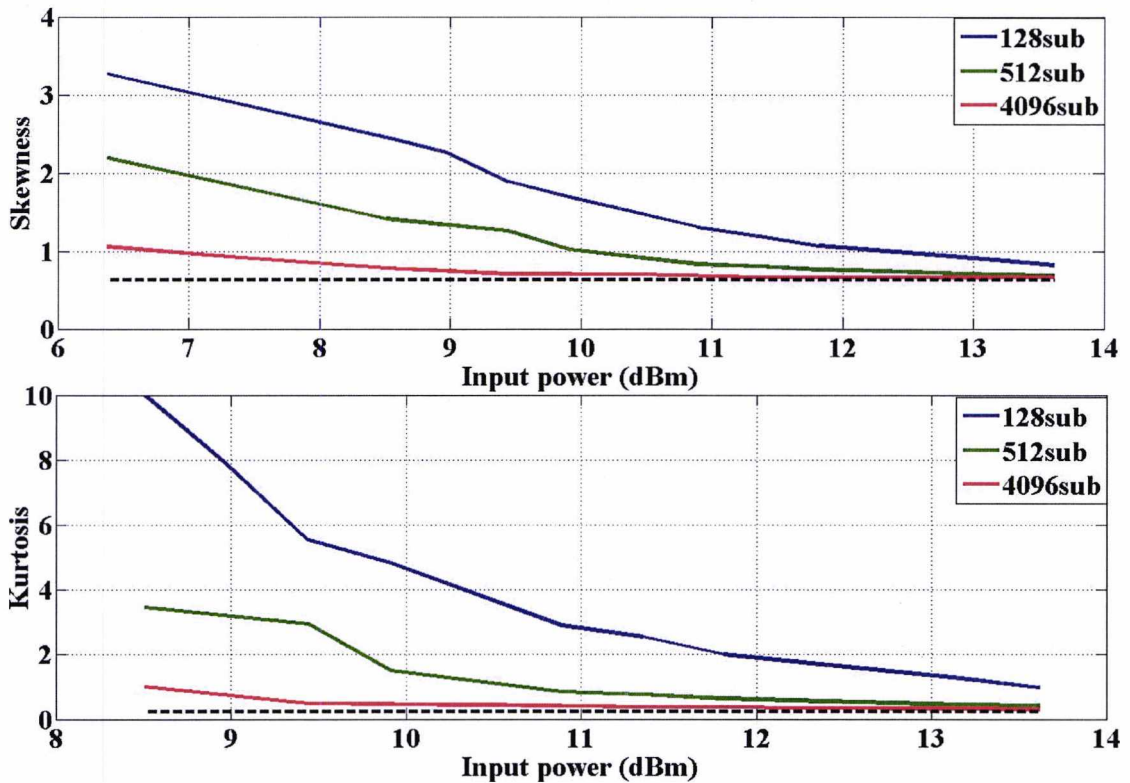


Fig. 4.20: Skew and kurtosis of the raw EVM distributions for 128, 512 and 4096 subcarriers. The dashed traces are the Rayleigh distribution skew and kurtosis.

For example, assuming that the variance of the Real and Imaginary components in the numerator of (4.4) is lower for signals with lower number of subcarriers (as would be expected due to the lower statistical PAPR), the higher skew for these signals will result in a greater



difference between mean and median compared to signals with more subcarriers. This can also be seen in Fig. 4.18, where the distance between the mean and the median increases for lower numbers of subcarriers. Thus, as these distributions possess different amounts of skew, the mean is not the best measure of performance and instead the median should be used, which is less prone to extreme values. Fig. 4.21 shows the absolute difference between the mean and the median for 128 and 512 subcarriers. As the input powers are increased the two traces come closer together as expected from the skew result.

The median of the raw distributions is given by:

$$\mu_r = EVM_{\frac{m+1}{2}} \quad (4.10)$$

for $EVM_1 < EVM_2 < \dots < EVM_m$.

From the definition of the median:

$$P(EVM_r \geq \mu_r) = P(EVM_r \leq \mu_r) = 0.5.$$

Therefore, the median EVM gives the 50% value i.e. the value from which half of the measured EVM values are above and half are below. For distributions with even symmetry, the median and mean coincide and both give the 50 % point. But for skewed distributions, the percentage point given by the mean will depend on the skew and therefore on the distortion conditions. As such, it will depend on the particular conditions and performance during each measurement. For this reason the median point is clearly advantageous for analysis purposes as it is independent (not in terms of its value but in terms of the probability size it describes) of the underlying distribution at different input powers.

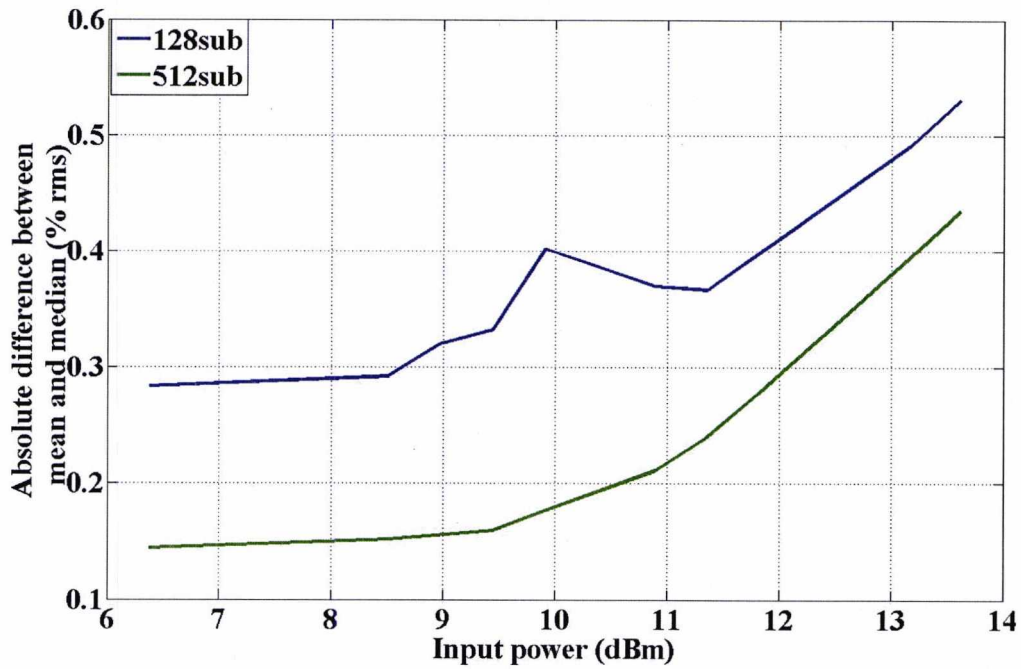


Fig. 4.21: Absolute difference between mean and median for 128 and 512 subcarriers. The general trend shows that the absolute difference between mean and median reduces with input power and the two traces come closer together. The deviations from the general trend observed in the 128 subcarrier trace are attributed to measurement variations (note that the peak observed corresponds only to a single measurement result).

Fig. 4.22 shows the result for both the mean and the median of the raw EVM distributions. The mean of the raw EVM distribution is equal to the mean of the EVM per frame distribution (see Fig. 4.8) as expected from (4.6). The reduction in EVM when using the median compared to the mean is significant and becomes greater as the number of subcarriers is reduced, as expected from the trends in the skew result of Fig. 4.20. Differences in the back-off requirements between the different traces are difficult to observe in Fig. 4.22, as the mean EVM results for Equalizer 1 do not provide us with a clear trend. But with Equalizer 2 (Fig. 4.23), the mean EVM results for different numbers of subcarriers more clearly overlap. It can be seen, that for the median EVM results, the trend for reduced back-off with lower numbers of subcarriers (lower PAPR) is more clearly observed.

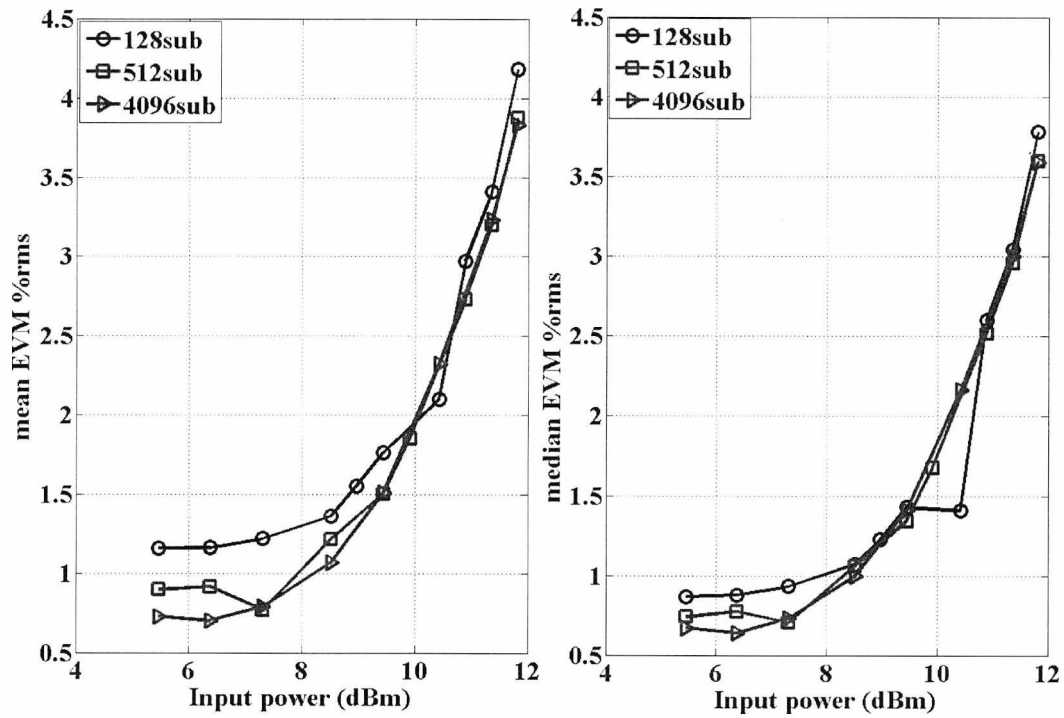


Fig. 4.22: Mean and median results of the raw EVM distributions versus input power for Equalizer 1.

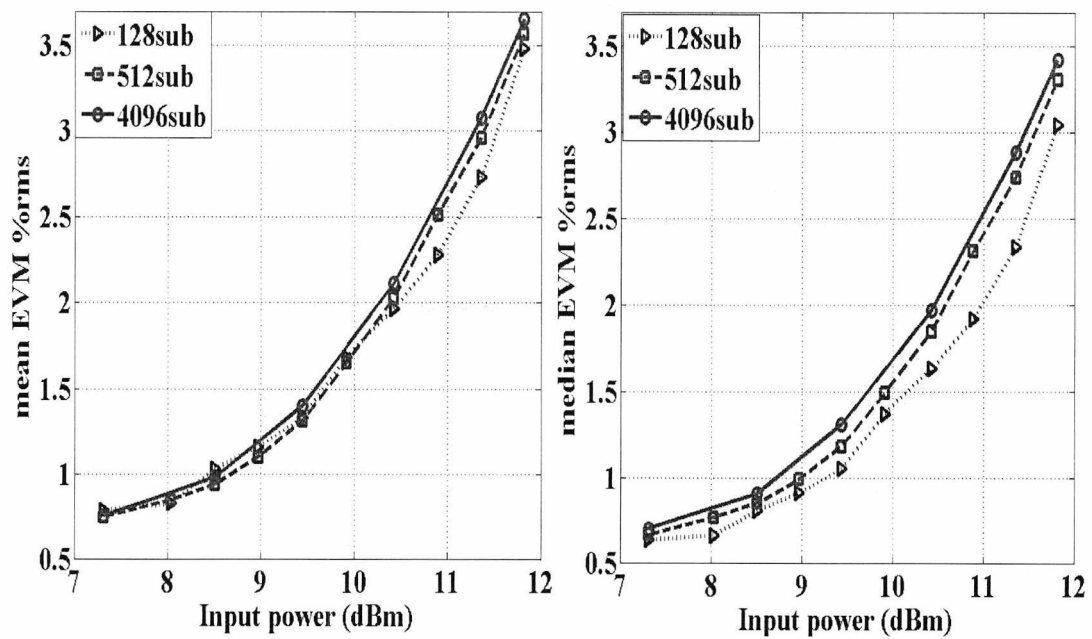


Fig. 4.23: Mean and median results of the raw EVM distributions versus input power for Equalizer 2.

Another way to "inspect" the differences in back-off with Equalizer 1 when using the median instead of the mean is by normalizing all the traces to the same mean value (i.e. as if the mean raw EVM is exactly equal for different numbers of subcarriers). The median traces are then obtained by subtracting from this normalized mean the absolute difference between mean and median (that was plotted in Fig. 4.21) for each signal. This process is necessary in order to take away any "biases" from non-ideal equalization that can mask differences between the results. The result of this process is shown in Fig. 4.24. A difference in the back-off requirement is clearly observed. The 0.9% EVM point occurs with a difference in input power of 1 dB between 128 and 512 subcarriers and 0.7 dB between 512 and 4096 subcarriers. For the 1% point these differences are 0.8 dB and 0.6 dB respectively. Note also that as expected, the 512 and 4096 subcarrier traces meet at a lower input power compared to the 512 and 128 subcarrier traces. At the lower input powers it would be expected that the traces would meet at some input power (as distortion becomes negligible). This point would occur at a lower input power for 512 and 4096 subcarriers as distortion effects are expected to occur sooner. This behaviour is not observed here and in general, it can be "masked" by non-ideal equalization, measurement equipment noise floor etc.

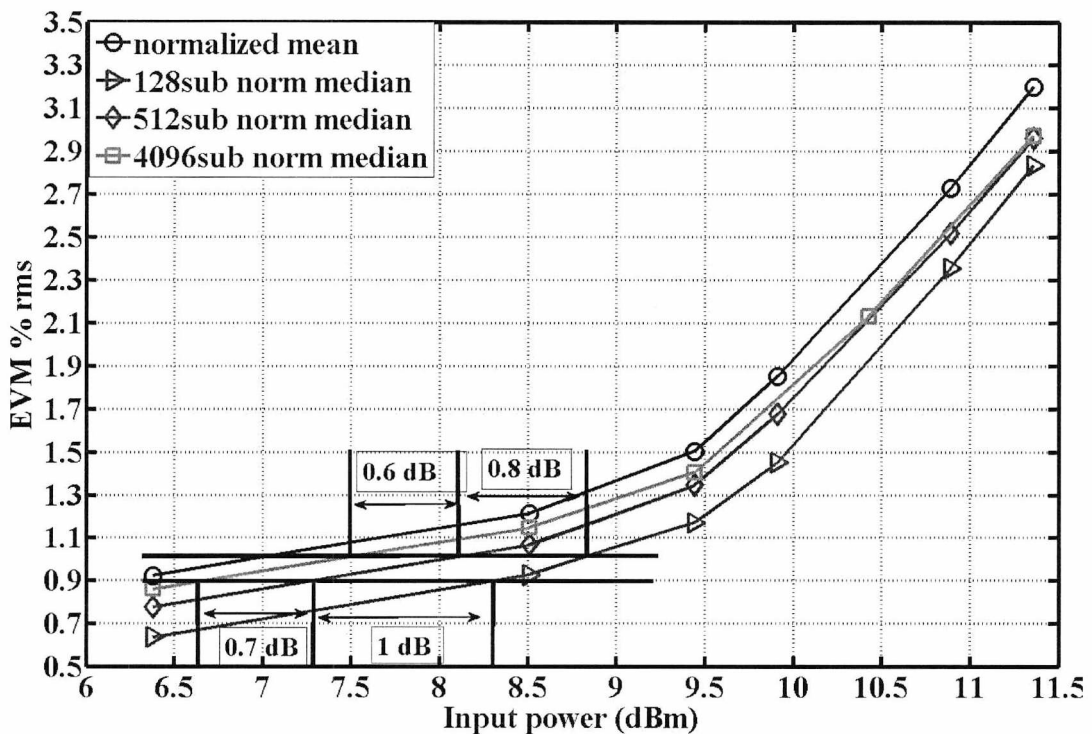


Fig. 4.24: Normalized median result for 128, 512 and 4096 subcarriers.

4.7 Conclusions

EVM measurement results for a directly modulated RoF link transporting a large number of OFDM frames with QPSK modulation are presented. The mean EVM results (with the mean calculated over each OFDM frame) indicate that the amount of input power back-off from the P1dB required does not depend on the number of subcarriers (at least to the extent expected by the statistical PAPR for different numbers of subcarriers). In the noise limited range of measurement (low RF input power), the distribution of the mean EVM results is approximately Gaussian, resulting in the same mean, but a variance which depends inversely on the number of subcarriers due to the averaging in the estimation of the mean EVM. However, the distribution of the mean EVM at intermediate RF input powers, where the distortion starts to dominate the performance, is positively skewed and better approximated by a log-normal distribution. This effect is a direct consequence of the way the OFDM modulation and demodulation operate in a per-frame manner. In the limit, as the number of subcarriers and/or input power are increased, the skew reduces and the distribution converges asymptotically to a Gaussian one. The distribution of the raw EVM is also skewed, and more so for lower numbers of subcarriers. This is a result of skew in the noise plus distortion distribution. Again, in the limit, as the numbers of subcarriers and/or input power are increased the distribution converges asymptotically to a Rayleigh distribution. The results indicate that if the median of the EVM is observed instead of the mean, the change in back-off requirements between signals with different numbers of subcarriers becomes more apparent.

5 Back-off estimations and EVM at different locations in the signal band

5.1 Introduction

In this chapter some of the observations carried out in chapter 4 are extended further. Particularly, an investigation is carried out into how basic statistical concepts can be used to estimate the proportion of the mean EVM per frame values that will exceed some EVM threshold. Looking at the EVM per frame instead of the raw EVM is more useful as the OFDM transmission works by sending contiguous blocks of subcarriers. A frame with a high mean EVM implies that most of the subcarriers in that frame will also be affected by distortion and will also possess a high EVM.

Furthermore, an estimation of the number of frames required in order to obtain an accurate estimate of the mean EVM is carried out.

Finally, EVM results for subcarriers in different positions in the signal band at varying input powers are presented.

5.2 Back-off estimation from the mean EVM per frame

In Section 4.5 it was shown that the EVM per frame is approximately log-normally distributed. It was also shown that as the input power and/or IFFT size increase, the distribution of the EVM per frame tends to normality. Based on these observations, certain theoretical results can be used to predict, in theory, the EVM per frame distributions of signals with different IFFT sizes. Figures 5.1 and 5.2 show the variation of the sigma parameter (S) and the skew respectively of the log-normal distribution with variance at different mean values. If it is assumed that the variance varies inversely proportionally with the IFFT size, then knowing the mean and variance of the EVM per frame for one IFFT size, one can make a rough estimate using these theoretical results for the corresponding statistical parameters of the log-normal

distribution of a signal with a different IFFT size. For example, if the variance of a signal at one IFFT size is known then it can be assumed that a signal with double the IFFT size will have the same mean and half the variance. From this information, the sigma parameter and skew for the second signal can be obtained directly from Fig. 5.1 and Fig. 5.2.

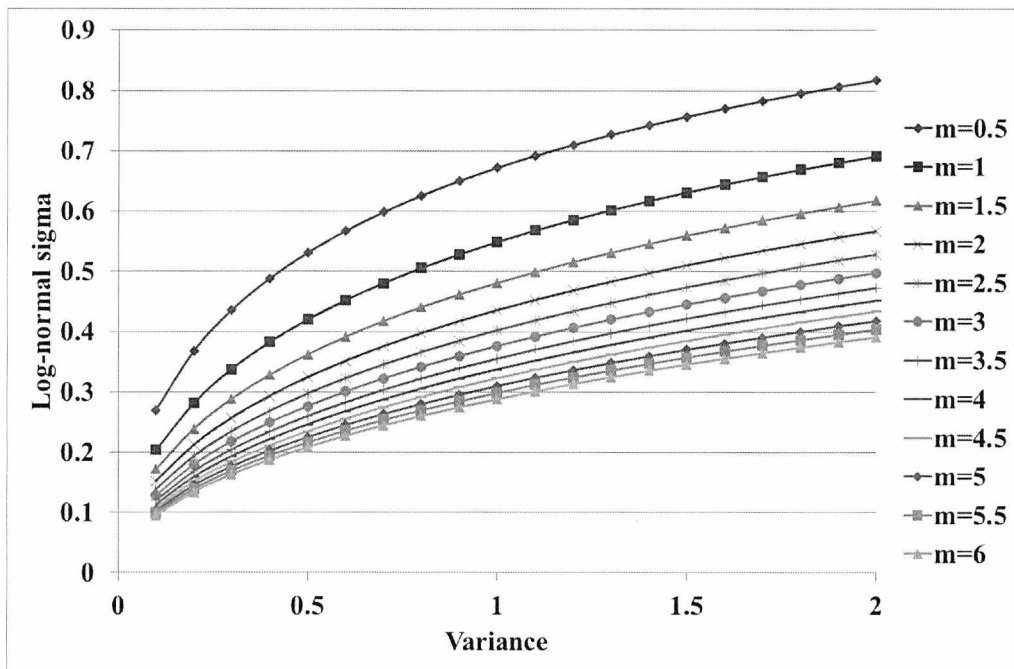


Fig. 5.1: Theoretical variation of the log-normal sigma parameter with variance for a log-normal distribution at different mean values.

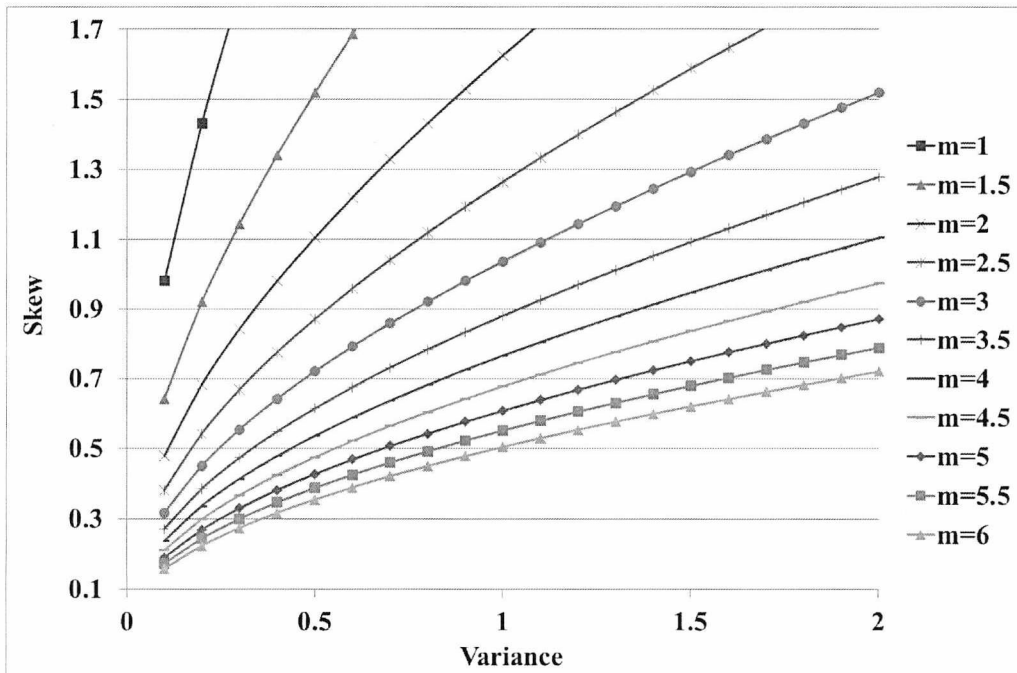


Fig. 5.2: Theoretical variation of skew with variance for a log-normal distribution at different mean values.

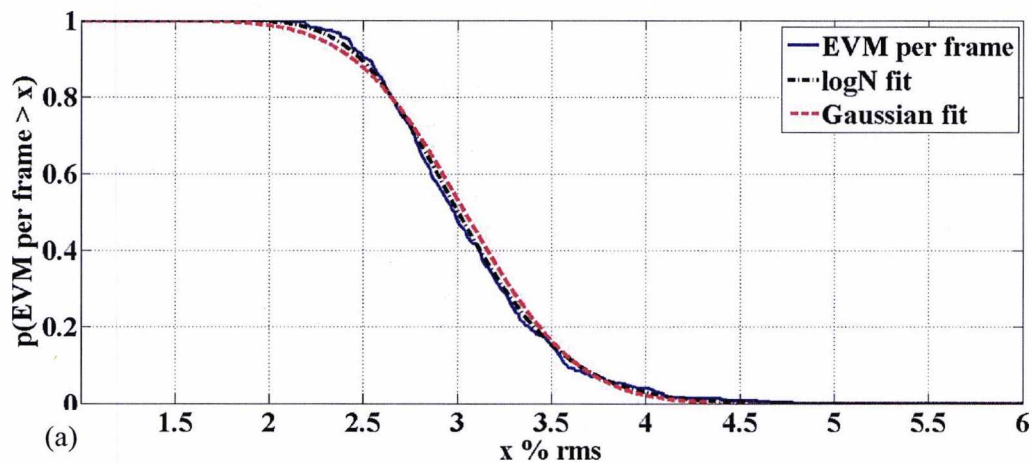
Although the mean of the EVM per frame distributions can be used for back-off estimation it does not provide any information concerning the proportion of the EVM per frame values that will exceed a given EVM threshold. This is important information as differences in the variance between signals with different subcarriers imply that, although these signals might have the same mean, they will have different proportions of frames with mean EVMs above a certain value. That is, their EVM can exceed the EVM standard specifications more often. For this, the variance and skew of the distributions have to be taken into account. At higher input powers and/or large IFFT sizes (say above 1024 subcarriers) the skew reduces and the distributions tend to Gaussian distributions. Using the standard deviation of the EVM per frame distribution, one can choose an input power at which the proportion of EVM per frame values that exceed a specific EVM threshold is below some pre-defined level. Fig. 5.3 shows the EVM per frame CCDF plots for 1024 and 2048 subcarriers with log-normal and Gaussian fits at an input power of 10.9 dBm. While the log-normal distribution compared to the Gaussian provides a better overall fit, the differences between the two at this input power are quite small. Fig. 5.4 shows the Gaussian PDFs fitted on the two EVM per frame distributions. The means of the two distributions are approximately equal ($\approx 3\%$) while the standard deviations are 0.47 and 0.33 for 1024 and 2048 subcarriers respectively (the standard deviation of 1024

subcarriers is higher approximately by a factor of $\sqrt{2}$ than that of 2048 subcarriers). For 2048 subcarriers, approximately 16 % and 2.275 % of EVM per frame values are above one σ and 2σ respectively. These percentages correspond to EVM values of 3.36 (% RMS) and 3.69 (% RMS) respectively. The probability that the EVM per frame for 1024 subcarriers will exceed these values can be given using the following expression which is based on the definition of the CCDF of the normal distribution:

$$P(EVM_{f,1024sub} > m + n\sigma_{2048}) = \frac{1}{2} \operatorname{erfc}\left(\frac{\sigma_{2048} n}{\sigma_{1024} \sqrt{2}}\right) = \frac{1}{2} \operatorname{erfc}\left(\frac{n}{2}\right) \quad (5.1)$$

for $n = 1, 2..$

Equation (5.1) gives for 1024 subcarriers a percentage probability of 24.135 % and 3.93 % for the two EVM per frame values. That is, for 1024 subcarriers, a higher percentage of mean EVM per frame values will be above 3.36 % and 3.69%.



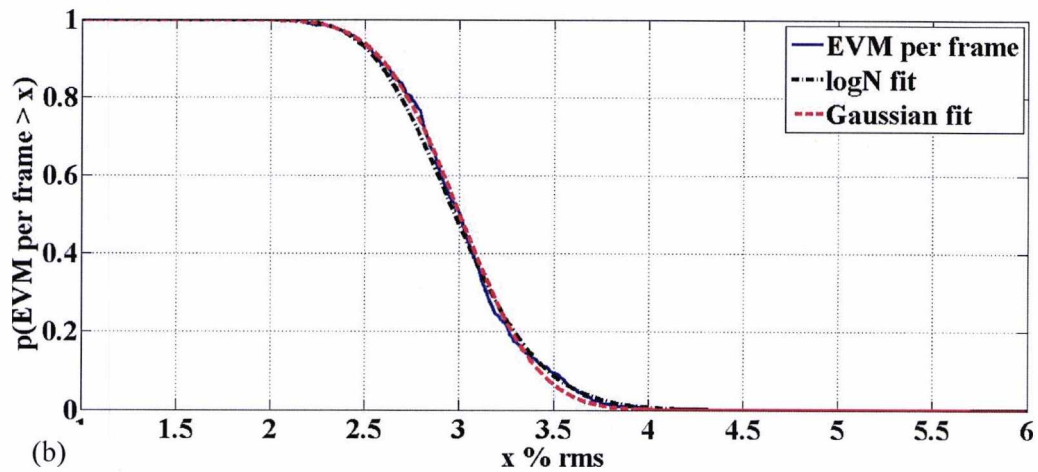


Fig. 5.3: CCDF at an input power of 10.9 dBm with log-normal and Gaussian fits for (a) 1024 subcarriers and (b) 2048 subcarriers.

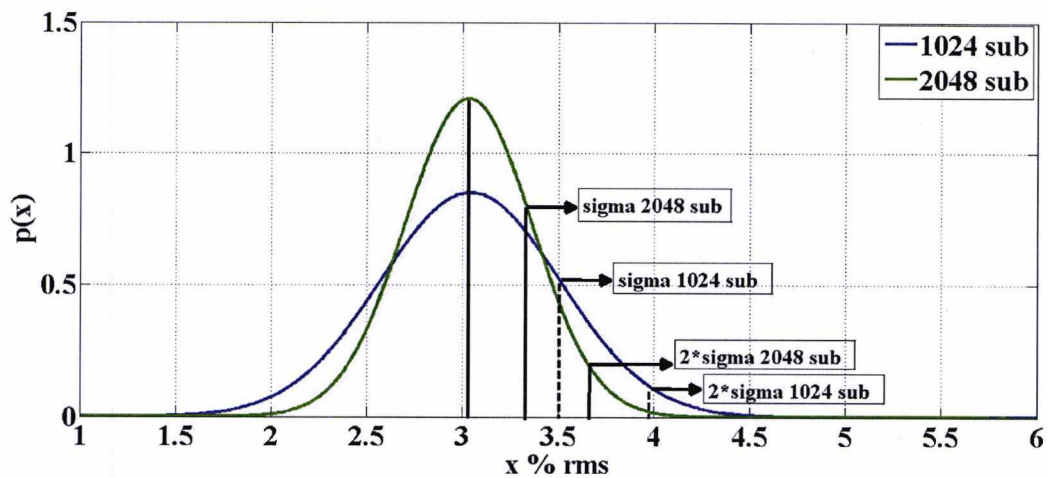


Fig. 5.4: Gaussian fitted PDFs for 1024 and 2048 subcarriers at an input power of 10.9 dBm with annotated confidence intervals at one and two standard deviations from the mean.

At lower input power where the skew is higher, confidence intervals ($m+n\sigma$, for $n=1,2,\dots$) can be calculated by log-transforming the original EVM per frame values [82]. The transformation changes the distribution from a log-normal to a Gaussian one. This is shown in Fig. 5.6 for the EVM per frame distribution of a signal with 512 subcarriers whose CCDF is shown in Fig. 5.5. Using the empirical confidence intervals shown in Fig. 5.4 or by using (5.1) the corresponding values for the Gaussian distribution resulting from the log-transformation can be obtained.

The final EVM values for the original log-normal distribution at the confidence intervals of interest are obtained by taking the anti-log of the log-transformed values:

$$EVM_{f,m+n\sigma} = e^{EVM_{\log\text{transformed},m+n\sigma}}. \quad (5.2)$$

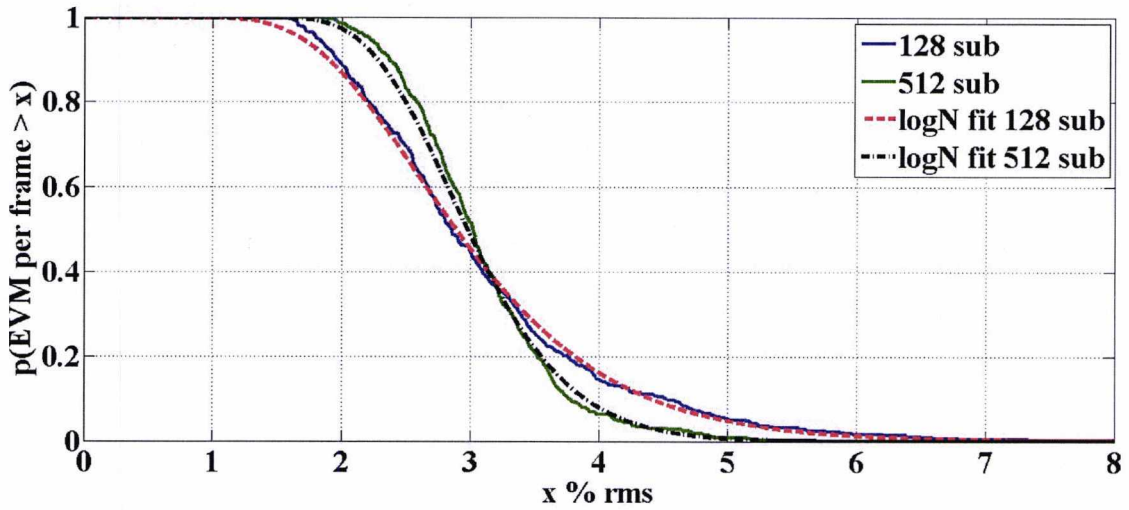


Fig. 5.5: CCDF plots for 128 and 512 subcarriers at an input power of 10.9 dBm with log-normal fits.

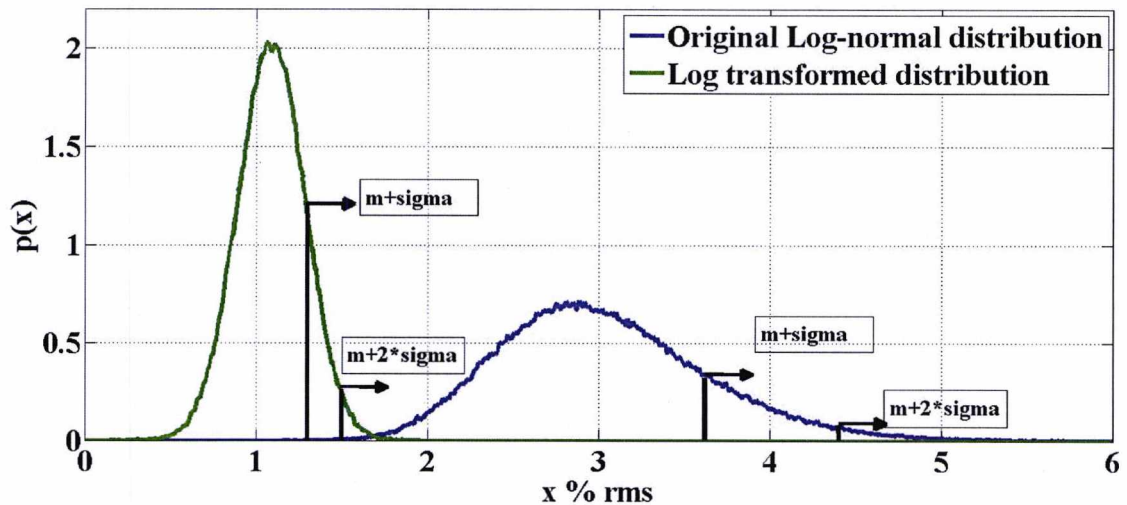


Fig. 5.6: Original PDF for 512 subcarriers at an input power of 10.9 dBm and the log transformed PDF showing confidence intervals at one and two standard deviations from the mean. The corresponding EVM values at those confidence intervals for the original distribution are obtained by taking anti-logs of the values of the log-transformed distribution.

5.3 Effect of the number of transmitted frames in the back-off estimation from the EVM measured result

In order to obtain an accurate estimate of the mean of the EVM per frame distribution, the number of transmitted OFDM frames is in itself an important parameter. The required number will depend on the number of subcarriers employed by the signal, and will be higher for signals with smaller numbers of subcarriers. In general, it is not standard practice in the literature to mention the number of transmitted frames that was used in a measurement. Additionally, measurement equipment (e.g. VSAs) by default might transmit only a single frame repeatedly (see for example the Agilent *signal studio N7617B*). This means that the different statistical realizations of the OFDM signals are not measured.

Fig. 5.7 shows the average EVM versus input power result for 512 subcarriers when the averaging is done over different numbers of frames. For each case, a different (random) selection of frames is used and the result shows the variation in the EVM estimate from one selection to the next. In general 50 to 100 frames are required for 512 subcarriers (this is an empirical estimation). It can be assumed that a number 4 times larger will be required for 128 subcarriers (due to (4.7)). Fig. 5.8 shows the same result for 4096 subcarriers. The variation between different selections of frames is reduced significantly compared to the case of 512 subcarriers. Note however, that as the number of subcarriers is increased the differences in the variance between different OFDM signals deviates from those expected from (4.7) as shown in Fig. 4.13. Fig. 5.9 shows the theoretical 95% confidence interval for different numbers of OFDM frames. It is assumed here that the differences in the EVM per frame variance for the different IFFT sizes are those predicted by (4.7). The annotations correspond to an interval size of 0.31% (i.e. the interval within which 95% of EVM per frame values will reside) and it can be seen that this interval size, requires a number of transmitted OFDM frames that scales inversely proportionally with the IFFT size. The confidence interval sizes of Fig. 5.9 are based on the normal distribution and are obtained using:

$$m_f \pm c \sqrt{\frac{\sigma_f^2}{F}} \quad (5.3)$$

where c is the confidence interval, F is the number of frames, m_f is the mean EVM per frame and σ_f^2 is the variance of the EVM per frame distribution.

For the prediction of Fig. 5.9 the value used for c was 1.96 which corresponds to the 95 % interval for a standard normal distribution, for m_f was 7 % and for σ_f^2 was equal to the variance for the 512 subcarrier signal at an input power of 13.6 dBm. It was also assumed that the variance, σ_f^2 , scales inversely proportionally with the IFFT size according to (4.7).

Note that these results practically represent an upper bound for the required number of transmitted frames for these measurements. This is because the variances used in (5.3) for these results, correspond to those at the highest input power (13.6 dBm) used in the measurements. At lower input powers, the variances of the results reduce, meaning that a lower numbers of frames will be required to obtain the same confidence intervals.

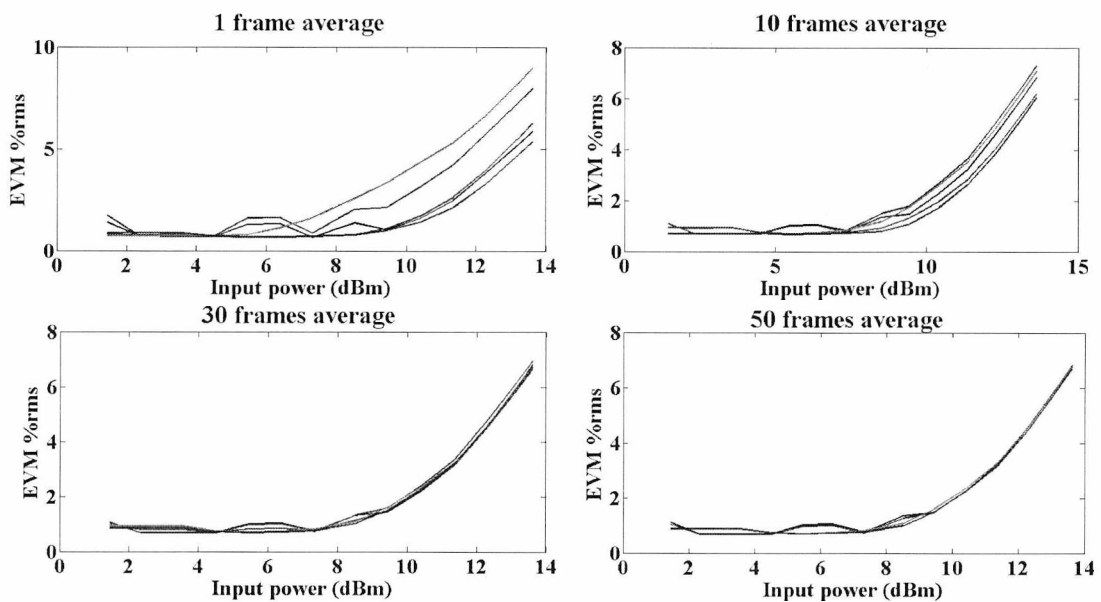


Fig. 5.7: Average EVM versus input power result for 512 sub-carriers and QPSK modulation for different numbers of OFDM frames showing the differences in the average result between different selections of frames.

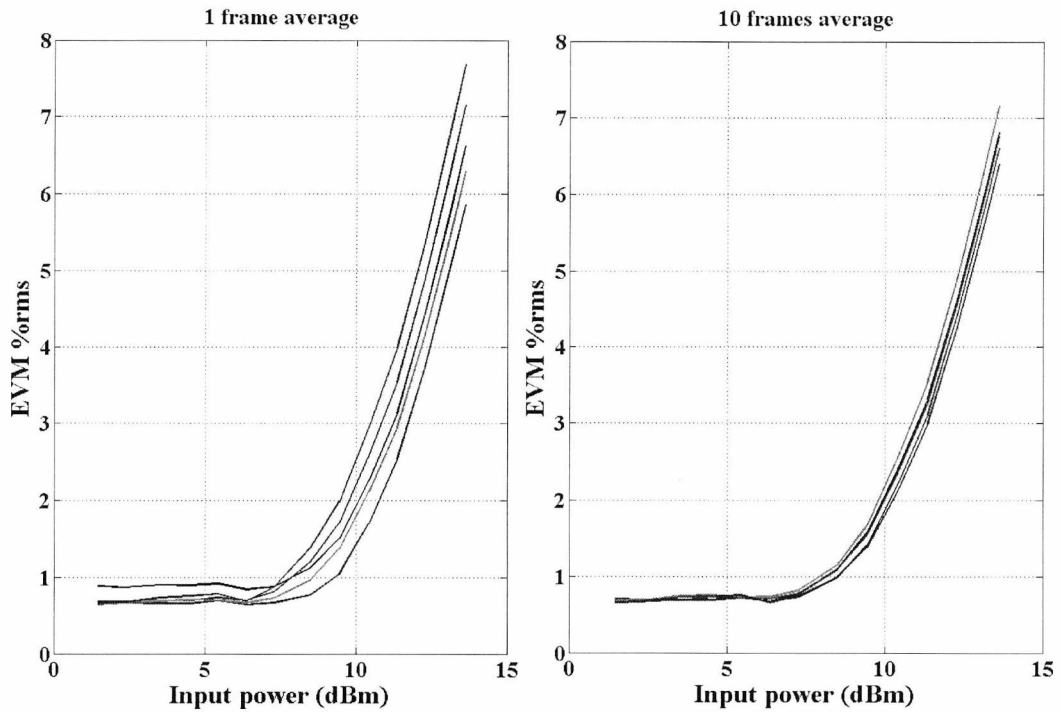


Fig. 5.8: Average EVM versus input power result for 4096 sub-carriers and QPSK modulation for different numbers of OFDM frames showing the differences in the average result between different selections of frames.

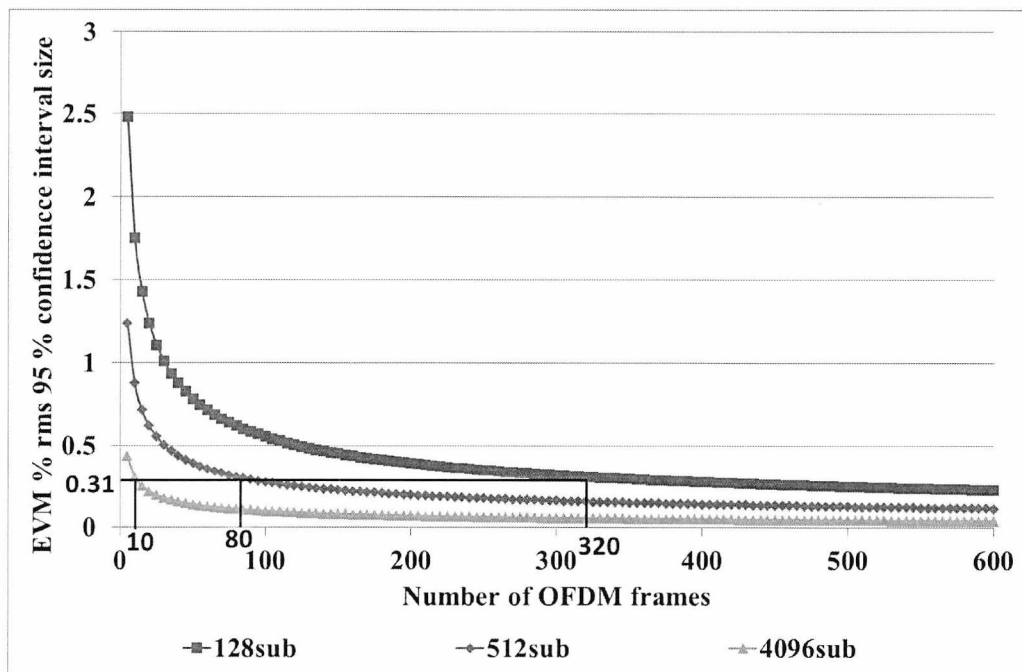


Fig. 5.9: 95% confidence interval size versus number of OFDM frames for different IFFT sizes.

5.4 EVM of subcarriers at different locations in the signal band

Fig. 5.10 is a plot of EVM across the OFDM subcarriers for over 10 OFDM symbols (signal used was with 512 subcarriers of which 420 were data subcarriers). The specific measurement is at an input power of 8.5 dBm. Each point in the x-axis is half an OFDM symbol length (length in terms of the number of subcarriers). It is seen that in the case of no equalisation large peaks occur at the edges of the OFDM symbol, while smaller peaks are observed in the middle of the symbol. This effect can be attributed to IQ timing offsets [83].

With equalisation, the peaks are dramatically reduced and this shows that in principle proper equalization should be able to mitigate this effect. A result of the IQ timing offset is that the skew of the EVM distributions at low powers (before distortion starts to dominate) is not zero (as was discussed in Section 4.5) as would be expected (see Fig. 4.2). It is also the reason of the EVM floor observed in Fig. 4.7. The term “non-ideal” equalization will be used to describe the effects of IQ timing offset for the remainder of this chapter.

The average EVM for the 10 symbols in Fig. 5.10 is 2.6 % and 1 % for the un-equalised and equalised case respectively. Fig. 5.11 shows the average EVM (averaged over 450 OFDM frames) versus subcarrier number, at an input power of 8.5 dBm with and without equalization for 512 and 4069 subcarriers respectively. The edge effects observed (high peaks in the EVM on the left side of the figures) are attributed to the equalization method but span across fewer than five subcarriers. As such their effect in the average EVM will be negligible.

As the input power is increased the limitation will come from distortion (Fig. 5.12). The effects of distortion now become more white noise like.

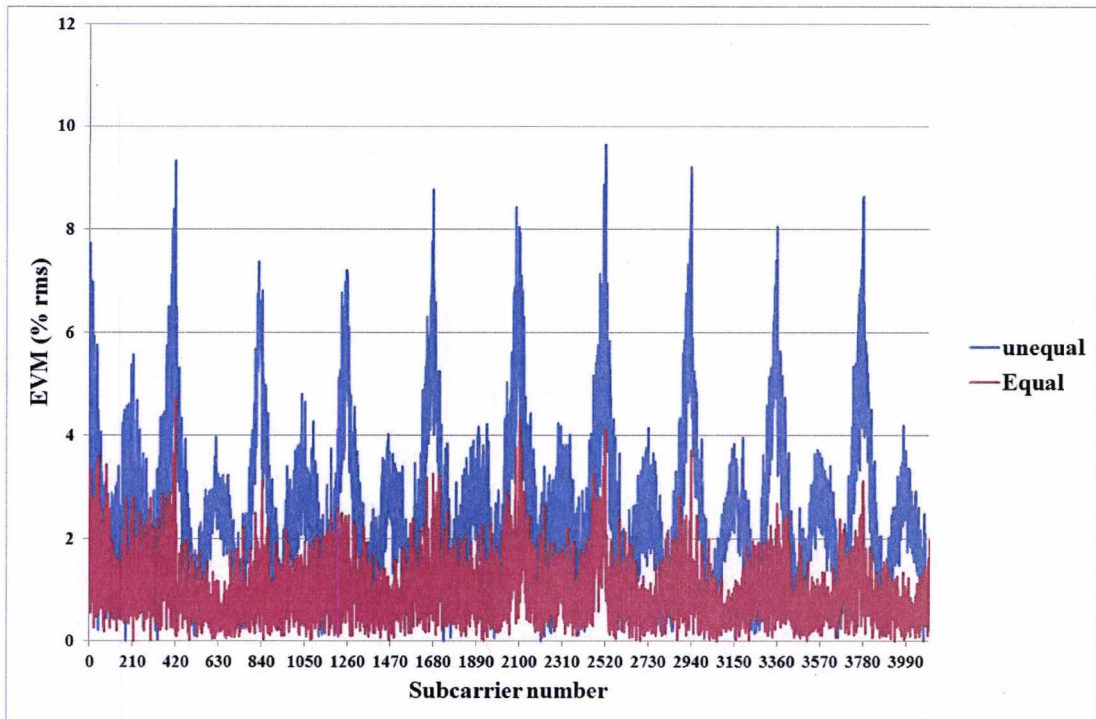
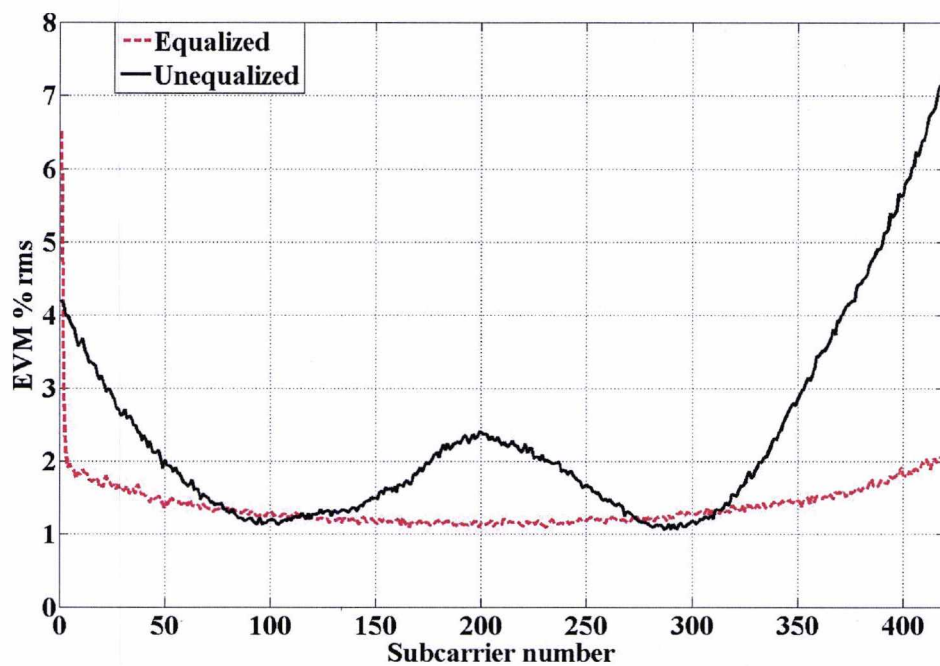


Fig. 5.10: Evm versus subcarrier number across 10 symbols with 512 (420 data) subcarriers at an input power of 8.5 dBm.



(a)

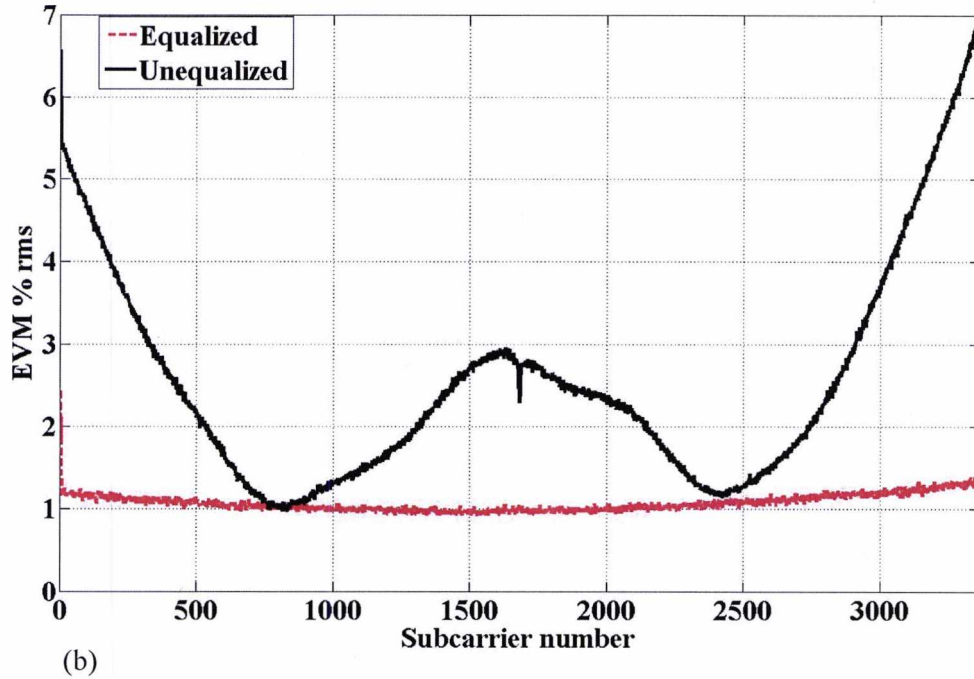


Fig. 5.11: EVM versus subcarrier number for (a) 512 subcarriers and (b) 4096 subcarriers at an input power of 8.5 dBm.

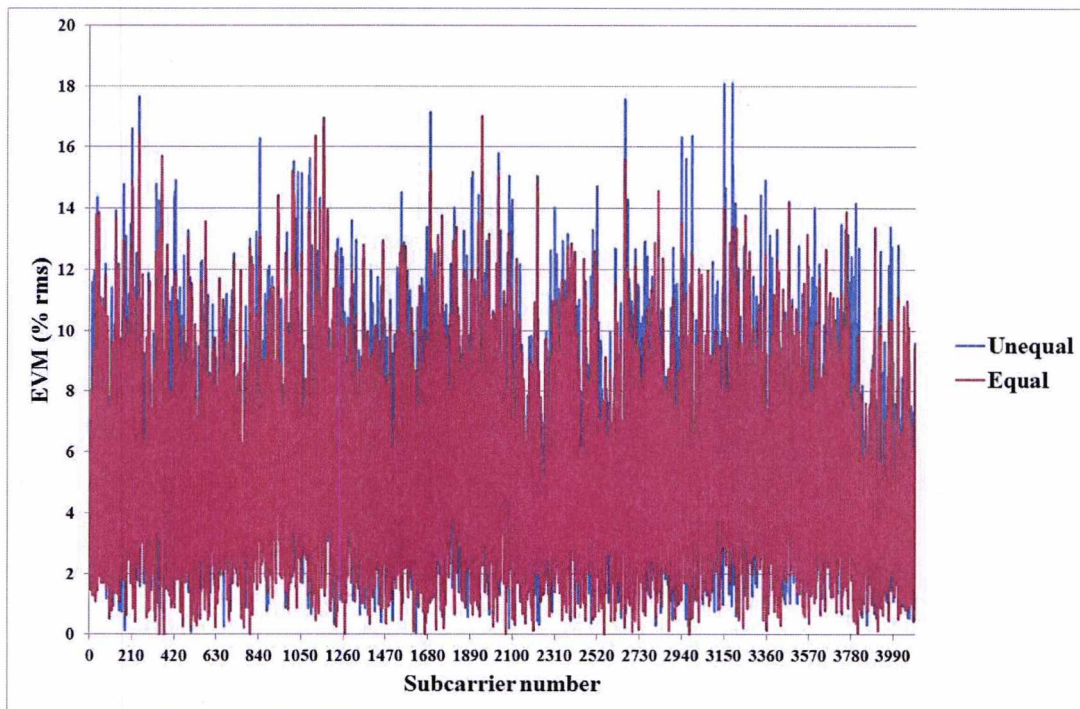


Fig. 5.12: Evm versus subcarrier number over 10 symbols with 512 (420 data) subcarriers at an input power of 13.2 dBm.

By looking at individual subcarriers, one can obtain information about the main impairments (non-ideal equalization and distortion) at different points in the signal band. This would be in interest for systems where users are allocated specific subcarriers at different parts of the band (e.g. OFDMA systems). Figures 5.13, 5.14 and 5.15 show the EVM results for different subcarriers in the band for 4096, 512 and 128 IFFT sizes respectively. The blue traces are the mean EVM results for the 152nd subcarrier from the edge of the band for the 4096 subcarrier signal, the 19th subcarrier for the 512 subcarrier signal and the 5th subcarrier for the 128 subcarrier signal. The red traces are the mean EVMs for subcarriers that are located at the same distances but from the middle of the band. The chosen subcarriers are located approximately in the same position in the signal band for all signals. The green traces are the average EVM results from (4.8).

At lower input powers, the EVM for the subcarrier at the edge of the band is higher. This is due to non-ideal equalization which predominately affects the edge subcarriers. As the power is increased, the mean EVM for the subcarrier at the middle of the band increase at a faster rate and eventually surpasses the EVM at the edge of the band. This is a clear indication that once distortion dominates, it does not behave as white noise and instead behaves more like coloured noise affecting the subcarriers in the middle of the band to a larger extent. This behaviour is more clearly evident in the 4096 subcarrier signal. Note that the trace of the average EVM (over all subcarriers and transmitted frames) is, at a first glance, the average behaviour between the two performances in the edge and in the middle of the band. The blue and red EVM traces meet at an input power of approximately 10.7 dBm for 512 subcarriers and approximately 9.5 dBm for 4096 subcarriers. This difference in power is equal to the difference in the median of the statistical PAPR between the two signals (~ 1.2 dB). For 128 subcarriers this is harder to estimate due to the strong variations in all the traces. As an indication, we can look for the power at which the trace of the average EVM crosses the trace of the EVM of the middle subcarrier for the first time. This occurs at an input power of approximately 11.6 dBm. The difference in power with the 512 subcarrier signal is approximately 0.9 dB which is very close to the value expected from the statistical PAPR (~ 0.8 dB).

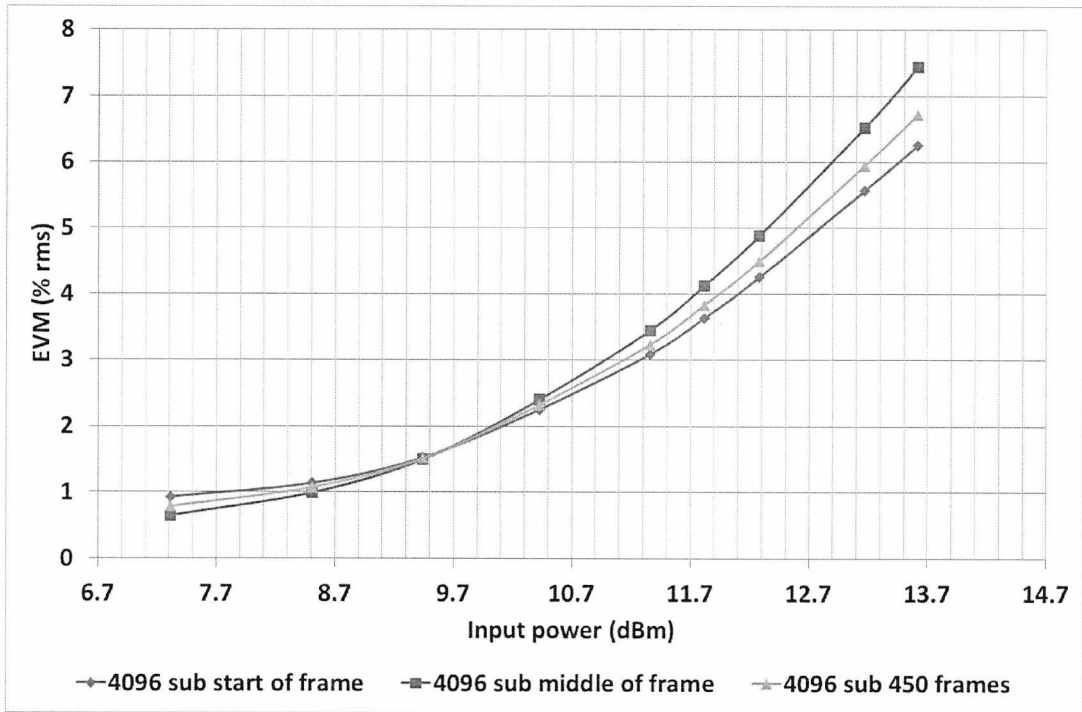


Fig. 5.13: Mean EVM results for subcarriers at the edge and middle of the band and average EVM across all transmitted subcarriers in all the frames for a signal with 4096 subcarriers.

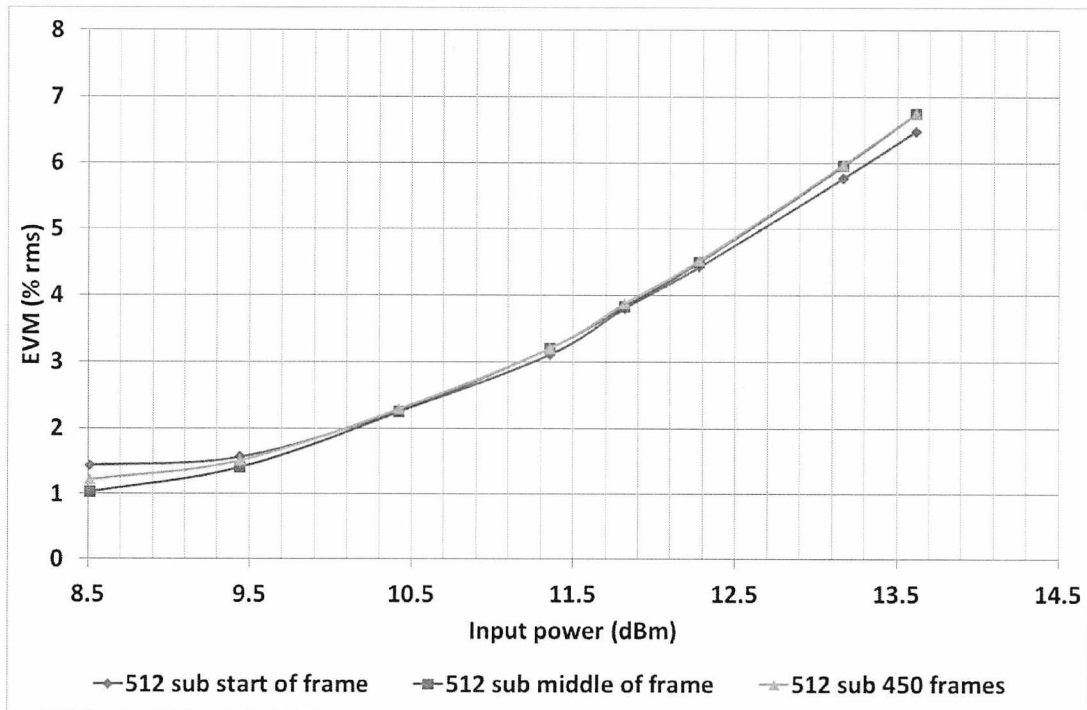


Fig. 5.14: Mean EVM results for subcarriers at the edge and middle of the band and average EVM across all transmitted subcarriers in all the frames for a signal with 512 subcarriers.

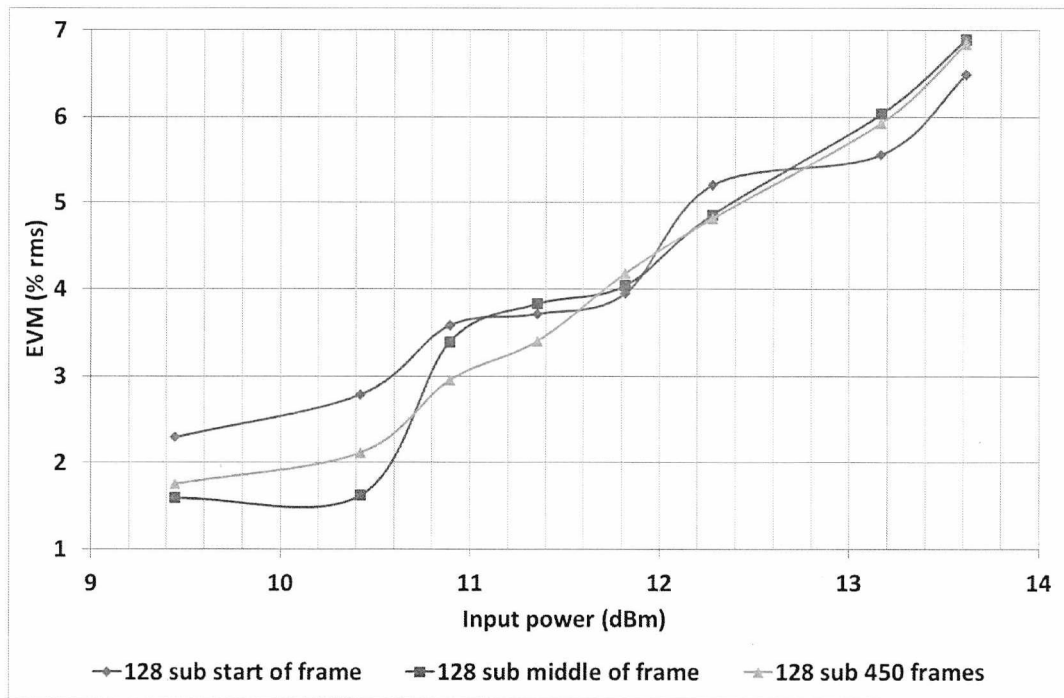


Fig. 5.15: Mean EVM results for subcarriers at the edge and middle of the band and average EVM across all transmitted subcarriers in all the frames for a signal with 128 subcarriers.

Figures 5.16 and 5.17 show the variation with input power of the mean, median, skew and variance, for the signal with 512 subcarriers, for a subcarrier at the edge and the middle of the band respectively. It can be seen that the variance at the middle of the band is higher due to stronger distortion effects. The skew is also higher at the middle of the band where non ideal equalization effects are at a minimum and is therefore a result of the onset of distortion. Figures 5.18 and 5.19 show the same information but for a 4096 subcarrier signal. Similar trends for the variance and skew are observed in this case as well.

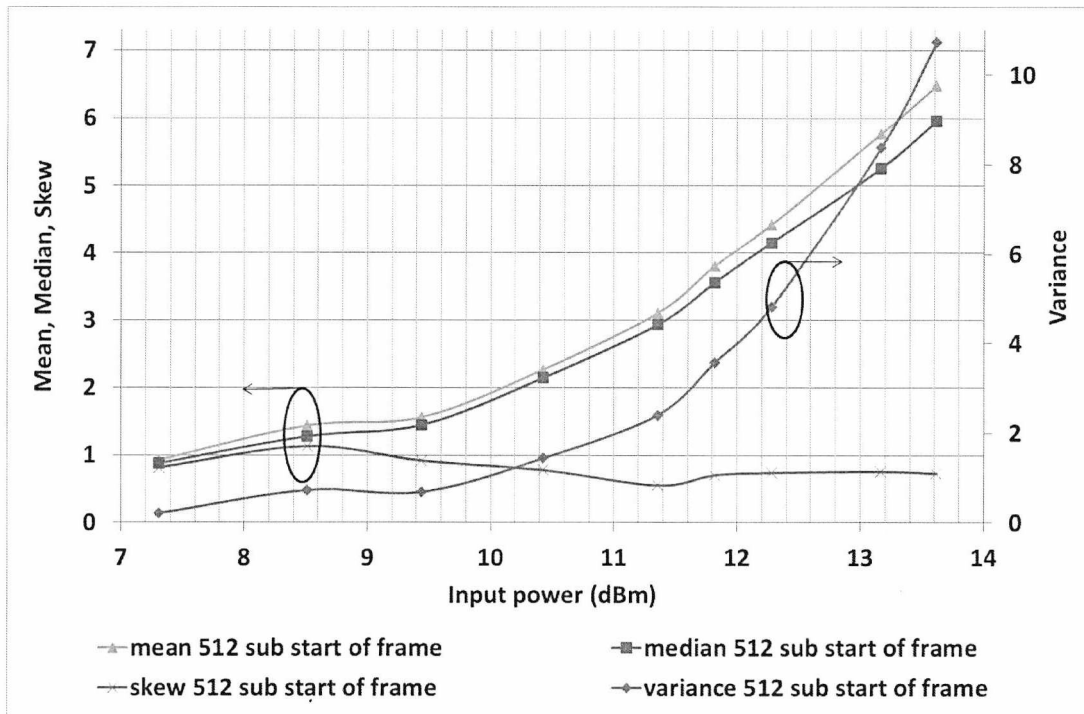


Fig. 5.16: Variation of four statistical measures (mean, median, variance and skew) with input power for a subcarrier located at the edge of the band for a signal with 512 subcarriers.

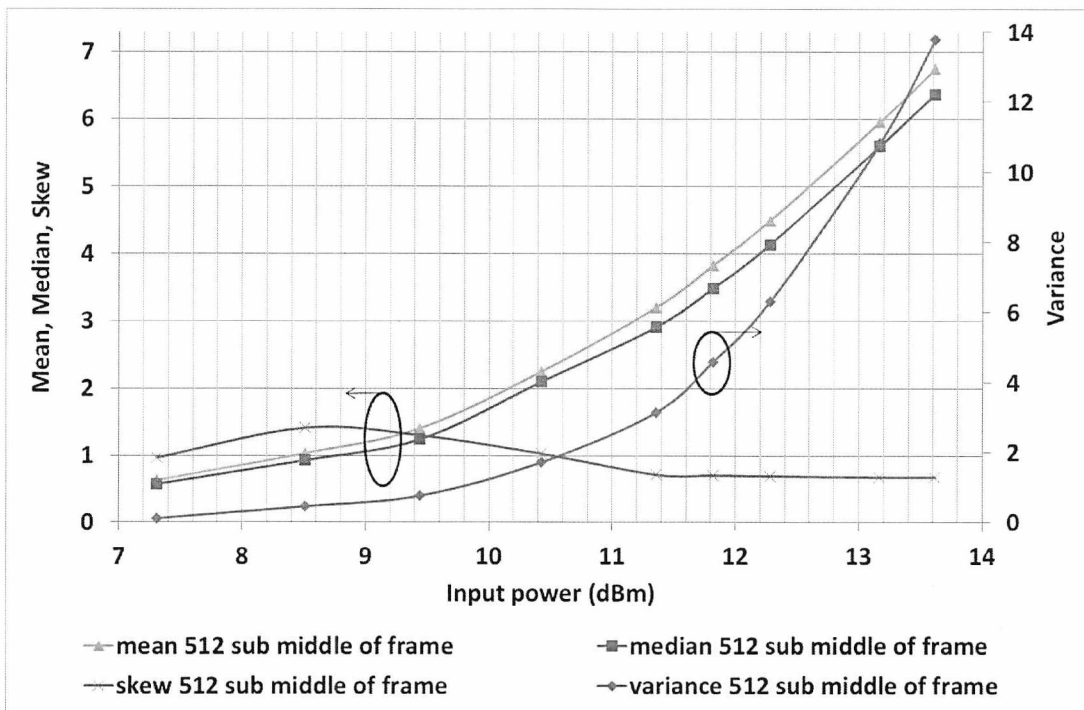


Fig. 5.17: Variation of four statistical measures (mean, median, variance and skew) with input power for a subcarrier located at the middle of the band for a signal with 512 subcarriers.

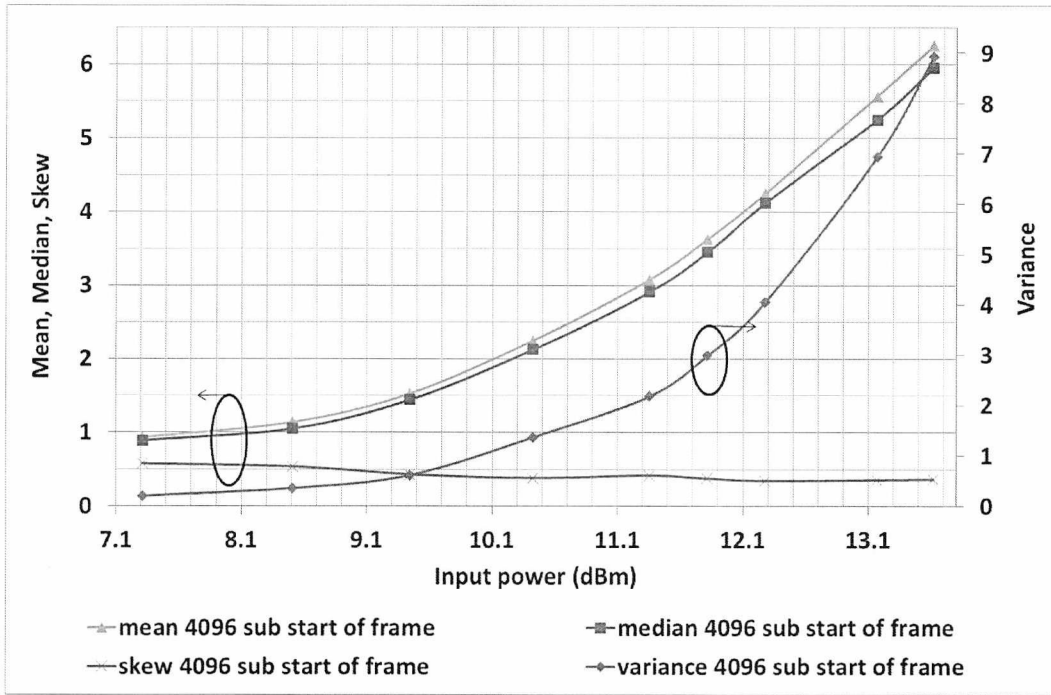


Fig. 5.18: Variation of four statistical measures (mean, median, variance and skew) with input power for a subcarrier located at the edge of the band for a signal with 4096 subcarriers.

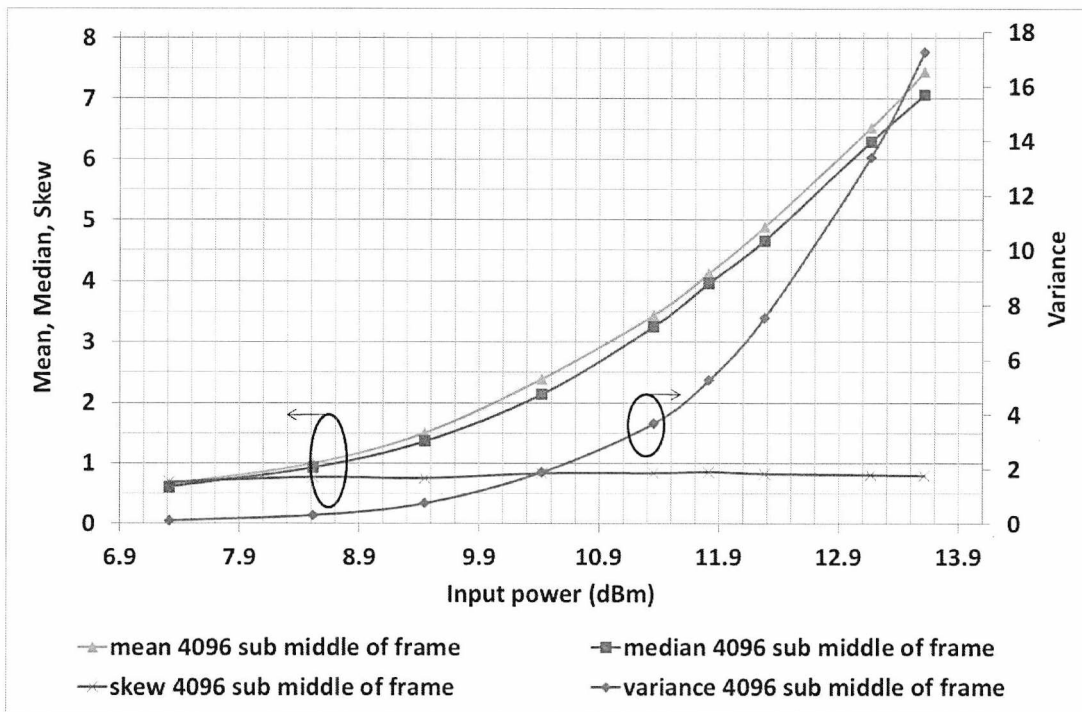


Fig. 5.19: Variation of four statistical measures (mean, median, variance and skew) with input power for a subcarrier located at the middle of the band for a signal with 4096 subcarriers.

5.5 Conclusions

It was shown how confidence interval analysis can be used to predict the proportion of EVM per frame values that will exceed some pre-defined EVM threshold. In the case where the EVM per frame follows a Gaussian distribution, this is straightforward as empirical confidence intervals for the Gaussian distribution can be used. This can be extended for the cases where the EVM per frame follows a log-normal distribution by log-transforming the EVM per frame values.

The worst case of EVM per frame variance (highest input power) is used to predict the number of OFDM frames required in the measurement in order to obtain an accurate estimate (within a well-defined confidence interval size) of the mean EVM. The required number of frames changes inversely proportionally with the number of subcarriers, assuming that the EVM per frame variance also changes inversely proportionally with number of subcarriers (which is close to the actual result, see Fig. 4.13). A number of 320 OFDM frames for 128 subcarriers is predicted for a 95 % confidence interval size of 0.31 %.

The EVM results for subcarriers at the edge and middle of the signal band show that distortion affects the subcarriers at the middle of the band to a stronger degree. The results also indicate that distortion wins over non ideal equalization and this occurs at a difference in input power between the different signals that is close in value to the difference in the median of their statistical PAPR.

6 Use of Companding for Radio over Fibre Links

6.1 Introduction

The transmission of OFDM signals through any nonlinear link requires good control of the signal levels and/or link components so that distortion is minimized. This is a particularly stringent requirement due to the nature of OFDM signals (and any multicarrier signal) which possess a large dynamic range. For direct IM-DD RoF links and short- to medium-reach applications (<20 km) the main source of distortion is the laser diode. A diagram of a directly modulated IM-DD RoF link is shown in Fig. 6.1. Here, RF signals from a base station directly modulate a laser diode. The intensity-modulated optical signal is then transmitted through an optical fibre to a RAU where it is directly detected by a PIN-PD. The RF signal exiting the PIN-PD is then amplified for transmission through the wireless channel. In the uplink direction the opposite processes take place. In the downlink direction, an attenuator is used before the laser diode to reduce the input signal powers to levels appropriate for the power handling capabilities of the laser diode.

Focusing on the downlink direction, in the case where the laser diode is overdriven either due to insufficient back-off or due to high peaks in the transmitted signals (much higher than the signal's average level), as in the case of OFDM transmission, distortion will occur, both in-band that will reduce the effective SNR, and out-of-band that may affect neighbouring channels

Note, that the amount of input power back-off and the amount of amplification required in the RAU are directly related. Backing-off the RF power prior to modulating the laser diode implies that more amplification will be required at the RAU in order to meet the targeted transmit power (based on the sensitivity requirements of the mobile units).

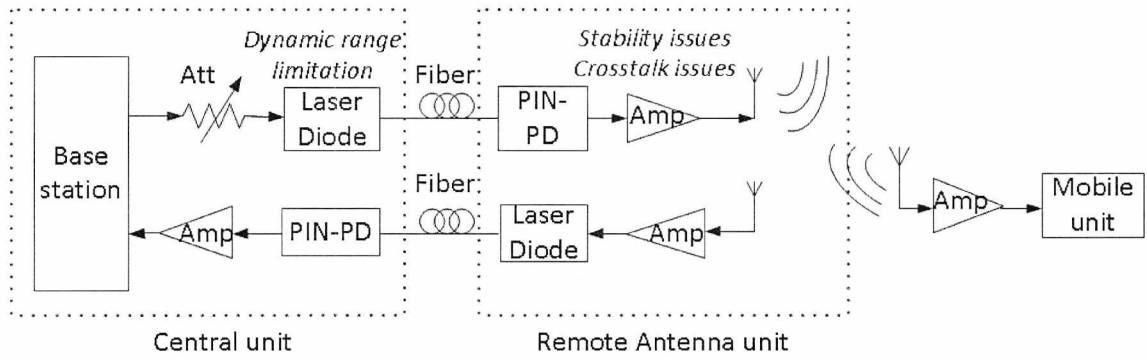


Fig. 6.1: Diagram of directly modulated IM-DD RoF architecture. Att: Attenuator, Amp: Amplifier, PIN-PD: PIN photodiode.

4th generation mobile systems in outdoor applications will require sufficient transmit power at the RAUs in order to achieve their desired wireless ranges (see for example [13, 14, 53]). Fig. 6.2 shows a simplified diagram of a Subcarrier Multiplexing (SCM) architecture similar to that proposed in the FUTON project [13, 14]. Here, channels at different subcarrier frequencies are power combined and then the combined RF signals directly modulate the laser diode. The channels are then separated at the RAU and typically amplified (not shown in Fig. 6.2) for transmission through a wireless channel. The amount of input power back off for these systems must be higher than that of a single channel system by a factor of n , where n is the number of multiplexed channels (this issue will be covered in Section 7.4). Therefore, the amplification requirements at the RAU will be even greater for such systems.

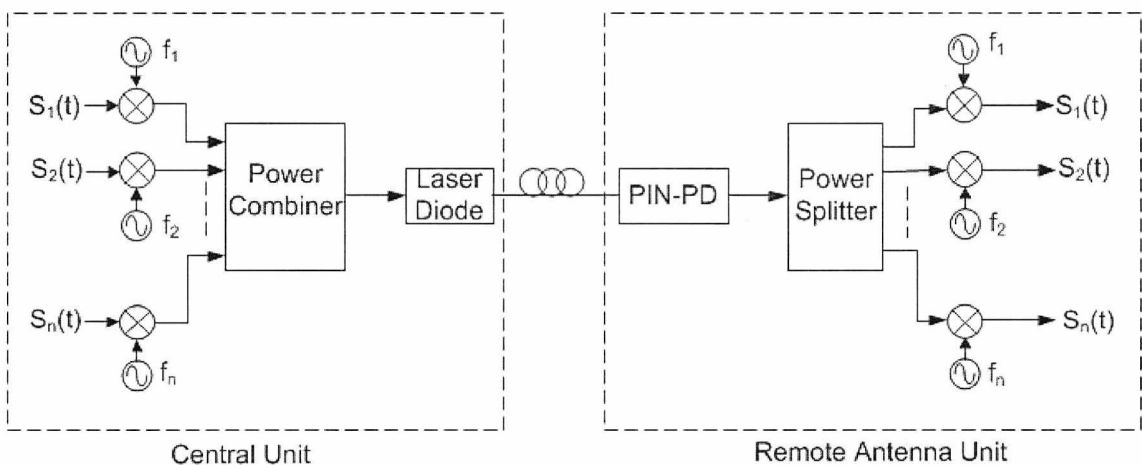


Fig. 6.2: Simplified diagram of SCM architecture.

Companding has been used to reduce the Peak-to-Average Power Ratio (PAPR) of OFDM signals [84-87]. Here, it is experimentally demonstrated how companding can be used to reduce the amplification requirements (and therefore the isolation requirements) in the RAU.

6.2 Amplifier stability and crosstalk issues

Two issues that are often overlooked in IM-DD RoF links are crosstalk and amplifier stability. These effects are shown conceptually in Fig. 6.3:

Issue 1: Power transmitted in the downlink antenna is received by the uplink antenna. In FDD systems, this can be filtered out. In TDD systems, in conjunction with the limited isolation between the laser diode and downlink amplifier ports, it can lead to oscillations [22].

Issue 2: Self-interference crosstalk exists due to finite isolation between the antenna and the input port of the downlink amplifier. Again, the self-interference signal can lead to oscillations [88].

The severity of these crosstalk issues depends on the amount of isolation in the relevant sections of the RAU that are affected by the crosstalk. In turn, the achievable isolation defines the maximum gain that can be provided by the amplifiers in the downlink and uplink sections of the RAU.

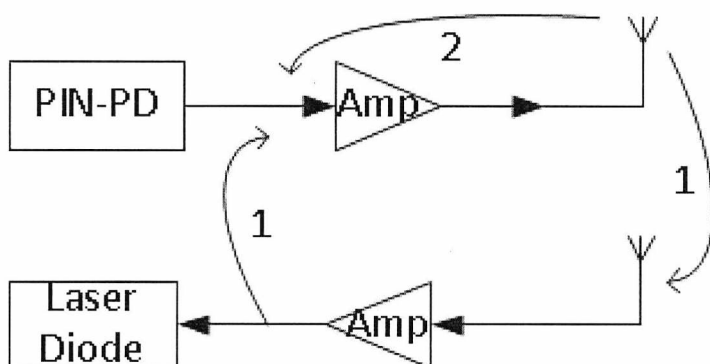


Fig. 6.3: RAU diagram showing the two issues discussed here.

In what follows, the effects of issue 2 on the signals transmitted on the downlink direction will be further analysed.

Fig. 6.4 shows a basic typical downlink RAU setup and the parameters (amplifier gain, photodiode RF power and crosstalk signal power) which affect the transmit power level. It is assumed that all of the components in Fig. 6.4 are impedance matched to each other.

The wanted and feedback crosstalk signal ratio, R , is given by:

$$R = \frac{P_{PD}}{R_{DL}} \quad (6.1)$$

where P_{PD} and R_{DL} are the wanted signal and unwanted self-interfering crosstalk signals at the photodiode output respectively, as illustrated in Fig. 6.4. The isolation, I , between the downlink antenna and the photodiode path to the input of the downlink amplifier with gain G_{DL} , is given by:

$$I = G_{DL}R. \quad (6.2)$$

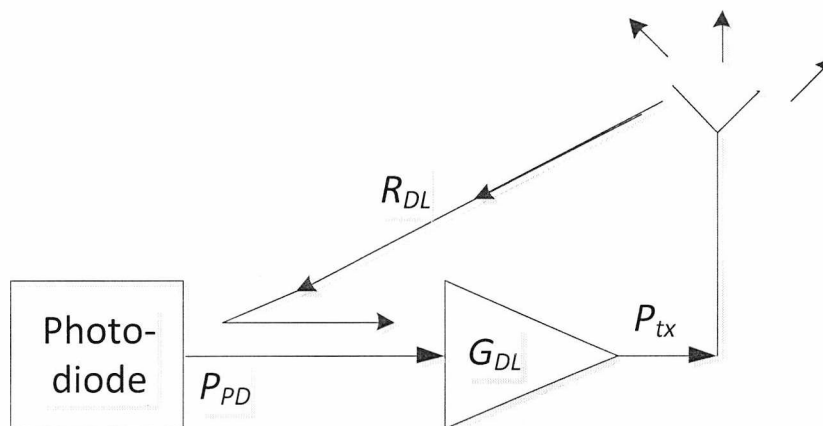


Fig. 6.4: Diagram of the downlink section of a RAU, showing how the crosstalk signal interferes with the signal exiting the PD.

The plot in Fig. 6.5 examines how the downlink signal power will behave for the two extreme cases of interference. The first case is when the interference is 180° out of phase with the signal exiting the PD resulting in a reduction in power. The second case is when the interference adds coherently with the signal exiting the PD resulting in an increase in power. Fig. 6.5 indicates that the best compromise for R is 10 dB (arbitrarily chosen by inspection) as the improvement achieved with higher ratios is negligible.

Fig. 6.6 shows the requirements for the downlink amplifier gain, G_{DL} , and isolation, I , between the antenna and the photodiode path to the downlink amplifier, as P_{PD} increases from -40 dBm towards 0 dBm. Two targeted RAU transmit powers have been assumed in Fig. 6.6, one at 20 dBm (medium power) and one at 30 dBm (high power). Note that I incorporates a targeted wanted and feedback signal ratio, R , of 10dB. The results of Fig. 6.6 indicate that in terms of logarithmic values both G_{DL} and I reduce linearly with increasing P_{PD} for both targeted transmit powers. Reduction of G_{DL} and I leads to less expensive RAUs in terms of less amplifiers and lower cost enclosures as RF shielding requirements are reduced.

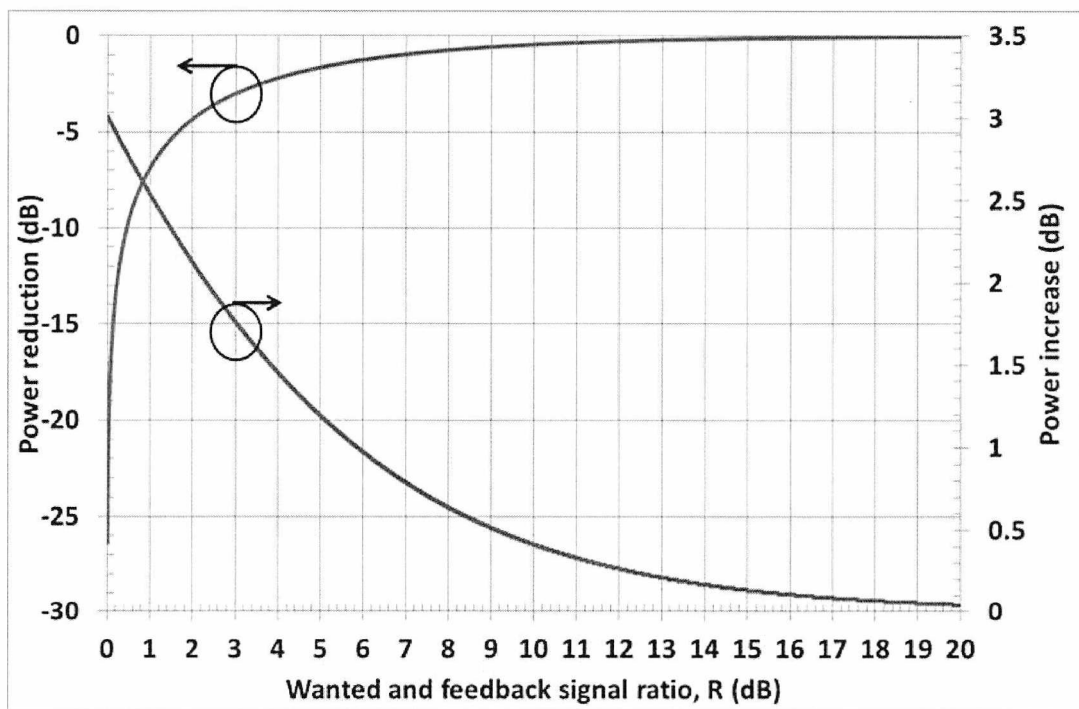


Fig. 6.5: Effect on downlink signal power in the presence of in phase and out of phase feedback crosstalk interference.

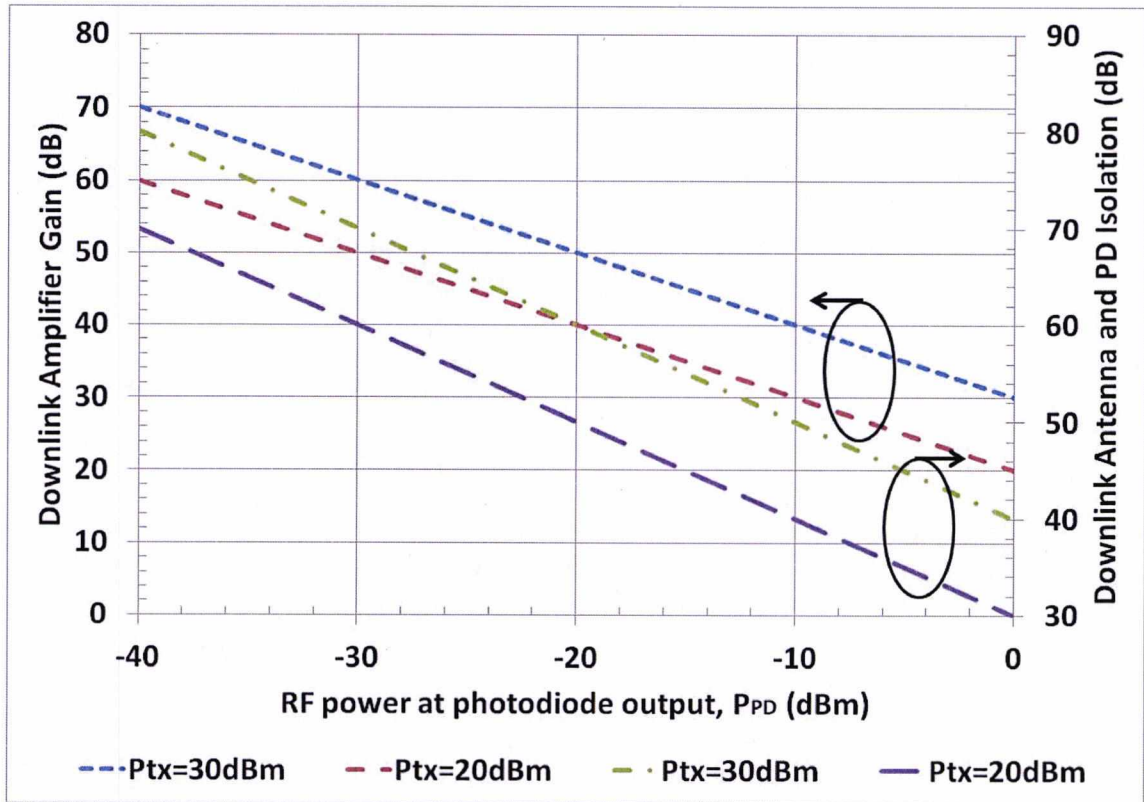


Fig. 6.6: Downlink amplifier gain and antenna/photodiode isolation requirements for different levels of RF power at the photodiode output for targeted RAU transmit powers of 20dBm and 30dBm. Antenna-PD isolation also incorporates a targeted wanted and feedback signal ratio (R) of 10dB. P_{PD} = RF power exiting photodiode.

6.3 Companding procedure

Companding is achieved by first compressing the signal before the nonlinear link and then expanding it at the receiver. While any form of companding function can be used for the application discussed here, as an example we demonstrate the use of μ -law envelope companding that is shown in Fig. 6.7. With this method, the baseband OFDM signal is first separated into its phase and magnitude components. Then, the magnitude is compressed by the μ -law function and the magnitude and phase components are re-combined before RF up-conversion. The opposite processes take place at the receiver. All the processes prior to RF up-conversion (and after RF down-conversion at the receiver) are carried out in a simulation environment in Matlab.

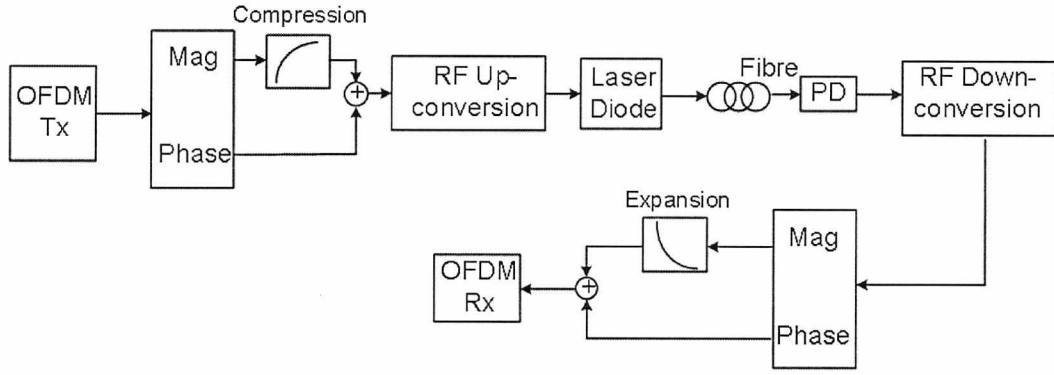


Fig. 6.7: Diagram of the RoF link showing the envelope companding process.

The compression function for μ -law envelope companding is given by [89, p.147]:

$$y(t) = V_{max} \frac{\ln\left(1 + \mu \frac{x(t)}{V_{max}}\right)}{\ln(1 + \mu)} \quad (6.3)$$

where $x(t)$ is the input signal, V_{max} is a normalization parameter and μ controls the amount of compression. The expansion function at the receiver will be the inverse of (3) given by:

$$x(t) = \frac{V_{max}}{\mu} \left[e^{\frac{y(t) \ln(1+\mu)}{V_{max}}} - 1 \right] = \frac{V_{max}}{\mu} \left[(1 + \mu)^{\frac{y(t)}{V_{max}}} - 1 \right] \quad (6.4)$$

Compression functions for different μ values are shown in Fig.6.8. It can be seen that smaller values of μ lead to lower amounts of expansion (or amplification) and a smoother transition into saturation.

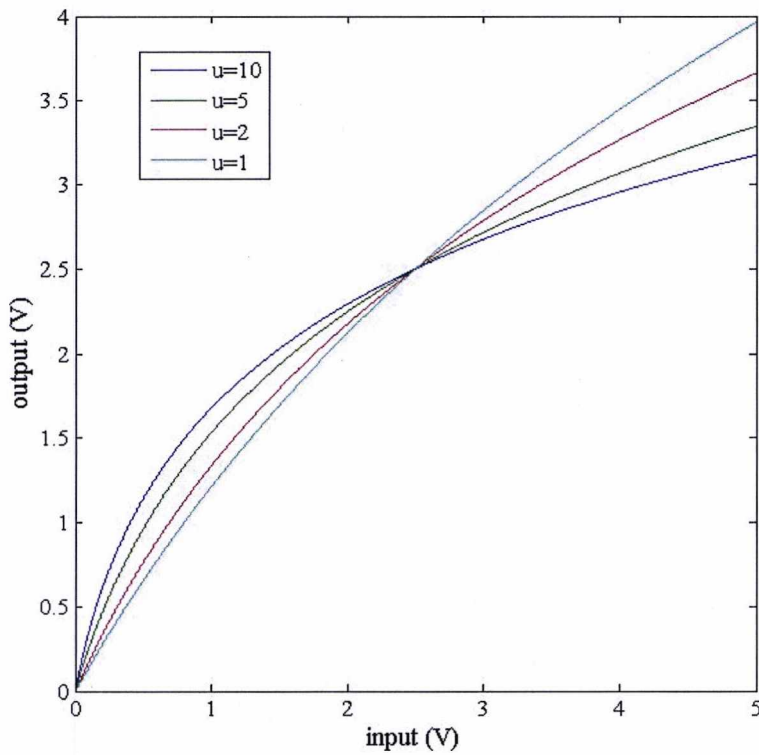


Fig. 6.8: Compression functions for different μ values.

Fig. 6.9 shows the different companding regimes based on the choice of the V_{max} value for any given μ value and the effect it has on the signal PAPR.

With regime 1, the V_{max} parameter in the compressor is set to a value that is equal to the maximum amplitude of the input signal. The compression function then, will leave the peak of the signal un-altered but will increase the lower amplitude levels, resulting in a reduction in PAPR.

With regime 2, the V_{max} parameter is set to a value that is higher than the maximum amplitude of the input signal. The compressor function then, will increase both the peak and the lower amplitude levels, but the latter by a higher amount. As a result, the PAPR will be reduced.

With regime 3, the V_{max} parameter is set to a value that is lower than the maximum amplitude of the input signal. The compressor function then, reduces both the peak and the lower amplitude levels, but the former by a larger amount, resulting in a reduction in PAPR.

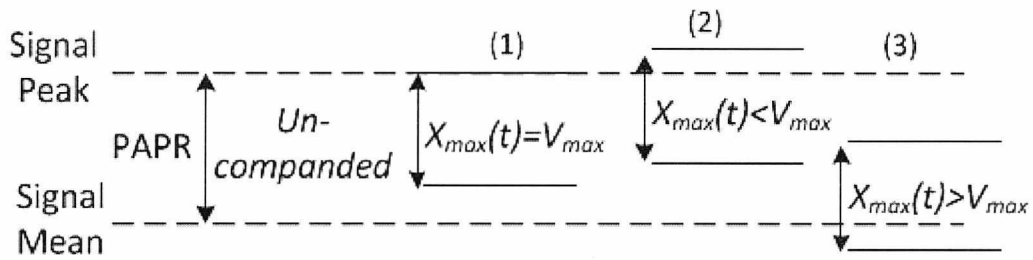


Fig. 6.9: Different companding regimes based on the choice of the V_{max} parameter for a given μ value. $x_{max}(t)$ is the maximum amplitude of the input signal and PAPR is the peak-to-average power ratio of the signal.

Note, however that the amount of change in the mean power of the signal at the output of the compression function will also depend on the μ value in some limiting cases (for example, if the V_{max} parameter is set to a value that is only slightly lower than the maximum amplitude of the input signal, then depending on the μ parameter the output power may not be lower than the input power).

Regime 3 might be of interest when the goal is to obtain a higher power at the output of the expander, as the initial mean power reduction at the compressor can be regained at the expander. However, this regime may lead to a reduction in the SNR.

Assuming a Rayleigh PDF with parameter σ for the input envelope signal, $r(t)$, the PDF at the output of the compressor, $p_R(r)$, will be given by:

$$p_R(r) = \frac{k}{\mu\sigma^2} e^{-\frac{k^2}{2\sigma^2}(1+\mu)\frac{r}{V_{max}}} \ln(1+\mu) \quad (6.5)$$

$$\text{where } k = \frac{V_{max}}{\mu} \left[(1+\mu)^{\frac{r(t)}{V_{max}}} - 1 \right].$$

The resulting PDF for different μ values is shown in Fig. 6.10.

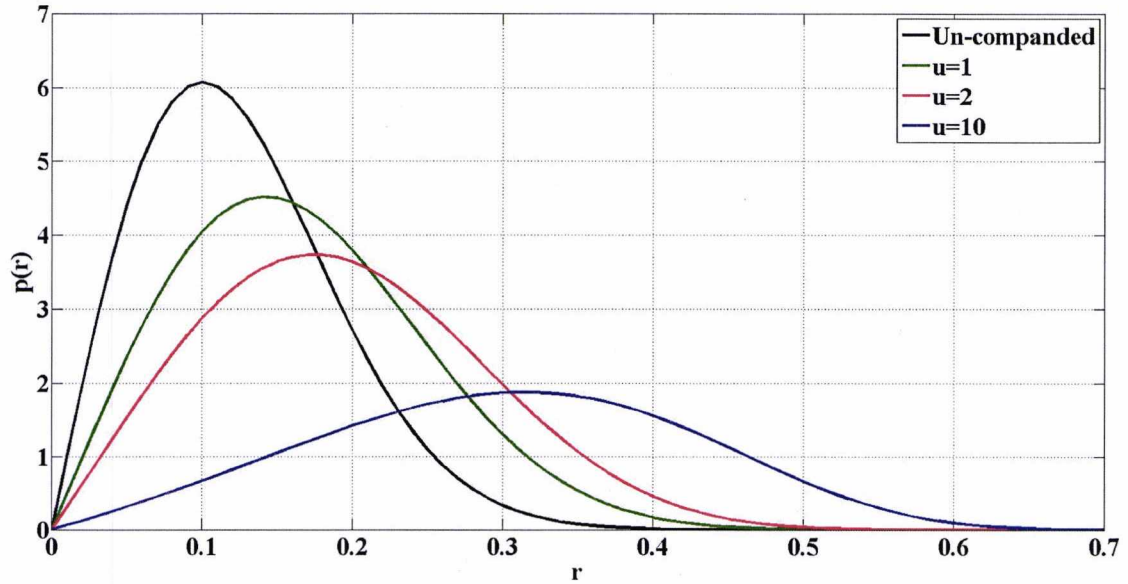


Fig. 6.10: Input and output PDFs for μ values of 1, 2 and 10 with $V_{max}=1$ and $\sigma=0.1$.

As the compression and expansion functions are inverse functions, if the channel has some gain, the expander V_{max} parameter needs to be normalized by the channel gain, otherwise the overall response (compression plus expansion) will be nonlinear. For example, if the channel has a gain, g , then the parameter in the expander should be V_{max}/g . If the parameter is normalized properly, the overall response will be linear but the mean output power from the expander will be scaled by the channel gain. In practical systems, the information about the channel gain will be available at the mobile units (for example through the use of pilot tones) so that the expander parameter can be adjusted. Another issue is bandwidth expansion that inevitably occurs with this compression function. One way to deal with this issue is to aim for smaller compression factors (and thus smaller PAPR reductions) and combine companding with different matching techniques (other than resistive) in the RoF link with the goal of obtaining the higher targeted signal powers at the output. Another option would be to filter the companded signal. But this technique would lead to a certain amount of distortion at the output of the expander that will depend on the amount of filtering applied, as the compression function with filtering will no longer be the inverse of the expansion function.

However, previous work has shown that bandwidth expansion caused by the companding function is not very high and relatively insensitive to the choice of the μ parameter [90].

6.4 Measurement procedure

Power sweeps have been carried out for the optical link with and without companding. Different companding regimes were used in order to investigate how the output power and optical link dynamic range are affected. This was done by using different values for the μ parameter. Fig 6.11 shows a flowchart of the measurement procedure. A user-defined 16-QAM OFDM signal in baseband was generated in Matlab-Simulink. The symbol rate of the signal was set to 9 MSps with a bandwidth of 10 MHz. The OFDM signal does not consist of any pilot symbols and the IFFT size is 1024 (840 data subcarrier and 184 nulls). An oversampling factor of 4 and cyclic prefix of 1/8 were used. An Agilent VSG was used to up-convert the companded OFDM signal to the appropriate carrier frequency. The up-converted signal was transported through an optical link consisting of an un-cooled Teradian DFB laser, 1 meter length of SMF patch-cord and an Appointech PIN-PD. An Agilent VSA was used to capture and down convert into baseband the OFDM signal exiting the photodiode. The down converted signal was saved as a Matlab data file for offline signal processing. The offline processing includes timing synchronization, companding expansion, blind equalization and blind frequency offset correction.

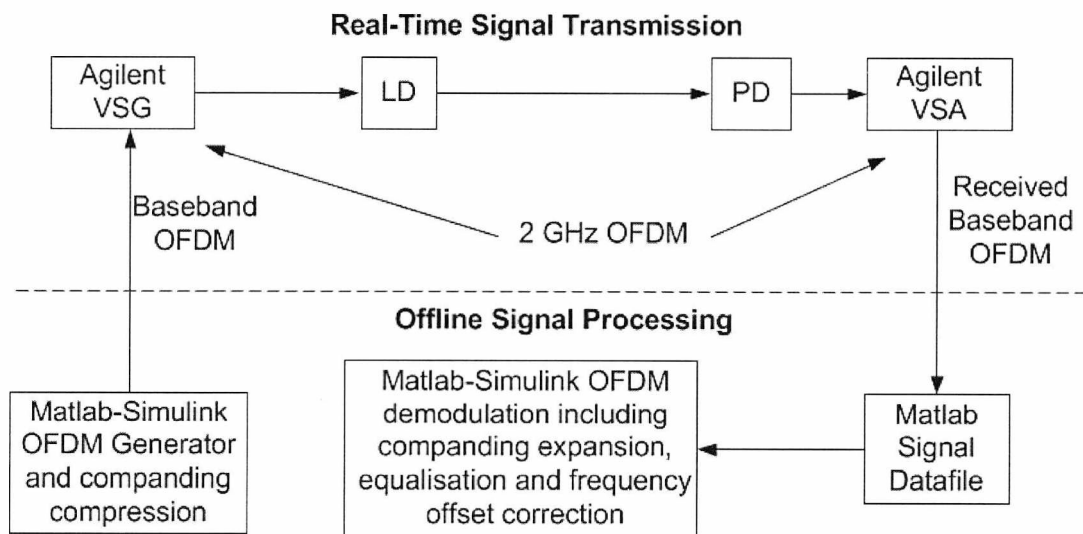


Fig. 6.11: Flow-chart of the measurement procedure. LD: Laser Diode, PD: Photodiode, VSG: Vector Signal Generator, VSA: Vector Signal Analyser.

6.5 Measurement Results

In the results that follow, a comparison is performed between the un-companded optical link and the link with companding in terms of the input and output powers of the RoF link. The measurements were carried out at a carrier frequency of 2 GHz. The PAPR of the baseband OFDM signal which consisted of 100 OFDM symbols was found in simulation to be 11.8 dB. The input P1dB of the laser at this carrier frequency was measured at 15 dBm. The input EVM for the optical link without companding started rising at an input power of approximately 3 dBm, that is, at around 12 dB lower than the P1dB of the laser diode.

Fig. 6.12 shows the EVM (% RMS) versus input power for the whole range of powers for different μ values with $V_{\max} = 1/4$. The corresponding PAPR values at the output of the compressor are shown in Table 6.1.

It is noted that for stronger compression the noise floor (low power range of EVM) is increased. This is due to the expander, expanding the noise added by the channel, in this case the optical link noise plus measurement equipment (VSA) noise. Also, for higher μ values, the EVM floor (range of lowest EVM) increases due to greater reduction in the mean power at the output of the compressor, as shown for regime 3 in Fig. 6.9, which leads to a reduction in the SNR.

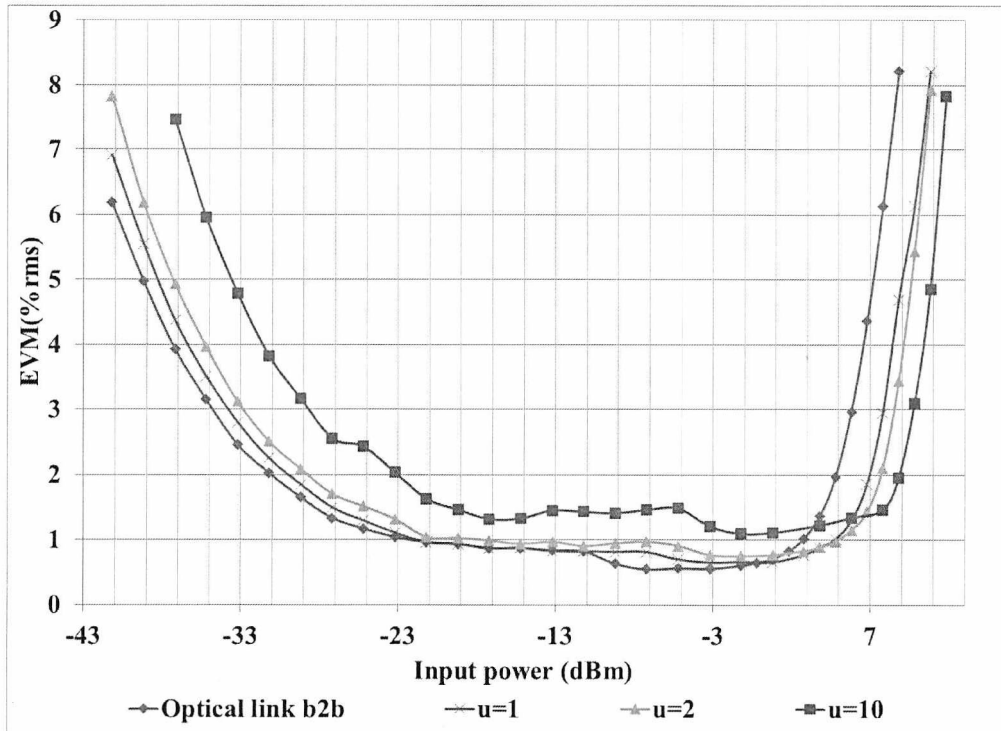


Fig. 6.12: EVM versus input power for $V_{\max} = 1/4$ and μ of 10, 2 and 1. Optical link b2b is the case without companding.

Table 6.1: PAPR values for different μ parameters when $V_{\max} = 1/4$. The PAPR of the uncompanded signal is 11.8 dB.

μ (for $V_{\max} = 1/4$)	PAPR (dB)
1	7.2
2	6.15
10	4

Fig. 6.13 shows the EVM (% RMS) versus output power measurement result for the range of high output powers. This is an important result, as it shows the amount of increase in the output RF power of the optical link for a given EVM value. Annotated in the plot are the resulting output power increases for the $\mu=10$ case at two different EVM transmitter requirements of 5.6% and 2%. The 5.6% requirement is based on the WiMAX transmitter specification for 16-QAM (see Table 2.3). The 2% requirement is not based on any standard but

simply assumes a transmitter with very stringent requirements. The resulting improvements in output power are approximately 4.7 dB and 4.9 dB respectively. Also annotated in the plot is the difference (in dB) in the output power between the $\mu=10$ and the un-companded cases at which the turning point (point where the EVM starts to rise quickly due to distortion) of the EVM occurs. This difference is approximately 7.6 dB which is close to the PAPR reduction value for $\mu=10$ (see Table 6.1). These results show that a given reduction in PAPR with companding does not translate directly to an equal increase in the high end of the dynamic range of the system, when this dynamic range is defined in terms of the EVM percentage limiting points.

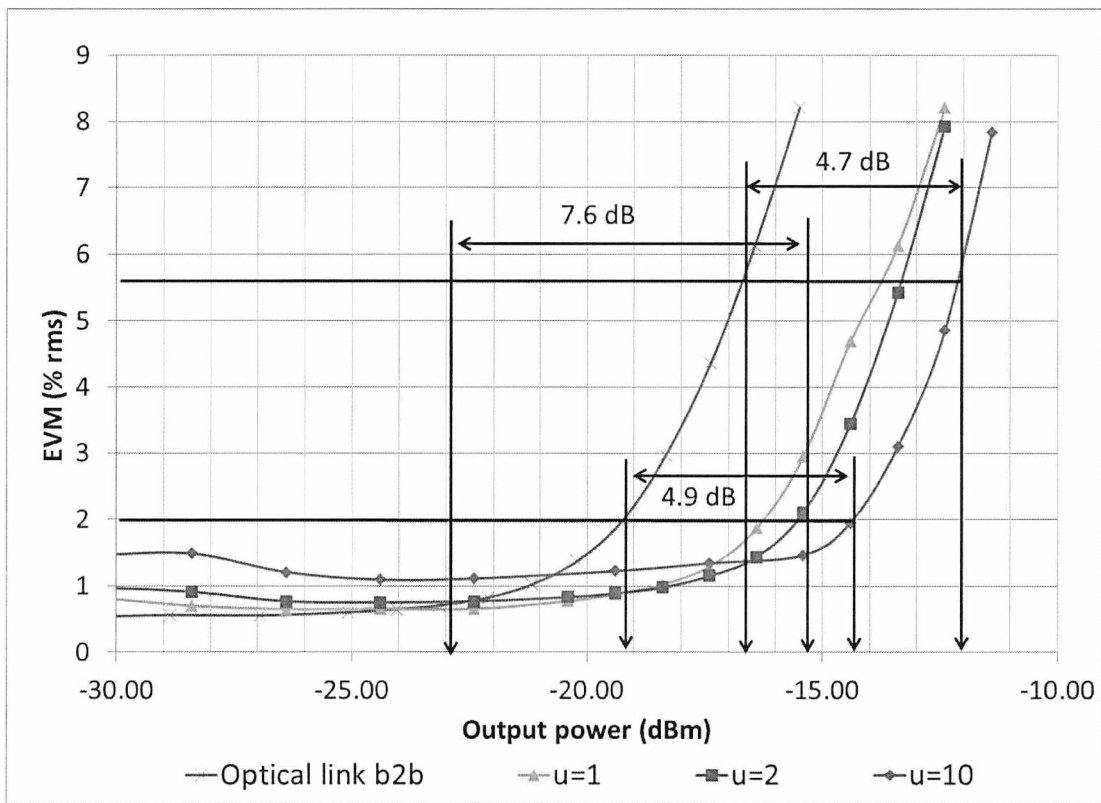


Fig. 6.13: EVM versus output power for $V_{\max} = 1/4$ and μ of 10, 2 and 1. Optical link b2b is the case without companding.

6.6 Conclusions

We have demonstrated the use of companding in a RoF link with the aim of reducing the amplification requirements (and therefore the isolation requirements) in the RAU. Different parameters in the companding function were used, showing the feasibility of using companding for obtaining higher powers at the output of the RoF link. The increase in output power means that the amplification (and isolation) requirements in the RAU decrease by an equal amount. In effect, through companding, the dynamic range of the link at the output is “transferred” to a range of powers more appropriate for meeting the potential transmit power requirements (based on the sensitivity requirements of mobile users). These requirements would otherwise need to be obtained through higher amplification (and therefore higher isolation) in the RAU.

7 Rate equation modelling

7.1 Introduction

The need for wide area coverage, high capacity and high bandwidth efficiency can be obtained with the use of Distributed Antenna Systems (DAS) that employ RoF techniques [21]. The use of Subcarrier Multiplexing (SCM) with direct intensity modulation of the laser diode and direct detection by the photodiode can provide the high capacity [54]. A modelling approach for such a system is beneficial as it can provide predictions for performance prior to actual experimental verification of the system. The major performance impairment in a RoF architecture comes from the laser diode itself. Unfortunately, modelling the behaviour of a laser diode in all its aspects can become quite problematic. Simple models based on the static behaviour cannot model dynamic effects that come from modulation. On the other hand, black box techniques for modelling the behaviour at specific powers and frequencies offer limited accuracy and cannot model the full extent of the dynamic behaviour arising from the intrinsic nonlinearity of the laser diode. A rate equation model [91-94], can model a large number of effects that take place inside the laser cavity. Again, though, rate equations are an abstraction of more complicated processes and for increased modelling capability there is an increase in the complexity of the model itself (e.g. travelling wave forms that can model non uniformities within the laser cavity). However, by using simpler forms of the rate equations [95], a balance can be found between complexity and the goal of obtaining a more accurate model for specific performance metrics of interest. The complexity of the model can be reduced by not modelling effects that are not critical for the envisaged application. An example of such an effect for a subcarrier multiplexed system operating at frequencies in the low microwave range and short to medium reach is fibre dispersion in conjunction with chirp. As a result of not taking into account chirp, phase modulation that results in laser linewidth enhancement can be ignored.

The major issue with fitting a rate equation model to measured performance results is the number of terms required to accurately match the measured characteristic of the device. Additionally, the coupled nature of rate equations means that usually any change in one parameter in order to improve the fit with the measured performance, will couple to another parameter resulting in oscillations in the result (or outcome) of the fitting process itself. There

are methods of grouping parameters together in order to simplify the fitting process [96]. In such cases, the fitting is done by adjusting a parameter that is given in terms of a number of intrinsic laser parameters. The goal in general is to reduce the number of parameters to ones that are directly extractable from simple (as possible) measurements [97-99].

Another approach is frequency response subtraction [100, 101], which is employed in order to remove bias independent effects that arise from parasitic elements from packaging.

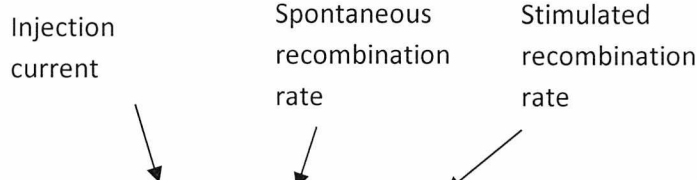
In this chapter, the approach of using a simple form of the rate equations is employed. Furthermore, the main focus is on matching the EVM measured behaviour. The aim is to see whether a simple rate equation system can adequately model the EVM performance at different carrier frequencies. This is done through a simple fitting process. Various mechanisms are neglected such as dispersion and chirp. The overall frequency response is obtained in a very simple and straight forward manner, by combining the intrinsic response of the laser diode with the response of electrical filters. The intrinsic response of the laser diode (resonance frequency and damping factor) is not made to fit; instead (through the intrinsic parameters that produce it) it is used as a “free” parameter for the fitting process.

Once the fit of the model with the measured performance has been obtained, the model is used to predict through a simulation process, the performance of a four-channel subcarrier multiplexed system transmitting 4th generation signals with bandwidths of 100 MHz and high-level modulation (256-QAM).

7.2 Rate Equations

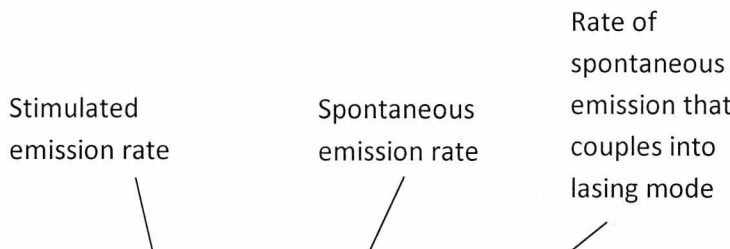
The behavior of the laser is characterized by a set of coupled differential equations which describe the interactions between carriers and photons in the laser cavity [92, 93]. The rate equations for single mode operation are given by:

Injection current
Spontaneous recombination rate
Stimulated recombination rate



$$\frac{dN}{dt} = \left(\frac{I}{eV}\right) - \left(\frac{N}{\tau_c}\right) - \left[\frac{v_g G_m(N)P}{(1 + \varepsilon P)}\right] \quad (7.1)$$

Stimulated emission rate
Spontaneous emission rate
Rate of spontaneous emission that couples into lasing mode



$$\frac{dP}{dt} = \left[\frac{\Gamma v_g G_m(N)P}{(1 + \varepsilon P)}\right] - \left(\frac{P}{\tau_p}\right) + (\beta\Gamma B N^2) \quad (7.2)$$

where N and P , are the densities (m^{-3}) of carriers and photons respectively in the active region, I is the injection current (A), τ_c (s) is the carrier lifetime, τ_p (s) is the photon lifetime, v_g (ms^{-1}) is the group velocity, e is the charge of the electron (C), V is the active region volume (m^3), Γ is the confinement factor, ε is the gain compression factor (m^3) and B is the spontaneous radiative recombination coefficient (m^3s^{-1}).

The term $G_m(N)$ describes the dependence of the material gain on the carrier density (see Fig. 7.1). Above the transparency point, the material gain dependence can be approximated by a linear dependence given by $\alpha(N-N_0)$, where α (m^2) is the differential gain which describes the change of the material gain per unit of length with respect to the carrier density, N .

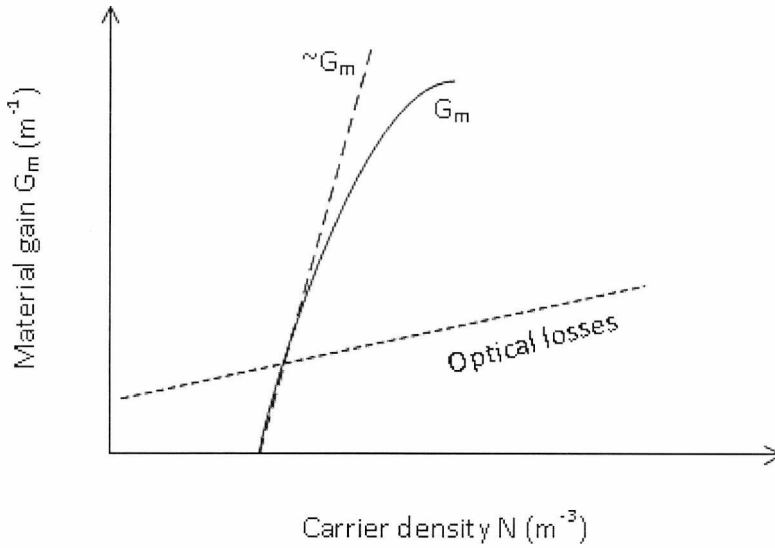


Fig. 7.1: Dependence of material gain to carrier density. Above transparency, the dependence is approximately linear.

The term $1/(1+\varepsilon P)$ describes the gain compression at high photon densities. The term N/τ_c describes the spontaneous recombination rate (this includes spontaneous recombinations that result in both radiative and non-radiative processes) and is given by [93]:

$$\tau_c = (A_{nr} + BN + CN^2)^{-1} \quad (7.3)$$

where A_{nr} is the non-radiative coefficient and C is the Auger coefficient. The term β in (7.2) is a coefficient which describes the proportion of spontaneous recombinations that result in emissions that add coherently to the stimulated light.

The term P/τ_p describes the rate at which photons are lost from the laser cavity per unit time and the term τ_p is the time constant of the exponential decrease in the power of the photons in the cavity. For FP laser diodes, it is given by [93]:

$$\tau_p = L \left[v_g \left(L\alpha_{int} + \log_e \frac{1}{R} \right) \right]^{-1} = [v_g(\alpha_{int} + \alpha_m)]^{-1} \quad (7.4)$$

where L (m) is the cavity length, α_{int} (m^{-1}) is the absorption and scattering loss in the cavity material, α_m (m^{-1}) is the facet (or mirror) loss and from the above equation it is deduced that:

$$\alpha_m = \frac{1}{L} \log_e \frac{1}{R} \quad (7.5)$$

where R is the reflectivity of the end facets, assuming $R = R_{left} = R_{right}$.

As the carrier density builds up due to the external pump source (for semiconductor lasers this will be a current source), the gain changes from a negative to a positive value (see Fig. 7.1). At this point (transparency point) population inversion is achieved: stimulated emission wins over absorption and the material exhibits gain. However, the gain must exceed the cavity material loss α_{int} (only a portion of which is due to absorption) and the facet loss (α_m) for lasing to occur.

7.2.1 Steady state conditions

Under steady state conditions, $dN/dt = 0$. From (7.1):

$$\frac{dN}{dt} = 0 = \left(\frac{\bar{I}}{eV} \right) - \left(\frac{\bar{N}}{\tau_c} \right) - \left[\frac{v_g \alpha (\bar{N} - N_T) \bar{P}}{(1 + \epsilon \bar{P})} \right] \quad (7.6)$$

At threshold we can assume that $\bar{P} \approx 0$. Therefore, the following balanced expression results:

$$\left(\frac{I_T}{eV} \right) \approx \left(\frac{\bar{N}}{\tau_c} \right) \quad (7.7)$$

where I_T is the threshold current.

Therefore, the injection current rate is almost equal to the spontaneous recombination rate.

For some current \bar{I} where, $\bar{I} > I_T$, from (7.2) we can write $dP/dt=0$:

$$\frac{dP}{dt} = 0 = \left[\frac{\Gamma v_g \alpha (\bar{N} - N_T) \bar{P}}{(1 + \epsilon \bar{P})} \right] - \left(\frac{\bar{P}}{\tau_p} \right) + (\beta \Gamma_B \bar{N}^2) \quad (7.8)$$

Assuming that $\beta \approx 0$ (this assumption is justified as above threshold the spontaneous emission rate is very small compared to the stimulated emission rate) and $\epsilon=0$, the following expression is deduced:

$$\Gamma v_g \alpha (\bar{N} - N_T) \bar{P} \approx \left(\frac{\bar{P}}{\tau_p} \right) \quad (7.9)$$

Therefore, the stimulated emission rate is almost equal to the rate of photon loss.

From (7.9) we can also deduce that:

$$\bar{N} \approx (\tau_p \Gamma v_g \alpha)^{-1} + N_T \quad (7.10)$$

Therefore the carrier density, \bar{N} , above threshold is approximately constant and independent of the photon density.

Since the material gain is proportional to the carrier density (above the transparency point), it follows from (7.10), that the gain increases linearly with the bias current until lasing occurs and the gain remains almost constant thereafter.

The output power from the laser facet above threshold is given by [94]:

$$\overline{P_{out}} = \frac{n_d h \nu_g}{e} (\bar{I} - I_T) \quad (7.11)$$

where n_d is the external quantum efficiency (fraction of photons that escape from the mirrors) and h is Planck's constant.

7.2.2 Dynamic effects

The response of the laser under small signal modulation can be described by treating the input signal as a form of harmonic perturbation superimposed on the bias. The angular resonance frequency can be approximated by [93-95]:

$$\omega_r = \sqrt{\frac{\Gamma \nu_g a}{eV} (\bar{I} - I_T)} \quad (7.12)$$

Large signal modulation will result in various terms in (7.1) and (7.2) (that in a small signal analysis are assumed to have negligible effect) that cause harmonic and intermodulation distortion. There are a multitude of mechanisms that take part in distortion creation. For a brief overview of many of these effects see [102].

7.3 Laser modelling

The coupled rate equations are inherently non-linear, requiring the use of numerical solutions (5th order *Runge-Kutta* algorithm in the case of VPI). However, simpler expressions that can aid the modelling process are obtained under steady state and small signal conditions as was shown from (7.7) to (7.10). These expressions can give an insight into which parameters can be adjusted to fit the model to the measured data.

From (7.7) the threshold current (I_T) will be given by:

$$I_T \approx \bar{N}eV \left(\frac{1}{\tau_c} \right) \quad (7.13)$$

And thus the threshold current is approximately inversely proportional to the carrier lifetime, and can be fitted by adjusting τ_c .

From (7.6) and (7.7), for a bias current \bar{I} where $\bar{I} > I_T$, and assuming $\varepsilon=0$, we can write:

$$\bar{J} = \left(\frac{\bar{N}}{\tau_c} \right) + v_g a (\bar{N} - N_T) \bar{P}$$

where $\bar{J} = \bar{I}/eV$.

Now, from (7.7) we can substitute \bar{N}/τ_c for J_T , and from (7.9) $\alpha(\bar{N}-N_T)\bar{P} = \bar{P}/(\tau_c\Gamma)$ and solve for $\Delta\bar{J}$ where $\Delta\bar{J} = \bar{J} - J_T$:

$$\Delta\bar{J} = \frac{\Delta\bar{P}}{\tau_p\Gamma}$$

Now, substituting back for \bar{J} :

$$\frac{\Delta\bar{P}}{\Delta\bar{I}} = \frac{\tau_p\Gamma}{eV} \quad (7.14)$$

Therefore the slope efficiency is approximately proportional to the photon lifetime, τ_p , and can be fitted by adjusting τ_p and the confinement factor Γ .

The photon lifetime, τ_p , cannot be directly calculated from the effective mirror loss of the DFB laser, as this information is not available. Instead, the photon lifetime will be inserted directly as a parameter into the model.

The resonance frequency under small signal modulation is fitted using equation (7.12).

Using expressions (7.12)–(7.14) the static and dynamic responses are matched to the measured performance. The static response determines the DC gain and the static nonlinearity that results from clipping due to signal excursions below the threshold current and compression at high powers due to device heating and carrier leakage (Fig. 7.2). The dynamic response determines the AC gain and the intrinsic laser nonlinearity (Fig. 7.3). The important thing to note here is that the intrinsic response is “masked” by parasitic packaging filtering. Based on this effect, it is not critical to match the intrinsic response which can now be used (indirectly through other intrinsic parameters) as an additional “free” parameter for the fitting process. In other words, once the static response has been fit, the EVM response in the nonlinear region is made to fit by adjusting the intrinsic response. This is also important as certain mechanisms that affect the static nonlinearity are not modelled, such as device heating and carrier leakage. The overall response is obtained through the use of external electrical filters. Additional mechanisms that are not modelled include carrier transport delays and spatial hole burning (the latter is modelled to some extent by a nonlinear gain coefficient, only).

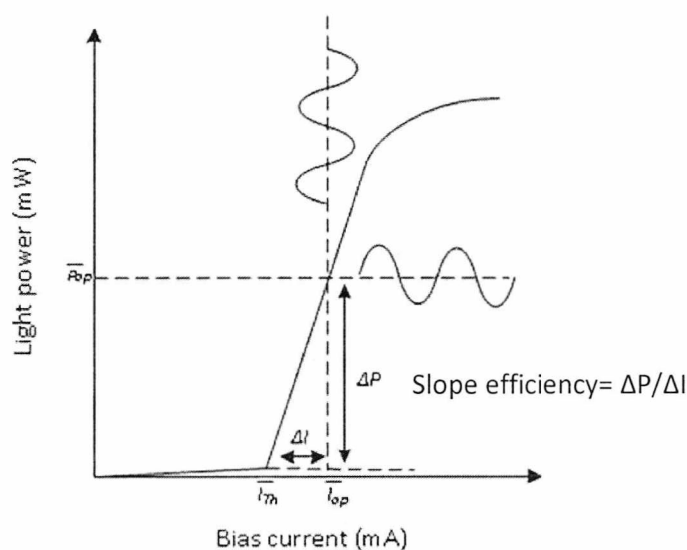


Fig. 7.2: Example of laser diode static response showing the two parameters that are fit: threshold current and slope efficiency.

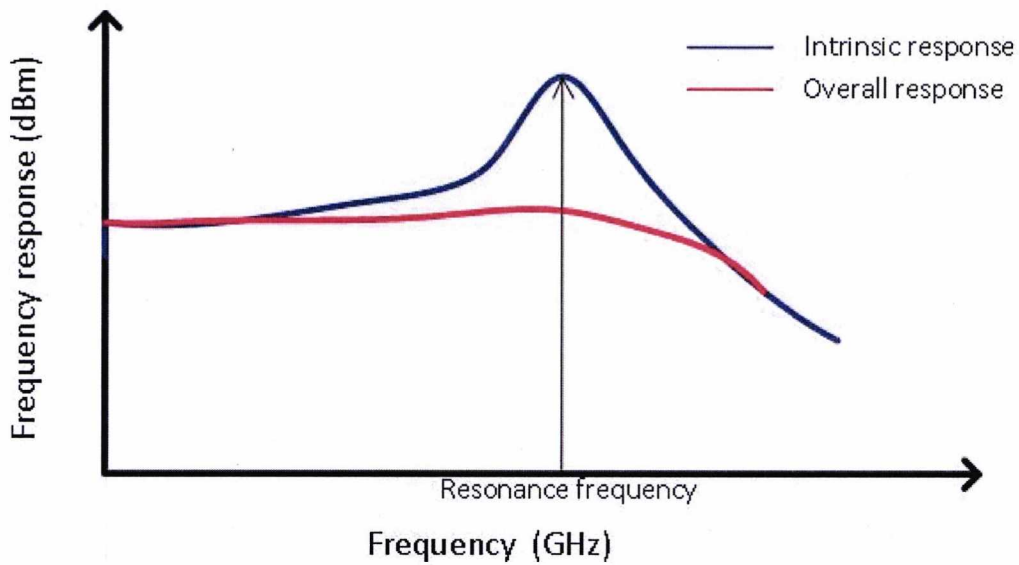


Fig. 7.3: Example of laser diode dynamic response showing how the intrinsic response is “masked” by parasitic packaging filtering.

Thus, the fitting process is divided into the following main steps:

1. Fit static response (slope efficiency, threshold current)
2. Coarsely Fit frequency response (laser intrinsic, packaging parasitics):

Intrinsic response is not critical and can be used as a fitting parameter.

3. Simulate EVM performance

If fitting needs improvement re-adjust step 2. Once fitting is adequate, resume to step 4.

4. Simulate P1dB: not-critical
5. Simulate 2-tone test: 2nd order distortion also important

7.3.1 Model results

The threshold current of the laser diode was measured between 7 mA and 7.5 mA at various instances (temperature effects etc., may cause variations) while the measured slope efficiency was between 0.116 W/A and 0.124 W/A. The measured and modelled P-I characteristics are

shown in Fig. 7.4. For the model the parameters are 7.2 mA for the threshold current and 0.12 W/A for the slope efficiency.

Table 7.1: Parameters used for the modelling of the DFB laser diode.

Parameter	Value	Units
Optical coupling efficiency	0.23	
Differential gain	6e-20	m ²
Carrier density (transparency)	2.9e24	m ⁻³
Confinement factor	0.15	
Group effective index	3.5	
Right facet reflectivity	0.3	
Photon lifetime	3.8	ps
Carrier lifetime	3	ns
Spontaneous emission factor	1e-4	
Nonlinear gain coef. (Tucker)	6e-23	m ³

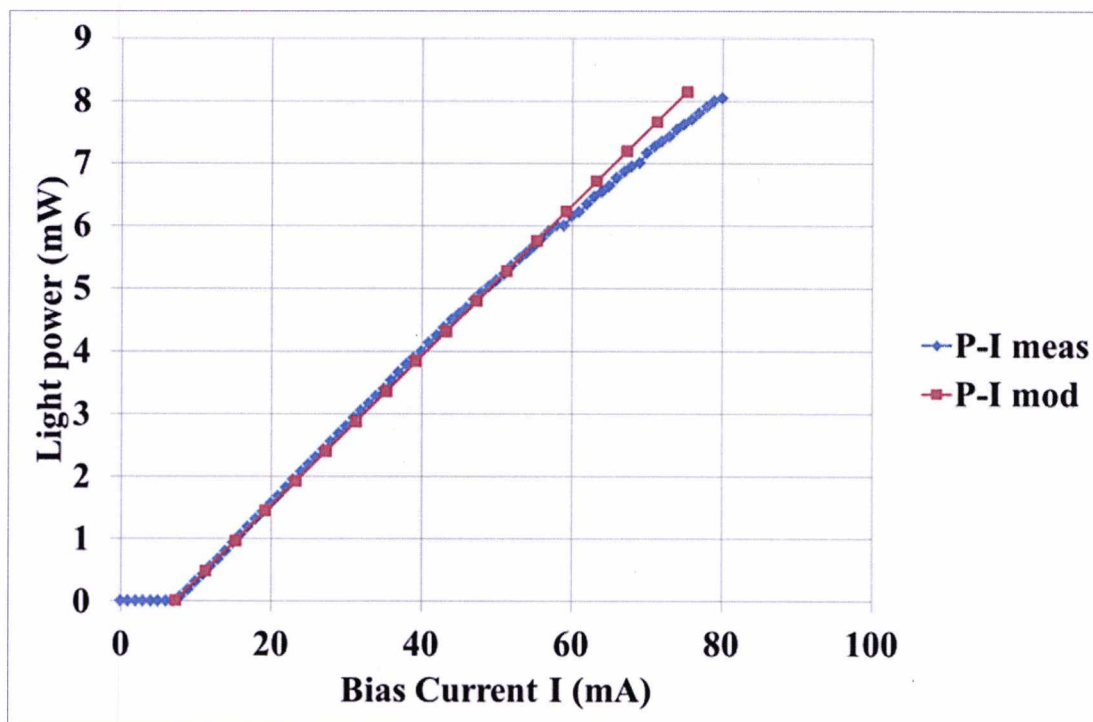


Fig. 7.4: Modelled and measured P-I characteristics (output light power versus input bias current).

The measured frequency response exhibits various dips due to electrical effects that make the matching of the modelled response more difficult. The modelled and measured frequency responses are shown in Fig. 7.5. The various dips in the response are attributed to the parasitic device packaging impedances. The modelled response does not attempt to model these sharp discontinuities in the electrical behaviour, but instead models the overall frequency roll-off by using electrical filter models prior to the intrinsic laser rate equation model. Two low-pass Bessel filters are used. One is a low order filter with a lower cut-off frequency, used in order to match the slow roll-off prior to the resonance frequency point. The second is a higher order filter, with a higher cut-off point to match the sharp roll-off after the resonance frequency point. The sharp discontinuities in the response could potentially cause a problem as, depending on the equalization technique, they might not be fully rectified, although, the use of OFDM means that smaller coherence bandwidths can be tolerated (depending on the number of OFDM subcarriers). The discontinuities, can also lead to unequal input power distribution between the IF channels. The source of these frequency effects are the packaging parasitics and this has been verified through a frequency subtraction technique [100] the result of which is shown in Fig. 7.6.

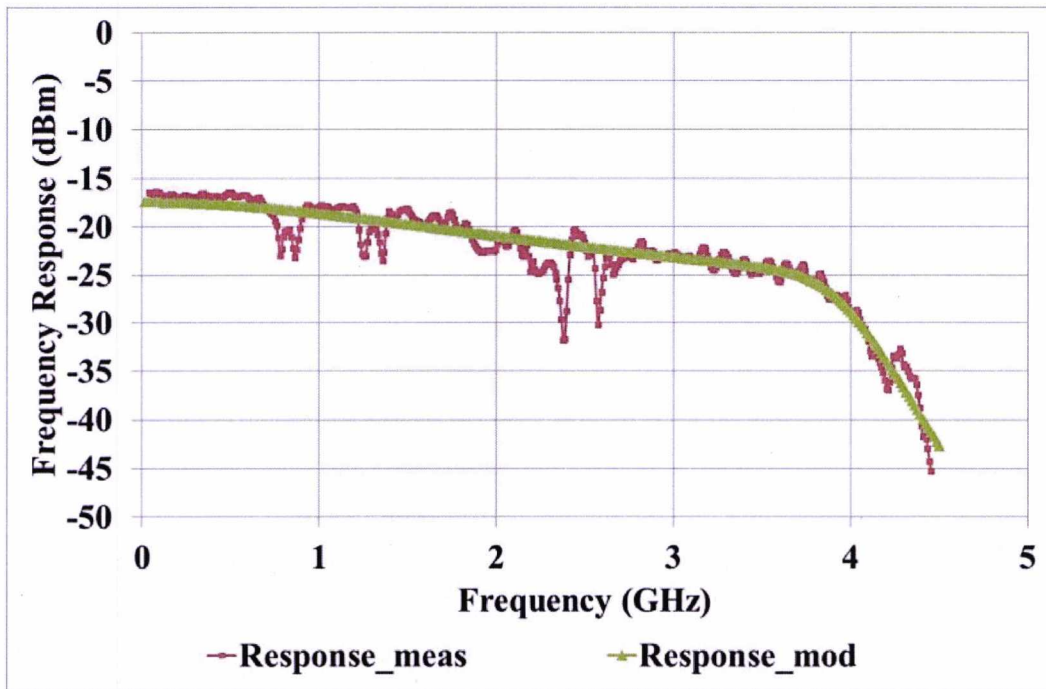


Fig. 7.5: Measured and modelled frequency responses at a bias of 40 mA.

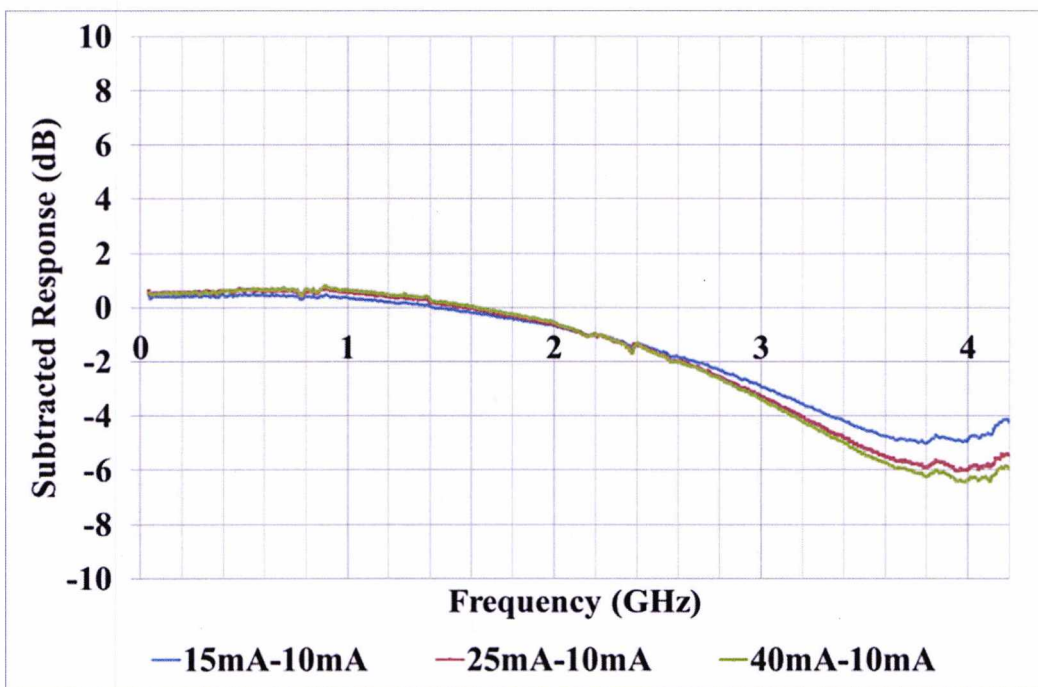


Fig. 7.6 : Subtracted frequency responses obtained by subtracting the response at 10 mA bias current from the responses at 15 mA, 25 mA and 40 mA bias currents.

P1dB measurements and simulations were carried out at the four subcarrier frequencies. A 10 dB optical attenuator was used during the measurements to emulate fibre and additional channel losses (splices, connectors etc.). The results of the simulations at two frequencies are shown in Fig. 7.7 and Fig. 7.8 while a summary of the results is shown in Table 7.2.

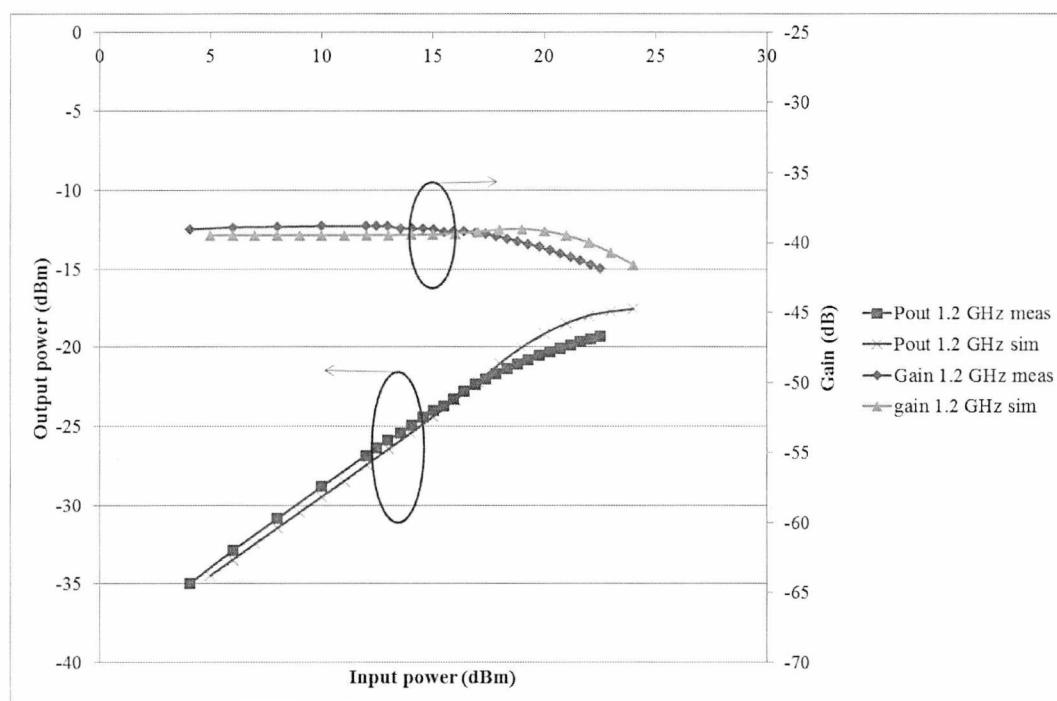


Fig. 7.7: Measured and modelled P1dB results at 1.2 GHz.

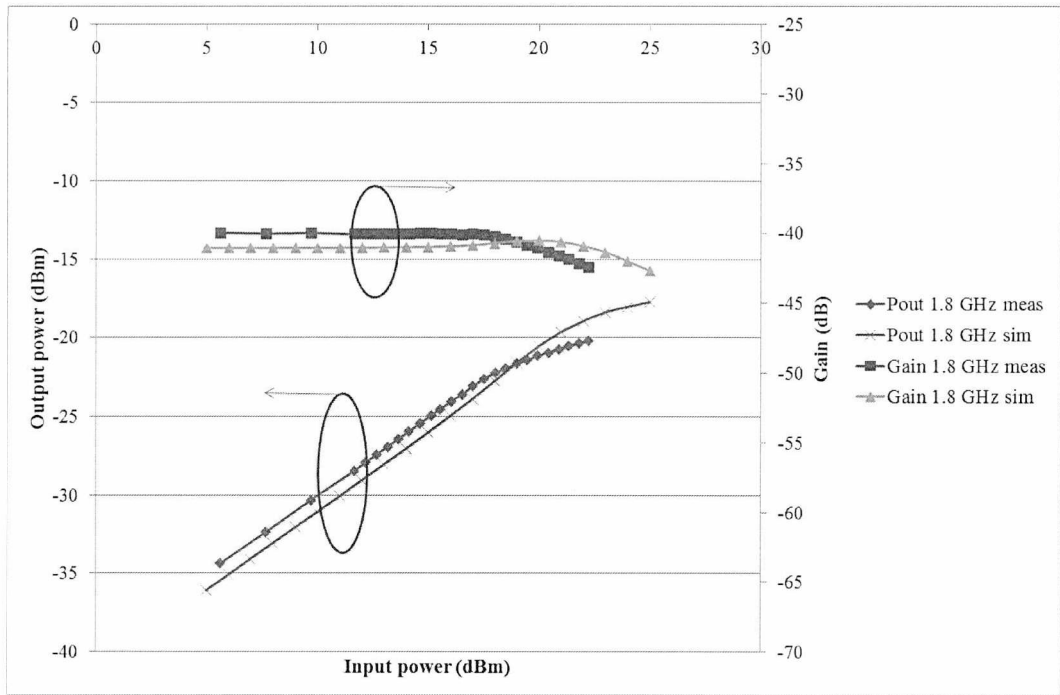


Fig. 7.8: Measured and modelled P1dB results at 1.8 GHz.

Table 7.2: Summarized results for measured and modelled P1dB results at 1.2 GHz, 1.4 GHz, 1.6 GHz and 1.8 GHz.

Frequency/ GHz	Measured 1 dB comp. point/ dBm	Modelled 1 dB comp. point/ dBm
1.8	20	23
1.6	19.5	22.5
1.4	19.3	22.2
1.2	19.6	22

The difference between measured and modelled P1dB at 1.2 GHz was 2.4 dB, while at 1.8 GHz the difference was at 3 dB. Differences between simulated and modelled results may be due to the variations in the laser diode frequency response that will have an effect on the P1dB (as they will affect the signal coupled into the laser), and as was stated previously, the finer detail in the frequency response has not been modelled.

A 2-tone simulation was also carried out to examine the match between measured and modelled intermodulation distortion. The frequencies of the two tones were set at 1.8 GHz and 1.801 GHz. The agreement was good for both second and third order nonlinearities (Fig. 7.9). The measured and modelled results are summarized in Table 7.3.

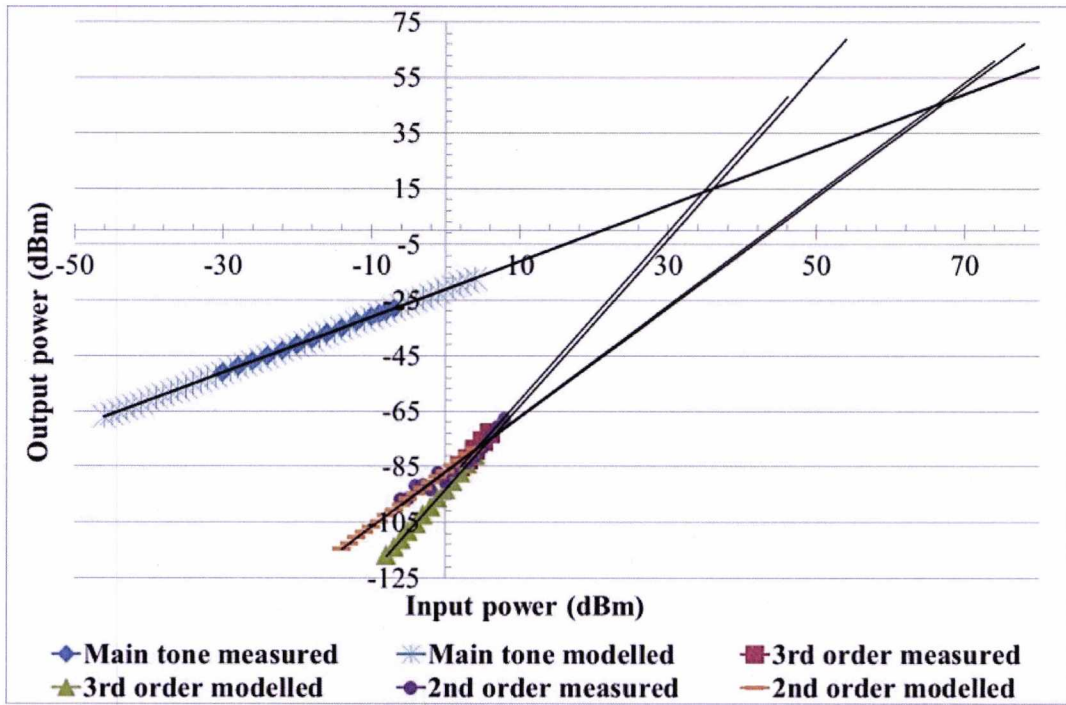


Fig. 7.9: Modelled and measured 2-tone test results with overlaid linear trend lines (dark traces) for intercept point estimation. The main tone frequency is at 1.8 GHz. Note that for these results no optical attenuation was used as it was found that in this way the measurement results were more stable. The effect of a 10 dB optical attenuator would be to reduce the OIP₃ by 20 dB while the IIP₃ would remain the same.

Table 7.3: Summarized results for 2-tone test at 1.8 GHz. (M) stands for Model and (E) stands for experiment, IIP stands for Input Intercept Point and OIP stands for Output Intercept Point.

	IIP ₃ /dBm	OIP ₃ /dBm	IIP ₂ /dBm	OIP ₂ /dBm
1.8 GHz (M)	36	15	66	45
1.8 GHz (E)	34.8	14.1	68	47.5

7.3.2 Model validation with EVM 802.11g measured results

EVM versus input power simulation results were obtained at the four channel frequencies. These measurements were used for validating the model but were also part of the design iteration process for the model. That is, EVM was also used in the adjustment and estimation of the model parameters. The signal in the simulations consisted of a single RF carrier modulated by a 64 subcarrier OFDM signal with a CP of 0.25 and square-root-raised cosine filtering with a roll-off factor of 0.5. The measurements were performed with an 802.11g signal with the same parameters. The laser was biased at 40 mA. The set-up for the simulation is shown in Fig. 7.10 and Fig. 7.11, with Fig. 7.11 showing the actual set-up in the simulator environment.

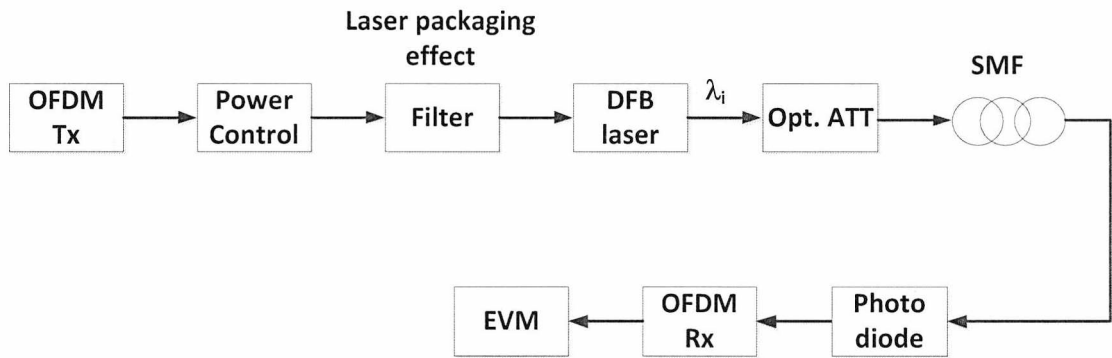


Fig. 7.10: Set up for single channel 802.11g simulations in VPI (note that some blocks that were used during simulation have been omitted to simplify the diagram).

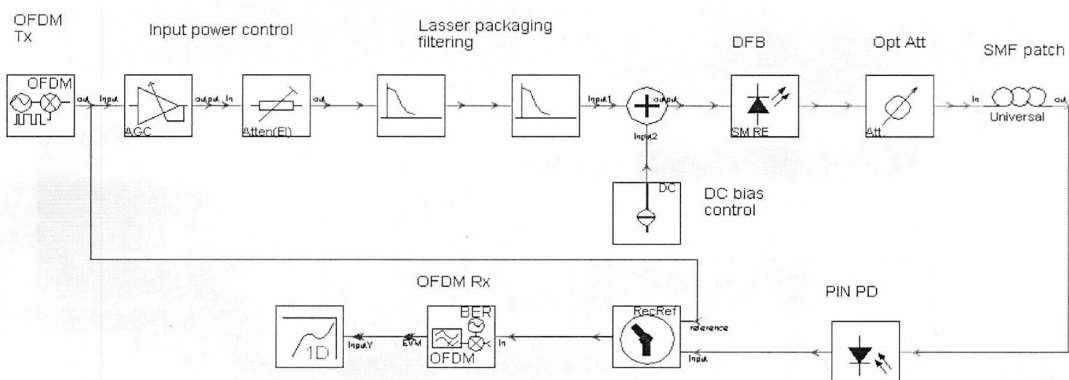
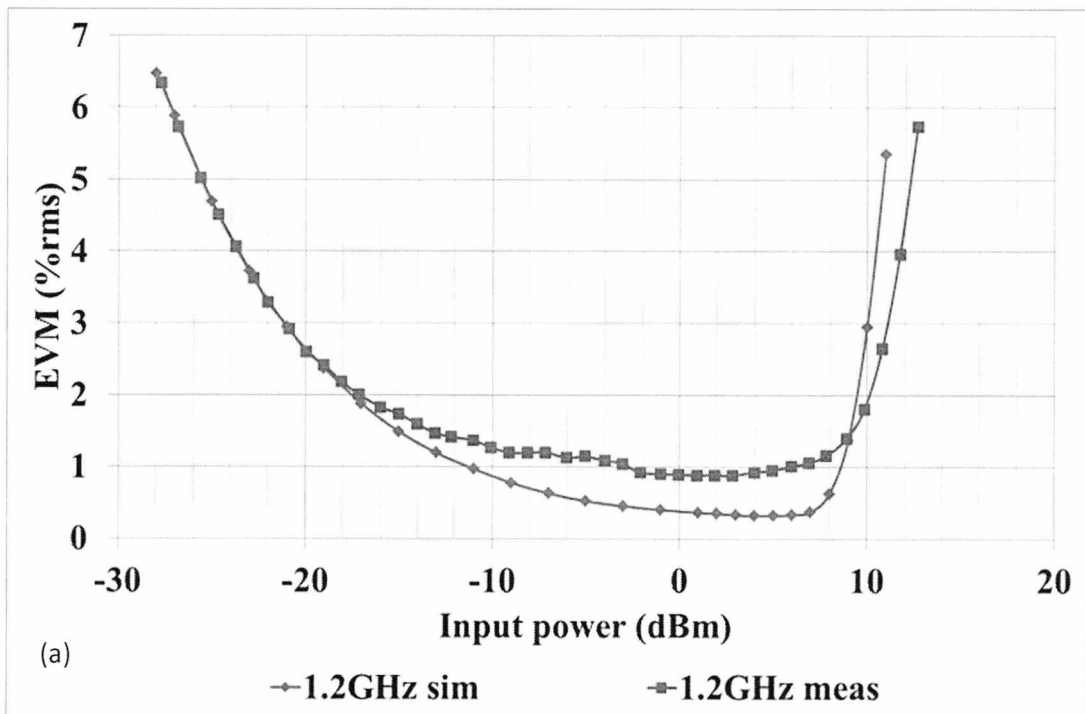


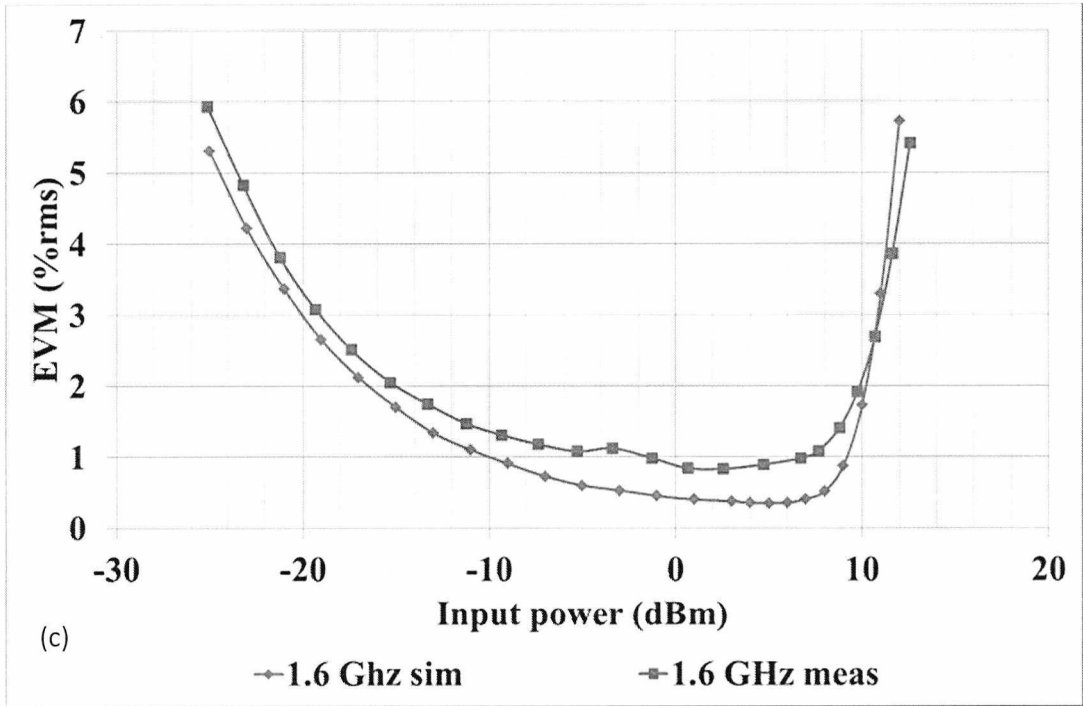
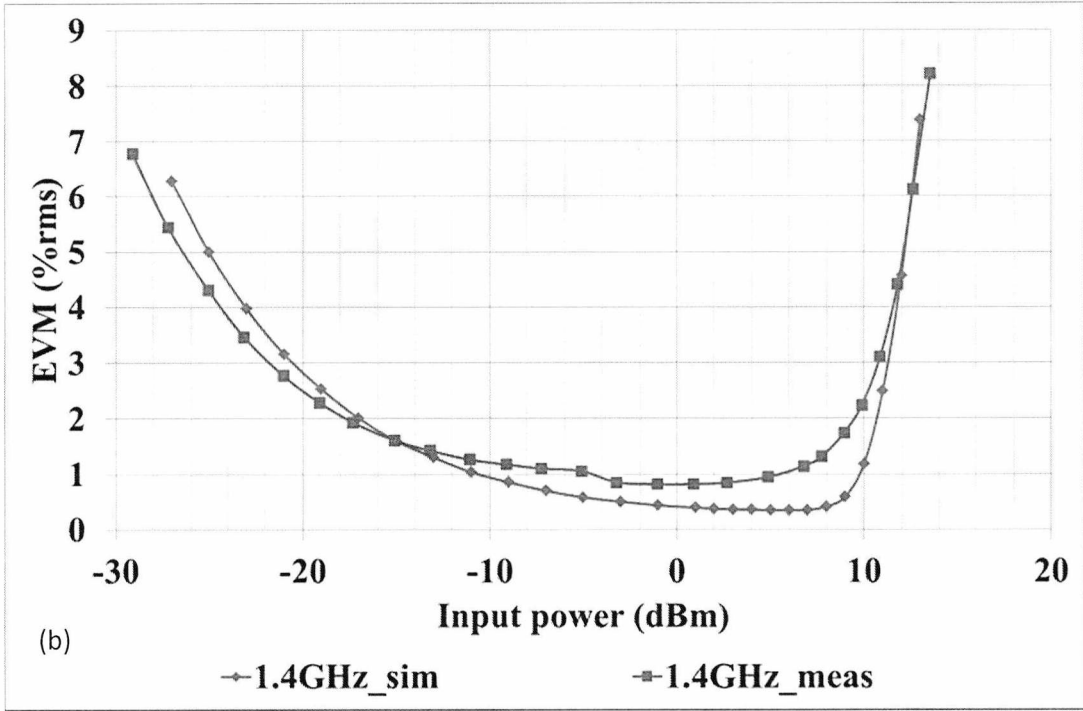
Fig. 7.11: Set up for single channel 802.11g simulations in VPI.

The target application envisages fibre lengths of up to 10 km [54]. A 10 dB optical attenuator was used to emulate fibre attenuation and additional channel losses (splices, connectors etc.). Although this does not take into account fibre dispersion (particularly in conjunction with laser chirp), separate experiments with 802.11n (40MHz bandwidth) signals at higher modulation rates and with up to 20km of fibre [103] and simulations with varying lengths of fibre in [104] both confirm that fibre dispersion has negligible effect at such signal frequencies and bandwidths.

The results for the simulated EVM rise slightly faster than the experimental measurements, as shown in Fig. 7.12. This may be due to the shape of the nonlinearity itself after the onset of saturation. The matching at the low power end of the EVM curves shows some variation with frequency. This may be due to differences between modelled and measured frequency responses, and variations in the frequency responses of components used during the measured EVM versus input power sweeps (e.g. amplifiers). Note that the transmitter noise

floor is not modelled and this is the reason for the differences in the EVM values between the measured and simulated results in the range of very low EVM. Modelling the EVM response in this region is not important as it mainly depends on transmitter noise and therefore, particular measurement equipment can be expected to give different results in this range. It can be modelled in a straight forward manner by adding a noise source prior to the modelled link. But here, focus is given to the regions limited by receiver noise (and components following the optical link) and by distortion.





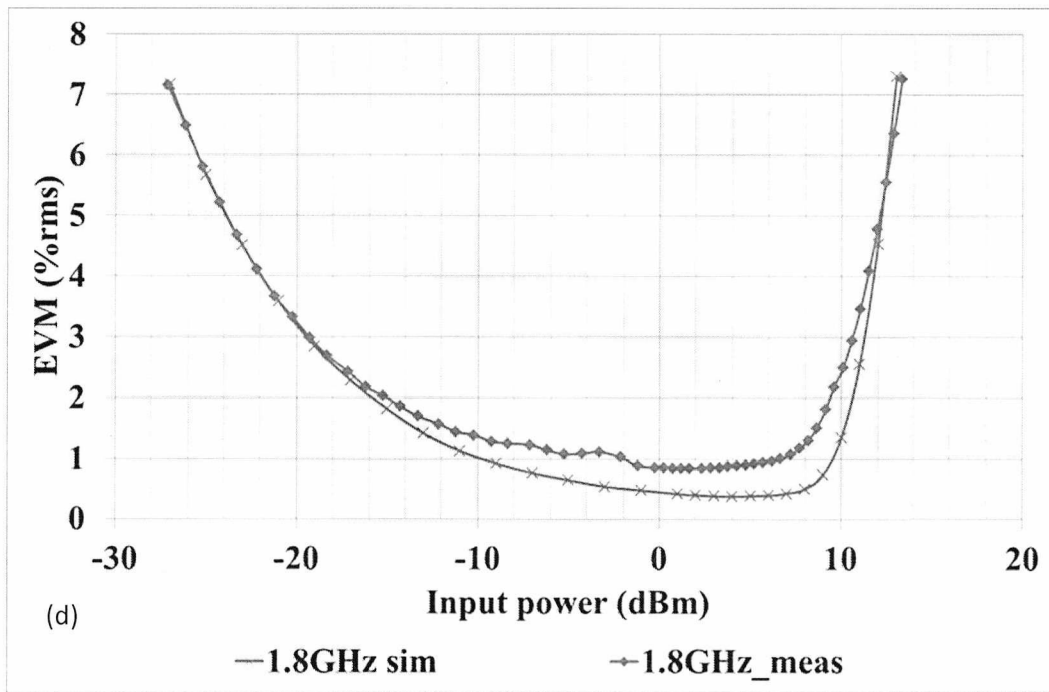


Fig. 7.12: Measured and modelled EVM results at carrier frequencies of (a) 1.2GHz, (b) 1.4 GHz, (c) 1.6 GHz and (d) 1.8 GHz.

7.3.3 Model validation with EVM 802.11n measured results

The 802.11n signal possesses a bandwidth of 40 MHz. The simulation set-up is the same as the one used for the 802.11g simulations in Section 7.3.2.

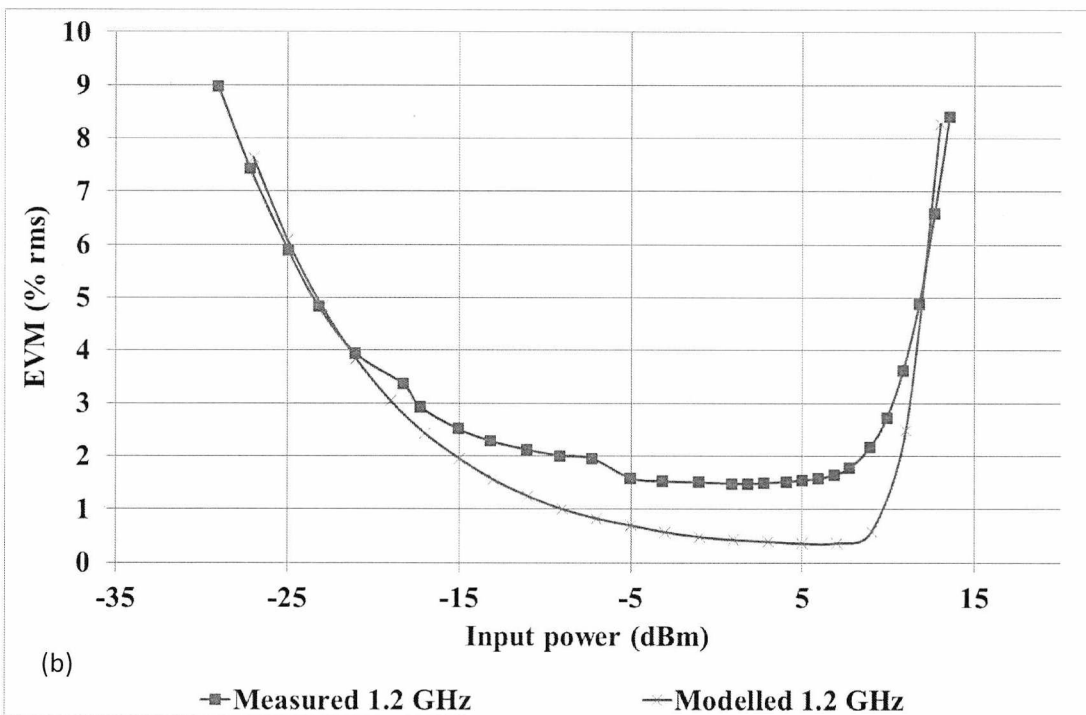
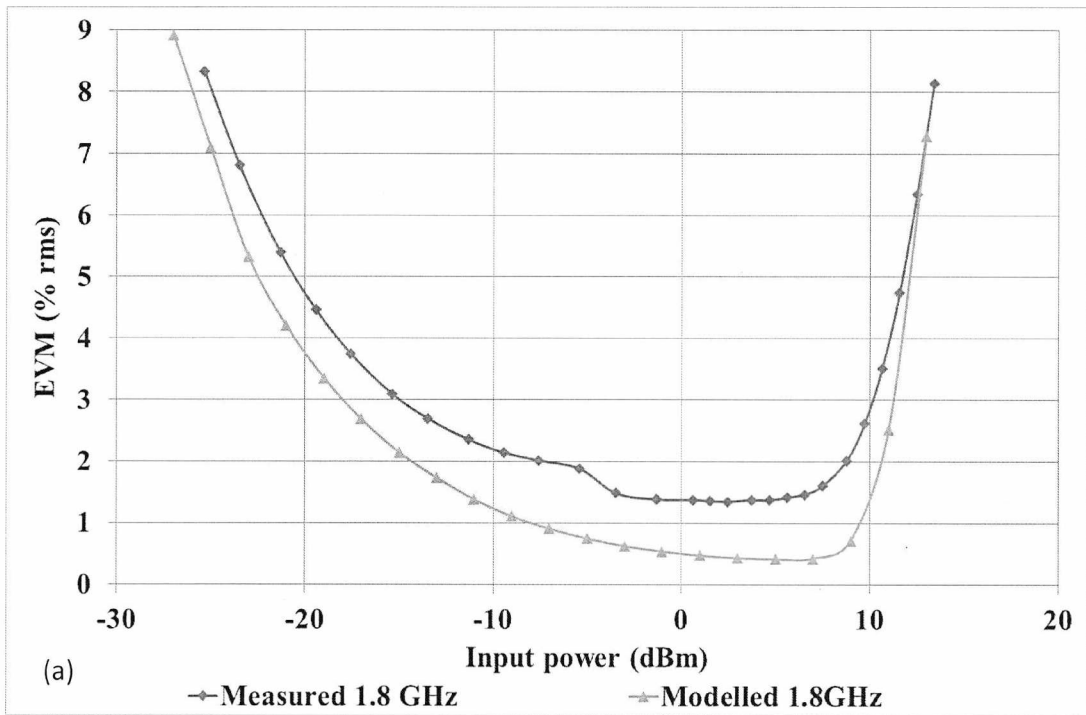


Fig. 7.13: Measured and modelled EVM 802.11n results at carrier frequencies of (a) 1.2GHz and (b) 1.8 GHz.

7.4 Multi-channel performance predictions

The simulation was carried out for the simultaneous transmission of the 4 channels. The simulation set-up is shown in Figures 7.14 and 7.15. Various required electrical components that are not shown in the high level system design in Fig. 7.14 (RF Amplifiers, Filters etc.) are included in the simulation (Fig. 7.15) by their noise figures using typical noise parameters [105].

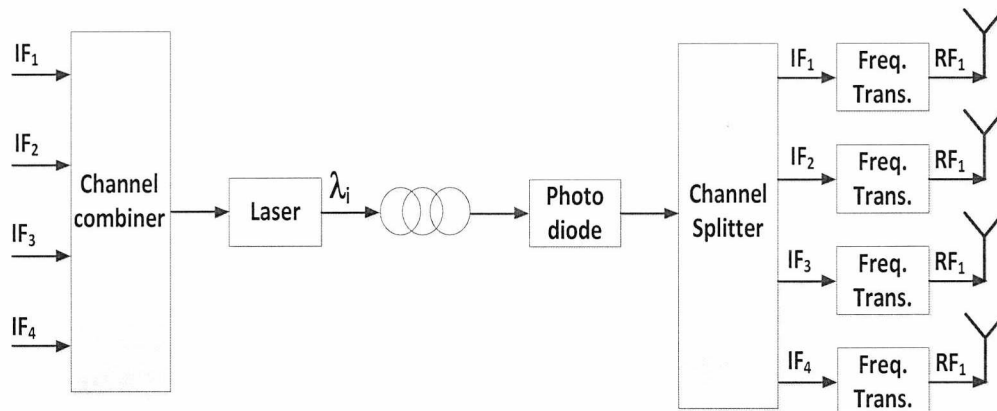


Fig. 7.14: Simplified diagram of SCM RoF system. IF is Intermediate Frequency, λ is wavelength.

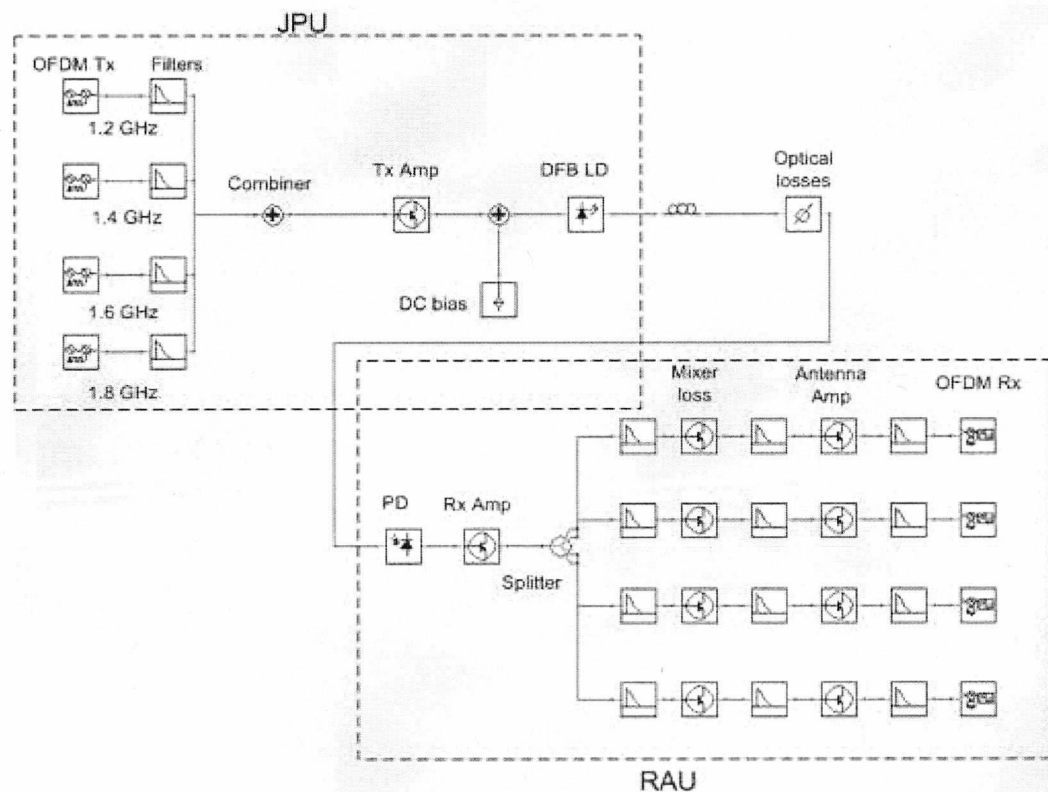


Fig. 7.15: Actual SCM RoF system simulation set-up in VPI.

Here, all channels have a 3 dB bandwidth of approximately 100 MHz (in line with the architecture presented in this Section, as opposed to the experimental validation of Sections 7.3.2 and 7.3.3), the CP was set to 1/4 of the symbol duration and a root-raised cosine filter was used with a roll off factor of 0.18. Electrical component nonlinear characteristics are not modelled as it is assumed that in a real implementation, electrical component choice will not lead to further impairments in the overall performance. The optical links of all 4 sections are the same as the one shown in Fig. 7.10 (including the laser packaging filtering parasitic modelling and optical attenuation). A simulation with 512 OFDM subcarriers and 256-QAM was carried out for the simultaneous transmission of the 4 channels. Single channel transmission at 1.2 GHz was also simulated to investigate the change in the back-off requirements from the 4 channel transmission. The data rate for each channel is 800 Mbps.

As can be seen in the results of Fig. 7.16, the input power where the EVM starts to rise due to distortion differs by approximately 6 dB between the 4-channel and single channel cases. The 6 dB difference in back-off is a result of the addition of the IF channels. The increase in back-off is given by: $10\log(N)$ where N is the number of IF channels. As there is no wireless standard specification for OFDM with 256 QAM, the EVM requirement is obtained by extrapolating from the 802.11n requirement in Table 2.3 for 64 QAM. More specifically, it is assumed that the required SNR increases by 6 dB between 64 QAM and 256 QAM [9]. Then, using (2.15) the EVM requirement for 256 QAM is obtained. As the envisaged application will operate over higher wireless ranges than 802.11n, the EVM requirement is assumed to be more stringent and this is taken into account by reducing the EVM transmitter requirement obtained from (2.15) by 0.5%. Thus, here, it is assumed that the EVM transmitter requirement is at 1.5%. This requirement is met over a range of approximately 5.1 dB for the 1.8 GHz channel and 7.6 dB for the 1.2 GHz channel. In order to meet the EVM requirement of 1.5 %, the input power must be backed-off to 3.1 dBm and 4.4 dBm for the 1.8 GHz and 1.2 GHz channels respectively. As an uplink architecture, assuming a receiver EVM requirement of 3 %, the system dynamic range is 16.5 dB for the 1.2 GHz channel and 13.8 dB for the 1.8 GHz channel. In order to meet the EVM requirement, the input power must be backed-off to 6.1 dBm for the 1.2 GHz channel and 4.6 dBm for the 1.8 GHz channel. The system dynamic ranges and back-off points are indicated on Fig. 7.16. Note that these dynamic ranges will depend on receiver noise and will be different from system to system, depending on receiver noise specifications. However, they serve as an indication on the ability of the architecture under consideration, to allow for some variation in component operating conditions (due to aging, temperature conditions etc.), which will occur in practical implementations, to be tolerated. The uplink system dynamic range is also important

as it can accommodate variations in the received signal powers from mobile units (signals that will experience different attenuations due to the wireless channel). In a typical implementation scenario it can be assumed that some form of power control in the mobile units will be implemented. Therefore, the predicted dynamic ranges can adequately allow for some variation on the received powers from the mobile units. Figures 7.17, 7.18 and 7.19 show the results for 64 QAM and different IFFT sizes (note that Fig. 7.19 was obtained by co-simulation with Matlab). In this case, as the modulation is 64 QAM, the EVM transmitter requirement is at 4 % while the EVM receiver requirement is at 5.6 %. The corresponding downlink and uplink system dynamic ranges are shown with annotations on the figures. The lowest dynamic range occurs consistently for the 1.8 GHz channel and this can be attributed to the channel being closer to the device resonance frequency which will result in stronger intrinsic distortion.

Experimental demonstration with wireless transmission for a system based on the simulated topology has been carried out in [14].

It is apparent that the number of IF channels has a major effect on the input power at which distortion starts to dominate the performance. The number of OFDM subcarriers itself seems to have an insignificant effect in the performance of the system. This can be verified from Fig. 7.20, which shows the EVM performance for a single channel transmission at 1.2 GHz with 512 and 2048 subcarriers and 256 QAM modulation. This result is in agreement with one of the conclusions of Chapter 4, namely that when looking at the mean of the EVM, performance differences between signals with different number of subcarriers due to differences in the PAPR cannot be observed.

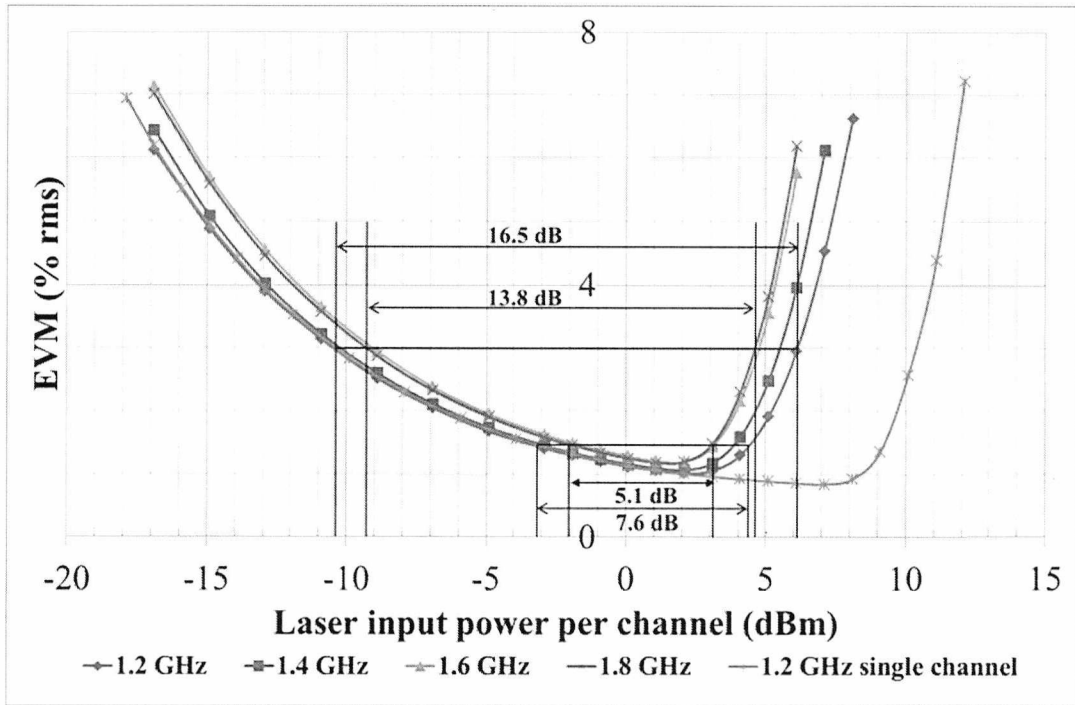


Fig. 7.16: Prediction of EVM performance for simultaneous 4-channel and single 1.2 GHz channel transmissions with 512 OFDM subcarriers and 256 QAM.

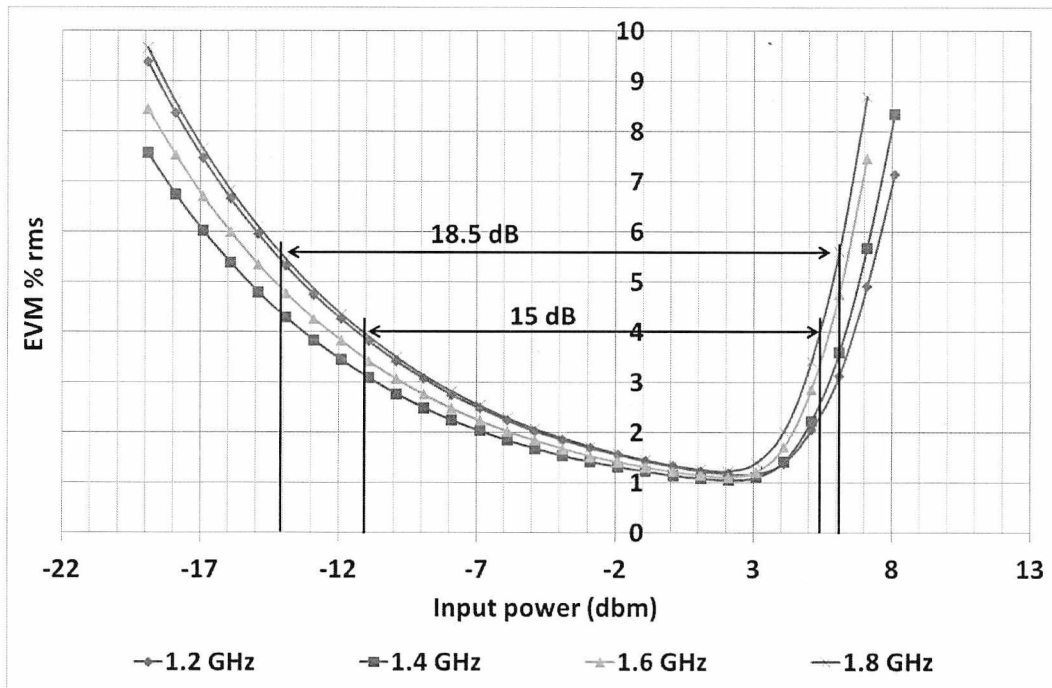


Fig. 7.17: Prediction of EVM performance for simultaneous 4-channel transmission with 128 OFDM subcarriers and 64 QAM.

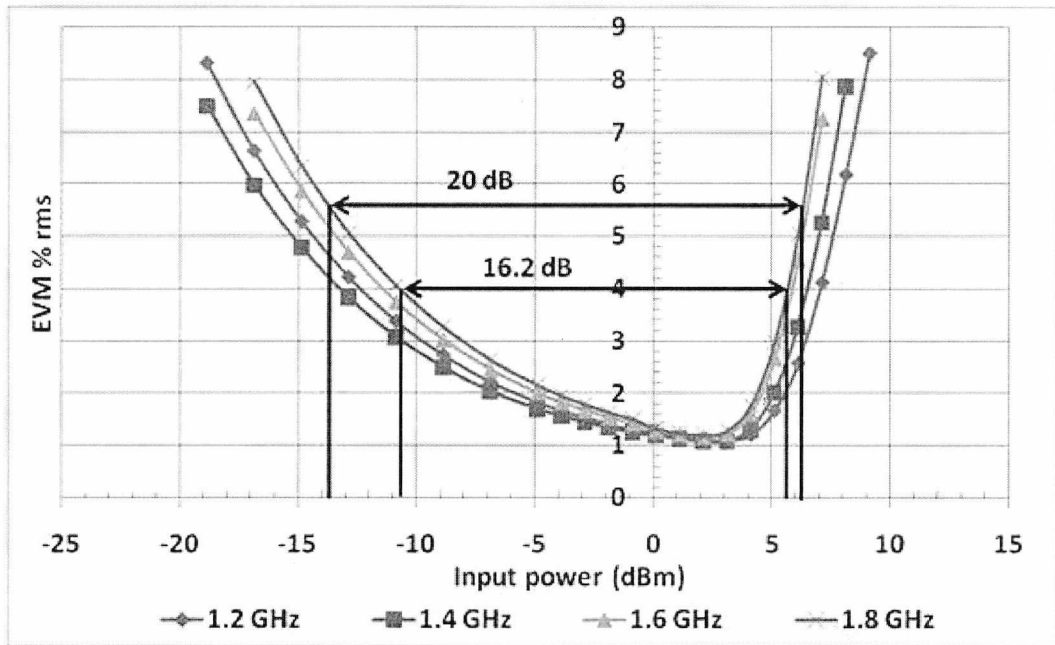


Fig. 7.18: Prediction of EVM performance for simultaneous 4-channel transmission with 512 OFDM subcarriers and 64 QAM.

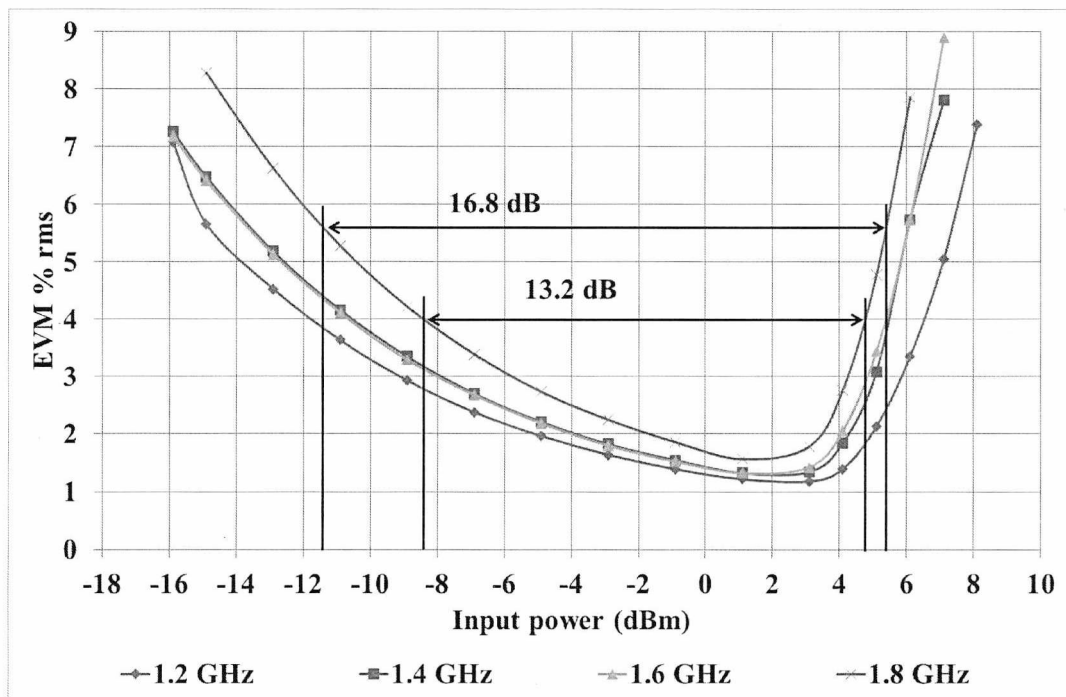


Fig. 7.19: Prediction of EVM performance for simultaneous 4-channel transmission with 1024 OFDM subcarriers and 64 QAM.

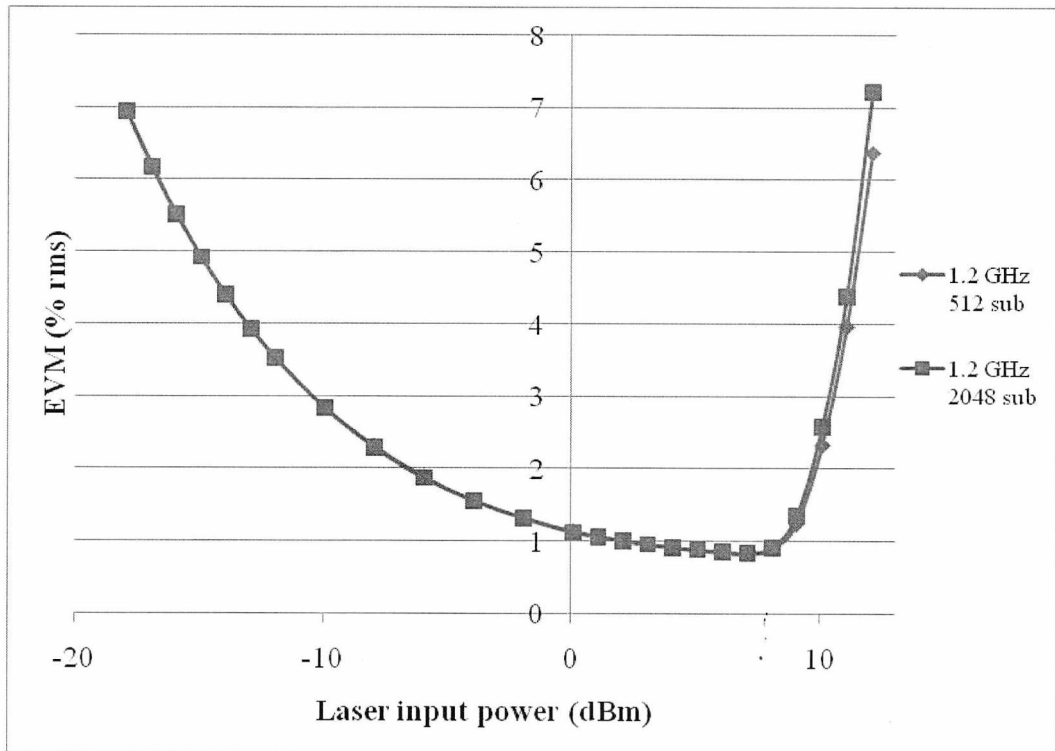


Fig. 7.20: Comparison between 512 and 2048 IFFT sizes with 256 QAM modulation at a frequency of 1.2 GHz.

7.5 Conclusions

A rate-equation model for an un-cooled DFB laser is validated through various measured performance characteristics including P-I curve, frequency response, P1dB, 2-tone test and EVM versus input power. The model is based on a simple form of the rate equations, and it is shown, that such a model with a simple fitting process over the various performance metrics (including EVM versus input power), and iteration steps in the design process for further adjustment of model parameters, can produce a good quality fit over a wide range of performance metrics.

The model is then used to make a simulation-based prediction for the performance of a 4-channel SCM-RoF system for the transmission of 4th generation mobile/wireless signals. The simulation results indicate the feasibility of such a system in transmitting a combined raw data rate of 3.2 Gbps employing a multilevel, 256-QAM transmission scheme with OFDM of 512 and

2048 IFFT sizes. A system with dynamic range, based on a 1.5% EVM transmitter requirement for OFDM with 256 QAM, of approximately 5.1 dB (at least) is predicted. This dynamic range, in a practical implementation, would allow for any tight control on component/device operating point variability to be relaxed. As an uplink implementation, the system can provide a dynamic range of 13.8 dB (at least) assuming a receiver EVM requirement of 3%.

8 Conclusions and Future work

8.1 Conclusions

Through a statistical description of the amplitude distribution of the OFDM signal, a more practical statistical PAPR measure can be obtained. In Chapter 3, the CCDF and PDF of the statistical PAPR were presented. Then, from the PDF, the median points were used as an estimation of the input power at which the turning point of the EVM occurs. An empirical formula, based on the Gaussian assumption for the amplitude of the up-converted OFDM signal gave a good match with the simulated PAPR. The PDF of the PAPR shows that the median of the PAPR increases by approximately 0.4 dB for every doubling of the number of subcarriers. Above 2048 subcarriers, this value of increase reduces to approximately 0.3 dB.

The Gaussian assumption for the amplitude distribution of the OFDM signal means that statistical nonlinear models for a RoF link can be used. These statistical models assume instantaneous functions (i.e. memoryless nonlinearities). They can be based on either a complex envelope representation (i.e. a passband nonlinear model) or on the real nonlinear function. For the former, it was shown how crude estimates of the effective SNR and EVM can be obtained for a low biased laser diode by applying the direct method. For the latter, the output auto-correlation function of the signal at the output of an optical link with a low biased laser was formulated. The final expression depends directly on parameters from the static response of the optical link. It can also be used to model the distortion power at different frequency ranges.

In Chapter 4, EVM measurement results for a directly modulated RoF link transporting a large number of OFDM frames with QPSK modulation have been presented. The mean EVM results (with the mean calculated over each OFDM frame) do not indicate that the amount of input power back-off required from the P1dB depends on the number of subcarriers (at least to the extent expected by the statistical PAPR for different numbers of subcarriers). The reason is found to be that with distortion, the raw EVM distributions are skewed, with the skew being higher for signals with lower numbers of subcarriers. The higher skew for these signals causes the mean to increase by a higher amount than in signals with higher numbers of subcarriers, as the mean is more susceptible to outliers. However, when using the median of the raw EVM,

differences in the EVM performance between signals with different numbers of subcarriers become more apparent. As a result, statistical PAPR can be related, in principle, with differences in the required input power back-off for these signals. The observed trends are independent of the nonlinearity and would also apply to any nonlinear system transporting OFDM signals (including other high bit rate RoF systems and non-RoF systems).

Additionally, it was shown, that in the noise limited range of measurement (low RF input power), the distribution of the mean EVM results is approximately Gaussian, resulting in the same mean, but a variance which depends inversely on the number of subcarriers due to the averaging in the estimation of the mean EVM. However, the distribution of the mean EVM in the distortion limited region (intermediate RF input power range) is positively skewed and better approximated by a log-normal distribution. This effect is a direct consequence of the way the OFDM modulation and demodulation operate in a per-frame manner. In the limit, as the number of subcarriers and/or input power are increased, the skew reduces and the distribution converges asymptotically to a Gaussian. The skew in the raw EVM distributions, is a result of skew in the noise plus distortion distribution. Again, in the limit, as the numbers of subcarriers and/or input power are increased the distribution converges asymptotically to a Rayleigh distribution.

The knowledge gained concerning the EVM statistical distributions from Chapter 4, is used In Chapter 5 to show how confidence interval analysis can be used to estimate the proportion of frames that will exceed some EVM threshold value. For high number of subcarriers (say 1024 and above) or high input powers, the EVM per frame distributions are approximately Gaussian. Therefore, empirical confidence intervals based on the Gaussian distribution can be used. For lower input powers or low numbers of subcarriers, where the distributions are more closely approximated by log-normal distributions, confidence intervals can be obtained by log-transforming the EVM per frame values.

A further investigation was carried out into the number of OFDM frames that must be used in a measurement to obtain an accurate mean EVM estimate (within a well-defined confidence interval). To this extent, the highest EVM variance (highest input power) obtained from a measurement was used. The required number of frames changes inversely proportionally with the number of subcarriers within the frame and it was predicted that for a signal with 128 subcarriers, 320 frames would be required for a 95 % confidence interval size of 0.31 %.

Finally, the variation of EVM within the signal band (i.e. different subcarrier locations) was investigated. The results show that with distortion, subcarriers located at the middle of the band are affected to a stronger degree compared to subcarriers at the edge of the band (even at the maximum input power used for these measurements). Furthermore, for this specific link, at lower powers the dominant source of impairment was found to be due to IQ timing offset. It was then shown that distortion, wins over the IQ timing offset impairment at a difference in input power between the different signals that is close in value to the difference in the medians of their statistical PAPR.

In Chapter 6, the use of companding was demonstrated as a means of reducing the PAPR of the input signal, allowing for the laser diode to be driven at higher input powers. As a result, the RF power at the output of the optical link can be increased. In turn, this increase in output power means that amplification and thus isolation requirements in the RAU can be reduced by an equal amount. In effect, through companding, the EVM dynamic range at the output of the link is "transferred" to a range of powers that are appropriate for meeting the EVM transmitter requirements of the transported signals.

In Chapter 7, a rate-equation model for an un-cooled DFB laser was designed and validated through various measured performance characteristics. These included the laser diode P-I curve, frequency response, P1dB, 2-tone test and EVM versus input power. The model was based on a simple form of the rate equations. It was shown, that by neglecting certain effects (such as dispersion in conjunction with chirp) that are expected to have negligible effect on the performance for the envisaged application, such a model with a simple fitting process over the various performance metrics (including EVM versus input power), and iteration steps in the design process for further adjustment of model parameters, can produce a good quality fit over a wide range of performance metrics.

The model was then used to make a simulation-based prediction for the performance of a 4-channel SCM-RoF system for the transmission of 4th generation mobile/wireless signals. The simulation results indicate that the system is capable of transmitting a combined raw data rate of 3.2 Gbps employing a multilevel, 256-QAM transmission scheme with OFDM of 512 and 2048 IFFT sizes with adequate performance (i.e. within the EVM transmitter and receiver requirements of the different modulation levels). A system with dynamic range, based on a 1.5% EVM transmitter requirement for OFDM with 256 QAM, of approximately 5.1 dB (at least) is predicted. This dynamic range, in a practical implementation, would allow for any tight control on component/device operating point variability, to be relaxed. As an uplink

implementation, the system can provide a dynamic range of 13.8 dB (at least) assuming a receiver EVM requirement of 3%.

8.2 Main Contributions of the Thesis

An operation regime for an IM-DD RoF system that has not, in general, been investigated in the literature, is one with a low bias laser diode. This regime may be useful for PoF applications. Statistical nonlinearity models become more mathematically tractable in the limiting case of a low biased laser diode. Note also, that such models have not been used extensively in the case of OFDM transmission through directly modulated IM-DD links.

The specific mathematical formulation of the PAPR for the up-converted OFDM signal and the use of the median point of its distribution as a metric for back-off estimation have been presented for the first time. In the literature, there has been no direct connection between the statistical PAPR and input power back-off in terms of EVM simulation or measured results. Conformity with EVM transmitter and receiver requirements is based on the mean EVM (through an averaging process). But with this approach differences in the required back-off for signals with different numbers of subcarriers cannot be observed. The connection between statistical PAPR and the median of the raw EVM distribution is an important result as it can lead directly to varying amounts of input power back-off for signals with different numbers of subcarriers. The statistical analysis of the EVM measured results based on idealized processes (i.i.d assumption) and the connection between the EVM per frame (with the specific formulation used) and the raw EVM distributions is carried out in this way for the first time. Additionally, it provides a very straightforward way for inspecting the asymptotic convergence of an actual EVM measurement result to the idealised case (i.i.d). The normality of the EVM per frame distributions was examined through skew, Kurtosis and coefficient of variation results. Again this form of analysis has not been carried out for EVM measurement results in the literature.

The use of confidence interval analysis and the treatment of EVM variance as an important parameter for defining back-off points have been suggested. Furthermore, results for an IM-DD link that is limited by IQ timing offset and distortion have been presented for the first time. Additionally, the results show clearly the non-white nature of the distortion even for high input powers and very high numbers of subcarriers. Although the non-white nature of

distortion is an expected result from intermodulation theory, it has not been shown before in terms of EVM and in the specific regimes (input powers and numbers of subcarriers).

The use of companding in a directly modulated IM-DD link in order to obtain increased RF signal powers at the output of the optical link has been presented for the first time. In particular, the use of companding as a method for the alleviation of amplification (and isolation) requirements, which can simplify the RAU design, is demonstrated. Also, in the literature, optimum companding regimes are investigated in terms of SNR and bit-error rates (BER). This approach is not necessarily optimal in terms of performance analysis, when this is based on EVM and specifically EVM standard requirements.

The design and use of a simple rate-equation model for OFDM transmission in a subcarrier multiplexed IM-DD link transporting signals complying with 4th generation standards have been presented for the first time. Specifically, the main focus was towards fitting the EVM measured performance and with the envisaged application in mind, certain phenomena (such as fibre dispersion in conjunction with chirp) were neglected in the model design process. Additionally, the intrinsic frequency response of the laser diode that is usually masked by parasitic packaging filtering was not made to fit and instead was used (through related intrinsic parameters) as a “free” fitting parameter, aiding the modelling process. Through simulations with high data rate signals (with channel bandwidths on the order of 100 MHz and high level modulation), dynamic ranges within EVM compliance levels were presented. These results show the possibility for an IM-DD SCM system to support these next generation standards.

8.3 Future work

A further investigation into the analytical modelling of RoF links can be carried out (extended to higher bias levels). More specifically, a comparison can be carried out between an AM/AM model and a quasi-memoryless model (AM/PM). This comparison can include the effects of different bias current levels and operating carrier frequencies.

A strong correlation with the median of the statistical PAPR was evident in certain results (see the Skew and kurtosis results in Fig. 4.14 and Fig. 4.17, and the results for subcarriers at different locations in the signal band in Fig. 5.13-Fig. 5.15). These correlations can be re-tested

through simulation with clipping functions and very closely spaced input power intervals in order to obtain results with a higher accuracy.

Similarly, the exact relation between the median of the PAPR and the median results of the EVM (see Fig. 4.23) can be further investigated, again through simulations at a higher accuracy. In turn a more accurate relationship between median of the PAPR and the input power back-off can be obtained.

An investigation could be carried out in order to see if these results can be compared to analytical models (other than statistical ones) that depend on the number of subcarriers such as [74] and [106]. However, polynomial models such as the one in [106] are in general small-signal models and it is not certain how accurately they can model laser diode nonlinearities that possess a clipping behaviour.

Furthermore, the analysis carried out in Chapter 4 can be extended to the Symbol Error Rate (SER) metric which should, in theory, show similar trends with the EVM results.

In the literature, EVM transmitter and receiver requirements are based on the mean EVM. But, it would be interesting to define an additional metric for the proportion of frames or subcarriers (based on the EVM variance) that can exceed (or are allowed to exceed by the specific system transporting them) a certain EVM threshold.

In Chapter 5, a confidence interval analysis was carried out based on the distribution of the EVM per frame. A similar analysis can be carried out in terms of the median estimation of a Rayleigh process (following from the Rayleigh distribution of the raw EVM results).

In terms of the analysis of a sequence of EVM measurements (treated as a random process) as was done in Chapter 4, an investigation can be carried out in terms of estimation theory for non-stationary processes. This investigation could, in principle, provide information on the asymmetry (skew) of the distributions.

For certain EVM per frame results (for certain input powers and numbers of subcarriers) that can be approximated by log-normal distributions, it was said that confidence intervals can be obtained by log-transforming the EVM per frame values. However, the accuracy of this method was not tested. Other methods are available (e.g. through maximum likelihood estimators) that could potentially offer higher estimation accuracies. A comparison between these methods could be carried out.

In Chapter 6, the use of companding in a RoF link was demonstrated. The companding function was implemented in Matlab. But in practical situations, the companding function can be implemented in the DAC at the transmitter section (*see* Fig. 2.1), for example by separately compressing the In-phase and Quadrature components. Furthermore, the companding regime can be optimized (optimization of the companding parameters was not in the scope of Chapter 6) in terms of parameter selection. The effects of bandwidth expansion can be investigated as companded signals can potentially violate spectral mask requirements. This investigation can be done in conjunction with the optimization of companding parameters. Furthermore, an investigation into the effects of variations between the compression and expansion parameters in the transmitter and receiver respectively is important as these variations can lead to signal distortions.

In Chapter 7, the simulated results gave predictions for the system dynamic range of a SCM architecture transporting 4th generation signals. A model can be made to fit and a simulation based prediction carried out for other laser diodes of the same manufacturing batch. The aim would be to see if the same rate equation model is a good fit for other devices, and how much the fitting depends on packaging related effects (e.g. packaging parasitic filtering).

The simulation itself can be extended to include the effects of the wireless channel, for example, by implementing an empirical model based on a Manhattan scenario as envisaged for FUTON. The results of this simulation can then be used to re-define the acceptable EVM system dynamic ranges. A Manhattan based scenario may be better modelled through Rician fading statistics (and not Rayleigh statistics) and as such, some of the EVM requirements may be relaxed. Therefore, the predicted system dynamic ranges can potentially increase.

References

- [1] D. Wake, "Trends and prospects for radio over fibre picocells," in *Microwave Photonics, 2002. International Topical Meeting on*, 2002, pp. 21-24.
- [2] M. Sauer, A. Kobayakov, and J. George, "Radio Over Fiber for Picocellular Network Architectures," *J. Lightwave Technol.*, vol. 25, pp. 3301-3320, 2007.
- [3] N. J. Gomes, A. Nkansah, and D. Wake, "Radio-Over-MMF Techniques-Part I: RF to Microwave Frequency Systems," *Lightwave Technology, Journal of*, vol. 26, pp. 2388-2395, 2008.
- [4] Y. Chien-Hung, C. Chi-Wai, L. Yen-Liang, W. Sz-Kai, C. Shi-Yang, S. Chorng-Ren, T. Min-Chien, L. Jiunn-Liang, H. Dar-Zu, and C. Sien, "Theory and Technology for Standard WiMAX Over Fiber in High Speed Train Systems," *Lightwave Technology, Journal of*, vol. 28, pp. 2327-2336, 2010.
- [5] A. Nkansah, A. Das, C. Lethien, J. P. Vilcot, N. J. Gomes, I. J. Garcia, J. C. Batchelor, and D. Wake, "Simultaneous Dual Band Transmission Over Multimode Fiber-Fed Indoor Wireless Network," *Microwave and Wireless Components Letters, IEEE*, vol. 16, pp. 627-629, 2006.
- [6] D. Wake, A. Nkansah, N. J. Gomes, G. de Valicourt, R. Brenot, M. Violas, L. Zhansheng, F. Ferreira, and S. Pato, "A Comparison of Radio Over Fiber Link Types for the Support of Wideband Radio Channels," *Lightwave Technology, Journal of*, vol. 28, pp. 2416-2422, 2010.
- [7] *Wireless LAN Medium Access Control (MAC) and Physical Layer (PHY) Specifications: Higher-Speed Physical Layer Extension in the 2.4 GHz Band*, 2000.
- [8] *IEEE Standard for Local and Metropolitan Area Networks, Part 16: Air Interface for Fixed and Mobile Broadband Wireless Access Systems, Amendment 2: Physical and Medium Access Control Layers for Combined Fixed and Mobile Operation in Licensed Bands, and IEEE Std. 802.16-2004/Cor1-2005*, 2005.
- [9] *Digital video broadcasting; Framing structure, channel coding and modulation for digital terrestrial television*, 2008, ETSI EN 300 744 v1.1.6.
- [10] J. A. C. Bingham, "Multicarrier modulation for data transmission: an idea whose time has come," *Communications Magazine, IEEE*, vol. 28, pp. 5-14, 1990.
- [11] C. H. Cox, *Analog optical links : theory and practice*. New York: Cambridge University Press, 2004.
- [12] C. H. Cox, III, E. I. Ackerman, G. E. Betts, and J. L. Prince, "Limits on the performance of RF-over-fiber links and their impact on device design," *Microwave Theory and Techniques, IEEE Transactions on*, vol. 54, pp. 906-920, 2006.
- [13] S. Pato, P. Monteiro, N. J. Gomes, A. Gameiro, and T. Kawanishi, "Next-generation distributed and heterogeneous radio architectures: The FUTON project," *Proc. Asia-Pacific Microw. Photon. Conf.*, 2009.
- [14] F. Diehm, J. Holfeld, G. Fettweis, N. J. Gomes, D. Wake, A. Nkansah, and E. L. Casariego, "The FUTON prototype: Broadband communication through coordinated multi-point using a novel integrated optical/wireless architecture," in *GLOBECOM Workshops (GC Wkshps), 2010 IEEE*, 2010, pp. 757-762.
- [15] FUTON project deliverable D1.1, "Project Presentation", 2008. Available: <http://www.ict-futon.eu/private/docs/Deliverables/D1.1.pdf>
- [16] W. B. Davenport, W. L. Root, and IEEE Communications Society., *An introduction to the theory of random signals and noise*. New York: IEEE Press, 1987.

- [17] R. Gross and D. Veeneman, "Clipping distortion in DMT ADSL systems," *Electronics Letters*, vol. 29, pp. 2080-2081, 1993.
- [18] P. Banelli and S. Cacapardi, "Theoretical analysis and performance of OFDM signals in nonlinear AWGN channels," *Communications, IEEE Transactions on*, vol. 48, pp. 430-441, 2000.
- [19] D. Wake, A. Nkansah, N. J. Gomes, C. Lethien, C. Sion, and J. P. Vilcot, "Optically Powered Remote Units for Radio-Over-Fiber Systems," *Lightwave Technology, Journal of*, vol. 26, pp. 2484-2491, 2008.
- [20] J. Tellado, *Multicarrier modulation with low par : applications to DSL and wireless*. Boston, Mass.: Kluwer Academic Publishers, 2000.
- [21] N. J. Gomes, M. Morant, A. Alphones, B. Cabon, J. E. Mitchell, C. Lethien, M. Csörnyei, A. Stöhr, and S. Iezekiel, "Radio-over-fiber transport for the support of wireless broadband services [Invited]," *J. Opt. Netw.*, vol. 8, pp. 156-178, 2009.
- [22] A. Das, A. Nkansah, N. J. Gomes, I. J. Garcia, J. C. Batchelor, and D. Wake, "Design of low-cost multimode fiber-fed indoor wireless networks," *Microwave Theory and Techniques, IEEE Transactions on*, vol. 54, pp. 3426-3432, 2006.
- [23] L. Hanzo, *OFDM and MC-CDMA for broadband multi-user communications, WLANs, and broadcasting*. New York: J. Wiley, 2003.
- [24] J. G. Andrews, A. Ghosh, and R. Muhamed, *Fundamentals of WiMAX : understanding broadband wireless networking*. Upper Saddle River, NJ: Prentice Hall, 2007.
- [25] T. Pollet, M. Van Bladel, and M. Moeneclaey, "BER sensitivity of OFDM systems to carrier frequency offset and Wiener phase noise," *Communications, IEEE Transactions on*, vol. 43, pp. 191-193, 1995.
- [26] J. K. Cavers, "An analysis of pilot symbol assisted modulation for Rayleigh fading channels [mobile radio]," *Vehicular Technology, IEEE Transactions on*, vol. 40, pp. 686-693, 1991.
- [27] T. Wakutsu and M. Serizawa, "A carrier frequency offset and timing offset detection scheme for OFDM systems utilizing pilot sub-carriers," *IEICE Trans. Commun.*, vol. E83-B, pp. 1854-1863, 2000.
- [28] F. Classen and H. Meyr, "Frequency synchronization algorithms for OFDM systems suitable for communication over frequency selective fading channels," in *Vehicular Technology Conference, 1994 IEEE 44th*, 1994, pp. 1655-1659 vol.3.
- [29] M. Sliskovic, "Carrier and sampling frequency offset estimation and correction in multicarrier systems," in *Global Telecommunications Conference, 2001. GLOBECOM '01. IEEE*, 2001, pp. 285-289 vol.1.
- [30] J. J. van de Beek, M. Sandell, and P. O. Borjesson, "ML estimation of time and frequency offset in OFDM systems," *Signal Processing, IEEE Transactions on*, vol. 45, pp. 1800-1805, 1997.
- [31] M. Sandell, J. J. Van de Beek, and P. O. Borjesson, "Timing and frequency synchronization in OFDM systems using the cyclic prefix," *Int. Symposium Synchronization*, pp. 16-19, 1995.
- [32] L. Chia-Horng, "On the Study of End-to-End IQ Imbalance Problem in OFDM Systems," in *Vehicular Technology Conference, 2008. VTC 2008-Fall. IEEE 68th*, 2008, pp. 1-5.
- [33] W. Ren, Z. G. Shi, and K. S. Chen, "Combined impacts of IQ imbalance from both transmitter and receiver in OFDM systems," in *Wireless, Mobile and Multimedia Networks, 2006 IET International Conference on*, 2006, pp. 1-4.
- [34] M. Windisch and G. Fettweis, "Standard-independent I/Q imbalance compensation in OFDM direct-conversion receivers," *Proc. 9th International OFDM Workshop*, 2004.
- [35] "IEEE Standard for Information technology--Telecommunications and information exchange between systems--Local and metropolitan area networks--Specific requirements Part 11: Wireless LAN Medium Access Control (MAC) and Physical Layer

- (PHY) Specifications Amendment 5: Enhancements for Higher Throughput," *IEEE Std 802.11n-2009 (Amendment to IEEE Std 802.11-2007 as amended by IEEE Std 802.11k-2008, IEEE Std 802.11r-2008, IEEE Std 802.11y-2008, and IEEE Std 802.11w-2009)*, pp. c1-502, 2009.
- [36] S. Forestier, P. Bouysse, R. Quere, A. Mallet, J. M. Nebus, and L. Lapierre, "Joint optimization of the power-added efficiency and the error-vector measurement of 20-GHz pHEMT amplifier through a new dynamic bias-control method," *Microwave Theory and Techniques, IEEE Transactions on*, vol. 52, pp. 1132-1141, 2004.
- [37] V. Sittakul and M. J. Cryan, "A 2.4-GHz Wireless-Over-Fibre System Using Photonic Active Integrated Antennas (PhAIAs) and Lossless Matching Circuits," *Lightwave Technology, Journal of*, vol. 27, pp. 2724-2731, 2009.
- [38] I. A. Kostko, M. E. M. Pasandi, M. M. Sisto, S. Larochelle, L. A. Rusch, and D. V. Plant, "A radio-over-fiber link for OFDM transmission without RF amplification," in *Lasers and Electro-Optics Society, 2007. LEOS 2007. The 20th Annual Meeting of the IEEE, 2007*, pp. 339-340.
- [39] V. Sittakul and M. J. Cryan, "A Fully Bidirectional 2.4-GHz Wireless-Over-Fiber System Using Photonic Active Integrated Antennas (PhAIAs)," *Lightwave Technology, Journal of*, vol. 25, pp. 3358-3365, 2007.
- [40] H. T. Friis, "Noise Figures of Radio Receivers," *Proceedings of the IRE*, vol. 32, pp. 419-422, 1944.
- [41] R. Ludwig and P. Bretchko, *RF circuit design : theory and applications*. Upper Saddle River, NJ: Prentice-Hall, 2000.
- [42] J. Vuolevi and T. Rahkonen, *Distortion in RF power amplifiers*. Boston: Artech House, 2003.
- [43] J. J. Carr, *Secrets of RF circuit design*, 3rd ed. New York: McGraw-Hill, 2001.
- [44] "IEEE Standard for Local and Metropolitan Area Networks Part 16: Air Interface for Fixed and Mobile Broadband Wireless Access Systems Amendment 2: Physical and Medium Access Control Layers for Combined Fixed and Mobile Operation in Licensed Bands and Corrigendum 1," *IEEE Std 802.16e-2005 and IEEE Std 802.16-2004/Cor 1-2005 (Amendment and Corrigendum to IEEE Std 802.16-2004)*, pp. 0_1-822, 2006.
- [45] N. J. Gomes, A. Das, A. Nkansah, M. Mjeku, and D. Wake, "Multimode Fiber-fed Indoor Wireless Networks," in *Microwave Photonics, 2006. MWP '06. International Topical Meeting on*, 2006, pp. 1-4.
- [46] V. Sittakul and M. J. Cryan, "Modeling of radio-over-fiber links for 802.11g wireless local area networks," *Microwave and Optical Technology Letters*, vol. 52, pp. 2672-2675, 2010.
- [47] P. Assimakopoulos, A. Nkansah, and N. J. Gomes, "Use of commercial Access Point employing spatial diversity in a Distributed Antenna Network with different fiber lengths," in *Microwave photonics, 2008. jointly held with the 2008 asia-pacific microwave photonics conference. mwp/apmp 2008. international topical meeting on*, 2008, pp. 189-192.
- [48] M. Y. W. Chia, B. Luo, M. L. Yee, and E. J. Z. Hao, "Radio over multimode fibre transmission for wireless LAN using VCSELs," *Electronics Letters*, vol. 39, pp. 1143-1144, 2003.
- [49] P. Assimakopoulos, V. Sittakul, A. Nkansah, N. Gomes, M. Cryan, and D. Wake, "Comparison between remote Antenna Units with Detachable antennas and Photonic Active Integrated Antennas for indoor applications," in *General Assembly and Scientific Symposium, 2011 XXXth URSI*, 2011, pp. 1-4.
- [50] L. Raddatz, D. Hardacre, I. H. White, R. V. Penty, D. G. Cunningham, M. R. T. Tan, and S. Y. Wang, "High bandwidth data transmission in multimode fibre links using subcarrier multiplexing with VCSELs," *Electronics Letters*, vol. 34, pp. 686-688, 1998.

- [51] A. Flatman, "In-Premises Optical Fiber Installed Base Analysis to 2007," *10 Gb/s on FDDI-Grade MM Fiber*, 2004.
- [52] M. J. Crisp, L. Sheng, A. Watts, R. V. Penty, and I. H. White, "Uplink and Downlink Coverage Improvements of 802.11g Signals Using a Distributed Antenna Network," *Lightwave Technology, Journal of*, vol. 25, pp. 3388-3395, 2007.
- [53] D. Wake, A. Nkansah, and N. J. Gomes, "Radio Over Fiber Link Design for Next Generation Wireless Systems," *Lightwave Technology, Journal of*, vol. 28, pp. 2456-2464, 2010.
- [54] D. Wake, A. Nkansah, P. Assimakopolous, N. Gomes, M. Violas, L. Zhansheng, S. Pato, F. Ferreira, G. De Valicourt, R. Brenot, and F. Van Dijk, "Design and performance of radio over fibre links for next generation wireless systems using distributed antennas," in *Future Network and Mobile Summit, 2010*, 2010, pp. 1-9.
- [55] P. Golden, H. Dedieu, and K. Jacobsen, *Fundamentals of DSL technology*. Boca Raton, FL: Auerbach Publications, 2006.
- [56] A. Papoulis, *Probability, random variables, and stochastic processes*, 3rd ed. New York: McGraw-Hill, 1991.
- [57] R. van Nee and A. de Wild, "Reducing the peak-to-average power ratio of OFDM," in *Vehicular Technology Conference, 1998. VTC 98. 48th IEEE*, 1998, pp. 2072-2076 vol.3.
- [58] H. Ochiai and H. Imai, "On the distribution of the peak-to-average power ratio in OFDM signals," *Communications, IEEE Transactions on*, vol. 49, pp. 282-289, 2001.
- [59] R. J. Baxley and G. T. Zhou, "Power savings analysis of peak-to-average power ratio in OFDM," *Consumer Electronics, IEEE Transactions on*, vol. 50, pp. 792-798, 2004.
- [60] J. J. Bussgang, "Cross correlation function of amplitude-distorted Gaussian signals," *Res. Lab. Electron.*, 1952.
- [61] H. E. Rowe, "Memoryless nonlinearities with Gaussian inputs: Elementary results," *The Bell System technical journal*, vol. 61, pp. 1519-1525, 1982.
- [62] C. Rapp, "Effects of HPA-nonlinearity on 4-DPSK-OFDM-signal for a digital sound broadcasting system," *Proc. 2nd European Conference on Satellite Communications*, 1991.
- [63] R. Price, "A useful theorem for nonlinear devices having Gaussian inputs," *Information Theory, IRE Transactions on*, vol. 4, pp. 69-72, 1958.
- [64] S. Qun, "OFDM in bandpass nonlinearity," *Consumer Electronics, IEEE Transactions on*, vol. 42, pp. 253-258, 1996.
- [65] L. Chin Hee, V. Postoyalko, and T. O'Farrell, "Analysis and simulation of AM-AM/PM nonlinear distortion due to direct laser modulation in radio over fibre systems," in *Microwave Photonics, 2002. International Topical Meeting on*, 2002, pp. 137-140.
- [66] P. Assimakopoulos, L. C. Vieira, A. Nkansah, D. Wake, N. J. Gomes, and F. van Dijk, "Modelling of a DFB laser at low bias directly modulated with an OFDM signal for RoF applications," in *Microwave Photonics, 2009. MWP '09. International Topical Meeting on*, 2009, pp. 1-4.
- [67] S. O. Rice, "Mathematical Analysis of Random Noise," *Bell Systems Tech. J., Volume 23*, p. 282-332, vol. 23, pp. 282-332, 1944.
- [68] J. Minkoff, "The Role of AM-to-PM Conversion in Memoryless Nonlinear Systems," *Communications, IEEE Transactions on*, vol. 33, pp. 139-144, 1985.
- [69] M. C. Jeruchim, P. Balaban, and K. S. Shanmugan, *Simulation of communication systems : modeling, methodology, and techniques*, 2nd ed. New York: Kluwer Academic/Plenum Publishers, 2000.
- [70] A. Kaye, D. George, and M. Eric, "Analysis and Compensation of Bandpass Nonlinearities for Communications," *Communications, IEEE Transactions on*, vol. 20, pp. 965-972, 1972.

- [71] M. Sauer, A. Kobayakov, and J. George, "Radio Over Fiber for Picocellular Network Architectures," *Lightwave Technology, Journal of*, vol. 25, pp. 3301-3320, 2007.
- [72] D. Dardari, V. Tralli, and A. Vaccari, "A theoretical characterization of nonlinear distortion effects in OFDM systems," *Communications, IEEE Transactions on*, vol. 48, pp. 1755-1764, 2000.
- [73] R. O'Neill and L. B. Lopes, "Envelope variations and spectral splatter in clipped multicarrier signals," in *Personal, Indoor and Mobile Radio Communications, 1995. PIMRC'95. 'Wireless: Merging onto the Information Superhighway'. Sixth IEEE International Symposium on*, 1995, pp. 71-75 vol.1.
- [74] M. R. D. Rodrigues, J. E. Mitchell, and I. Darwazeh, "On the error probability performance of non-linearly distorted OFDM signals," in *Vehicular Technology Conference, 2003. VTC 2003-Spring. The 57th IEEE Semiannual*, 2003, pp. 1278-1282 vol.2.
- [75] L. Xiaodong and L. J. Cimini, Jr., "Effects of clipping and filtering on the performance of OFDM," in *Vehicular Technology Conference, 1997, IEEE 47th*, 1997, pp. 1634-1638 vol.3.
- [76] P. Horvath and I. Frigyes, "Effects of the nonlinearity of a Mach-Zehnder modulator on OFDM radio-over-fiber transmission," *Communications Letters, IEEE*, vol. 9, pp. 921-923, 2005.
- [77] T. Berceli, M. Csornyei, B. Klein, and T. Banky, "Nonlinear effects in optical-wireless OFDM signal transmission," in *Microwave Photonics, 2002. International Topical Meeting on*, 2002, pp. 225-228.
- [78] B. Zhang, Y. Lu, J. Zhang, and B. Yang, "Nonlinear Effect of OFDM in Radio-over-Fiber transmission," in *Microwave and Millimeter Wave Technology, 2007. ICMMT '07. International Conference on*, 2007, pp. 1-3.
- [79] J. G. Proakis and D. G. Manolakis, *Digital signal processing*, 4th ed. Upper Saddle River, N.J.: Pearson Prentice Hall, 2007.
- [80] H. Ochiai and H. Imai, "Performance analysis of deliberately clipped OFDM signals," *IEEE Trans. Commun.*, vol. 50, pp. 89-101, Jan., 2002.
- [81] J. D. Jobson. (1991). *Applied Multivariate Data Analysis: Regression and Experimental Design*.
- [82] E. Limpert, W. A. Stahel and M. Abbt, "Log-normal Distributions across the Sciences: Keys and Clues". Available: <http://stat.ethz.ch/~stahel/lognormal/bioscience.pdf>
- [83] B. Cutler, "Effects of physical layer impairments on OFDM systems". Available: <http://images.industryclick.com/files/4/0502Cutler36.pdf>
- [84] W. Xianbin, T. T. Tjhung, and C. S. Ng, "Reduction of peak-to-average power ratio of OFDM system using a companding technique," *Broadcasting, IEEE Transactions on*, vol. 45, pp. 303-307, 1999.
- [85] X. Huang, J. Lu, J. Zheng, J. Chuang, and J. Gu, "Reduction of peak-to-average power ratio of OFDM signals with companding transform," *Electronics Letters*, vol. 37, pp. 506-507, 2001.
- [86] T. G. Pratt, N. Jones, L. Smee, and M. Torrey, "OFDM link performance with companding for PAPR reduction in the presence of non-linear amplification," *Broadcasting, IEEE Transactions on*, vol. 52, pp. 261-267, 2006.
- [87] J. Tao and Z. Guangxi, "Nonlinear companding transform for reducing peak-to-average power ratio of OFDM signals," *Broadcasting, IEEE Transactions on*, vol. 50, pp. 342-346, 2004.
- [88] P. Assimakopoulos, A. Nkansah, N. Gomes, and D. Wake, "Multi-channel signal transmission through radio over fiber architecture," in *IEEE GLOBECOM Workshops (GC Wkshps)*, 2011, pp. 152-156.

- [89] L. W. Couch, *Digital and analog communication systems*, 7th ed. Upper Saddle River, N.J.: Pearson/Prentice Hall, 2007.
- [90] W. Xianbin, T. T. Tjhung, and C. S. Ng, "Reply to the comments on Reduction of peak-to-average power ratio of OFDM system using a companding technique," *Broadcasting, IEEE Transactions on*, vol. 45, pp. 420-422, 1999.
- [91] M. Ahmed, M. Yamada, and M. Saito, "Numerical modeling of intensity and phase noise in semiconductor lasers," *Quantum Electronics, IEEE Journal of*, vol. 37, pp. 1600-1610, 2001.
- [92] K. Petermann, *Laser diode modulation and noise*. Dordrecht ; Boston: Kluwer Academic Publishers, 1988.
- [93] W. S. C. Chang, *RF photonic technology in optical fiber links*. Cambridge, UK ; New York: Cambridge University Press, 2002.
- [94] L. A. Coldren and S. W. Corzine, *Diode lasers and photonic integrated circuits*. New York: Wiley, 1995.
- [95] Virtual Photonics Incorporated, *Photonic modules reference manual*. Available: <http://www.vpiphotonics.com>.
- [96] F. Habibullah and W.-P. Huang, "A self-consistent analysis of semiconductor laser rate equations for system simulation purpose," *Optics Communications*, vol. 258, pp. 230-242, 2006.
- [97] L. Bjerkan, A. Royset, L. Hafskjaer, and D. Myhre, "Measurement of laser parameters for simulation of high-speed fiberoptic systems," *Lightwave Technology, Journal of*, vol. 14, pp. 839-850, 1996.
- [98] G. Jianjun, L. Xiuping, J. Flucke, and G. Boeck, "Direct parameter-extraction method for laser diode rate-equation model," *Lightwave Technology, Journal of*, vol. 22, pp. 1604-1609, 2004.
- [99] I. Tomkos, I. Roudas, R. Hesse, N. Antoniadis, A. Boskovic, and R. Vodhanel, "Extraction of laser rate equations parameters for representative simulations of metropolitan-area transmission systems and networks," *Optics Communications*, vol. 194, pp. 109-129, 2001.
- [100] P. A. Morton, T. Tanbun-Ek, R. A. Logan, A. M. Sergent, P. F. Sciortino, and D. L. Coblentz, "Frequency response subtraction for simple measurement of intrinsic laser dynamic properties," *Photonics Technology Letters, IEEE*, vol. 4, pp. 133-136, 1992.
- [101] J. C. Cartledge and R. C. Srinivasan, "Extraction of DFB laser rate equation parameters for system simulation purposes," *Lightwave Technology, Journal of*, vol. 15, pp. 852-860, 1997.
- [102] G. P. Agrawal, *Fiber-optic communication systems*, 3rd ed. New York: Wiley-Interscience, 2002.
- [103] FUTON project Deliverable D5.7, "Performance of radio over fibre distribution network", 2010. Available: www.ict-futon.eu
- [104] B. Dhivagar, M. Ganesh Madhan, and X. Fernando, "Analysis of OFDM signal through optical fiber for Radio-over-Fiber transmission," in *Access Networks & Workshops, 2007. AccessNets '07. Second International Conference on*, 2007, pp. 1-8.
- [105] FUTON project Deliverable D5.3, "Modelling and interim predicted performance of radio over fibre distribution network", 2009. Available: www.ict-futon.eu
- [106] C. van den Bos, M. H. L. Kouwenhoven, and W. A. Serdijn, "Effect of smooth non-linear distortion on OFDM BER," in *Circuits and Systems, 2000. Proceedings. ISCAS 2000 Geneva. The 2000 IEEE International Symposium on*, 2000, pp. 469-472 vol.4.